UNIVERSITY OF SOUTHAMPTON

FACULTY OF PHYSICAL SCIENCES AND ENGINEERING

Physics & Astronomy

Z' phenomenology in $t\bar{t}$ and its asymmetries at the LHC

by

Ken A V Mimasu

Thesis for the degree of Doctor of Philosophy

January 2014

UNIVERSITY OF SOUTHAMPTON

ABSTRACT

FACULTY OF PHYSICAL SCIENCES AND ENGINEERING
Physics & Astronomy

Doctor of Philosophy

Z' PHENOMENOLOGY IN $T\bar{T}$ AND ITS ASYMMETRIES AT THE LHC

by Ken A V Mimasu

This thesis presents a collection of studies considering Z' physics in the $t\bar{t}$ final state at the Large Hadron Collider (LHC), focusing largely on its charge and spin asymmetry observables. The analyses employ parton level simulations in the presence of the tree-level backgrounds and realistic reconstruction efficiency estimates. A number of extra $U(1)$ models are studied, including various common benchmark models currently considered at the LHC as well as models more suited to $t\bar{t}$ searches from composite Higgs scenarios and extra dimensions. The studies address the ability of $t\bar{t}$, with its asymmetries, to distinguish models from the Standard Model background and one another, both on its own and as a complementary channel to other, more traditional final states with the view to a complete characterisation of the Z' couplings. Scenarios with two quasi-degenerate resonances are also considered where $t\bar{t}$ asymmetries can identify their presence when cross section observables cannot resolve the two peaks.

Contents

List of Figures

List of Tables

Declaration of Authorship

I, Ken A V Mimasu , declare that the thesis entitled *Z' phenomenology in $t\bar{t}$ and its asymmetries at the LHC* and the work presented in the thesis are both my own, and have been generated by me as the result of my own original research. I confirm that:

- this work was done wholly or mainly while in candidature for a research degree at this University;
- where any part of this thesis has previously been submitted for a degree or any other qualification at this University or any other institution, this has been clearly stated;
- where I have consulted the published work of others, this is always clearly attributed;
- where I have quoted from the work of others, the source is always given. With the exception of such quotations, this thesis is entirely my own work;
- I have acknowledged all main sources of help;
- where the thesis is based on work done by myself jointly with others, I have made clear exactly what was done by others and what I have contributed myself;
- parts of this work have been published as: [1], [2], [3] and [4]

Signed:.....

Date:.....

Acknowledgements

Firstly, I would like to thank my supervisor, Stefano Moretti, for his guidance and encouragement and with whom it has been a pleasure to learn under and collaborate. My experience over the past few years has been immeasurably enhanced by the colleagues who shared the journey; I am fortunate to have been in such good company both inside and outside of the office. Specifically, thanks to: Diego Becciolini for sharing your physics knowledge, the great music recommendations and the silly memes; Matthew Brown for being the ultimate sounding board, our daily discussions (mostly about physics) were beyond invaluable; James Callaghan for raising my pool and poker games and for all the good times in the process; James Lyon for always patiently explaining things to me and especially for being my Python guru; Luca Marzola for your role as the office's Italian language supervisor and my series-watching buddy; Ben Samways for having been on the journey with me since the beginning, my belly and I particularly loved our time at CERN; Patrik Svantesson, our many conversations, both serious and not-so-serious, were much appreciated.

I am also very grateful toward the people I have collaborated with, many of whom gave me a good deal of help and also for those who contributed to the many fruitful discussions that undoubtedly improved the work we produced. To name a few: Elena Accomando, Daniele Barducci, Lorenzo Basso, Sasha Belyaev and Giacomo Cacciapaglia.

Finally, I would like to thank my family and friends for everything up until now and beyond, the love and support I have received all of my life could not have been any better. The list is by no means exhaustive and thanks go out to all of the other students in the group and others outside of SHEP who made my PhD life an enjoyable one, with special mention going to Hugh, Tasha, Jordan and Delphine.

Nomenclature

SM	Standard Model
BSM	Beyond the Standard Model
GWS	Glashow–Weinberg–Salam
QED	Quantum Electrodynamics
QCD	Quantum Chromodynamics
GUT	Grand Unified Theory
KK	Kaluza–Klein
SSM	Sequential Standard Model
LR	Left-Right symmetric
B-L	Baryon minus Lepton number
TC	Technicolour
4DCHM	Four-Dimensional Composite Higgs Model
(A)ADD	(Antoniadis–)Arkani-Hamed–Dvali–Dimopoulos
UED	Universal Extra Dimensions
VEV	Vacuum-Expectation-Value
(p)NGB	(pseudo) Nambu–Goldstone Boson
PDF	Parton Density Function
pp	proton proton
$p\bar{p}$	proton anti-proton
gg	gluon gluon
$q\bar{q}$	quark anti-quark
CM	Centre of Mass
LO	Leading Order
LL	Leading Logarithm
DY	Drell–Yan
BR	Branching Ratio
FCNC	Flavour Changing Neutral Current
EWPT	Electroweak Precision Test
NWA	Narrow Width Approximation
M_P	Planck Mass

Chapter 1

Introduction: The Standard Model and beyond

The work in this thesis aims to connect the phenomenology of two major aspects of physics beyond the Standard Model (SM). Firstly, the ubiquitous Z', arising in a multitude of different new physics scenarios as a consequence of the minimal continuous symmetry group $U(1)$, so often a relic of extending the symmetries of the SM. This neutral vector particle, resembling a heavy version of the Z–boson, is one of the primary discovery candidates at the LHC, owing to its widespread occurrence in new theories and relatively simple resonant signal in collider experiments. The second aspect is that of top quark physics and specifically the top anti-top or $t\bar{t}$ channel at the LHC. The very large mass of the top quark and its associated radiative contribution to the Higgs mass in the SM is strong motivation behind its likely important role in the mechanism of Electroweak Symmetry Breaking (EWSB). Naturally generating the large top mass while protecting the mass of the Higgs against radiative corrections often leads to theories where the top has a major role and is strongly coupled to new sectors. It is no coincidence that $t\bar{t}$ production is one of the major cross sections at the LHC, which is often termed a "top factory".

Not only is the $t\bar{t}$ channel one of the primary areas in collider searches for physics beyond the SM, the short lifetime of the top quark ensures that it decays before hadronisation, allowing new asymmetry observables to be defined in terms of its decay products to extract the spin information of the parent top. These observables display unique dependences on the chiral couplings of resonant signals such as Z's and could provide new information on such an object should it be discovered at the LHC. Thus, a variety of Z' scenarios will be tested, focusing of asymmetries in the $t\bar{t}$ final state. The aim will be to discuss the ability of $t\bar{t}$ to distinguish models from the SM background and amongst themselves both on its own and in conjunction with other channels. The unique coupling dependence of the asymmetry observables will be exploited to this end for a number of

standard benchmarks as well as models more suited to $t\bar{t}$ searches through enhanced third generation quark couplings or suppressed leptonic couplings. A new way of identifying the presence of multiple, quasi-degenerate resonant physics will also be shown using asymmetries in a scenario where the mass resolution of the search channels cannot determine the presence of two peaks. Ultimately, the goal of this work is to motivate a full use of this final state and its asymmetries to characterise as much as possible the couplings of Z's, should they be observed at the LHC, with a particular focus on asymmetries and what they can offer over simpler cross section based observables.

Beginning with introductions to the SM, top quark physics and Z's in the context of asymmetries in Chapters 2 and 3, the thesis will then follow into a number of studies. The first step, in Chapter 4, is to consider the most common Z' benchmark scenarios searched for at the LHC in di-lepton final states as a yardstick with which to compare $t\bar{t}$ and its ability to observe and distinguish them. Next, Chapter 5 examines the use of $t\bar{t}$ in conjunction with a number of other final states and their asymmetries to determine its utility as a complementary channel in disentangling variants of a minimal $U(1)$ extension of the SM. Chapter 6 moves to the investigation of a general composite Higgs model where the new physics couples most strongly to the third generation quarks and involves a number of Z's. Finally, in Chapter 7, a novel method of using asymmetries to identify quasi-degenerate resonances is demonstrated using a realistic implementation of a model of extra dimensions which simultaneously possesses enhanced quark and suppressed leptonic couplings. Chapter 8 presents the final conclusions and outlook.

The SM of particle physics represents the cutting edge in our understanding of the elementary particles in our universe and their interactions via three of the four fundamental forces: the strong force, the weak force and electromagnetism. It is the culmination of theoretical progress from the classical to the quantum level resulting in a quantum field theory which consistently describes the dynamics of the sub atomic world that has, so far, stood the test of time since its formalisation in the mid 1970s. The Glashow-Weinberg-Salam (GWS) Lagrangian [5] along with Quantum Chromodynamics (QCD) encapsulates all of these properties and interactions with only 17 free parameters in addition to the strong coupling[1], a testament to the reductionist principles of theoretical physics. This chapter presents a brief overview of the principles of gauge symmetry and spontaneous symmetry breaking and how they are realised in the SM. Some considerations on why theories beyond the SM are needed are discussed, particularly in the context of the Higgs and the top quark.

[1] A further parameter associated with strong CP exists in principle, but is assumed to be zero and not discussed in detail in this thesis. Furthermore, the SM does not incorporate the, now experimentally established, fact that neutrinos have a mass which would further increase the number of parameters by 7 or 9 depending on the, as yet unknown, Dirac or Majorana nature of neutrinos.

1.1 Gauge structure and matter content

The key principle behind the simplicity of the SM is that of gauge symmetry. From a physical and mathematical perspective, it has always been vital to recognise and exploit the presence of symmetries in order to describe the behaviour of interacting systems. Classically, these result in conservation laws for the currents associated to a particular global symmetry of a Lagrangian. Noether's theorem elucidated this notion by which translational symmetry in time and space, for example, lead to the conservation of energy and momentum respectively. Local or gauge symmetries, however, are a property attached to each point in space-time that require the presence of a new interaction with a force carrier to ensure they are preserved. The simple example of a local phase transformation illustrates this for a Lagrangian density describing a free, massless fermion field

$$\mathcal{L}_{Dirac} = i\bar{\psi}\partial\!\!\!/\psi. \tag{1.1}$$

The usual Feynman slashed notation denotes the contraction of a Lorentz four-vector with the gamma matrices defined below. These are constructed to realise the spin-$\frac{1}{2}$, spinor representations of the Lorentz group in which fermions live, ensuring that the quantity $\bar{\psi}\gamma^{\mu}\psi$ also transforms as four-vector. A common basis in which to express these spinor-space matrices is the so-called Weyl basis where:

$$\begin{aligned} \gamma^{\mu} &= \begin{pmatrix} 0 & \sigma^{\mu} \\ \bar{\sigma}^{\mu} & 0 \end{pmatrix}, \\ \sigma^{\mu} &= (I, \vec{\sigma}); \quad \bar{\sigma}^{\mu} = (I, -\vec{\sigma}), \end{aligned} \tag{1.2}$$

with $\vec{\sigma}$ representing the three-vector of Pauli matrices. The objects form a Clifford algebra characterised by an anti-commutation relation,

$$\{\gamma^{\mu}, \gamma^{\nu}\} = -2g^{\mu\nu}, \tag{1.3}$$

where $g^{\mu\nu}$ is the usual Minkowski metric. Equation 1.1 is manifestly invariant under a global phase shift $\psi \to e^{i\alpha}\psi$. However, in order to preserve the symmetry under a local phase transformation $\alpha \to \alpha(x)$, one should introduce a connection or gauge field, A_{μ}, with specific transformation properties under $U = e^{i\alpha(x)}$ coupling to the matter field with strength e as:

$$\mathcal{L}_{U(1)} = \frac{1}{4}F^{\mu\nu}F_{\mu\nu} + i\bar{\psi}D\!\!\!/\psi, \tag{1.4}$$

$$D_{\mu} = \partial_{\mu} + ieA_{\mu}, \tag{1.5}$$

$$F_{\mu\nu} \equiv -\frac{i}{e}[D_{\mu}, D_{\nu}] = \partial_{\mu}A_{\nu} - \partial_{\nu}A_{\mu}, \tag{1.6}$$

$$A_{\mu} \to -\frac{i}{e}UD_{\mu}U^{\dagger} = A_{\mu} - \frac{1}{e}\partial_{\mu}\alpha \tag{1.7}$$

where a minimal coupling has been introduced via the covariant derivative, D_μ, and also the kinetic term for the vector field via the field strength tensor, $F_{\mu\nu}$. The subscript $U(1)$ alludes to the fact that this particular transformation is associated to the Lie group of that name. While seemingly arbitrary, quantisation of this theory is the basis for the description of the electromagnetic interaction or Quantum Electrodynamics (QED). The Noether current of this symmetry, $J_\mu = \bar{\psi}\gamma_\mu\psi$, is associated to the conservation of electric charge and couples directly to the gauge field which we identify as the photon. The gauge symmetry governing this theory "protects" it and ensures consistent predictivity upon quantisation. If the gauge coupling, e, is considered small, perturbation theory is a good way of calculating observables.

The SM consists of the combination of three such symmetries whose specific properties associate them to a particular group structure. This combined structure can be summarised as an $SU(3)_C \times SU(2)_L \times U(1)_Y$ gauge group, where C, L and Y denote colour, left-handed weak isospin and hypercharge respectively. The gauge interactions of the SM are thus characterised according to this group construct and the representations in which the fermionic matter fields transform under each gauge group. The matter fields, quarks and leptons, come in three generations differing only by the increasing mass of the particle. The final ingredient, which will be introduced later, is the Higgs boson, responsible for generating masses in a gauge invariant way.

1.2 Quantum Chromodynamics

QCD refers to the $SU(3)_C$ component of the gauge group and is responsible for the strong interaction between quarks, which live in the dimension 3 fundamental representation – hence the labels "red", "green" and "blue" to denote their charge. The eight generators of the group give rise to eight gluons that mediate the force. The Lagrangian for this theory can be written in two terms, one describing the gluons and the other, the quarks.

$$\mathcal{L} = -\frac{1}{4}G_a^{\mu\nu}G^a_{\mu\nu} + \sum_{quarks} i\bar{\psi}\not{D}\psi, \tag{1.8}$$

where $G_a^{\mu\nu}$ denotes the non-Abelian field strength tensor for the gluon fields, A^a_μ, and the covariant derivative, D_μ, incorporates the interactions of quarks with the gluons necessitated by the requirement of $SU(3)$ gauge invariance. All of this can be seen as a generalisation of Equations 1.4–1.7 to a non-Abelian group.

$$G^a_{\mu\nu} = \partial_\mu A^a_\nu - \partial_\nu A^a_\mu + g_s f^a_{bc} A^b_\mu A^c_\nu, \tag{1.9}$$

$$D_\mu = \partial_\mu + ig_s\vec{A}_\mu, \tag{1.10}$$

$$\vec{A}_\mu \to -\frac{i}{g}UD^a_\mu U^\dagger = \vec{A}_\mu - \frac{1}{g}\partial_\mu\vec{\alpha} - f_{abc}\alpha^a A^b_\mu T^c. \tag{1.11}$$

The gauge transformation $U = e^{i\vec{\alpha}}$ is now parameterised by a set of "angles", α_a, as $\vec{\alpha} = \alpha_a T^a$ where the T^a are the $SU(3)$ generators. Each gluon is equally associated with a generator as $\vec{A}_\mu = T_a A^a_\mu$, whose non-Abelian nature defines a set of structure constants via $[T^a, T^b] = i f^{ab}_c T^c$, modifying the gauge transformation properties of the gluons with respect to the Abelian case in Section 1.1. This property of $SU(3)$ is what leads to the three and four-point self-interactions of the gluons, which arise from expanding the gluon field strength term to recover a normal Abelian gauge-kinetic term plus said self-interactions. The interaction of the gluons with the quarks is vector-like (meaning it treats right- and left-handed chiral components equally) and flavour blind, conserving charge (C) and parity (P) symmetries separately.

In the massless limit the theory possesses a global symmetry in which the right and left-handed chiral components of the N flavours of quarks can be independently rotated among themselves. This is known as an $SU(N)_L \times SU(N)_R$ chiral symmetry. This symmetry is dynamically broken to $SU(N)_V$ by non perturbative effects which, in short, cause the quark bilinear operator, $q^\dagger_L q_R$, to develop a non-zero vacuum expectation value (VEV). The V denotes "vectorial", meaning that the action is now only invariant under transformations which rotate left and right-handed components identically. Pseudoscalar meson multiplets arise as the Nambu-Goldstone bosons associated to the $N^2 - 1$ broken axial (treating left and right oppositely) generators of the symmetry group. These mesons are, in fact, pseudo Nambu-Goldstone bosons (pNGB) since the chiral symmetry is also explicitly broken by quark mass terms of the form $m_q\, q^\dagger_L q_R$, giving these objects a relatively small mass compared to other mesons of similar quark content. The mass terms are generated by the spontaneous breaking of Electroweak (EW) symmetry discussed in the next section. We now know of the existence of 6 types of quarks named the up, down, charm, strange, bottom and top in order of increasing mass. The approximate chiral symmetry tends to be restricted to $N = 3$ with the u, d, s triplets giving rise to the famous "eightfold way" meson spectrum of the pions, kaons and etas.

Working in the perturbative regime, it can be shown that radiative (loop) corrections to the two and three-point correlation functions and subsequent renormalisation of the QCD gauge coupling, g_s, introduces a scale dependence, or running, such that the theory becomes non perturbative at energies below a GeV. Conversely, as one increases the energy the strong coupling becomes gradually weaker. This is known as asymptotic freedom or infra-red slavery and is observed to lead to quark confinement, whereby quarks cannot be observed as a free particle due to a potential between interacting coloured objects which grows linearly with separation (i.e. decreasing scale). This has also been shown with lattice QCD computations. Consequently, quarks or gluons produced at collider experiments, rather than travelling freely, cause hadronisation and are seen as jets of mesons and/or baryons. In other words, the large energy density of the increasing potential promotes the pair creation of quarks, which bind into colour singlet states.

1.3 Electroweak theory

The remaining $SU(2)_L \times U(1)_Y$ factor of the SM gauge structure describes the unified electromagnetic and weak nuclear forces in an elegant formalism summarised by the GWS Lagrangian. The gauge structure itself does not present anything new compared to QCD in that $SU(2)$ is also a non-Abelian group whose structure constants are the totally antisymmetric epsilon tensor, ϵ_{ijk}. The hypercharge $U(1)$ is no different from the symmetry under a local phase change of QED with a different charge, Y. The gauge sector now describes four gauge fields and the covariant derivative for this sector can then be written as in the case of QCD with new gauge couplings g and g' as:

$$\mathcal{L}_{gauge} = -\frac{1}{4} W_i^{\mu\nu} W^i_{\mu\nu} - \frac{1}{4} B^{\mu\nu} B_{\mu\nu}, \tag{1.12}$$

$$D_\mu = \partial_\mu + ig\vec{W}_\mu + ig'\frac{Y}{2}B_\mu. \tag{1.13}$$

As a non abelian gauge field $W^i_{\mu\nu}$ has the same structure as the QCD field strength tensor $G^a_{\mu\nu}$, while the hypercharge field strength tensor corresponds to the QED-like Abelian one, $B_{\mu\nu} = \partial_\mu B_\nu - \partial_\nu B_\mu$. A distinguishing feature of the Electroweak interaction with respect to QCD is that the interaction is chiral. This means that the left and right-handed components of matter fermions transform in different representations of $SU(2)_L$. As suggested by the subscript, right-handed fermions are singlets under the gauge groups meaning they transform in the trivial representation while left-handed ones transform in the fundamental as doublets. The 3 generators can be represented by the Pauli matrices, $T_i = \frac{1}{2}\sigma_i$, which act on doublets of left-handed up and down-type quarks, $(u,d)_L$, $(c,s)_L$ and $(t,b)_L$ and also charged leptons and their neutrino, $(\nu_e, e)_L$, $(\nu_\mu, \mu)_L$ and $(\nu_\tau, \tau)_L$.

What further separates this sector from a theory like QCD is the fact that the weak nuclear force is short-range. First observed in radioactive beta decay, it appeared to be a four point interaction between an up quark, a down quark, a lepton and a neutrino. This is explained by the fact that the gauge fields themselves are massive and their propagation leads to a force described by a Yukawa potential $\propto exp(-Mr)$, with M the mass of the force carrier. This implies that Electroweak symmetry must somehow be broken since explicit mass terms for gauge fields, $\sim M^2 A_\mu A^\mu$, not originating from any mechanism in particular manifestly break gauge invariance. In fact, naive fermion mass terms also break gauge invariance in a chiral theory. Thus, a mechanism is needed to generate the observed masses of the SM fields.

1.4 Electroweak symmetry breaking

The SM describes the spontaneous breaking of the symmetry by a complex, scalar $SU(2)_L$ doublet, ϕ, with hypercharge 1. The mechanism is attributed to a number of people and is known in its most politically correct form as the Anderson-Brout-Englert-Guralnik-Hagen-Higgs-Kibble-'t Hooft mechanism (ABEGHHK'tH for short). Writing all of the allowed gauge invariant terms of mass dimension 4 describes the dynamics of this field with the Lagrangian composed of the covariant kinetic term and a general potential, V:

$$\mathcal{L}_{Higgs} = (D^\mu\phi)^\dagger(D_\mu\phi) - V(\phi); \quad \phi = \begin{pmatrix}\phi^+\\ \phi^0\end{pmatrix}, \tag{1.14}$$

$$V(\phi) = -\mu^2\phi^\dagger\phi + \frac{\lambda}{2}(\phi^\dagger\phi)^2. \tag{1.15}$$

with λ and μ real, along with some additional terms describing a Yukawa interaction with matter fields:

$$\mathcal{L}_{Yukawa} = \{Y^d_{ij}\bar{Q}^i_L\,\phi\,d^j_R + Y^u_{ij}\bar{Q}^i_L\,\tilde{\phi}\,u^j_R + Y^e_{ij}\bar{L}^i_L\,\tilde{\phi}\,e^j_R\} \;+\; h.c. \tag{1.16}$$

where Q and L denote quark and lepton $SU(2)_L$ doublets, d, u and e indicate down-type quarks, up-type quarks and charged leptons respectively and the Yukawa couplings,Y^f_{ij} are a set of matrices over generational indices i, j. The conjugate field $\tilde{\phi} = i\sigma_2\phi^*$ has also been introduced. These Yukawa couplings account for 9 of the free parameters of the SM.

The Higgs field allows for the presence of mass-like terms for both gauge bosons and fermions that were formerly forbidden by gauge symmetry. Mass terms are then generated by allowing the Higgs field to develop a non-zero vacuum-expectation-value, dictated by the minimisation of the potential described in Equation 1.14,

$$\Phi^\dagger\Phi = v^2, \tag{1.17}$$

$$v^2 = \frac{\mu^2}{\lambda}; \quad \mu^2, \lambda > 0. \tag{1.18}$$

A simple way to express the minimised field is in so-called unitary gauge. Since only the modulus squared of the Higgs field is constrained by Equation 1.17, a simple choice is to set the value of one of the four real components to v. Provided the other three components satisfy $\sum\varphi_i^2 = 0$, we are free to choose any value for them, including zero. Rotating around this invariant space lead to equivalent solutions to the Higgs' equation of motion while oscillations about the "radial" direction around v correspond to the

physical, scalar degree of freedom of the Higgs boson, $h(x)$.

$$\Phi = \begin{pmatrix} 0 \\ v + \frac{1}{\sqrt{2}}h(x) \end{pmatrix}. \tag{1.19}$$

This gauge choice hides the presence of the unphysical Goldstone modes associated with the broken generators of $SU(2)_L \times U(1)_Y$. Expanding the gauge interactions and potential using Φ leads to a canonical kinetic term for the boson h with mass $2\lambda v^2$ along with several self-coupling terms, a set of interactions between h and the EW gauge bosons and, most importantly, their mass terms:

$$\begin{aligned} \mathcal{L}_{EWSB} = \frac{1}{2}(\partial h)^2 - \lambda v^2 h^2 - \frac{\lambda v}{\sqrt{2}}h^3 - \frac{\lambda}{8}h^4 + \frac{1}{4}\left(v + \tfrac{1}{\sqrt{2}}h\right)^2 \\ \times \left(2g^2 W_\mu^+ W_-^\mu + \begin{pmatrix} B_\mu & W_\mu^3 \end{pmatrix} \begin{pmatrix} g^2 & -gg' \\ -gg' & g'^2 \end{pmatrix} \begin{pmatrix} B_\mu \\ W_\mu^3 \end{pmatrix} \right). \end{aligned} \tag{1.20}$$

A basis rotation for the charged currents, $W_{1,2}$, has been made defining the W bosons, $\sqrt{2}W_\pm = W_1 \pm iW_2$, with mass $M_W = \frac{1}{\sqrt{2}}gv$. The neutral current sector is then diagonalised by moving to the basis (Z, A) using a rotation by the Weinberg angle θ_W, which – when related to the gauge couplings by $Yg' = g\tan\theta_W$ – allows one to identify the two mass eigenstates of the photon and Z boson with masses of zero and $\frac{M_W}{\cos\theta_W}$. The particular combination of the two diagonal generators T^3 and Y that makes up the massless mode is precisely that which annihilates the vacuum, v_i, implying that a gauge transformation in this direction leaves it invariant. The other orthogonal combinations which do not respect this correspond to the broken directions, continuously transforming the ground state among degenerate vacua. Although the gauge symmetry is said to have been spontaneously broken, it having been hidden is a better description of what has happened given that the theory is still technically gauge invariant, just not manifestly so.

It is commonly said that the massive EW gauge bosons have "eaten" the Goldstone modes corresponding to the three broken generators in going from $SU(2)_L \times U(1)_Y \to U(1)_{EM}$. The now massive gauge bosons have accrued a longitudinal (zero helicity) polarisation, for which $\partial^\mu A_\mu \neq 0$, with which the Goldstone degrees of freedom can be shown to mix [6]. The Goldstone equivalence theorem is a statement of this correspondence between the Goldstone bosons of a spontaneously broken gauge theory and the longitudinal polarisations of the gauge fields, V, stipulating that in the high energy limit, $E \gg M_V$, amplitudes involving the latter in external legs are equivalent to those which they are replaced by the Goldstone modes themselves.

The masses of the W and Z bosons have been measured to be 80.385±0.015 and 91.1876±0.0021 GeV [7] respectively, fixing the value of the Weinberg angle. Measurement of the Fermi constant, G_F, associated with the effective description of the weak interaction can then fix the value of the Higgs VEV to 246 GeV. The Higgs mass, on

the other hand, is a free parameter of the theory. In fact, one can adequately describe the mechanism of mass generation with an effective chiral Lagrangian in the decoupling limit of the dynamical Higgs field i.e. taking $m_H \to \infty$. However, in this limit problems arise when considering vector boson scattering at high energies. For example, the amplitude for the process $W^+W^- \to W^+W^-$ shows an undersirable quadratic dependence on $\sqrt{s}$, the centre-of-mass (CM) energy, arising from the logitudinal components of the scattered particles. This implies a violation of unitarity at a scale around Λ =1.2 TeV and is linked to the non-renormalizability of the effective theory, which describes only the Goldstone bosons. Unitarity is restored by bringing the Higgs back into the picture through its interactions with the vector bosons and also places an upper bound on the Higgs mass of around 800 GeV [8].

1.5 Fermion interactions, masses and mixing

Considering the couplings with fermionic currents, we can now identify the electromagnetic coupling, $e = g \sin\theta_W$, as the coupling of the photon with an electromagnetic current of charge $Q = T_3 + Y/2$, where $T_3 = \pm\frac{1}{2}$ is the eigenvalue of the corresponding $SU(2)_L$ generator. The charged currents couple with strength g to the left-handed $SU(2)$ doublets in the weak basis, L, while the Z couples to a chiral current with couplings g_L and g_R

$$\mathcal{L}^{\pm} = i\frac{g}{\sqrt{2}}\mathbf{W}^{\pm}_{\mu}\bar{\psi}^i\gamma^{\mu}P_L\psi^j, \tag{1.21}$$

$$\mathcal{L}^{0} = ieQA_{\mu}\bar{\psi}\gamma^{\mu}\psi - i\frac{e}{\sin 2\theta_W}Z_{\mu}\bar{\psi}\gamma^{\mu}\left(P_L g_L + P_R g_R\right)\psi, \tag{1.22}$$

$$\begin{aligned} g_L &= T_3 - Q\sin^2\theta_W, \\ g_R &= Q\sin^2\theta_W. \end{aligned} \tag{1.23}$$

The fields $\mathbf{W}^{\pm}_{\mu} = T^1W_1 \pm iT^2W_2$ are associated with the correct combination of $SU(2)_L$ generators as defined in the previous section. The chiral projection operators $P_{L,R} = \frac{1}{2}(1\pm\gamma^5)$ have been introduced here to single out left and right-handed Weyl components of the Dirac spinors. Here, a new matrix,

$$\gamma^5 = \begin{pmatrix} I & 0 \\ 0 & -I \end{pmatrix}, \tag{1.24}$$

in the Weyl basis, is defined which anti-commutes with the other γ-matrices of Equation 1.2, is Hermitian and squares to one, allowing for the convenient definition of the projectors. The chiral nature of the EW interaction means that it explicitly violates parity, as opposed to QCD.

The same spontaneous breaking is responsible for fermion masses via the Yukawa terms described in Equation 1.16, with the Higgs field expanded around its VEV. Again, the

Yukawa matrices are generically non-diagonal and must be diagonalised to obtain the mass eigenstates of the theory. The change of basis occurs in 3 dimensional flavour space and can be written as a separate unitary transformation on each of the the up, down and charged lepton triplets

$$f_L^\alpha \to (U^f)_i^\alpha f_L^i\,; \quad f_R^\alpha \to (V^f)_i^\alpha f_R^i\,; \quad f = u, d, e \tag{1.25}$$

such that the mass matrices, M^f, are defined in the Yukawa terms as

$$\mathcal{L}_{Yukawa} = \{M^d_{\alpha\beta}\bar{d}_L^\alpha\, d_R^\beta + M^u_{\alpha\beta}\,\bar{u}_L^\alpha u_R^\beta + M^e_{\alpha\beta}\,\bar{e}_L^\alpha e_R^\beta\} \;+\; h.c. \tag{1.26}$$

$$M^f_{\alpha\beta} = v(U^{f\dagger})^i_\alpha Y^f_{ij}(V^f)^j_\beta = \delta_{\alpha\beta} m^f_\alpha \tag{1.27}$$

This basis change propagates to the quark charged current interaction, making it non-diagonal and described by the so-called Cabbibo-Kobayashi-Maskawa (CKM) matrix, $V_{\alpha\beta}$:

$$\mathcal{L}^\pm = i\frac{g}{\sqrt{2}} V_{\alpha\beta} W^+_\mu \bar{u}_L^\alpha \gamma^\mu d_L^\beta \;+\; h.c. \tag{1.28}$$

$$V_{\alpha\beta} = (U^{u\dagger})_{i,\alpha}(U^d)^i_\beta. \tag{1.29}$$

The CKM matrix describes the mixing of quarks via the charged current interaction in the mass basis. Although it is a complex 3 by 3 matrix, unitarity reduces the number of degrees of freedom from 18 to 9. Furthermore, each quark field can be freely redefined up to a phase, although an overall phase factor applied to all cannot be observed. This reduces the degrees of freedom by a further 5, characterising quark mixing by 4 real parameters. These are typically expressed by three mixing angles, θ_i and one complex phase δ_{CP} that characterises CP-violation in the charged-current interactions. The neutral current interaction, being diagonal in flavour space, is unaffected by this rotation and therefore is CP-conserving. Note that all of the above remains in the assumption of massless neutrinos. Neutrino oscillations observed in appearance and disappearance experiments provide experimental evidence for non-zero neutrino masses making of the most fundamental goals of extending the SM to incorporate neutrino masses in some way. This will also lead to an equivalent mixing in the leptonic sector described by the so-called Pontecorvo–Maki–Nakagawa–Sakata (PMNS) matrix.

1.6 State of the art

We can thus summarise the Standard Model as a renormalisable gauge theory with 18 free, continuous parameters listed as:

- 1 strong coupling constant $\alpha_s = \frac{g_s^2}{4\pi}$
- 9 Yukawa couplings Y_{ij}

SM rep.	Q_{EM}	$SU(3)_C$	$SU(2)_L$	$U(1)_Y$
Gauge sector				
G^a	0	**8**	–	–
$W^\pm$	± 1	–	$T_1 \pm iT_2$	–
Z, A	0	–	T_3	Y
Fermion sector (3 generations)				
$(u_L,\, d_L)$	$(+\frac{2}{3},\, -\frac{1}{3})$	**3**	**2**	$\frac{1}{3}$
u_R	$+\frac{2}{3}$	**3**	**1**	$+\frac{2}{3}$
d_R	$-\frac{1}{3}$	**3**	**1**	$-\frac{1}{3}$
$(\nu_L^e,\, e_L)$	$(\,0,\, -1\,)$	**1**	**2**	-1
e_R	-1	**1**	**1**	-2
Scalar sector				
(ϕ^+, ϕ^0)	$(\,1,\, 0\,)$	**1**	**2**	1

Table 1.1: Table collecting the SM gauge bosons and matter representations along with the Higgs field detailing their gauge quantum numbers and electric charges. The neutral gauge bosons Z, A are schematically denoted to belong to both $SU(2)_L$ and $U(1)_Y$ being an admixture of the diagonal components of both of these. The physical Higgs boson, $h \subset \phi^0$, is contained in the neutral component of the complex scalar doublet and can be chosen as its real part.

- 4 quark mixing parameters θ_i, δ_{CP}
- 4 EW parameters m_H, g, g', v or preferred combination thereof

The matter content can be classified according to its Lorentz transformation properties and quantum numbers under the three gauge groups, in addition to the force carriers associated to each one, as shown in Table 1.1.

The last 30 years of experimental particle physics have largely been devoted to precision measurements of these parameters in order to test the theory. So far, it can be said that the data agree extremely well with the SM hypothesis. However, one of the main missing ingredients until very recently was that, although being the main ingredient in the mechanism of EWSB, the Higgs boson itself had not been discovered and was beginning to be constrained by Large Electron-Positron collider (LEP) and Tevatron data. This milestone was finally reached in July of 2012 when the Large Hadron Collider (LHC) collaborations announced the discovery of a resonant signal, first in the $\gamma\gamma$ channel and subsequently in all of the measurable channels into which a Higgs could possibly decay [9]. The mass of the particle in question has been measured to be between 125 and 126 GeV [10]. With this discovery, the "missing ingredient" of the SM seems to have been discovered, although it remains to be seen whether its properties line up with those postulated by the SM. It goes without saying that the precise measurement of the production rates of this Higgs-like object in different channels and its branching

fractions to its decay modes is an essential test of the SM and could provide insight into physics beyond our current paradigm. One reason for this is that the couplings entering both the primary production mode (gluon-gluon fusion dominated by top loops) and discovery decay channel ($\gamma\gamma$ predominantly via both W and top loops) arise radiatively, meaning that new, high scale physics could enter in these loops and modify the rates. Many extensions of the SM (Supersymmetry, or SUSY, being the most widely quoted example) also postulate the presence of more than one Higgs-like scalar field that could share the burden of mass generation. In this case, couplings to the rest of the SM particles could be shared in some way between the observed resonance and some, as yet unobserved, particles. So far, with data from the two low-energy stages of the LHC (7 and 8 TeV), there have not been any truly significant deviations from the properties predicted by the SM, bearing in mind that we are at the very beginning of a "precision Higgs" era of particle physics.

1.7 Beyond

The success of the SM is beyond doubt in that it can account for an enormous amount of experimental observations in a vast array of different sectors. The recent discovery of a resonant object in the Higgs-like channels with angular distributions seeming to favour that of a CP-even scalar [11] further solidifies the status of the SM as the state of the art theory of fundamental interactions. That said, there are a number of reasons why it is also widely accepted that the SM is, thankfully, not the final word in the theoretical paradigm of particle physics. The very first, most glaring fact is that a consistent formulation of gravity at the quantum level has yet to be discovered, not least since it acts on a scale far removed from energies associated with the other forces, namely the Planck scale $M_P \simeq 10^{19}$GeV. The SM only does the quarters of the job in accounting for three out of the four known fundamental forces. A number of other reservations arise from more aesthetical grounds in the form of arguments about hierarchies of scales and "naturalness" while others are supported by experimental observations. Many of the issues can be linked to the free parameters of the SM since, by definition, the model itself does not explain why they take the particular values they do.

One such aspect of the free parameters is linked to the hierarchy in the masses of known fermions. It was already alluded to that the very small neutrino masses are not included in the standard formalism, even though their necessity has been determined experimentally. However, even without their inclusion, there is already a difference of six orders of magnitude between the top quark mass and that of the electron. This translates directly to a hierarchy in the Yukawa parameters. If one were to naively add neutrino masses assuming they arise from the same mechanism, said hierarchy would grow to 12 orders of magnitude. Such large differences between professed fundamental parameters of a theory do not sit well with most theoreticians and most people would

find it preferable to find a deeper reason for the range of scales spanned by the fermion mass spectrum.

Yet more potential discomfort with the SM can be associated to the Higgs boson and its self coupling, λ. While it is essentially a free parameter at our scales, it is subject to radiative corrections and therefore has an intrinsic scale dependence as discussed for the strong coupling in Section 1.2. One of the requirements of the Higgs mechanism is the positivity of this quantity, which ensures the mexican hat or wine bottle shape of the potential that allows for the development of a nonzero VEV. Furthermore, if the the coupling runs negative at some scale, μ, it may imply the existence of another, energetically favourable vacuum, rendering our present state unstable. From this stability bound, one can derive a lower limit on the Higgs mass by requiring that the lifetime of our current vacuum state tunnelling into the lower vacuum be longer than the age of the universe. One may also ask for $\lambda(\mu)$ not to become too large since the Higgs mass is defined in terms of it (Equation 1.18) and, given the fact that these calculations are performed perturbatively, we would like the interaction to also remain perturbative. In the limit $\mu \to \infty$, the only solution satisfying this is $\lambda = 0$. If, on the other hand, one assumes that some new physics appears at a higher scale, Λ, requiring $\lambda(\Lambda) \leq 1$ translates to a maximum Higgs mass. Since we would not expect the value of m_H to be greater than Λ, an upper "triviality" bound on the Higgs mass of around 1 TeV can be obtained.

In principle, none of this presents any problems since it so happens that the mass of the observed resonance as well as the values of the parameters that contribute most to the running of λ, m_{top} and α_S, appear to take values which may not violate either of the stability or triviality conditions up to M_P, bearing in mind that the theoretical uncertainty on such a statement is non negligible. However, calculating radiative corrections to the Higgs mass itself using a cutoff regularisation scheme, or the Higgs' two point correlation function as opposed to the four point one, reveals a quadratic sensitivity to the assumed cutoff. The dominant contributions come from top quark loops, EW gauge bosons, and the Higgs self couplings. Since we associate this cutoff to the scale at which new physics appears, Λ, one would hope that it is not too far off. Otherwise, renormalising the quantity by setting the bare mass to cancel the potentially large contributions to restore a Higgs mass around the EW scale becomes increasingly fune-tuned to higher and higher orders of magnitude as we increase Λ. This questions the naturalness of the theory, which admits a fundamental scalar whose mass is not protected by any symmetry in the way that gauge boson and fermion masses are protected by gauge and chiral symmetries respectively. This "protection" is manifest in the observation that setting, for example, the fermion mass to zero increases the symmetry of the Lagrangian by restoring exact chiral symmetry [12]. Consequently, the radiative corrections to the fermion mass are proportional to the mass itself and therefore vanish in this limit.

The so-called hierarchy problem in the SM can be expressed through the vast difference in the EW and Planck scales, between which the SM does not predict anything until gravitational interactions become important. Assuming M_P as our cutoff requires a vast fine-tuning of m_H to 30 orders of magnitude to prevent the Higgs mass from being pulled up to the high scale. In order to avoid these issues, theories beyond the Standard Model (BSM) can invoke the presence of new particles that interact with the Higgs in a way that cancels the quadratic divergences. Other possibilities include postulating the Higgs as not a fundamental but a composite state arising as a pNGB of a dynamically broken symmetry at a higher scale, thus providing a low cutoff for the SM. Alternatively, the Higgs can also occur as a dilaton of a higher conformal field theory. The presence of extra dimensions can also serve to dilute relative strengths of forces. Allowing gravity to propagate in the bulk, for example, can explain why gravity appears so weak in our 4-dimensional world, potentially reconciling the EW and Planck scales. Some phenomenology of examples of the two latter types of models will be presented in this thesis.

Although the topic is somewhat further removed from the collider-oriented discussions of this work, one should at least mention that the validity of the SM is also questioned by cosmological observations. From a fundamental point of view, the dominance of matter over anti-matter in the observable universe cannot be explained by the SM. Furthermore, concrete astronomical data regarding galaxy rotation curves, velocity dispersions and gravitational lensing, to name a few, predict that visible matter can only account for 15% of the total matter content of the universe. In the standard model of cosmology, Λ_{CDM}, the additional mass is termed dark matter as is not accounted for by the SM. Further still, another 70% of the mass-energy of the universe, termed dark energy, which is necessitated by the observations that the expansion of the universe is accelerating, also remains unexplained. It is plausible that some or all of these observations can be accounted for in a particle physics context.

Chapter 2

The top quark

The top quark, aside from the recently discovered Higgs candidate discussed in Chapter 1 is the heaviest and most recently discovered fundamental particle in the context of the Standard Model. Its existence was suspected since the observation of the bottom quark in 1977. The fact that the SM was capable of describing a great deal of observations by grouping quarks into weak iso-doublets, in addition to an elegant three family structure to mimic the lepton sector suggested that an "up" type quark was yet to be discovered. Its large mass was hinted at by precision EW fits made with LEP data and it was finally discovered at the Tevatron in 1995 [13]. While it was certainly unexpected that it would be so much heavier than the rest of the quarks, the discovery of the top quark spawned a new branch of particle physics which can now be counted amongst the most active sectors in the field today. On the one hand, its very large mass is the main culprit in the mysterious fermion mass hierarchy while on the other, the very same property makes it comparatively much closer to the EW scale and thus the mechanism behind mass generation. The most accurate measurement of the top quark mass to date, summarised in the recent LHC combination [14], which also uses the previously published Tevatron combination [15], quotes a value of 173.3±1.4 GeV, combining both statistical and systematic uncertainties. This sub-percent precision is a testament to the fact that we are in an era of precision top physics where many quantities are being measured with accuracies that are beginning to supersede the theoretical precision of higher order QCD calculations involving the top.

This chapter summarises the main features of the top quark and the motivations for searching for new physics in its production and decay. Experimental considerations on how tops decay and are reconstructed at collider experiments are reviewed. The $t\bar{t}$ channel is then discussed, defining the charge and spin asymmetry observables considered in this work.

2.1 Motivation

As mentioned, one of the main motivations for studying the top quark is the fact that, since its mass is so large, it must be strongly coupled to the EW symmetry breaking sector, namely the Higgs boson in the SM. In light of the recent discovery of a Higgs-like resonance at the LHC, the importance of pinning down the properties of the top quark as well as investigating possibilities of new physics connected to it is clear. As discussed in Section 1.7, the top quark is not only the main contributor to the quadratic divergence in the radiative corrections to the Higgs mass, it also plays an important role in its production and decay at collider experiments. The primary production channel is via gluon-gluon fusion to which the top loop is the main contributor, while the top also provides the largest fermionic loop contribution to one of the key investigation channels at the LHC, the decay to two photons, $h \to \gamma\gamma$. Both of these are mediated by the large Yukawa coupling of the top quark, for which the SM does not offer a natural explanation. As a consequence, the top is often an important part of BSM scenarios that seek to connect the large top mass with an alternative or more fundamental mechanism for EW symmetry breaking.

Finally, one of the key features of the top quark with respect to the work presented here is its extremely short lifetime due to its large decay width, Γ_t. The fact that $\Gamma_t \sim 1.3$ GeV is so much higher than the typical hadronisation scale of quarks, Λ_{QCD}, means that it decays almost immediately after it has been produced and most importantly, before hadronisation. This allows the top quark to pass on information to its decay products, something that lighter quarks cannot do before the hadronisation process washes out their partonic features. Naturally, this means that the top quark is a very different object from other quarks whose collider signatures are all characterised by single, hadronic jets, albeit with potentially discernible characteristics in the case of b- and c-jets. Although the top will be visible through the reconstruction of its decay products, an undoubtedly more difficult task than reconstructing a single hadronic jet, the rewards lie in the extra information that has been preserved in these daughter particles, allowing for the determination of the spin, charge and parity of the parent top. Thus the top is the closest one can get to observing a free quark, something which one can take advantage of by defining other observables, discussed later, which cannot be defined for lighter quarks and, indeed, all non-decaying objects. From both a theoretical and experimental point of view, it is fair to say that, in the top quark, we have an important player in the field of modern particle physics through the LHC era and beyond.

2.2 Reconstructing a top decay

When a top quark is produced at a collider experiment, it decays via the EW charged current interaction $W^{\pm}_{\mu}\bar{t}_L\gamma^{\mu}b_L$ of Equation 1.21, since the CKM element $V_{tb} \sim 1$. The

process is then $t \to bX$ where the two-body system, X, is the pair of leptonic or hadronic decay products of the virtual W boson. Thus a decaying top will yield a jet associated with a b-quark along with either a charged lepton and missing energy from the neutrino or a pair of light quark jets as depicted in Figure 2.1. The leptonic mode allows for a

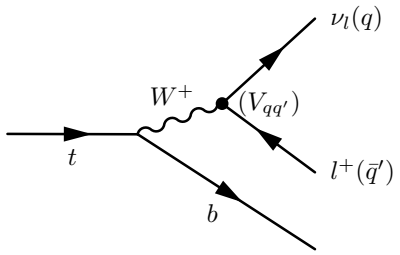

Figure 2.1: Feynman diagram for the leptonic(hadronic) decay of a top quark. In this case, q and q' denote a first or second generation up and down type quark respectively, and the decay rate is proportional to the corresponding CKM element $|V_{qq'}|^2$.

simple identification of the top charge with the drawback of missing energy. The hadronic mode does not have any missing energy but suffers from a poorer energy resolution in reconstructing jets compared to leptons. Furthermore, the absence of any leptons in the signature leads to more difficulty in distinguishing this mode from the large QCD background present at hadron colliders. It is clear that the task of reconstructing a top quark will be a relatively involved process using potentially all layers of the detector from the tracker through to the muon detector. This will have an impact on the efficiency with which events containing top quarks can be accurately identified and reconstructed. There are a number of important factors that should be elaborated on in more detail.

b-tagging

Mesons produced in the hadronisation of a b-quark have characteristic lifetimes which mean that they decay within the detector as opposed to light quark hadrons which have much longer lifetimes. Because of this, b-jets tend to originate at a displaced point with respect to the production vertex of the quark itself. This information combined with several other, more subtle, kinematical considerations and possibly also requiring the presence of a lepton arising from the semi-leptonic decay of a b-hadron can be combined into some algorithm which allows for the differentiation of b-jets from light quark and gluon initiated jets. A variety of algorithms are used, none of which are foolproof but nonetheless perform well in separating these objects, with the exception of charm quark jets, which sometimes also lead to similar signatures. b-tagging is an important component of not only top physics but various other major analyses performed the CMS and ATLAS collaborations such as Higgs searches and supersymmetry. As such, it is important to have a good understanding of the efficiencies and mis-tagging rates of these algorithms and to tailor them to suit the analysis at hand [16].

Neutrino momenta

The leptonic decay of a top quark presents both advantages and inconveniences in the sense that, even though two out of the three possible daughter leptons (e, μ) are much cleaner objects which can be reconstructed efficiently and accurately, the associated neutrino does not interact with the detector at all. The decay involving τs is treated separately since it is, in itself, a decaying object. The only information that may suggest the presence of a neutrino is the fact that net momentum in the plane transverse to the beam direction should be conserved and may not appear so if a neutrino has been produced. This statement is only true at parton level and is partially spoiled by a combination of initial state radiation and Parton Density Function (PDF) effects. Nonetheless, to a good approximation, the component of missing transverse momentum, $\not{p}_T$, can be equated to the actual p_T of invisible objects in an event. In the case of a decaying top, the single neutrino momentum can be determined in principle by assuming that it originates, together with the lepton, from the decay of a W-boson i.e. $(p_\nu + p_l)^2 \simeq M_W^2$. This leads to a quadratic equation in the unknown longitudinal (z) component of the neutrino four-momentum, which is the same as its energy since it is effectively massless ($p_\nu^2 \simeq 0$). The subsequently two-fold degeneracy can be resolved by assuming that the three daughter particles arose from the decay of a top such that $(p_\nu + p_l + p_b)^2 \simeq m_t^2$.

2.3 The $t\bar{t}$ channel

Having highlighted the fact that the top quark is one of the most important particles investigated at current generation of collider experiments, it is relevant to briefly discuss how it is produced and observed. The multi-TeV energies of the two most recent hadron colliders (LHC and Tevatron) have been ideal for producing tops either in pairs or on their own associated with either a lighter quark or a W boson. Since the top quark essentially cannot be found in the proton, the single top modes will always involve at least one weak interaction, while the pair production occurs purely via QCD and is dominated by gluon-gluon fusion. Figure 2.2 depicts the Feynman diagrams for tree-level QCD production of the $t\bar{t}$ final state. The PDF for the gluon initial state is dominant over that of a quark and anti-quark at the LHC at lower partonic momentum fractions. This can be illustrated by considering the parton luminosities, $\mathcal{L}$, of the two initial states as a function of partonic centre-of-mass (CM) energy, $\sqrt{\hat{s}}$. These are defined as [17]:

$$\mathcal{L}_{ij} \equiv \frac{\tau}{\hat{s}} \frac{dL_{ij}}{d\tau} = \frac{\tau/\hat{s}}{1+\delta_{ij}} \int_\tau^1 dx \, [f_i^a(x,Q^2) f_j^b(\tau/x,Q^2) + f_j^a(x,Q^2) f_i^b(\tau/x,Q^2)]/x, \quad (2.1)$$

where $f_p^h(x,Q^2)$ is the PDF, representing the probability of finding a parton, p, carrying a fraction, x, of the momentum of a hadron h defined at a factorisation scale, Q, and τ is the ratio of the collider and partonic CM energies. They are constructed to have

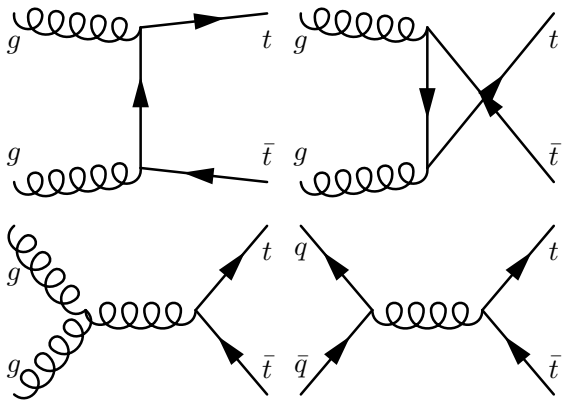

Figure 2.2: Feynman diagrams for leading order $t\bar{t}$ production via QCD. The main production mode is via the three gluon initiated diagram with an additional s-channel gluon mediated $q\bar{q}$ initial state.

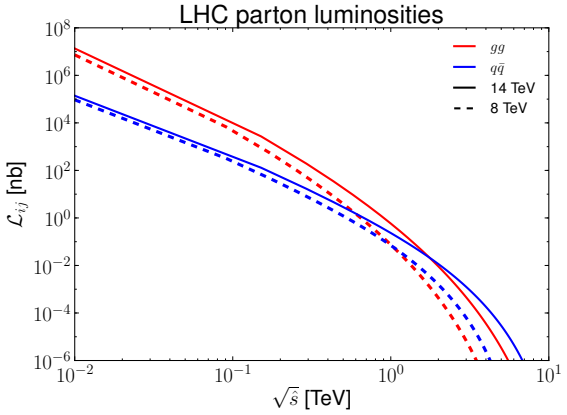

Figure 2.3: Parton luminosities as defined in Equation 2.1 for the gluon-gluon (red) and quark-antiquark (blue) as a function of partonic CM energy, $\sqrt{\hat{s}}$, for the LHC at 8 (dashed) and 14 (solid) TeV. The CTEQ6L1 leading order PDF sets were used at a factorisation scale $Q = \sqrt{s}$.

the dimensions of a cross section and provide an idea of the relative importance of different initial states while capturing the behaviour of certain typical (s-channel) cross sections that fall off with $\hat{s}$. Figure 2.3 compares the gluon-gluon luminosity to the quark-antiquark one using the CTEQ6L1 [18] PDF sets, clearly showing that for a large part of the lower energies, the gluons dominate with the cross-over occurring around 1–2 TeV. This corresponds well with the $t\bar{t}$ threshold and reinforces the fact that the production cross-section for $t\bar{t}$ is larger than that of single top production. Therefore, pair production the optimum way to produce large top quark samples at the LHC. In fact, the LHC has often been labeled as a "top factory" due to the large $t\bar{t}$ event rate expected at its design energy of 14 TeV. For this reason, the $t\bar{t}$ invariant mass distribution is a promising place in which to look for new physics in the search for potential resonant objects or deviations from SM predictions. This will be one of the main observables presented in the Z' studies presented in the later chapters and is essentially a counting exercise where events are binned according to their invariant mass, $M_{t\bar{t}}$.

In addition to being important for SM tests and BSM searches in its own right, the $t\bar{t}$ channel is also an important background to many other analyses, whose signatures the top decay products could mimic. It is therefore important that the theoretical uncertainties on top pair production be well under control. Thanks to the large top quark mass, the top pair threshold is an energy at which perturbative QCD calculations can be trusted and the determination of integrated and differential top quark observables to higher and higher orders at hadron colliders is an active field. This is particularly relevant since QCD is a strongly interacting theory. As an example, the multiplicative k-factor associated with going from tree-level to next-to-leading order (NLO) inclusive $t\bar{t}$ production at the LHC is of order 100%. Various higher order QCD [19] and pure or mixed EW [20] NLO ($\alpha_S^3, \alpha_S^2\alpha_{EW}$) corrections have been calculated in the past 30 years and the latest calculations for this process are at Next-to-Next-to-Leading Order (NNLO) in α_S and also incorporate the resummation of some large logarithms. This is a procedure by which logarithmic terms, L, that are determined to be large in the perturbative loop calculations are included by an exponentiation of the perturbative series taking $\alpha_S L$ as a new expansion parameter. In this way, partial higher order terms determined to be dominant are included to all orders in the hope that they better approximate reality and reduce theoretical uncertainties such as the sensitivity to the factorisation and/or renormalisation scale. To quote a recent result, the inclusive $t\bar{t}$ production cross section at the LHC with centre-of-mass energy, $\sqrt{s} = 14$ TeV, calculated to NNLO and resumming Next-to-Next-to-Leading Logarithms (NNLL) is 953.6 pb with a total uncertainty of about 4% [21]. Thus a nominal integrated luminosity of 100 fb^{-1} at the high energy run of the LHC should produce around one hundred million $t\bar{t}$ events.

On the experimental side, measurements of the $t\bar{t}$ production rates have been made at both low energy stages with the LHC combination for 7 TeV determined to be 173.3±10.1 pb while a number of uncombined measurements have been made in different channels by both the CMS and ATLAS collaborations for the 8 TeV run quoting a rate of 220-240 pb with uncertainties around 15% [22]. These can be compared with the predictions in [21] of 172 and 246 pb for the two energy stages, showing overall consistency between theory and experiment. The recent progression to a full NNLO calculation means that the degree of theoretical uncertainty has decreased compared to the most recent LHC measurements. Such progress is always important to maintain as experimental uncertainties continue to decrease with increasing statistics and a better understanding of detector systematics.

The $t\bar{t}$ system can, like for the single top decay, be characterised by the decay mode of the two W bosons with three possibilities termed fully hadronic, semi-leptonic and di-leptonic. Decays including τ leptons are often considered apart since they are also unstable objects. Their branching fractions are 45.7%, 43.8% (30% of which are τ's) and 10.5% (56% of which contain τ's) respectively [23]. The reconstruction of these events involves some additional complications compared to the single case. Firstly, the

di-leptonic channel now includes two neutrinos, meaning that even with the constraints discussed in the previous section, the system is under-constrained since now the number of unknowns has grown to four (the three momentum components of one neutrino and the longitudinal component of the other). Reasonable solutions can be determined by a combination of analytical and numerical methods including fits to simulated neutrino spectra [24], paying the price of larger systematic uncertainties and poorer mass resolutions. One the other side, the presence of two leptons and a minimum of two jets, two of which should fulfil b-tagging requirements, makes this a very clear signature, unpolluted by a large amount of hadronic activity. The fully hadronic channel represents the opposite case where one is faced with a large jet multiplicity and the additional combinatoric issue of which light quark jet to associate with which W boson. Typically the semi-leptonic channel is favoured for the majority of analyses as a compromise between the two where the neutrino momentum ambiguity is soluble and there are not too many light jets.

2.4 Asymmetries at colliders

The most basic measurements that one can perform at collider experiments involve measuring rates by counting events. Selecting reconstructed events that meet certain requirements related to particle content and kinematics then enables you to test hypotheses which may predict deviations from SM expectations. Naturally, a good understanding of the detectors environments, backgrounds and theoretical predictions is required in order to quantify the uncertainties involved in making a particular measurement. Pure statistical uncertainties aside, these can vary from uncertainties in object reconstruction stemming from detector limitations or intrinsic uncertainties on collider parameters such as the beam luminosity on the experimental side to Monte Carlo (MC) systematics or scale and PDF uncertainties on the theoretical side. Much of this depends on the type of objects being sought out and the information needed to construct the observable in question.

Beyond counting experiments, asymmetries are a class of observables designed to reduce errors by taking a ratio of events rather than an absolute number. It is clear that taking ratios of quantities measured in a similar way can reduce the dependence on common factors and hence the systematics associated with these. The dependence on the luminosity, $\mathcal{L}$, for example, drops out since number of events are related to cross sections, σ, by $N \propto \mathcal{L}\sigma$. This is beneficial as the luminosity uncertainty, limited by our understanding of the collider beam itself rather than detector effects, will not affect the uncertainty in an asymmetry. Furthermore, such observables also are typically not dependent on the normalisation of background fits to data. Often, these observables provide different information from cross section measurements and can be useful to both test the predictions of the SM and also have the potential to investigate the properties of

new physics. Asymmetries are defined taking a total number of events, N_T, and defining a criteria by which to divide them into two categories, N_A and N_B. The observable is then constructed as:

$$A = \frac{N_A - N_B}{N_A + N_B}. \tag{2.2}$$

From here, one can then define the statistical uncertainty on an asymmetry observable starting from the statistical uncertainty on the cross sections that given rise to N_A and N_B observed events assuming they obey Poisson statistics. For sufficiently large N, the events will be distributed according to a Gaussian with mean N and standard deviation, or error, $\sqrt{N}$ giving

$$\delta\sigma = \frac{\delta N}{\mathcal{L}} = \sqrt{\frac{\sigma}{\mathcal{L}}}, \tag{2.3}$$

$$\delta A = \sqrt{\frac{1 - A^2}{\mathcal{L}\sigma}}. \tag{2.4}$$

This measure will be used throughout this thesis. Naturally, both uncertainties scale inversely with increasing integrated luminosity. Furthermore, δA has a nonlinear dependence on the A, as opposed to a cross section measurement, and scales as a function of σ in the same way as its relative error $\sim \delta\sigma/\sigma$. The work discussed in this thesis focuses on two types of asymmetries commonly considered at collider experiments, termed charge and spin. The focus will remain on the $t\bar{t}$ channel although such observables can be measured in other final states.

2.4.1 Charge asymmetry

Charge or spatial asymmetry in collider physics is a measure of the symmetry of a particular process under charge conjugation. For an interaction which preserves CP, this translates into an asymmetry in the angular (spatial) dependence of the matrix element for the production of a two-body final state. At a hadron collider, for example, defining a polar angle, θ, as the angle between a final state particle and one of the incoming partons in the CM frame, variables that are function of this angle can be constructed to probe the asymmetry of the distribution of said angle. Such an asymmetry can only be generated from a charge asymmetric initial state such as $q\bar{q}$, as opposed to, for example, the gg initial state. In QCD, the asymmetry for the $t\bar{t}$ final state is generated dominantly at NLO via the interference of leading order $q\bar{q} \to t\bar{t}$ (see Figure 2.2) with the corresponding box diagram as well as by the interference between initial and final state gluon radiation [25]. As will be discussed later, the fact that QCD is a purely vector-like interaction means that the asymmetry cannot be generated at tree-level. There is also a subleading contribution from EW processes, both at tree- and loop-level from the chiral (parity violating) Z and/or W couplings as well as a very small effect similar to the

QCD contribution arising in QED. Charge asymmetry is one of the most well known asymmetry observables and has been used since the advent of collider experiments. The issue of defining the observable depends on the collider setup and relies on the ability to define an absolute reference direction as will be discussed by comparing the cases of the Tevatron and the LHC.

Tevatron

The Tevatron, being a $p\bar{p}$ collider, is an ideal place to measure spatial asymmetries since the polar angle in the collider frame can more or less be identified with that of the CM frame modulo PDF effects. Statistically, both incoming partons will be valence quarks and an absolute preferred direction can be unambiguously defined. The forward-backward asymmetry A_{FB}, arguably the simplest way to define the charge asymmetry, splits the fiducial region of the detector into two hemispheres and compares the number of (anti-)tops detected in either side.

$$A_{FB} = \frac{N_{t(\bar{t})}(y > 0) - N_{t(\bar{t})}(y < 0)}{N_{t(\bar{t})}(y > 0) + N_{t(\bar{t})}(y < 0)}, \tag{2.5}$$

where y is the rapidity of the observed (anti-)top and $N_{t(\bar{t})}$ denotes the number of (anti-)top quarks observed in the forward ($y > 0$) or backward ($y < 0$) direction. The rapidity is defined in terms of the observed quark four-momentum as follows:

$$y = \ln\left(\frac{E + p_z}{E - p_z}\right), \tag{2.6}$$

where E and p_z denote the energy and z-momentum of the quark and the z-direction coincides with the beam axis. For this observable, the SM prediction is of order 5%, and, interestingly, both the CDF and D$\emptyset$ collaborations report a deviation [26] from this expectation. This has generated a good deal of discussion and, so far, it appears difficult to reconcile the deviation of the A_{FB} measurement with the apparent consistency of production cross section measurements with the SM prediction.

LHC

The definition of a charge asymmetry at the LHC, however, is somewhat more involved. First, the C-symmetric di-gluon initial state dominates for a significant amount of the invariant mass range for $t\bar{t}$ final states, until the parton luminosities for $q\bar{q}$ become dominant, matching that of gg at around 1–2 TeV and remaining significant from there on, as shown in Figure 2.3. This large zero contribution dilutes the predicted SM asymmetry down to $\sim$ 1%. Secondly, even when the contribution from initial state quarks becomes important, the fact that the pp initial state itself is also C-invariant

necessitates a redefinition of the measured quantity. In this case, no preferred direction can be defined because the incoming quark will generally be a valence quark, while the antiquark must come from the sea, making it equally likely that the quark came from either proton. However, one can exploit the fact that the incoming quark will statistically carry a larger momentum fraction than the anti-quark, resulting in a correlation between the boost of the $t\bar{t}$ frame and the direction of the incoming quark. Thus, specifying the polar angle as the angle between the incoming quark and the outgoing top quark, for example, one would expect the top rapidity distribution in the lab frame to be different from the anti-top one. This is illustrated in Figure 2.4 where the two possibilities for the direction of the incoming quark are depicted for a given event producing the $t\bar{t}$ system in a fixed axis in the CM frame.

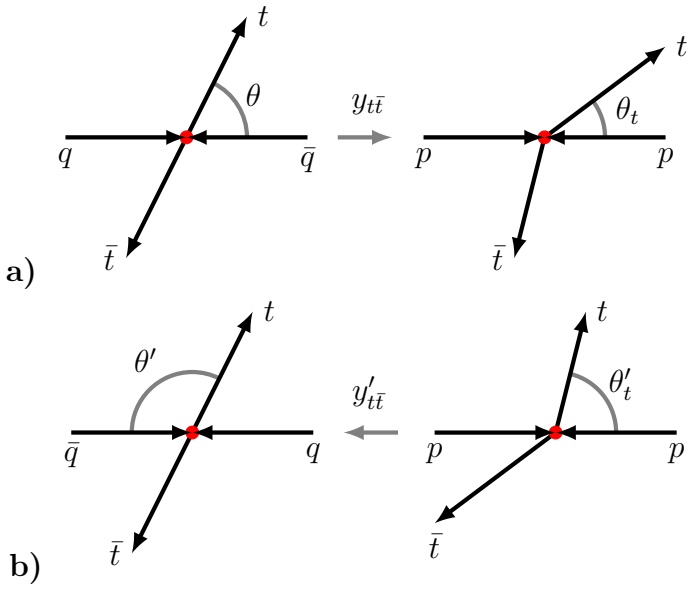

Figure 2.4: Schematic diagrams depicting the kinematics of a $q\bar{q} \to t\bar{t}$ event at the LHC where the quark came from *a*) the left or *b*) the right side proton. The left column shows the process in CM frame while the right hand column represents the observable polar angles of the top after boosting to the lab frame.

It is clear that these two configurations correspond to the partonic process characterised by two opposite angles, θ and $\theta' = \pi - \theta$. Assuming that the $t\bar{t}$ system will be boosted in the direction of the incoming quark, the left hand side sketches the resulting angles $\theta_t^{(\prime)}$ of the top quark in the lab frame. Possibility *a*) leads to an increase in the top rapidity and a corresponding decrease in that of the anti-top, while possibility *b*) does the opposite. Therefore, a degree of angular asymmetry in the partonic matrix element, i.e. $\mathcal{M}(q\bar{q} \to t\bar{t};\, \theta) \neq \mathcal{M}(q\bar{q} \to t\bar{t};\, \theta')$, will lead to different rapidity distributions for the top and anti-top.

The asymmetry can then be measured by exploiting this fact and a number of methods are employed at the LHC. One possibility is to restrict the rapidity range over which the top quarks are selected [27] and comparing the number of tops and anti-tops in

that region. Alternatively, one can construct variables that are function of the absolute rapidity difference of the top and anti-top, $\Delta y = |y_t| - |y_{\bar{t}}|$, which is sensitive to the CM polar angle and independent of the $t\bar{t}$ frame boost. Several incarnations of this observable are used throughout this work and they will be defined as they are used. An important final point to make concerning these observables at the LHC is that it is also possible to enforce certain kinematic selections that attempt to reduce the gluon-gluon initiated $t\bar{t}$ events which serve only to dilute the measured value of charge asymmetry. A simple choice is to recognise that, as opposed to the $q\bar{q}$ initial state, the two momentum fractions of the two initial state gluons should be more similar, leadings to lower boosts. Choosing events that are more boosted [28] can help to reduce the dilution effect of gluon initiated processes.

2.4.2 Spin asymmetries

As discussed before, one of the interesting features of the top quark is the fact that it decays before hadronising and passes charge and spin information onto its decay products. Specifically, the angular distributions of the decay products of the top quark depend on the its initial polarisation. This can be defined in different bases, a popular choice being the helicity basis, where the spin of the top is quantised in its direction of motion. The helicity eigenstates are related to chirality states and are equivalent to them in the massless limit. Calculating the polarised matrix element for the top decay diagram shown in Figure 2.1, gives

$$\mathcal{M}\left(t(\lambda_t) \to b\, f\, \bar{f}\right) = 2g^4 |V_{f\bar{f}}|^2 p_b \cdot p_f \left(p_{\bar{f}} \cdot (p_t - m_t\, \lambda_t \eta_3)\right) S\left(p_f \cdot p_{\bar{f}}\right) \tag{2.7}$$

where $S(Q)$ is the W propagator function carrying momentum, Q, and η_i is a spin four-vector for a top quark of momentum p_t as commonly used to project out polarisation states in a Lorentz covariant way [24, 29]. They form an orthonormal basis, $\eta^i \cdot \eta^j = \delta^{ij}$, and obey $\eta^i \cdot \vec{p}_t = 0$. The third of these, η_3, is used to obtain the component in the direction $\hat{p}_t$.

$$S(Q) = \frac{1}{(Q^2 - M_W^2)^2 + M_W \Gamma_W^2} \tag{2.8}$$

$$\eta_3^\mu = \begin{cases} \left(\frac{|\vec{p}_t|}{m_t}, \frac{E}{m_t}\hat{p}_t\right) \\ \left(0, \delta^{ij}\right) \text{ if } |\vec{p}_t| = 0 \end{cases} \tag{2.9}$$

Equation 2.7 clearly shows that the polarisation state of the decaying top, $\lambda_t = \pm 1$, in this basis will determine relative angles between decay products. Performing the full phase space integration shows that the differential decay width of the top with respect

to the angle of one of its decay products goes as:

$$\frac{1}{\Gamma_t}\frac{d\Gamma}{d\cos\theta_i} \propto (1 + P\kappa_i \cos\theta_i), \tag{2.10}$$

a result commonly cited in the literature (see, for example [30, 31, 32, 33]). Here, the angle θ_i, refers to the angle of the decay product with the spin quantisation axis while κ_i is a kinematical factor termed "spin analysing power" which depends on the decay product in question. For charged leptons, for example, $\kappa = 1$, while for the b-quark it is reduced to 0.4. In the case of $t\bar{t}$, there are many decay products and correlations between angles of decay products coming from each particle that may also be useful to consider. It is important to note that, experimentally, the polarisation is measured together with the spin analysing power of the given channel. Extracting the true value of P relies on making assumptions on the κ's, typically by using those predicted by the SM. This assumes that no new physics effects such as modifications of the tbW vertex are significantly altering the top decay process. The double angular differential distribution of a pair of fermions coming from the $t\bar{t}$ decay can similarly be written as [31, 34, 35]:

$$\frac{1}{\sigma}\frac{d\sigma}{d\cos\theta_t d\cos\theta_{\bar{t}}} \propto (1 + P_t\kappa_t \cos\theta_t + P_{\bar{t}}\kappa_{\bar{t}} \cos\theta_{\bar{t}} + C\kappa_{\bar{t}}\kappa_t \cos\theta_t \cos\theta_{\bar{t}}) \tag{2.11}$$

where the angles are again relative to the spin axis with subscripts t and $\bar{t}$ specifying the parent particle and C is a real coefficient. The $\kappa_{t(\bar{t})}$s denote the spin analysing power of the given final state particle coming from each decay. Both of these angular properties can be translated to asymmetries measured at colliders which provide useful information on the net polarisation and correlations in a sample of top quark events. All of the observables used in this work are constructed at the level of the partonic tops, before decay and can be defined directly in terms of the helicities of the outgoing $t\bar{t}$ pair. However, measuring these coefficients experimentally would eventually require analysing their decay products. The spin information can also be extracted by considering non angular distributions such as their energy fractions and p_T distributions.

The two observables considered are the so called top polarisation or single spin asymmetry, A_L, and the spin correlation or double spin asymmetry, A_{LL}. The former observable measures the net polarisation of the top (or anti-top) quark in a sample by comparing the number of positive and negative helicities, while summing over the helicity of the other.

$$A_L = \frac{N(-,-) + N(-,+) - N(+,+) - N(+,-)}{N(-,-) + N(-,+) + N(+,+) + N(+,-)} \tag{2.12}$$

where the $N(\lambda_t, \lambda_{\bar{t}})$ denotes the number of events observed with arguments, $\pm$, referring to the helicities of the top and anti-top respectively. The spin correlation, on the other hand, compares $t\bar{t}$ events where the top and anti-top have like helicities to those with

unlike helicities:

$$A_{LL} = \frac{N(+,+) + N(-,-) - N(+,-) - N(-,+)}{N(+,+) + N(-,-) + N(+,-) + N(-,+)}. \tag{2.13}$$

Both observables are extracted from fits to the angular distributions of the reconstructed decay products and correspond to the P and C coefficients of Equations 2.12 and 2.13. We will see in the next chapter that these asymmetries are sensitive to the presence of new resonant physics in the $t\bar{t}$ channel and are therefore particularly useful in the context of Z' physics.

2.5 Reconstructing $t\bar{t}$ observables

It is clear that the $t\bar{t}$ channel offers a wide choice of observables that are sensitive to new physics, particularly in the way of asymmetries. As mentioned, one of the primary complications of such analyses is the difficulty in reconstructing the six-body final state that results from the pair production of tops. Ideally, one would perform a full chain of event generation, showering and hadronisation, culminating in a detector simulation to get an accurate representation of the reconstruction process for observables of interest. The associated efficiencies will depend on the information required for the observable and the particular decay channel of the $t\bar{t}$ system. That is to say that, depending on what methods are used to extract a potential signal, the fraction of the number of events observed compared to the true number of $t\bar{t}$ pairs produced may differ. Since the studies presented in this thesis are limited to be at parton level, without subsequent decay of the tops, it was necessary to employ reasonable estimates of reconstruction efficiencies such that the predictions for the observables at the LHC correspond better to the reality of a detector environment. These are estimated in a conservative manner by gauging the efficiencies of the primary requirements of each observable in each decay channel and using a net efficiency weighted by the associated branching fraction.

The common experimental requirement between the asymmetry observables of interest and also the invariant mass distribution is a full reconstruction of the $t\bar{t}$ system. The only extra information needed for the asymmetries is the angular distributions of the decay products of one or two the tops when extracting the top spin observables. In the case of resonant physics, being able to represent the asymmetries in a binned way, like the cross section, would certainly be beneficial to extract the most information possible, given the striking lineshape of a resonant object. An important consideration for the analysis of new physics at several TeV is the likely boosted nature of the final states which will have an impact on the reconstruction process. As the scale for new physics is pushed up by ever increasing collider limits, particularly in the context of resonant objects in $t\bar{t}$, more and more energetic final states will be produced. As a result the decay products of the tops, back to back in its rest frame, will tend to become more

collimated as this frame is boosted with respect to the lab frame. This means that many traditionally reliable measurements such as b-tagging, invariant mass reconstruction and lepton isolation become hampered and must be adjusted. A variety of pruning and jet substructure methods are applied at the LHC [36] and quote efficiencies of about 30-40% to tag a hadronic top and a number of analyses have used such methods in recent resonance searches [37, 38], showing that including the boosted methods increases sensitivity to higher $t\bar{t}$ masses. The weighted efficiencies are quoted to be around 5 or 6% from each of the fully hadronic and semi-leptonic channels. As yet there are no asymmetry measurements nor analyses in the di-lepton channel using these techniques. Therefore, a total 10% efficiency is chosen as a conservative estimate to reconstruct high mass $t\bar{t}$ events. It is fair to say that the validation of boosted top reconstructions is a work in progress at the LHC and it is consequently difficult to estimate the efficacy of the varying methods used to apply to the parton level results presented in this work. It is therefore clear that, although not discussed further in this thesis, a validation of the forthcoming results including top decay, parton showering and detector effects is necessary.

Charge asymmetry measurements can be made in any of the three $t\bar{t}$ decay channels and a reconstruction of the top four momenta, after potential top-tagging using boosted methods, is sufficient to obtain the quantity and nothing extra is needed beyond sufficient statistics to represent them as a function of $M_{t\bar{t}}$. It is true, however, that determination of the top quark charge may be less precise in the case of a fully hadronic $t\bar{t}$ system. This can be done by looking at the average charge of tracks coming from a b-jet. For the studies presented later, the same reconstruction efficiency estimate of 10% is used for this observable as for the differential cross section. Spin asymmetries are more complicated to measure due to the need for reconstructing the angular distributions of decay products. What is clear is that the boosted systems will inhibit the measurement of such quantities as the collimation of the decay products approaches the angular resolution of the calorimeters. At this stage, a lack of experimental analyses makes it difficult to estimate how well they can be measured at high p_T. The top polarisation, has been discussed in this context and several potential solutions have been proposed, moving away from the requirement of fully reconstructing the decay products [33, 39]. Measurement of the spin correlation requires angular information from the decay products of both tops and should be even more difficult to reconstruct. Different reconstruction efficiencies were assumed in different studies showing the trend of becoming increasingly conservative as the importance of this issue became clearer. In fact, it may altogether be more realistic not to rely on being able to present the asymmetries in an observable, such as $M_{t\bar{t}}$, that requires the full reconstruction of the $t\bar{t}$ system.

Chapter 3

Z' physics and asymmetries

The term "Z'" most generally refers to any observed neutral resonance in a fermion–anti-fermion mass spectrum beyond those of the SM. Such a generic definition means that these objects are often present in many BSM scenarios, arising for a variety of reasons. Since the spin of a resonance cannot be determined simply by looking at the signal in the invariant mass spectrum, from an experimental point of view, scalar, vector and tensor objects all qualify for the title. However, a "true" Z' is typically considered to be a force carrier associated with a new gauge symmetry. While this somewhat reduces the possibilities for its origins, it remains true that such objects are ubiquitous in the model landscape of SM extensions are are amongst the most prevalent ingredients of theories which seek to extend the symmetries of nature. This, combined with the fact that they are simple objects with recognisable signatures in relatively simple discovery channels means that Z' searches have always been high on the agenda of collider analyses. In lieu of any direct observation, this leads to ever increasing limits on their masses and couplings.

The di-lepton final state (e, μ) is the one in which such objects are most easily and commonly looked for thanks to its good mass resolution and relatively low backgrounds. In this case it is typically assumed that, at hadron colliders, the boson is produced via the Drell-Yan (DY) process, $pp(\bar{p}) \to (\gamma, Z, Z') \to \ell^+\ell^-$, in which a quark-antiquark pair from the protons annihilate into the object of interest which subsequently decays into the pair of charged leptons. Theoretical uncertainties for processes involving Z's at hadron colliders are well under control, see, e.g., [40], including those associated to SM higher order effects, both from the QCD [41] and EW [42] sectors. Evidently, certain models which posses exotic sectors beyond the Z' may induce additional radiative corrections to the production and decay processes and also directly affect the partial widths to SM particles. Several phenomenological studies on how to measure Z' properties and couplings to SM particles in the DY channel have been performed, see [43, 44, 45, 46, 47, 48] for general studies and [49, 50, 51, 52, 53, 54, 55, 56] for more recent, model specific studies. The focus of this thesis is the consideration of the $t\bar{t}$ channel as an alternative

place to investigate such objects. The motivations for this are twofold and have mostly been covered in the previous two chapters. Theoretically, the top quark is likely to be strongly coupled to physics connected with the dynamics of EWSB and the Higgs. It is therefore natural to expect that new TeV scale resonant objects might preferentially appear in top final states. From an experimental perspective, the $t\bar{t}$ channel is an important part of the LHC physics programme thanks to the large amount of expected events in which to look for resonances. Additionally, it offers new observables not available to non-decaying final states such as spin asymmetries, based on the kinematic behaviour of the daughter particles. These can, in principle, provide extra handles to extract Z' properties such as their couplings, something which is discussed later in Section 3.2. This chapter introduces some of the potential origins of Z's along with certain theoretical and experimental constraints on models that predict these particles. The discussion is then moved into the context of $t\bar{t}$ and asymmetries and how they can be used to probe Z' signatures and complement more traditional channels and observables.

3.1 Extra gauge bosons

The principle of enlarging symmetries is, of course, an attractive option for extending physics beyond the current paradigm. One of the principle motivations for Z's comes from enlarging the gauge group of the theory such that the fundamental group contains the SM $SU(3)\times SU(2)\times U(1)$ structure, $\mathcal{G}_{SM}$, thus unifying the three fundamental gauge interactions. This was first considered using $SU(5)$ by Georgi and Glashow [57], as it is the minimal Lie group containing $\mathcal{G}_{SM}$ and has since been developed into a plethora of Grand Unified Theory (GUT) scenarios involving larger groups such as $SO(10)$ [58] and E_6 [59]. In these scenarios, the matter content of the SM is embedded into larger, irreducible representations of the parent group which is then broken down to the SM. In many cases, one is left with additional $U(1)$ factors that result in Z's. Gauge group extensions are therefore one of the most common ingredients in BSM theories that often lead to $U(1)$ factors which can serve certain purposes such as acting as a mediator for Supersymmetry breaking [60] or connecting the SM to a hidden sector [61]. Of course, neutral gauge bosons can also arise from non-Abelian gauge extensions as those associated with diagonal generators, as in the case of the Z boson and photon for $SU(2)_L\times U(1)_Y$. The Z's will generally be accompanied by other charged gauge bosons which are not the focus of this thesis. Some of these examples are taken as benchmark models in future chapters and will be described in more detail in Chapter 4.

A quite different possibility is to extend space-time symmetry itself by postulating the presence of extra, compact spatial dimensions. Although such notions were conceived almost a century ago by Kaluza and Klein, it took until the advent of String theory to place them on a sound theoretical footing. These models have had a resurgence in the last 25 years since the proposal of large extra dimensions [62, 63] as a mechanism to

soften the hierarchy between the EW and Planck scales by allowing gravity to propagate in the bulk. When particles are allowed to "feel" the bulk, towers of Kaluza-Klein (KK) excitations of these fields are predicted upon reducing the model down to our four dimensions. The excitations have masses linked to the compactification radius of the extra dimensions, whose pattern is dictated by the geometry of the compactified space. The extra space is required to be compactified since we observe ourselves to only exist in three spatial dimensions.

As an example, consider the case of a massless, Abelian vector boson field, $A_\mu(x) \to A_M(x,y)$, being promoted to also live in a single extra dimension. The coordinates, x, refer to our usual four dimensional space-time with a new direction introduced as y and the Lorentz index now has five componenents, $M = 0,1,2,3,5$. The action is trivially extended to include the fifth coordinate:

$$\begin{aligned} S_5 &= -\int d^4x\, dy\, \frac{1}{4} F^{MN} F_{MN}, \\ F_{MN} &= \partial_M A_N - \partial_N A_M. \end{aligned} \tag{3.1}$$

The vector field now contains five degrees of freedom and it can be shown that a gauge choice can always be made where $A_5 = 0$ [64]. The feature of compactification lies in having periodic boundary conditions on the extra direction. The symmetry $y = y + 2\pi nR$, for an integer, n, would correspond to the simplest case of compactifying on a circle of radius R. KK decomposition amounts to expanding the higher dimensional fields into modes on the compact space, each with a coefficient which is a field in four dimensions. In the case of a circle compactification the field can be expanded in Fourier modes.

$$A_M(x,y) = A_M^{(0)} + \sum_{n=1}^{\infty} A_M^{(n)}(x) e^{i\frac{ny}{R}} + h.c., \tag{3.2}$$

with the zero mode, $A^{(0)}$, independent of y and the $A_M^{(n)}$ a tower of n complex, vector fields depending only on the four dimensional coordinates. A subtle element of this process, which globally violates five dimensional Lorentz invariance, is that it is no longer generically true that A_5 can be "gauged away", i.e. set to zero by an appropriate gauge transformation. However, it is still possible to choose a gauge in which the field does not depend on y and hence only has a zero mode [64]. Interactions between the gauge field and A_5 are now present as a consequence although they are not explicitly included. Putting this expansion into the five dimensional action and integrating over the fifth coordinate yields:

$$S_4 = -2\pi R \int d^4x\, \frac{1}{4}\left(F_{\mu\nu}^{(0)}\right)^2 - \frac{1}{2}\left(\partial_\mu A_5\right)^2 + \sum_{n=1}^{\infty}\left[\frac{1}{2}\left|F_{\mu\nu}^{(n)}\right|^2 - \frac{n^2}{R^2}\left|A_\mu^{(n)}\right|^2\right] + \cdots . \tag{3.3}$$

The result of this expansion is that one re-obtains a four dimensional action for the

zero modes along with the infinite tower of KK modes which have now acquired a mass, $\frac{n}{R}$, in the last term of Equation 3.3, arising from the derivatives with respect to the fifth direction in F_{MN}. The A_5 mode is an additional scalar field only present at the zero level, its higher level counterparts having been "eaten" by the corresponding vector bosons, analogously to the Goldstone Bosons in EWSB. This chapter is concerned with the vector fields and hence will not discuss these scalar modes further. As such, a space-time symmetry in higher dimensions has been translated into an internal one in the decomposed theory in that conservation of momentum in the fifth dimension has now been reduced to conservation of KK number, n, in four dimensions, adding a whole tower of extra $U(1)$'s. Considering the canonical dimension of the fields, one will see that the gauge coupling in this theory has mass dimension $-\frac{1}{2}$, implying non-renormalisability. One should rescale the fields into a canonical form via a volume factor of $\sqrt{2\pi R}$. In particular, notice that the KK modes should be scaled by an extra $\sqrt{2}$ to obtain the same kinetic term as the zero mode. Further, the gauge coupling in 4D will also be rescaled by this factor when considering gauge interactions.

3.1.1 Mixing

Adding extra neutral vectors to the SM means that the mass basis of the set of fields that share the same quantum numbers can, in general, differ. The Z'(s) will mix with the B_μ and W^3_μ of hypercharge and weak isospin to form a new set of eigenstates to identify with the photon, Z and the new gauge field(s). This can proceed via two mechanisms, termed mass and kinetic mixing.

One way that mass mixing can occur is if the new gauge bosons acquire a mass from the spontaneous breaking of the extra $U(1)$ by the VEV of an electrically neutral component of a new scalar multiplet which is not a singlet of the EW group. This will ensure that the remaining unbroken direction corresponds to the correct admixture of T_3 and hypercharge to maintain the zero mass of the photon. Conversely, if the usual Higgs doublet is also charged under the new $U(1)$, its VEV will also contribute to the Z' mass. In either case, the neutral boson mass matrix of Equation 1.20 is extended to incorporate the new fields and can be diagonalised in the same way as before. The fact that the photon should remain massless means one can simply deal with the mixing in the basis of the Z boson and any mixing incurred will affect only the properties of the Z. The precise amount of mixing will depend on the representations of any new scalar multiplets under the EW group, their charges under the new $U(1)$ and also the charge of the SM Higgs boson under the new gauge group. In this case the tree-level properties of the Z boson such as its mass, width and couplings, will differ from SM predictions. It is important to mention that one of the key predictions of the SM is the relationship between the W and Z masses which can, in principle, be spoiled by such mechanisms. The ratio $M_W/M_Z = \cos\theta_W$ is preserved if the set of scalar fields that contribute to

the gauge boson masses all transform like $SU(2)_L$ doublets (or, trivially, are uncharged under the group) [46].

Gauge kinetic mixing is a possibility that is unique to $U(1)$ extensions of the SM, lying in the fact that the field strength tensor for an Abelian vector field, $F_{\mu\nu}$, is gauge invariant on its own. This means that mixed kinetic terms $\sim F^{\mu\nu}F'_{\mu\nu}$ between new $U(1)$ fields and the hypercharge gauge boson (or amongst one another if there is more than one new group) are not forbidden. Even if such terms are not present in the bare Lagrangian, they can be induced at higher orders. In this situation, the Z' incurs a component of hypercharge in its couplings.

3.1.2 Anomalies

One of the most fundamental constraints of any new physics involving new gauge bosons is the requirement that there be no gauge anomalies present. Anomalies describe instances when a classically conserved current of a theory associated with a particular symmetry is found to no longer be conserved in the presence of radiative corrections upon quantisation. The most common example of such a breakdown is associated with the so-called axial or chiral anomaly which mediates the pion decay into two photons. All gauge theories posses a global $U(1)$ symmetry under a phase shift related to the conservation of charge. The conservation of the associated vector current, $J_\mu = \bar{\psi}\gamma_\mu\psi$, is a statement of the Ward identity of QED [65] (Equation 3.4). The same theory also possesses a similar global symmetry under the transformation shown in Equation 3.5, associated with the axial current, $J^5_\mu = \bar{\psi}\gamma_\mu\gamma_5\psi$. The current is conserved in the massless limit and even in the massive case, yields an associated identity:

$$\psi \to e^{i\alpha}\psi : \quad \partial^\mu J_\mu = 0, \tag{3.4}$$

$$\psi \to e^{i\alpha\gamma_5}\psi : \partial^\mu J^5_\mu = 2m_\psi\bar{\psi}\gamma_5.\psi \tag{3.5}$$

When considering quantum corrections to the axial vertex between a gauge boson and a pair of fermions, it can be shown that the axial Ward identity is violated by a sub-diagram shown in Figure 3.1, corresponding to a piece of the correction [66]. This diagram, involving a closed triangular loop of fermions with one axial current interaction vertex, is contained in higher order diagrams with two external fermions. Although this "VVA" (vector-vector-axial) diagram is not the only one which contributes to the violation of the axial Ward identity, if this one is made to cancel, all others will also cancel. While this is not an issue for global symmetries, the preservation of the axial identity is important in chiral gauge theories like the SM as its violation would compromise their renormalisability. Remarkably, the exact matter content of the SM with quarks appearing in three colour copies from QCD satisfies the requirements of axial anomaly cancellation. These can be expressed as sums over charges of fermions contributing to the set of potentially anomalous triangle diagrams involving combinations

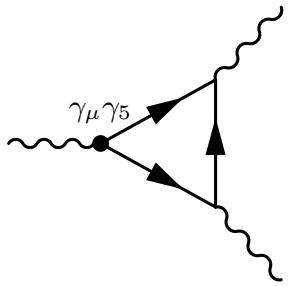

Figure 3.1: Feynman diagram depicting the "triangle" piece of the contribution to the axial vertex correction that violates the chiral anomaly. The dotted vertex corresponds to a coupling between the gauge boson and the axial current, J_5^μ while the undotted ones denote a vector coupling to J^μ

of external SM gauge fields, recalling that generators of non-Abelian groups are traceless. Specifically, since the anomaly originates from the presence of a single axial coupling, left-handed and right-handed fermions contribute with opposite sign.

Since the interactions of a new $U(1)$ gauge boson can be chiral, a set of new triangle diagrams are now potentially finite, and requiring these to vanish constrains the possibilities for fermionic charge assignments under the symmetry. These have external leg combinations involving two $SU(2)_L$ fields or gluons with the Z' along with all possibilities involving the hypercharge boson and the Z'. The conditions are as follows:

$$\begin{array}{ll} \sum Q_i Y_i^2 = 0; & \sum Q_i^2 Y_i = 0, \\ \sum Q_i^3 = 0; & \sum Q_i = 0, \\ \sum\limits_{SU(2)} Q_i = 0; & \sum\limits_{SU(3)} Q_i, = 0 \end{array} \tag{3.6}$$

where the labels $SU(2)$ and $SU(3)$ correspond to only summing over the EW doublets and colour triplets respectively. These conditions are extremely restrictive, so much so, that no other charges aside from a linear combination of Y and T^3 are allowed without introducing new fermions [47]. The most minimal matter that can be included are SM singlets such as the right-handed neutrino, which is often not considered an "exotic" fermion since it is required to give neutrinos a Dirac mass. Fermions that are vector-like with respect to $\mathcal{G}_{SM}$ would also not contribute to the SM anomalies and are often added to satisfy the new conditions.

3.1.3 Couplings

The most general way in which one can parameterise a new neutral current interaction is via the chiral couplings to left- and right-handed fermion components, $g_{L,R}$ or alternatively in the vector-axial basis, $g_{V,A}$. These bases are related by $g_L = g_V + g_A$, $g_R = g_V - g_A$. The Lagrangian term describing the interaction between a Z' and a

fermion, f, is then simply

$$\mathcal{L}_{\text{int}} = iZ'_\mu \, \bar{f} \, \gamma^\mu \left(P_L \, g_L^f + P_R \, g_R^f \right) \, f \tag{3.7}$$

$$\equiv iZ'_\mu \, \bar{f} \, \gamma^\mu \left(g_V^f - \gamma^5 g_A^f \right) \, f \tag{3.8}$$

where the projectors $P_{L,R} = \frac{1}{2}(1 \pm \gamma_5)$ select the chiral components of the Dirac spinors, f. An overall gauge coupling constant, g', is often factored out but is chosen here to be absorbed in the definition of the chiral couplings. Predictions for a given observable or production and decay rate can then be written in terms of the set of relevant couplings and the Z' mass and width, $M_{Z'}$ and $\Gamma_{Z'}$, for the model of choice.

If one only includes interactions with SM matter, there are in principle 21 (24 if one includes right-handed neutrinos) free couplings corresponding to $g_{L,R}$ for the three generations of quarks and leptons. Often, assumptions are made to reduce the number of parameters such as making the couplings generation universal and also requiring fields belonging to the same SM representation to have the same coupling to the Z'. The first assumption reduces the parameters by a factor of three and is relevant in that non-universal couplings can lead to Flavour-Changing Neutral Currents (FCNC) when moving from the weak basis to the mass basis for fermions. The latter assumption is a gauge invariance requirement for an extra $U(1)$ but can, in general, not hold for Z's arising from more complex gauge structures. The most minimal, model independent parametrisation, excluding right-handed neutrinos, therefore consists of 5 independent couplings to the left-handed lepton and quark doublets and the right-handed leptons and up and down type quarks e_L, q_L, e_R, u_R and d_R. The models considered in subsequent chapters will adhere to most, if not all of the minimal assumptions.

3.1.4 Indirect constraints

Being one of the simpler objects that one can parameterise as well as having potential mixing effects with the Z boson, Z's are constrained by a large number of indirect measurements before even considering direct searches at collider experiments. Most of the important constraints come from EW precision tests (EWPTs) which have virtually unanimously confirmed the SM to a great degree of accuracy. These can involve measurements of neutral current contributions to processes at various colliders including the Large Electron-Positron (LEP) collider, the Stanford Linear Collider (SLC), Tevatron and now the LHC as well as low energy experiments.

The Z-pole measurements of the four collaborations during the first LEP run and the SLAC Large Detector (SLD) experiment at the SLC measured a host of observables related to the Z boson to extremely high precision, thus being sensitive to very small deviations from SM predictions incurred by mixing effects with a Z'. Observables include the determination of properties of the Z such as its mass, width and total production

cross section, a number of partial widths to different leptonic and hadronic final states and ratios thereof as well as a host of asymmetries and line shapes. SLD also had the benefit of having a largely polarised electron beam, allowing for a number of additional measurements. These will place limits on a combination of the Z' mass and its mixing with the Z. The second LEP run increased the CM energy above the Z peak, scanning from 140 to 209 GeV. These measurements were more sensitive to direct Z' production and interference effects, allowing limits to be placed independently of the $Z - Z'$ mixing. Other precisely measured quantities such as the top and W masses can also be affected by radiative corrections involving new neutral vectors.

Other low energy experiments are additionally sensitive to non-mixing effects such as Z' contributions to effective leptonic, hadronic and mixed four fermion operators below the Z-pole, setting limits on the scale (mass) and couplings of new neutral current processes. These ranged from Atomic Parity Violation measurements which observe the effective interaction strength between atomic electrons and quarks in their nucleus, to neutrino deep inelastic scattering experiments at the NuTeV experiment at Fermilab or Moller-scattering ($e^-e^- \to e^-e^-$) cross section measurements. Potential Z' contributions to these observables can be quantified in a low energy effective description.

One typically performs model dependent fits to a large set of observables affected by the Z's to obtain bounds of the form $M_{Z'}/g_{Z'} > X$ TeV which tends to reside on the range $[1 - 10]$ TeV for familiar benchmarks [67] in the case of measurements not sensitive to the mixing. Alternatively, one can directly constrain a combination of mass and mixing for a specific model when including Z-pole measurements which typically result in very strong bounds on the mixing and limit Z' masses up to ~ 1 TeV [48].

Another potential source of constraints come from flavour physics considerations, measuring rates of meson mixing or rare decays and transitions such as $K^0 - \bar{K}^0$ mixing or $\mu(b) \to e(s)\gamma$. However, all of these effects rely on family non-universality of the Z' couplings. This is because, as mentioned in the previous section, if the couplings are non-diagonal with respect to fermion generations, the rotation from the weak basis to the mass basis effected by the CKM matrix shown in Section 1.5 as well as the equivalent PMNS matrix in the lepton sector will lead to FCNC interactions which can mediate these kinds of processes, sometimes at tree-level, that are GIM suppressed in the SM. GIM refers to the Glashow-Iliopoulos-Maiali mechanism which explained the weak charged current mixing in quarks as coming from a rotation between the basis of two doublets (u, c) and (d, s) that guarantees the flavour diagonality of neutral current interactions. Consequently, the rare FCNC processes in the SM are suppressed by loop factors and mass differences between quark generations [68]. Measurements of these processes are precise enough to strongly constrain non-universal Z' interactions in the first two generations [46] while third generation non-universality is less strongly constrained. This is another compelling reason to consider couplings to the top and fits well with the

notion that new physics is more likely to be coupled in a unique way to third generation fermions.

3.1.5 Direct searches

More than twenty years into the post-LEP era of hadron colliders, it is no surprise that the strongest limits on Z' models come from direct searches at the Tevatron and now the LHC. Once the capacity to reach a certain CM energy is attained, the observation of the Breit-Wigner resonance peak from direct production and decay becomes possible. Hadron colliders are perfect machines for this purpose since the composite nature of the (anti-)protons allows for the scanning of a wide range of energies in the hopes that a resonance might be observed. The unpolarised production matrix element for a massive fermion pair via light (assumed massless) quark annihilation into neutral vectors with CM energy, $\sqrt{\hat{s}}$, is

$$\begin{aligned}\widetilde{\mathcal{M}}^2_{q\bar{q}} &= \int d\theta |\mathcal{M}(q\bar{q} \to f\bar{f})|^2 \\ &= \frac{\pi \hat{s}^2}{12} \sum_{i,j} \frac{D_{ij}}{1+\delta_{ij}} C^q_{ij} \Big[C^f_{ij}\big(2+\beta^2\big) + 2M^f_{ij}\big(1-\beta^2\big) \Big];\end{aligned} \tag{3.9}$$

$$C^x_{ij} = x^i_L x^j_L + x^i_R x^j_R, \tag{3.10}$$

$$M^x_{ij} = x^i_L x^j_R + x^i_R x^j_L, \tag{3.11}$$

where the indices i, j label the vectors bosons in the model i.e. the photon, the Z and any Z's present. Here the polar angle, θ, defined as that between the quark and the fermion momenta, has been integrated over. The chiral couplings to the initial and final states are labeled $q^i_{L,R}$ and $f^i_{L,R}$ respectively and the $\beta = \sqrt{1 - \frac{4m_f^2}{\hat{s}}}$ factor accounts for the kinematical dependence on the final state mass m_f tending to one in the massless limit. The parity symmetric and mixed coupling combinations, $C^{f,q}_{ij}$ and $M^{f,q}_{ij}$, elucidate the coupling structure. The propagator function, D_{ij}, describes a generic interference term between the propagators of two particles of masses and widths denoted by m and Γ, reproducing the Breit-Wigner form for $i = j$.

$$D_{ij} = \frac{(\hat{s} - m_i^2)(\hat{s} - m_j^2) + m_i m_j \Gamma_i \Gamma_j}{\Big((\hat{s} - m_i^2)^2 + m_i^2 \Gamma_i^2\Big)\Big((\hat{s} - m_j^2)^2 + m_j^2 \Gamma_j^2\Big)} \tag{3.12}$$

The familiar $g_L^2 + g_R^2$ coupling dependence of these neutral current cross sections is apparent with the β factor also making manifest the mass-suppressed, chirality flipping component mixing the left and right-handed couplings.

The best observable to search for these signals, then, is the invariant mass distribution since the propagator functions depend exactly on this boost invariant quantity, $M^2_{f\bar{f}} = \hat{s} = (p_f + p_{\bar{f}})^2$. To translate the matrix element of Equation 3.9 into a differential cross

section at a hadron collider with CM energy, s, requires the integral over the two-body phase space, convolution with the PDFs in a similar way to Section 2.3 a sum over initial states to give

$$\begin{aligned} \frac{d\sigma}{d\sqrt{\hat{s}}} &= \frac{\beta}{16\pi\hat{s}^{\frac{3}{2}}} \sum_q a_{q\bar{q}}(\hat{s}, Q)|\widetilde{\mathcal{M}}^2_{q\bar{q}}| \\ a_{q\bar{q}}(\hat{s}, Q) &= \int dy \left[f_q^a(x_1, Q) f_{\bar{q}}^b(x_2, Q) + f_{\bar{q}}^a(x_1, Q) f_q^b(x_2, Q) \right] \end{aligned} \tag{3.13}$$

where the functions f are as defined in Equation 2.1 for the collision of hadrons a and b. y is the rapidity of the $q\bar{q}$ system and is related to the two partonic momentum fractions $x_{1,2}$ by

$$y = \frac{1}{2} \ln \left(\frac{x_1}{x_2} \right) \Rightarrow x_{1,2} = \sqrt{\tau} e^{\pm y} \tag{3.14}$$

and τ relates the partonic and collider CM energies and is equivalent to $x_1 x_2$. Thus, in this particular case the PDF convolution can be expressed as a multiplicative factor that is a function of $\hat{s}$ and the factorisation scale, Q. This is not generically possible for other differential cross sections such as those involving non Lorentz invariant quantities such as lab frame angles, for example. One can then test for signatures resembling these kinds of objects in various final states by superimposing this signal rate over a background prediction and comparing the observed events to the signal and background hypotheses.

For the reasons discussed earlier, the strongest limits on minimal Z' resonances come from the di-lepton (e, μ) final state at the LHC and Tevatron experiments, where the high invariant mass tail in the EW DY background is modelled by MC and normalised to the data in a lower mass region where it is assumed that no signal events occur. Often, the Narrow Width Approximation (NWA) is made where the resonance is assumed to be narrow enough such that the propagator is assumed to be a Dirac delta function centred at the resonance mass. This removes one degree of freedom in the phase space integral and allows the signal to be modelled by a Breit-Wigner shape with an area corresponding to the NWA cross section, taking into account the falling off of the PDFs. It should be stressed that this approximation neglects potential interference between the signal and the background. Although specific signal selections and analyses may differ slightly, most resonance searches in this channel proceed in this way.

Given the assumed signal shape, a binned likelihood analysis determines the likelihood of a particular signal hypothesis against the background only hypothesis in a chosen invariant mass window as a function of the resonance mass being searched for. Since no deviations from the background have been observed, the likelihoods can be interpreted as exclusions which place lower limits on the masses of Z' in this channel. Limits from the Tevatron reach masses of order 1 TeV [69] while the latest LHC limits [70] surpass 2 TeV, depending on the model, attaining close to 3 TeV for the Sequential SM (SSM)

benchmark (where a Z' with the same couplings as the Z is assumed). While this is certainly beginning to place relatively strong constraints on the minimal benchmark models, the approximations made in order to perform relatively model independent analyses mean that these results should be interpreted with caution. The searches neglect any potential exotic decay modes which would affect the Z' width as well as ignore potential interference effects, both of which would have an effect on the mass limit. The effect of these assumptions is discussed in [56, 71], showing that certain kinematical cuts can be made to reduce the interference and finite width effects, although ultimately retaining a degree of model dependency at the percent level.

Resonance searches are also performed in other final states such as di-jets, $\tau^+\tau^-$, $b\bar{b}$ and, of course, $t\bar{t}$ with lower mass reaches due to the overwhelming QCD background in di-jets and $b\bar{b}$ as well as the more involved reconstruction process in decaying τ's and tops or tagging b-jets. Such searches tend to be more useful to probe non minimal models which involve coloured resonances or have enhanced couplings to quarks (or suppressed leptonic couplings) or third generation fermions. The latter assumption may be a reasonable one considering that many BSM models are concerned with EWSB and mass generation as mentioned in Sections 1.7 and 2.1. Recent work has been done to use ratios of cross sections in different third generation final states as a distinguishing feature of Z' benchmarks [72]. The di-jet mass spectrum is also sensitive to many other types of resonances that can also decay into qg or gg as well as non resonant t-channel physics not considered in this work.

3.1.6 $Z' \to t\bar{t}$

The topic of this thesis is to consider the $t\bar{t}$ final state as a complementary channel for discovering and/or investigating the couplings of potential Z' signals. While the complicated reconstruction process discussed in Section 2.2 means that there is a statistical and systematic disadvantage to performing resonance analyses in this channel, the ability to define new asymmetry observables as well as the theoretical motivation for physics strongly coupled to third generation fermions makes $Z' \to t\bar{t}$ an interesting prospect.

One of the primary systematic effects of the reconstruction process is a loss of mass resolution, making it more difficult to see clear Breit-Wigner peaks in the invariant mass distributions. The main difference in this context between $t\bar{t}$ and the traditional di-lepton channel, aside from the fact that the top decays, is that the background comes dominantly from QCD as shown in the diagrams of Figure 2.2. Figure 2.3 suggests that the gluon and quark contributions will contribute similarly to the production at CM energies of order TeV. However, although a Z' signal will be mediated by the $q\bar{q}$ initial state, the fact that the gluon is a colour octet forbids interference with a colour singlet object in the s-channel. This can readily be seen by the fact that Feynman rule for the gluon-quark-quark vertex comes with an associated $SU(3)_C$ generator, T^a_{ij}. The

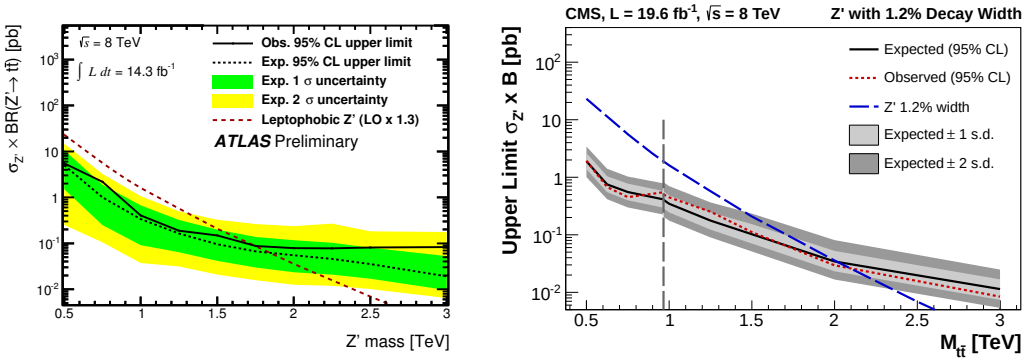

Figure 3.2: Latest Z' mass exclusions in the $t\bar{t}$ final state from an ATLAS (*left*) and CMS (*right*) analysis with 14.3 and 19.6 fb^{-1} of integrated luminosity of $\sqrt{s} = 8$ TeV, LHC data. The plotted reference models are the narrow width topcolor lepto-phobic Z' and a SSM Z' respectively. A multiplicative k-factor of 1.3 has been applied on the LO model prediction to approximately account for NLO QCD corrections.

interference between the two s-channels modes of a gluon and a colour neutral Z', which comes with a δ_{ij} factor in colour space will vanish due the subsequent fermionic trace over the colour indices thanks to the traceless property of the generators. Therefore the only interference effect that can occur are, as with the di-lepton case, with the neutral EW sector which is very subdominant in this case. A number of searches have been performed for resonant physics in this channel [37, 38, 73, 74, 75] yielding limits of order 1.5–2 TeV for specific benchmarks usually chosen for their enhanced top couplings relative to leptons. Figure 3.2 shows a selection of the latest exclusion plots from the ATLAS and CMS collaborations on a lepto-phobic "topcolor" [76] Z' – a common benchmark in $t\bar{t}$ resonance searches – and an SSM Z' respectively. Both analyses are tailored to account for high-mass events where the tops can be highly boosted and have collimated decay products, with a specific selection category for these types of events.

3.2 Asymmetries

In order to determine the sensitivity of asymmetry observables to the presence of a Z', it is instructive to calculate their dependence on its couplings as was done for the differential cross section in Equation 3.13. This will demonstrate the unique dependence on the couplings of the charge and spin asymmetry observables and motivate their use as an extra handle on the Z' couplings. Since all of the observables are normalised by the total cross section, the coupling dependence of interest is contained in the numerators of the asymmetry definitions. This is shown for each of the three asymmetries defined in Section 2.4.

3.2.1 Charge asymmetry

The coupling structure of the charge asymmetry can immediately be deduced by retaining the angular dependence of the matrix element shown in Equation 3.9.

$$|\mathcal{M}(q\bar{q} \to f\bar{f})|^2 = \frac{\hat{s}^2}{6} \sum_{i,j} \frac{D_{ij}}{1+\delta_{ij}} \Big[C_{ij}^q \Big(C_{ij}^f \big(1 + \beta^2 \cos^2\theta\big) + M_{ij}^f (1-\beta^2) \Big) + 2 A_{ij}^q A_{ij}^f \beta \cos\theta \Big], \tag{3.15}$$

$$A_{ij}^x = x_L^i x_L^j - x_R^i x_R^j, \tag{3.16}$$

where the coupling factors, C_{ij}^x and M_{ij}^x, and polar angle, θ, are those defined in Equation 3.9. Here, a new, parity asymmetric coupling combination, A_{ij}^x, appears. Although both additional terms integrate to zero over the angular range $\{0, \pi\}$, the final one is asymmetric in this region and is therefore the sole contributor to the charge asymmetry. Any observable attempting to extract this quantity from a neutral current interaction is measuring the parity asymmetric coupling combination

$$A_{FB} \propto \chi_{ij} \equiv A_{ij}^q A_{ij}^f = \big(q_L^i q_L^j - q_R^i q_R^j\big)\big(f_L^i f_L^j - f_R^i f_R^j\big). \tag{3.17}$$

In terms of the pure Z' contribution, $i = j = Z'$, the sign of this observable is sensitive to the relative chirality of the Z' couplings in both the initial and final states $(q_L^2 - q_R^2)(f_L^2 - f_R^2)$ simultaneously, as opposed to the cross section which depends on the sums of squares of the chiral couplings as seen in Equation 3.9, setting $i = j = Z'$. Although, as pointed out in Section 2.4, the PDF effects in hadron collider measurements prevent this quantity to be measured directly, some diluted version of χ_{ij} is ultimately the target in all charge asymmetry observables from neutral current exchange. The observable therefore provides a handle on the couplings not present in cross section measurements, albeit obfuscated somewhat by the fact that both initial and final state couplings can lead to a change in sign of χ_{ij}.

One of the main issues with attempts to explain the Tevatron $A_{FB}^{t\bar{t}}$ anomaly mentioned in Section 2.4.1, from a BSM perspective is the need to remain consistent with the measured cross section in the same kinematic region. The structure of this A_{ij} coefficient compared to the C_{ij} coefficients dictating the cross section shows that, in general, one will always obtain effects in both the cross section and charge asymmetry for a pure BSM contribution, $i = j$, while interference terms have the potential to affect A_{FB} more than the cross section, depending on the couplings. In particular, they motivate the explanation of the anomaly with a wide axigluon scenario [77], which is a colour octet, axial-vector counterpart of the gluon. In this case, the purely axial ($g_L^i = -g_R^i$) couplings will maximise charge asymmetry effects and minimise cross section in the interference contribution, i.e. $C_{ij}^x = 0$ and $A_{ij}^x \neq 0$ for i and j denoting the gluon and axigluon respectively. If the resonance is sufficiently wide or weakly coupled to suppress

a large $i = j$ contribution, the dominant contributions could arise from interference and potentially explain the anomaly while remaining consistent with the measured cross section. For the same reason, non-coloured resonances are ruled out as an explanation since their lack of interference with QCD means they can only generate a deviation in charge asymmetry along with an equal, if not more significant deviation in the cross section.

In addition to defining asymmetries, the angular distributions of decay products can also shed light on the spin of an observed resonance [55]. The $\cos\theta$ term in the matrix element of Equation 3.15, which generates the charge asymmetry, can also differentiate a spin-1 or 2 resonance from a scalar one, which cannot have this kind of dependence. Furthermore, spin-2 resonances can also have a $\cos^4\theta$ term, allowing one to potentially distinguish their angular distributions from the others.

3.2.2 Spin asymmetries

Since the spin asymmetries defined in Section 2.4 are constructed in terms of the helicity of the final state fermions, it is necessary to calculate the polarised matrix elements of Z' production and decay in order to determine the coupling structure of the numerator of A_L. These were calculated using helicity amplitude methods outlined in [78] and cross-checked with results from [79]. The details of the calculation can be found in Appendix A and decompose the Feynman amplitude into products of helicity eigenspinors in which the amplitudes for different processes, up to a phase, can be written in terms of the helicities of the incoming and outgoing fermions. The initial state quarks are, again, assumed to be massless. Out of the sixteen possible combinations, only eight are non-zero, given by:

$$\begin{aligned}
\mathcal{A}(+,-,\pm,\pm) &= \mp\frac{\hat{s}}{2}\sin\theta\sqrt{1-\beta^2}q_R(f_L+f_R),\\
\mathcal{A}(-,+,\pm,\pm) &= \mp\frac{\hat{s}}{2}\sin\theta\sqrt{1-\beta^2}q_L(f_L+f_R),\\
\mathcal{A}(+,-,\pm,\mp) &= \frac{\hat{s}}{2}(1\pm\cos\theta)q_R(f_L(1\mp\beta)+f_R(1\pm\beta)),\\
\mathcal{A}(-,+,\pm,\mp) &= \frac{\hat{s}}{2}(1\mp\cos\theta)q_L(f_L(1\mp\beta)+f_R(1\pm\beta)),
\end{aligned} \tag{3.18}$$

where the arguments of the amplitudes correspond to the eigenvalues of the initial and final state spinors under the helicity operator ordered as $\mathcal{A}(h_q, h_{\bar{q}}, h_f, h_{\bar{f}})$. Here, only the pure Z' contribution is shown to elucidate the coupling dependence, with the propagator factors dropped for simplicity. The mass suppressed spin flipping amplitudes, where the final state fermions have the same helicity, are apparent. Averaging over the initial state polarisations, the four polarised matrix elements for Z' production and decay into heavy

fermions, are

$$\begin{aligned}
|\mathcal{M}(\pm,\pm)|^2 &= \frac{\hat{s}^2}{48}\left(1-\beta^2\right)\left(q_L^2+q_R^2\right)\left(f_L+f_R\right)^2\sin^2\theta, \\
|\mathcal{M}(\pm,\mp)|^2 &= \frac{\hat{s}^2}{48}\left(\left(q_L^2+q_R^2\right)\left(1+\cos^2\theta\right)\mp 2(q_L^2-q_R^2)\cos\theta\right) \\
&\qquad\qquad \times\left((1\mp\beta)f_L+(1\pm\beta)f_R\right)^2,
\end{aligned} \tag{3.19}$$

from which we can express the numerator of the two spin asymmetries according to Section 2.4

$$\begin{aligned}
\mathcal{M}_{A_{LL}} &= |\mathcal{M}(+,+)|^2+|\mathcal{M}(-,-)|^2-|\mathcal{M}(-,+)|^2-|\mathcal{M}(+,-)|^2 \\
&= -\frac{\hat{s}^2}{12}\Big[2\left(q_L^2-q_R^2\right)\left(f_L^2-f_R^2\right)\beta\cos\theta+\left(q_L^2+q_R^2\right)\times \\
&\qquad\qquad \left(\left(\beta^2+\cos^2\theta\right)\left(f_L^2+f_R^2\right)+2\left(1-\beta^2\right)\cos^2\theta f_L f_R\right)\Big],
\end{aligned} \tag{3.20}$$

$$\begin{aligned}
\mathcal{M}_{A_L} &= |\mathcal{M}(-,+)|^2-|\mathcal{M}(+,-)|^2 \\
&= \frac{\hat{s}^2}{12}\Big[\left(q_L^2+q_R^2\right)\left(f_L^2-f_R^2\right)\left(1+\cos^2\theta\right)+2\left(q_L^2-q_R^2\right)\left(f_L^2+f_R^2\right)\cos\theta\Big].
\end{aligned} \tag{3.21}$$

In the spin correlation amplitude, $\mathcal{M}_{A_{LL}}$, we recognise similar coupling structures to the total cross section. Since, in the case of a Z', $\mathcal{M}_{A_{LL}}$ is essentially measuring the relative size of the helicity flipping amplitudes, the limit $\beta \to 1$ should recover the regular production matrix element of Equation 3.9. This is indeed the case although, due to the choice of sign in defining the asymmetry, $|\mathcal{M}_{A_{LL}}|^2_{(\beta\to 1)} = -|\mathcal{M}(q\bar{q}\to f\bar{f})|^2_{(i=j)}$. As for the spin polarisation, $\mathcal{M}_{A_L}$, a new combination of coupling coefficients appears which is a mix of the parity symmetric and antisymmetric coefficients, A and C. Integrating the two matrix elements over the polar angle illustrates how the asymmetry observables will depend on the couplings after phase space integration and therefore to which coupling combination the observable at collider experiments should be sensitive

$$A_{LL} \propto \left(q_L^2+q_R^2\right)\Big(2f_L f_R\left(\beta^2-1\right)-\left(f_L^2+f_R^2\right)\left(2\beta^2+1\right)\Big), \tag{3.22}$$

$$A_L \propto \beta\left(q_L^2+q_R^2\right)\left(f_L^2-f_R^2\right). \tag{3.23}$$

The mix of parity symmetric and asymmetric coefficients present in the A_L coupling dependence is an extremely interesting one as its removes the asymmetric dependence on the couplings to the initial state, which causes the obfuscation of the coupling dependence of A_{FB} pointed out in Section 3.2.1. The spin polarisation observable is therefore directly sensitive to the relative chirality of the Z' couplings to the final state, a unique feature among asymmetry observables at hadron colliders. These can readily be generalised to the many resonance case to take into account the EW background or models with more than one Z' in terms of the three coupling combinations defined in Equations 3.10, 3.11

and 3.16 to give

$$A_{LL} \propto -C_{ij}^{q}\Big(\big(2\beta^2+1\big)\, C_{ij}^{f} - \big(\beta^2-1\big)\, M_{ij}^{f}\Big), \tag{3.24}$$

$$A_{L} \propto \beta C_{ij}^{q} A_{ij}^{f}, \tag{3.25}$$

$$A_{FB} \propto A_{ij}^{q} A_{ij}^{f}, \tag{3.26}$$

$$\sigma \propto C_{ij}^{q}\Big(\big(\beta^2+2\big)\, C_{ij}^{f} - \big(\beta^2-1\big)\, M_{ij}^{f}\Big), \tag{3.27}$$

where the coupling dependences of the cross section, σ, and charge asymmetry, A_{FB}, have been included for comparison.

Having introduced the features of new physics involving Z's and the particular coupling structures that are accessible via cross section, charge and spin asymmetry observables, the remainder of this thesis will go on to apply this knowledge to a number of different models. Specifically, since one can define all of these observables in the $t\bar{t}$ channel, the focus of the work will be to investigate the use that can be made of such asymmetries to distinguish models either on their own, or to serve as a complement to other channels in profiling and extracting the couplings of any new observed resonances.

Chapter 4

Z' benchmarks in $t\bar{t}$

In order to analyse the scope of $t\bar{t}$ asymmetries in the context of Z' physics, it is logical to begin by looking at a set of popular benchmark models used in current LHC analyses. Since these models are used as examples in the di-lepton analyses, it is instructive to compare the reach of the $t\bar{t}$ channel compared to the former, as well as to ascertain any potential advantages that the new asymmetry observables may offer in discovering or distinguishing the differing coupling structures between these models. In this first study, the set of previously defined asymmetry observables, along with the differential cross section, are considered to assess the LHC's ability (at all of its planned energy and luminosity stages) to profile a Z' boson mediating $t\bar{t}$ production by adopting several realisations of the recalled sequential (G_{SM}), left-right symmetric (G_{LR}) and E_6 based Z' models (specifically, the same as those in [56]). The first section will review and expand on the motivations and generalised parameterisations of the benchmark model classes touched upon in Chapter 3. Section 4.2 describes the tools used for the calculations as well as the specific incarnations of the asymmetry observables used. Section 4.3 reports and comments on the results, covering the differential distributions and discriminating power of the observables with Section 4.4 presenting the conclusions and outlook. The following work has previously been published in [1].

4.1 Benchmark models

While a brief overview of the benchmark Z' models is presented here, the reader is directed to the original publication as well as those henceforth referred to for further details. All of the following models respect the minimal assumptions on Z' couplings outlined in Section 3.1.3 of universal couplings across fermion generations, negligible $Z-Z'$ mixing and equal charges for each SM representation, consistent with the presence of a $U(1)'$ enlarging $\mathcal{G}_{SM}$. Potential kinetic mixing with the hypercharge gauge boson is also neglected. Of the set of five independent couplings (neglecting right-handed

neutrinos), e_L, q_L, e_R, u_R and d_R, only the quark couplings, q_L, u_R and d_R, will be relevant in constructing the observables considered this work[1]. The coupling conventions used to discuss the benchmarks follow those of [56] where the gauge coupling, g', is explicitly factored out of the interactions.

4.1.1 E_6 model

This class of models describes phenomenological, GUT inspired implementations of additional $U(1)'$ factors that occur when decomposing GUT groups down to the $\mathcal{G}_{SM}$. These are motivated by heterotic string theory, whose ten dimensional supersymmetric vacua can lead to theories which come from $E_8 \times E_8$ gauge groups [49]. In particular, the E_6 and $SO(10)$ subgroups are the two most commonly considered. In general, the number of neutral gauge bosons present in a gauge theory is equal to its rank [44], the number of mutually commuting generators – also known as the Cartan subalgebra. In other words, these are the generators which can be simultaneously diagonalised, in accord with the definition of neutral gauge bosons as the subset of gauge bosons associated to diagonal generators. As mentioned in Section 3.1, $SU(5)$ is the smallest group containing $\mathcal{G}_{SM}$ and, being of rank 4, leaves no room for additional vector bosons. This is because, in addition to T_L^3 and Y, $SU(3)$ also has 2 generators in its Cartan subalgebra [80]. E_6 and $SO(10)$, on the other hand, are of ranks 6 and 5 respectively and can be decomposed as

$$\begin{aligned} E_6 &\to SO(10) \times U(1)_\psi, \\ SO(10) &\to SU(5) \times U(1)_\chi \to \mathcal{G}_{SM} \times U(1)_\chi. \end{aligned} \tag{4.1}$$

The groups can be spontaneously broken in a similar way to EW theory or by more involved higher order effects, the details of which are beyond the scope of this work. The extra Abelian factors, usually termed ψ and χ, predict two new Z's with fermionic interactions based on the specific embedding of the SM matter into irreducible representations of E_6 and subsequently $SO(10)$ and $SU(5)$. Each generation of fermions can be unified into the 27 dimensional, fundamental representation of E_6. The fermions remain in a complete (including right-handed neutrinos), dimension 16 spinorial representation of $SO(10)$ under which the left and right-handed fields have $U(1)_\psi$ charges of $\pm\frac{1}{2}$ [49]. This means that the Z' couplings will be family universal, with the complete E_6 representation ensuring freedom from gauge anomalies. Generally, using complete representations is conducive to the construction of anomaly-free gauge theories. Intuitively, the tracelessness of Lie group generators hints at this feature. From the beginning, the SM fields are embedded together with exotic matter content such as additional colour triplet quarks and additional Higgses. Typically, phenomenological studies of the Z' sector tend to decouple the exotic fields, assuming that some general linear combination

[1] Of course, the leptonic couplings do enter indirectly via the Z' widths

of the generators T_χ and T_ψ survives down to the TeV scale,

$$T' = T_\chi \cos\theta + T_\psi \sin\theta, \tag{4.2}$$

with fermionic couplings matching the particular admixture. A set of benchmark values for θ make up the set of E_6 GUT inspired Z''s, $\chi, \psi, \eta, I, N, S$, five of which couple to up type quarks and are considered in this study. The relevant couplings are summarised in Table 4.1. The gauge coupling is chosen to match the GUT normalised hypercharge coupling, g', of the SM [56], not to be confused with the hypercharge gauge coupling defined in Section 1.3. This is a factor $\sqrt{\frac{5}{3}}$ that is imposed on the hypercharge generator of $SU(5)$ in order to satisfy the correct Lie group normalisation conventions of $\mathcal{G}_{SM}$, i.e. $\mathrm{Tr}[T^a T^b] = \delta^{ab}$.

4.1.2 Generalised left-right symmetric models

Left-right symmetric models are also well motivated from a string theory perspective [81, 82], as they can arise from an alternative breaking of $SO(10)$. The decomposition of the enlarged product group, neglecting $SU(3)_C$, can be expressed as

$$SU(2)_L \times SU(2)_R \times U(1)_{B-L} \to SU(2)_L \times U(1)_Y. \tag{4.3}$$

The new isospin group acts analogously on the right-handed fields, which become isodoublets, restoring parity symmetry which is maximally violated by the EW interaction (since the weak isospin gauge bosons act uniquely on left-handed fields). $SU(2)_R$ therefore introduces 3 new, right-handed copies of the $SU(2)_L$ gauge bosons, one of which will be a neutral state associated to T_R^3. B and L refer to baryon and lepton number, associated with the conserved quantities arising from the global $U(1)$ invariance of the SM under independent transformations of the lepton and quark fields. The combination $U(1)_{B-L}$ can be gauged non-anomalously if one includes right-handed neutrinos. Gauging this particular quantity forbids baryon and lepton violating operators that could contribute to proton decay. Furthermore, the B-L charge, $T_{B-L} = (B - L)/2$ combined with the third component of right-handed isospin conveniently leads to correct hypercharge assignments required for the definition of electric charge in Section 1.5:

$$Q = T_L^3 + T_R^3 + T_{B-L} = T_L^3 + \frac{Y}{2}. \tag{4.4}$$

One then obtains the combination of the T_R^3 and T_{B-L} in terms of the $SU(2)_L$ and $SU(2)_R$ gauge couplings, g_L and g_R, by requiring that the orthogonal combination reproduces $U(1)_Y$

$$\begin{aligned} T_{LR} &= \alpha_{LR} T_R^3 - \frac{1}{\alpha_{LR}} T_{B-L}, \\ \alpha_{LR} &= \sqrt{\frac{g_R^2}{g_L^2} \cot^2 \theta_W - 1}. \end{aligned} \tag{4.5}$$

Assuming exact left-right symmetry, one can set $g_R = g_L$, to fully specify the interactions of this Z'. Generalising to a continuous parametrisation, G_{LR}, the additional gauge boson is, instead, assumed to be an arbitrary mixture of the T_R^3 and T_{B-L}, coupling with $g' T_{GLR}$, for

$$T_{GLR} = T_R^3 \cos\phi + T_{B-L} \sin\phi. \tag{4.6}$$

The true T_{LR} is recovered by a choice of parameters, $\phi = 0.128\pi$ and $g' = 0.595$. In addition to this benchmark (LR), the three points examined correspond to purely right-handed (R) and B-L (BL) resonances along with the orthogonal hypercharge (Y) combination.

Often, the right-handed neutrinos are made massive when the symmetry is broken and can contribute to a see-saw mechanism, generating the suppressed left-handed neutrino masses. Again, the particular symmetry breaking mechanisms are well documented in the literature and also often require extended Higgs sectors.

4.1.3 Generalised SSM

The SSM generalisation begins with the assumption that, as in the SM, the Z' couples to a combination of T_L^3 and electric charge, Q. The true SSM has identical couplings to the Z-boson, $Q_Z = T_L^3 - Q \sin^2\theta_W$, and is a common benchmark choice for BSM searches, albeit not particularly well motivated. Similarly to G_{LR}, this class is defined as a generalisation of the Z coupling mixing, such that

$$T_{GSM} = T_L^3 \cos\alpha + Q \sin\alpha, \tag{4.7}$$

so that the Z' coupling to fermions is $g' T_{GSM}$. The parameters which match the SSM can be found to be $\alpha = -0.072\pi$ and $g' = 0.76$. The model treats g' as fixed, freely varying α. Three points are typically chosen corresponding to the SSM (SM), pure left-handed isospin, (T_{3L}) and a heavy photon coupling to electric charge (Q) which is not considered in this work.

4.1.4 Overview

The benchmark models collected in Table 4.1 express the fermionic couplings in the vector-axial basis, shown in Equation 3.8.

$U(1)'$	Parameter	g_V^u	g_A^u	g_V^d	g_A^d
E_6 ($g' = 0.462$)	θ				
$U(1)_\chi$	0	0	-0.316	-0.632	0.316
$U(1)_\psi$	0.5π	0	0.408	0	0.408
$U(1)_\eta$	-0.29π	0	-0.516	-0.387	-0.129
$U(1)_S$	0.129π	0	-0.129	-0.581	0.452
$U(1)_N$	0.42π	0	0.316	-0.158	0.474
G_{LR} ($g' = 0.595$)	ϕ				
$U(1)_R$	0	0.5	-0.5	-0.5	0.5
$U(1)_{B-L}$	0.5π	0.333	0	0.333	0
$U(1)_{LR}$	-0.128π	0.329	-0.46	-0.591	0.46
$U(1)_Y$	0.25π	0.589	-0.354	-0.118	0.354
G_{SM} ($g' = 0.760$)	α				
$U(1)_{SM}$	-0.072π	0.193	0.5	-0.347	-0.5
$U(1)_{T_{3L}}$	0	0.5	0.5	-0.5	-0.5
$U(1)_Q$	0.5π	1.333	0	-0.666	0

Table 4.1: Benchmark Z' model parameters and couplings, as seen in [56]. The angles θ, ϕ, α are defined in the text.

In order to interpret the potential of these coupling configurations with respect to the observables considered, the coupling dependent coefficients of Equations 3.24–3.27 are re-expressed in the vector-axial basis as follows

$$A_{LL} \propto -\Big(q_V^i q_V^j + q_A^i q_A^j\Big)\Big(\left(2+\beta^2\right) f_V^i f_V^j + 3\beta^2 f_A^i f_A^j\Big), \tag{4.8}$$

$$A_L \propto \beta\Big(q_V^i q_V^j + q_A^i q_A^j\Big)\Big(f_V^i f_A^j + f_A^i f_V^j\Big), \tag{4.9}$$

$$A_{FB} \propto \Big(q_V^i q_A^j + q_A^i q_V^j\Big)\Big(f_V^i f_A^j + f_A^i f_V^j\Big), \tag{4.10}$$

$$\sigma \propto \Big(q_V^i q_V^j + q_A^i q_A^j\Big)\Big(\left(4-\beta^2\right) f_V^i f_V^j + \beta^2 f_A^i f_A^j\Big), \tag{4.11}$$

where q and f are, as before, the initial state quark and the final state fermion couplings with the indices i, j referring to the neutral resonances taking part in the process and V, A denote vector and axial respectively. The product of vector and axial couplings is equivalent, up to an overall factor, to the parity asymmetric combination, A_{ij}, defined in Equation 3.16. Similarly, the sum of squares of both sets of couplings are equivalent, also up to an overall factor. It is apparent, therefore, that resonances with purely vector or axial couplings may not be able to generate these observables on their own. Charge asymmetry requires this for both the initial and final state, while the spin polarisation is only sensitive to this feature in the final state couplings. In either case, the observable

would only be generated via interference with another neutral vector with different couplings.

The table shows that the $E_6(G_{LR}(BL))$ models share a general feature of the Z' having a purely axial(vector) coupling to up-type quarks. Hence, charge asymmetry can only be generated via interference with the EW background and is therefore expected to be very small for these models. Similarly for the spin asymmetries, Equations 4.8 and 4.9 imply that these will only have a non-vanishing A_{LL} (at the Z' peak), that could serve as an extra handle to pin down parameters for these models, while A_L is, again, generated only via interference.

The rest of the models have generic, non-zero vector and axial couplings which will generate charge asymmetry, A_{LL} and A_L. As mentioned in Section 3.2.2, A_L has the extra handle of distinguishing relative sign between the vector and axial couplings which is equivalent to being sensitive to the relative chirality of the Z' couplings, i.e. the size of g_L compared to g_R, although not their sign. Looking at the table, one would expect the G_{LR} and G_{SM} subclasses to therefore have opposite signs in A_L, since they couple to admixtures of a vector current with a right and left-handed current respectively. It is clear that A_L should provide a clear distinguishing feature that would not be anywhere near as striking in the cross section. For these reasons, the analysis is subdivided into that of the "E_6 type" models which will also include $G_{LR}(BL)$ and "Generalised" models comprising of the rest.

4.2 Calculation of observables

The code exploited for the study is based on helicity amplitudes, defined through the HELAS subroutines [83], and built up by means of MadGraph [84]. Initial state quarks were assumed to be massless while for the (anti-)top state, a mass of $m_t = 175$ GeV was taken. The latter has been kept on-shell. The PDFs used were CTEQ6L1 [18], with factorisation/renormalisation scale set to $Q = \mu = 2m_t$. VEGAS [85] was used for the multi-dimensional numerical integrations. The spin asymmetries are calculated at parton level, in terms of the top and anti-top helicities, while for the charge asymmetry, four observables were considered, two of which restrict the rapidity range of the event selection while the other two directly compared the top and anti-top rapidities all of which aim to observe the different rapidity distributions effected by charge asymmetry, as explained in Section 3.2.1. The efficacy of the different observables can hence be compared to pick an optimum choice among the four. In all cases, however, the kinematical restrictions imposed lead to a loss in statistics which, in retrospect, affects the overall significance of such observables compared to alternative definitions which make use of the full sample (see Chapter 6).

Considering both the inner and outer rapidity regions based on a fixed rapidity cut, y_{cut}, constructs the so-called "central" (C) and "forward" (F) asymmetries [27, 86]:

$$A_C = \frac{N_t(|y| < y^C_{cut}) - N_{\bar{t}}(|y| < y^C_{cut})}{N_t(|y| < y^C_{cut}) + N_{\bar{t}}(|y| < y^C_{cut})}, \tag{4.12}$$

$$A_F = \frac{N_t(|y| > y^F_{cut}) - N_{\bar{t}}(|y| > y^F_{cut})}{N_t(|y| > y^F_{cut}) + N_{\bar{t}}(|y| > y^F_{cut})}, \tag{4.13}$$

comparing the number of tops (N_t) and of anti-tops ($N_{\bar{t}}$) in that region. Taking $y^{C(F)}_{cut} \to \infty(0)$, for either observable, i.e. integrating them over the whole rapidity range, will restore $A_{C(F)} = 0$. In this analysis, the value was fixed at $y^C_{cut} = y^F_{cut} = 0.5$, chosen by looking at the top and anti-top rapidity distributions of a number of benchmark models.

The other two observables are a function of the absolute rapidity difference of the top and anti-top quarks, $\Delta y = |y_t| - |y_{\bar{t}}|$, which is sensitive to the CM polar angle and independent of the $t\bar{t}$ frame boost. These were implemented based on asymmetry-enhancing kinematical cuts proposed in [28], acting on the rapidity or on the momentum along the beam axis (e.g., the z one) of the top–anti-top pair, $y_{t\bar{t}} = \frac{1}{2}(y_t - y_{\bar{t}})$ and $p^z_{t\bar{t}} = p^z_t + p^z_{\bar{t}}$. Referred to as "rapidity dependent" (RFB) and "one-sided" (OFB) forward-backward asymmetries respectively, they are defined as

$$A_{RFB} = \left.\frac{N(\Delta y > 0) - N(\Delta y < 0)}{N(\Delta y > 0) + N(\Delta y < 0)}\right|_{|y_{t\bar{t}}| > |y^{cut}_{t\bar{t}}|}, \tag{4.14}$$

$$A_{OFB} = \left.\frac{N(\Delta y > 0) - N(\Delta y < 0)}{N(\Delta y > 0) + N(\Delta y < 0)}\right|_{|p^z_{t\bar{t}}| > p^z_{cut}}. \tag{4.15}$$

Such kinematical cuts are designed to enhance the contributions from the $q\bar{q}$ initial state by probing regions of high partonic momentum fraction, x, where the parton luminosity of interest is more important.

4.3 Results

A selection of results profiling the charge and spin asymmetry distributions of the benchmark Z' models are presented. The variables described in section 4.2 were computed as a function of the $t\bar{t}$ invariant mass within $\Delta M_{t\bar{t}} = |M_{Z'} - M_{t\bar{t}}| < 500$ GeV and compared to the tree-level SM predictions[2]. Z' boson masses of 1.7 and 2.0 TeV were taken and

[2]It has also been shown that the fraction of $q\bar{q}$ initiated events could be equally enhanced by other kinematical cuts, such as on the transverse momentum of each top quark [87] as well as on the $t\bar{t}$ system [88, 89]. However, the latter is not applicable to tree-level studies.

simulated for the LHC at 7, 8 and 14 TeV. Only results for 8 and 14 TeV CM energy are presented although the former energy can still be taken as representative for the 7 TeV run, as the corresponding results are very similar. The benchmarks are characterised by the couplings of Table 4.1 with their widths calculated at tree-level, only including decays to SM fermions, compensating for small NLO QCD effects in quark decays by a k-factor related to the strong coupling, α_S, at the Z' mass scale of $k = 1 + 1.045\,\alpha_S(M_{Z'})/\pi$ [90].

To be able to quantitatively address the distinguishability among the various models and the SM background, the statistical error of the predictions was calculated for some specific integrated luminosities as defined in Equation 2.4. Here, ε corresponds to an assumed 10% reconstruction efficiency of the $t\bar{t}$ system, considering all possible decay $t\bar{t}$ decay channels informed, at the time, by the projected efficiencies in the technical design reports [91]. In later work, the reconstruction efficiency estimates were taken to be more conservative in the view that the boosted topology may introduce difficulties in traditional reconstruction methods, particularly in the case of spin asymmetries, as discussed in Section 2.5. The continuous curves on the following plots are the central values for the given asymmetry, with a statistical error quantified by binning the cross sections in $M_{t\bar{t}}$ for a bin width of 50 GeV compatible with typical experimental resolutions in this quantity. This assumption has also been made more conservative in future work, guided by recent experimental analyses. A selection of two bin plots integrating the cross sections over an "on-peak" range ($\Delta M_{t\bar{t}} < 100$ GeV) and evaluating the corresponding partially integrated asymmetry are shown. Finally the totally integrated asymmetries are summarised in the corresponding tables, for both the $M_{t\bar{t}}$ window cuts. Invariant mass distributions of the total cross sections for $t\bar{t}$ production are also included for reference, with the statistical error normalised by the bin width.

Although only statistical uncertainties are estimated in this work, systematics may be important as well [87, 89]. However, although the mass window selection is expected to milden their actual contribution, their inclusion would require detailed detector simulations which are beyond the scope of this paper. In this respect, it should further be noted that, by the time the LHC will reach the 14 TeV stage, where the most interesting results are applicable, systematics will be much better understood than at present. Furthermore, the statistical "significance" of two measurements – in the context of this parton level study without subsequent top decay – is calculated as follows, relying on the assumption that they are independent:

$$s \equiv \frac{|A(1) - A(2)|}{\sqrt{\delta A(1)^2 + \delta A(2)^2}}\,. \tag{4.16}$$

$A(1,2)$ and $\delta A(1,2)$ refer to the observables and standard deviations respectively predicted by two hypotheses. Equation 4.16 will be used to establish a measure of the disentanglement power of the LHC for $\sqrt{s} = 14$ TeV with 100 fb^{-1}. It is an adaptation of a two sample z-test, comparing two independent data sets with known means and

standard deviations, assumed to be normally distributed. The z score can be converted to a p-value which corresponds to the probability that the difference between the measurements came from statistical fluctuations and that the two hypotheses are the same. The standard $S/\sqrt{B}$ measure of significance for counting experiments is an example of such a test in the limit where the signal, S, is much smaller than the background, B. Finally, given that the statistical error of Equation 2.4 has a $1/\sqrt{\mathcal{L}}$ dependence, it is clear that the significance of a measure, as for Equation 4.16, increases with luminosity. Inverting Equation 4.16 and solving for $\mathcal{L}$, the required luminosity to distinguish the models with respect to the irreducible SM background and among themselves can be determined, defining disentanglement by $s \geq 3$.

In the following, the differential distributions for the most significant asymmetries in each class will be presented and commented upon, i.e. A_{LL} for the E_6-type models and A_{LL}, A_L and A_{RFB} for the generalised models. The comparison among the two classes (and between elements within them) is made at the end, evaluating the significance of the presented distributions. As a final comment, recent di-lepton searches have now mostly excluded the masses of the particular benchmarks considered, as can be inferred from Section 3.1.5 and the references therein. Nevertheless, the main features of the analysis remain valid at higher masses, albeit without as high significances, as statistics decrease.

4.3.1 E_6-type models

Figure 4.1 presents the invariant mass distributions around the Z' peak for this subset of models with $M_{Z'}$ =1.7 TeV at both 14 and 8 TeV. These plots show that the various Z' bosons would certainly be visible in this channel, especially in the high energy and high luminosity scenario. The strength of each signal is related only to the coupling strength and width of the different models, which are also a function of the fermion couplings. Therefore, one would expect that the visibility in this decay mode would be suppressed compared to the di-lepton channel only by the impact on reconstruction efficiency and resolution associated with the six-body decay.

Figure 4.3 profiles A_{LL} in invariant mass for the LHC at 14 TeV and Table 4.2 summarises integrated values for these models at both 14 and 8 TeV. When calculating statistical uncertainties, an integrated luminosity of 100 and 15 fb^{-1} is assumed for the two energies, respectively. The analytical expression in Equation 4.8 shows that the observable depends on the top couplings in a similar way to the total cross section. This is reflected in the deviations from the SM shown in the figures, with large effects occurring on peak whose significances increase when restricting $\Delta M_{t\bar{t}}$ as shown in Table 4.2. This more or less parallels the effects seen in the invariant mass distributions. In the limit of $\sqrt{\hat{s}} >> 2m_t$, A_{LL} depends identically on the vector and axial couplings of the tops and therefore cannot distinguish between the purely vector and purely axial cases of

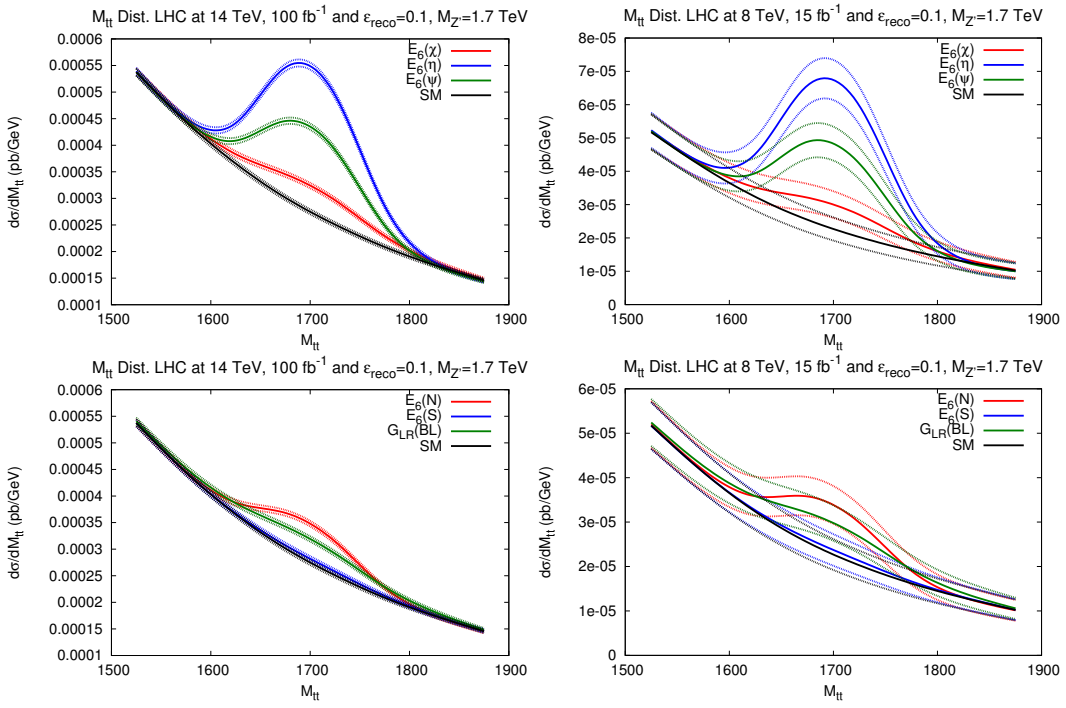

Figure 4.1: Invariant mass distributions for E_6-type models for $M_{Z'}$=1.7 TeV for the LHC at 14(8) TeV and 100(15) fb^{-1} of integrated luminosity. Dotted lines represent statistical uncertainty calculated as described in the text.

$G_{LR}(BL)$ and E_6 models. Furthermore, unlike A_L, not only is it insensitive to the relative sign between the couplings but it also tends to one in the high energy limit $\beta \to 1$. The insensitivity is reflected by the overlapping of the $G_{LR}(BL)$ and $E_6(\chi)$ cases, that differ in having purely vector and axial couplings respectively of different sign but of a similar magnitude. Such cases are never distinguishable, neither with total cross section nor A_{LL} measurements.

Aside from these limitations, Figure 4.3 shows clear distinguishability of models from the SM and between one another based on differences in couplings for the high energy case except when the up type coupling is too small, as for $E_6(S)$. (Table 4.1 implies that this model would be much better suited to the $b\bar{b}$ channel). Table 4.2 further improves on these numbers by comparing integrated values focused around the Z' peak which gives scope for sensitivity to deviations from the SM and limited distinguishability even at low energy.

4.3.2 Generalised models

In contrast to the E_6-type models, the generalised models have non-zero vector and axial couplings to all quarks meaning that all of the asymmetry observables can be generated at tree-level, on peak. The gauge coupling of the G_{LR} and G_{SM} classes is also larger than that of the E_6 class. Combined with their consequently higher cross sections

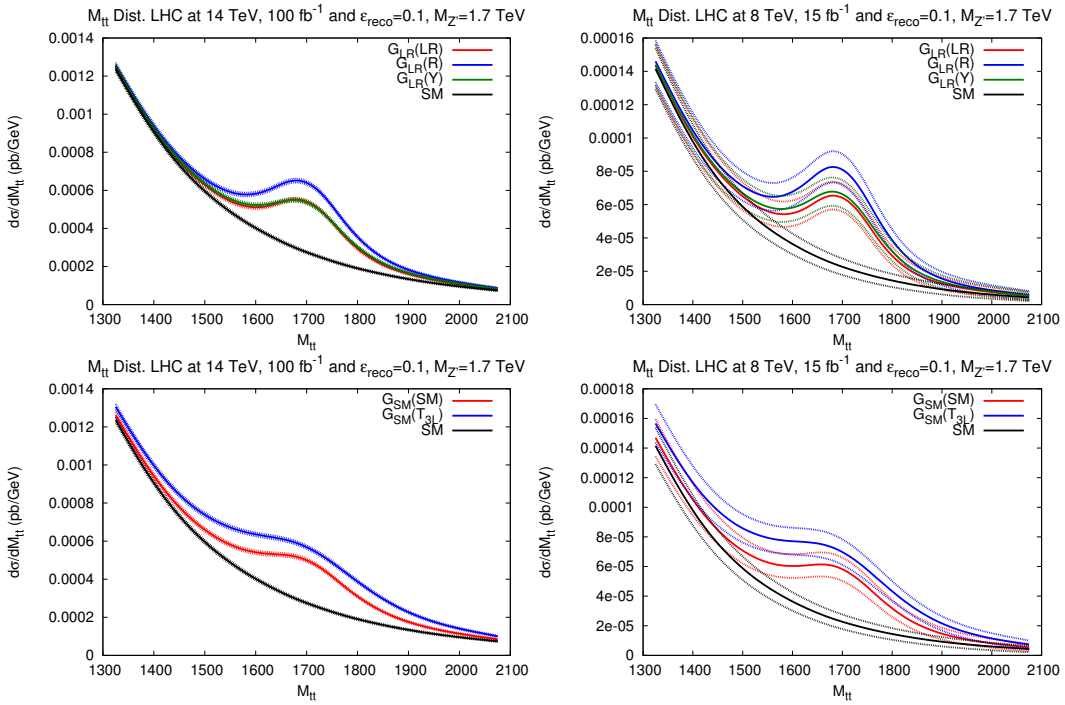

Figure 4.2: Invariant mass distributions for generalised models with $M_{Z'}$=1.7 TeV for the LHC at 14(8) TeV and 100(15) fb^{-1} of integrated luminosity. Dotted lines represent statistical uncertainty calculated as described in the text.

(proportional to g'^4), shown in the invariant mass distributions of Figure 4.2, this set of models has clear asymmetry signatures at the LHC, even at 8 TeV. Figures 4.4 and 4.5 and Tables 4.3 and 4.4 profile the spin asymmetry variables A_{LL} and A_L, showing large deviations from the SM case for the LHC at 14 TeV. As already noted, the difference in sign in the A_L contributions of the G_{LR} and G_{SM} models allows for the best distinguishing power over all the models investigated. This is particularly important for the specific case of the $G_{LR}(LR/Y)$ and $G_{SM}(SM)$ models that do not appear distinguishable in the invariant mass distributions nor in the other variables, but do so in the A_L two-bin plots. The spatial asymmetry variables are also clearly visible in these models and are all rather similar. It was found that A_{RFB}, employing the $t\bar{t}$ system rapidity cut offered the best discrimination power[3]. Figure 4.6 presents the observable in differential form while its integrated values are found in Table 4.5.

4.3.3 Significance and luminosity analysis

Table 4.6 summarises the significance measures between various models as defined in Equation 4.16 for A_{LL}, A_L and A_{RFB}, for the values given in Tables 4.2 to 4.5. Generally speaking, A_L provides the best overall discrimination power, when the variable is non-vanishing at the Z' peak. Beside preserving the relative sign between the top quark

[3]This is expected from the fact that the kinematical cut enhances the $q\bar{q}$ contribution to the initial state as discussed in Section 4.2

vector and axial couplings, allowing to distinguish the G_{SM} from the G_{LR} class, it also has the highest significance when comparing the Z' models in these classes with the SM expectation and among themselves. For the E_6-type cases, where A_L is too small to be measured, the other spin variable A_{LL} comes into play. We observe that its significance is always bigger than the spatial asymmetries, A_{RFB} being the biggest amongst the latter. As mentioned, this variable can be used to distinguish all the presented models from the SM background. Regarding the disentanglement among models, we observe that the narrower mass window and lower Z' mass always perform better thanks to the larger signal over background (S/B) and better statistics respectively. Models with very large width, such as the G_{SM} ones, deliver a bigger significance in the larger invariant mass cut.

From these tables it is clear that some models can be distinguished at early stages of the LHC at $\sqrt{s} = 14$ TeV, i.e., with less than 100 fb^{-1}. At the same time, the question of what the required luminosity is to discriminate among models also quantifies how powerful a variable is. Tables 4.7 and 4.8 address the distinguishability of the various models using the spin and spatial asymmetries with increasing integrated luminosity. Specifically, they give the required luminosity, when possible, to give a significance measure of 3. These reinforce the fact that the models can generally be separated using these observables for reasonable integrated luminosities when the sizes (and signs) of the relevant couplings differ enough. The spin asymmetries provide the best distinctions and A_{RFB} performs the best among the spatial asymmetries.

Although certain models remain unresolvable even with full luminosity, 300 fb^{-1}, $\mathcal{O}(1)$ fb^{-1} of integrated luminosity is already enough to begin disentangling the generalised models using A_L. In particular, the $G_{LR}(Y)$ and $G_{LR}(LR)$ become distinguishable at just over 100 fb^{-1}. With A_{LL}, E_6-type models start being distinguishable with $\mathcal{O}(10)$ fb^{-1}. $\mathcal{O}(50)$ fb^{-1} is required for full discrimination with A_{LL}, as well as to have confirmations for the generalised models with the spatial asymmetries, among which A_{RFB} outperforms all the others requiring less integrated luminosity.

4.4 Conclusions

A phenomenological study of classes of Z' models has been carried out in both spin and spatial asymmetries of $t\bar{t}$ production as a first look at the potential of this channel to investigate Z' signatures. A selection of observables has been defined and profiled as a function of the $t\bar{t}$ invariant mass showing that there is much scope to observe deviations from the SM and even distinguish between various models, particularly for spin asymmetries, using a narrow invariant mass range around the Z' peak. Further, a measure of distinguishability between models was quantified and considered the significance of such differences with respect to the integrated luminosity.

It is worth noting that, as stated in Section 4.1, the classes of models studied are a set of benchmarks put forward for experimentalists to set bounds on Z' masses which are best probed in the di-lepton channels. Other models featuring heavy neutral gauge bosons would be even better suited to the $t\bar{t}$ channel, such as lepto-phobic/top-phillic Z's occurring in composite/multi-site and extra-dimensional models (see Chapters 6 and 7). The profiling techniques discussed in this study would be increasingly more applicable in these top-friendly scenarios. Furthermore, it has been assumed that all other exotic matter states are decoupled for simplicity while they may have non-negligible effects on widths and branching ratios that should be considered when moving away from model independent methods.

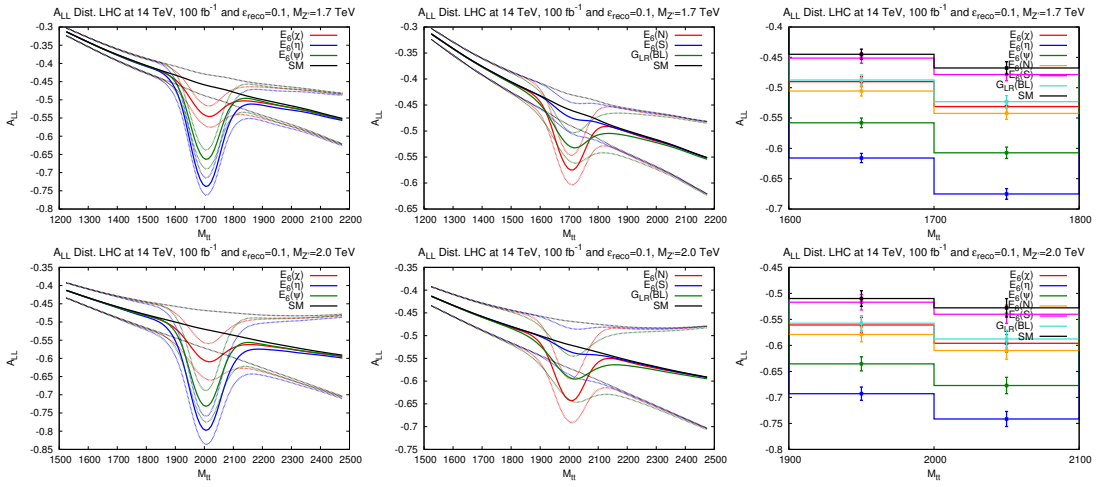

Figure 4.3: A_{LL} binned in $M_{t\bar{t}}$ for E_6-type models with $M_{Z'}$=1.7 (*upper*) and 2 (*lower*) TeV for the LHC at 14 TeV assuming 100 fb^{-1} of integrated luminosity. Rightmost plots show the distribution in two 100 GeV bins either side of the Z' peak. Dotted lines and error bars represent statistical uncertainty calculated as described in the text.

$A_{LL}(\times 10)$	$\sqrt{s} = 14$ TeV	$\mathcal{L}_{int} = 100$ fb^{-1}	$\sqrt{s} = 8$ TeV	$\mathcal{L}_{int} = 15$ fb^{-1}
$M_{Z'} = 1.7$ TeV	$\Delta M_{t\bar{t}} < 0.5$ TeV	$\Delta M_{t\bar{t}} < 0.1$ TeV	$\Delta M_{t\bar{t}} < 0.5$ TeV	$\Delta M_{t\bar{t}} < 0.1$ TeV
SM	-3.79 ± 0.05	-4.54 ± 0.07	-4.75 ± 0.39	-5.65 ± 0.61
$E_6(\chi)$	-3.88 ± 0.05	-5.07 ± 0.06	-4.85 ± 0.39	-6.35 ± 0.58
$E_6(\eta)$	-4.17 ± 0.05	-6.42 ± 0.06	-5.22 ± 0.38	-7.85 ± 0.48
$E_6(\psi)$	-4.01 ± 0.05	-5.79 ± 0.06	-5.02 ± 0.33	-7.22 ± 0.52
$E_6(N)$	-3.90 ± 0.05	-5.21 ± 0.06	-4.88 ± 0.39	-6.54 ± 0.57
$E_6(S)$	-3.80 ± 0.05	-4.62 ± 0.07	-4.76 ± 0.39	-5.76 ± 0.61
$G_{LR}(BL)$	-3.88 ± 0.05	-5.02 ± 0.06	-4.86 ± 0.39	-6.31 ± 0.57
$M_{Z'} = 2.0$ TeV	$\Delta M_{t\bar{t}} < 0.5$ TeV	$\Delta M_{t\bar{t}} < 0.1$ TeV	$\Delta M_{t\bar{t}} < 0.5$ TeV	$\Delta M_{t\bar{t}} < 0.1$ TeV
SM	-4.66 ± 0.09	-5.17 ± 0.11	-5.68 ± 0.84	-6.32 ± 1.23
$E_6(\chi)$	-4.77 ± 0.09	-5.76 ± 0.11	-5.81 ± 0.83	-7.03 ± 1.14
$E_6(\eta)$	-5.13 ± 0.09	-7.15 ± 0.10	-6.26 ± 0.80	-8.44 ± 0.89
$E_6(\psi)$	-4.94 ± 0.09	-6.54 ± 0.10	-6.02 ± 0.82	-7.90 ± 1.00
$E_6(N)$	-4.79 ± 0.09	-5.92 ± 0.11	-5.84 ± 0.83	-7.23 ± 1.11
$E_6(S)$	-4.67 ± 0.09	-5.27 ± 0.11	-5.70 ± 0.84	-6.43 ± 1.22
$G_{LR}(BL)$	-4.77 ± 0.09	-5.70 ± 0.11	-5.82 ± 0.83	-7.00 ± 1.13

Table 4.2: Summary of integrated A_{LL} values around the Z' peak for E_6-type models with $M_{Z'}$=1.7 and 2 TeV at the LHC at 14 and 8 TeV assuming 100 and 15 fb^{-1} of integrated luminosity respectively.

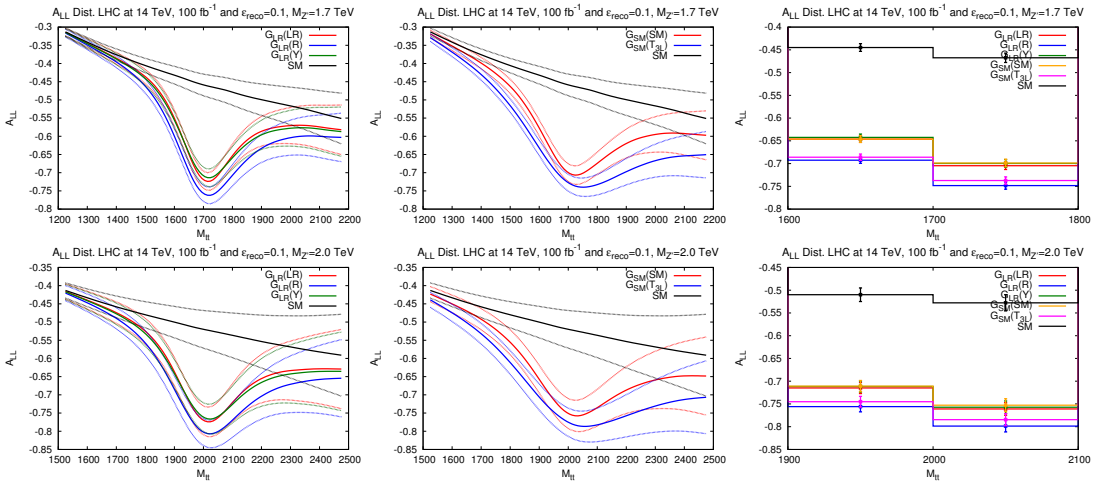

Figure 4.4: A_{LL} distributions binned in $M_{t\bar{t}}$ for generalised models with $M_{Z'}$=1.7 (*upper*) and 2 (*lower*) TeV for the LHC at 14 TeV assuming 100 fb^{-1} of integrated luminosity. Rightmost plots show the distribution in two 100 GeV bins either side of the Z' peak. Dotted lines and error bars represent statistical uncertainty calculated as described in the text.

$A_{LL}(\times 10)$	$\sqrt{s} = 14$ TeV	$\mathcal{L}_{int} = 100$ fb^{-1}	$\sqrt{s} = 8$ TeV	$\mathcal{L}_{int} = 15$ fb^{-1}
$M_{Z'} = 1.7$ TeV	$\Delta M_{t\bar{t}} < 0.5$ TeV	$\Delta M_{t\bar{t}} < 0.1$ TeV	$\Delta M_{t\bar{t}} < 0.5$ TeV	$\Delta M_{t\bar{t}} < 0.1$ TeV
SM	-3.79 ± 0.05	-4.54 ± 0.07	-4.75 ± 0.39	-5.65 ± 0.61
$G_{LR}(LR)$	-4.41 ± 0.05	-6.72 ± 0.06	-5.48 ± 0.37	-8.03 ± 0.45
$G_{LR}(R)$	-4.70 ± 0.05	-7.18 ± 0.05	-5.83 ± 0.36	-8.38 ± 0.41
$G_{LR}(Y)$	-4.43 ± 0.05	-6.68 ± 0.05	-5.55 ± 0.37	-8.02 ± 0.44
$G_{SM}(SM)$	-4.52 ± 0.05	-6.69 ± 0.06	-5.64 ± 0.37	-8.04 ± 0.45
$G_{SM}(T_{3L})$	-4.94 ± 0.04	-7.09 ± 0.05	-6.12 ± 0.35	-8.31 ± 0.41
$M_{Z'} = 2.0$ TeV	$\Delta M_{t\bar{t}} < 0.5$ TeV	$\Delta M_{t\bar{t}} < 0.1$ TeV	$\Delta M_{t\bar{t}} < 0.5$ TeV	$\Delta M_{t\bar{t}} < 0.1$ TeV
SM	-4.66 ± 0.09	-5.17 ± 0.11	-5.68 ± 0.84	-6.32 ± 1.23
$G_{LR}(LR)$	-5.41 ± 0.08	-7.36 ± 0.09	-6.53 ± 0.78	-8.51 ± 0.85
$G_{LR}(R)$	-5.74 ± 0.08	-7.75 ± 0.09	-6.90 ± 0.75	-8.79 ± 0.76
$G_{LR}(Y)$	-5.44 ± 0.08	-7.32 ± 0.09	-6.62 ± 0.77	-8.53 ± 0.82
$G_{SM}(SM)$	-5.53 ± 0.08	-7.30 ± 0.09	-6.69 ± 0.77	-8.51 ± 0.86
$G_{SM}(T_{3L})$	-5.99 ± 0.08	-7.63 ± 0.09	-7.16 ± 0.72	-8.72 ± 0.78

Table 4.3: Summary of integrated A_{LL} values around the Z' peak for the generalised models with $M_{Z'}$=1.7 and 2 TeV at the LHC at 14 and 8 TeV assuming 100 and 15 fb^{-1} of integrated luminosity respectively.

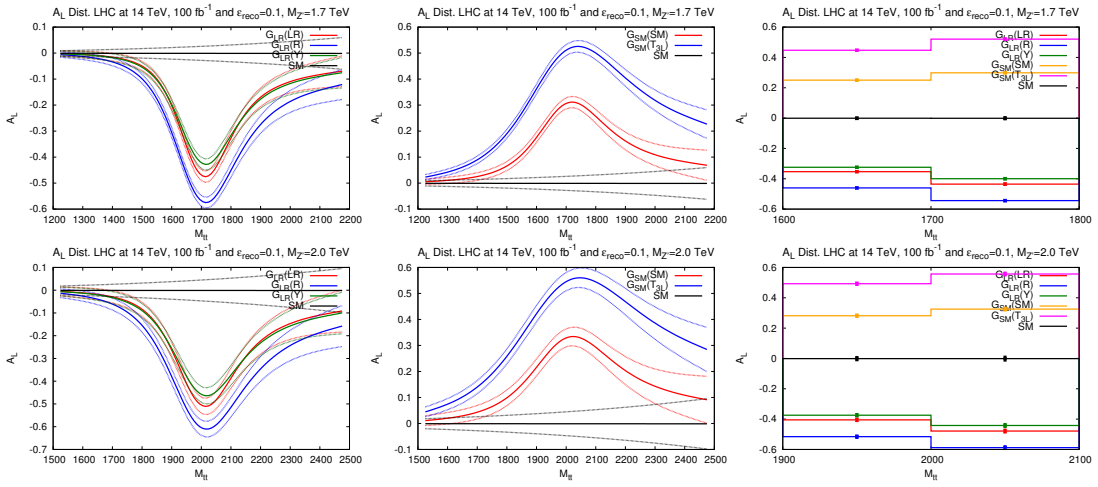

Figure 4.5: A_L binned in $M_{t\bar{t}}$ for generalised models with $M_{Z'}$=1.7 (*upper*) and 2 (*lower*) TeV for the LHC at 14 TeV assuming 100 fb^{-1} of integrated luminosity. Rightmost plots show the distribution in two 100 GeV bins either side of the Z' peak. Dotted lines and error bars represent statistical uncertainty calculated as described in the text.

$A_L(\times 10)$	$\sqrt{s} = 14$ TeV	$\mathcal{L}_{int} = 100$ fb^{-1}	$\sqrt{s} = 8$ TeV	$\mathcal{L}_{int} = 15$ fb^{-1}
$M_{Z'} = 1.7$ TeV	$\Delta M_{t\bar{t}} < 0.5$ TeV	$\Delta M_{t\bar{t}} < 0.1$ TeV	$\Delta M_{t\bar{t}} < 0.5$ TeV	$\Delta M_{t\bar{t}} < 0.1$ TeV
SM	-0.009 ± 0.044	-0.010 ± 0.059	-0.017 ± 0.35	-0.020 ± 0.53
$G_{LR}(LR)$	-0.971 ± 0.042	-3.90 ± 0.05	-1.37 ± 0.33	-5.36 ± 0.40
$G_{LR}(R)$	-1.51 ± 0.04	-4.98 ± 0.05	-2.14 ± 0.32	-6.53 ± 0.37
$G_{LR}(Y)$	-0.938 ± 0.042	-3.58 ± 0.05	-1.40 ± 0.33	-5.05 ± 0.38
$G_{SM}(SM)$	0.802 ± 0.042	2.71 ± 0.05	1.16 ± 0.32	3.79 ± 0.38
$G_{SM}(T_{3L})$	1.90 ± 0.04	4.80 ± 0.05	2.70 ± 0.31	6.36 ± 0.38
$M_{Z'} = 2.0$ TeV	$\Delta M_{t\bar{t}} < 0.5$ TeV	$\Delta M_{t\bar{t}} < 0.1$ TeV	$\Delta M_{t\bar{t}} < 0.5$ TeV	$\Delta M_{t\bar{t}} < 0.1$ TeV
SM	-0.011 ± 0.088	-0.012 ± 0.10	-0.020 ± 0.73	-0.020 ± 1.04
$G_{LR}(LR)$	-1.38 ± 0.07	-4.38 ± 0.08	-1.91 ± 0.66	-5.81 ± 0.75
$G_{LR}(R)$	-2.09 ± 0.07	-5.49 ± 0.08	-2.91 ± 0.64	-6.97 ± 0.69
$G_{LR}(Y)$	-1.34 ± 0.07	-4.05 ± 0.08	-1.99 ± 0.65	-5.54 ± 0.71
$G_{SM}(SM)$	1.12 ± 0.07	3.01 ± 0.08	1.59 ± 0.65	4.07 ± 0.71
$G_{SM}(T_{3L})$	2.55 ± 0.07	5.21 ± 0.08	3.53 ± 0.62	6.74 ± 0.71

Table 4.4: Summary of integrated A_L values around the Z' peak for the generalised models with $M_{Z'}$=1.7 and 2 TeV at the LHC at 14 and 8 TeV assuming 100 and 15 fb^{-1} of integrated luminosity respectively.

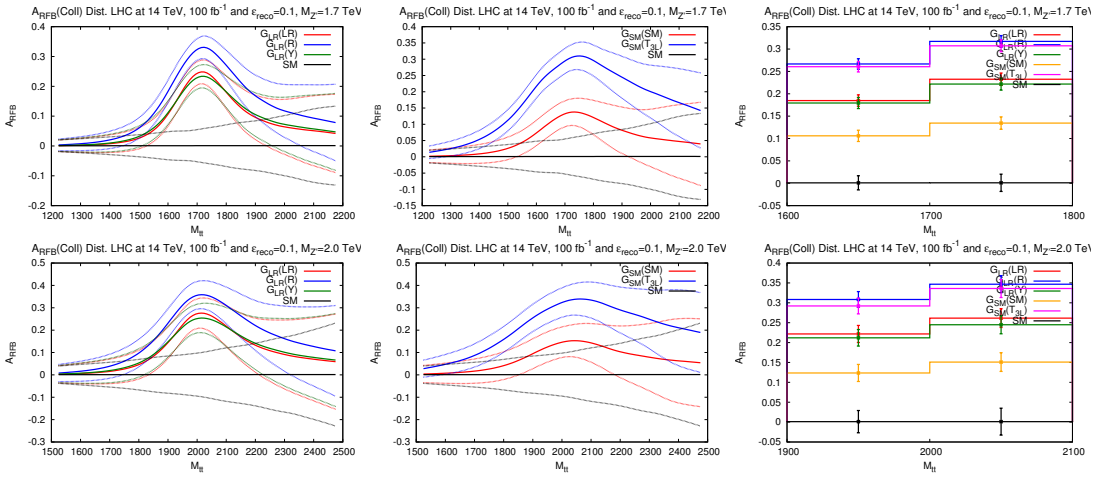

Figure 4.6: A_{RFB} binned in $M_{t\bar{t}}$ for generalised models with $M_{Z'}$=1.7 (*upper*) and 2 (*lower*) TeV for the LHC at 14 TeV assuming 100 fb^{-1} of integrated luminosity. Rightmost plots show the distribution in two 100 GeV bins either side of the Z' peak. Dotted lines and error bars represent statistical uncertainty calculated as described in the text.

$A_{RFB}(\times 10)$	$\sqrt{s} = 14$ TeV	$\mathcal{L}_{int} = 100$ fb^{-1}	$\sqrt{s} = 8$ TeV	$\mathcal{L}_{int} = 15$ fb^{-1}
$M_{Z'} = 1.7$ TeV	$\Delta M_{t\bar{t}} < 0.5$ TeV	$\Delta M_{t\bar{t}} < 0.1$ TeV	$\Delta M_{t\bar{t}} < 0.5$ TeV	$\Delta M_{t\bar{t}} < 0.1$ TeV
SM	0.008 ± 0.089	0.010 ± 0.122	0.018 ± 0.819	0.02 ± 1.35
$G_{LR}(LR)$	0.501 ± 0.084	2.07 ± 0.09	0.776 ± 0.760	3.27 ± 0.88
$G_{LR}(R)$	0.873 ± 0.081	2.89 ± 0.09	1.34 ± 0.73	4.24 ± 0.79
$G_{LR}(Y)$	0.523 ± 0.083	1.99 ± 0.09	0.807 ± 0.745	2.96 ± 0.82
$G_{SM}(SM)$	0.337 ± 0.083	1.19 ± 0.09	0.524 ± 0.743	1.88 ± 0.86
$G_{SM}(T_{3L})$	1.10 ± 0.08	2.81 ± 0.09	1.71 ± 0.70	4.15 ± 0.81
$M_{Z'} = 2.0$ TeV	$\Delta M_{t\bar{t}} < 0.5$ TeV	$\Delta M_{t\bar{t}} < 0.1$ TeV	$\Delta M_{t\bar{t}} < 0.5$ TeV	$\Delta M_{t\bar{t}} < 0.1$ TeV
SM	0.010 ± 0.167	0.011 ± 0.216	0.02 ± 1.86	0.03 ± 2.84
$G_{LR}(LR)$	0.745 ± 0.153	2.40 ± 0.16	1.13 ± 1.67	3.70 ± 1.82
$G_{LR}(R)$	1.26 ± 0.15	3.26 ± 0.14	1.90 ± 1.58	4.67 ± 1.62
$G_{LR}(Y)$	0.768 ± 0.151	2.27 ± 0.15	1.17 ± 1.62	3.30 ± 1.66
$G_{SM}(SM)$	0.495 ± 0.152	1.36 ± 0.16	0.75 ± 1.62	2.07 ± 1.73
$G_{SM}(T_{3L})$	1.54 ± 0.14	3.12 ± 0.15	2.33 ± 1.51	4.54 ± 1.67

Table 4.5: Summary of integrated A_{RFB} values around the Z' peak for generalised models with $M_{Z'}$=1.7 and 2 TeV at the LHC at 14 and 8 TeV assuming 100 and 15 fb^{-1} of integrated luminosity respectively.

A_{LL}	SM	$E_6(\chi)$	$E_6(\eta)$	$E_6(\psi)$	$E_6(N)$	$E_6(S)$	$G_{LR}(BL)$	$G_{LR}(LR)$	$G_{LR}(R)$	$G_{LR}(Y)$	$G_{SM}(SM)$	$G_{SM}(T_{3L})$
SM	–	5.7(1.3)	20.4(5.4)	13.6(3.1)	7.3(1.6)	0.8(0.1)	5.2(1.3)	23.6(8.8)	30.7(12.9)	24.9(9.1)	23.3(10.3)	29.6(18.0)
$E_6(\chi)$	3.8(0.9)	–	15.9(4.1)	8.5(1.8)	1.6(0.3)	4.9(1.1)	$0.6(\ll 1)$	19.4(7.5)	27.0(11.6)	20.6(7.8)	19.1(9.1)	25.9(16.6)
$E_6(\eta)$	13.3(3.7)	9.4(2.8)	–	7.4(2.3)	14.3(3.8)	19.5(5.2)	16.5(4.1)	3.5(3.4)	9.7(7.5)	3.3(3.7)	3.2(4.9)	8.6(12.0)
$E_6(\psi)$	9.2(2.2)	5.2(1.3)	4.3(1.5)	–	6.8(1.6)	12.7(3.0)	9.1(1.8)	11.0(5.7)	17.8(9.8)	11.4(5.9)	10.6(7.2)	16.6(14.5)
$E_6(N)$	4.8(1.0)	1.0(0.2)	8.3(2.7)	4.2(1.2)	–	6.4(1.4)	2.2(0.3)	17.8(7.2)	25.2(11.3)	18.8(7.5)	17.4(8.8)	24.1(16.2)
$E_6(S)$	0.6(0.1)	3.1(0.8)	12.6(3.6)	8.5(2.1)	4.2(0.9)	–	4.3(1.1)	22.8(8.6)	29.8(12.7)	23.9(8.9)	22.5(10.2)	28.7(17.8)
$G_{LR}(BL)$	3.4(0.9)	$0.4(\ll 1)$	9.8(2.8)	5.7(1.3)	1.4(0.2)	2.8(0.8)	–	20.0(7.5)	27.7(11.6)	21.3(7.8)	19.7(9.1)	26.5(16.6)
$G_{LR}(LR)$	15.4(6.2)	11.3(5.3)	1.6(2.3)	6.1(3.9)	10.1(5.1)	14.7(6.1)	11.7(5.3)	–	5.9(4.1)	0.5(0.3)	0.4(1.6)	4.7(8.3)
$G_{LR}(R)$	18.2(9.0)	14.0(8.1)	4.5(5.1)	9.0(6.6)	12.9(7.9)	17.4(8.9)	14.4(8.1)	3.1(2.9)	–	7.1(3.8)	6.3(2.5)	1.3(3.7)
$G_{LR}(Y)$	15.1(6.5)	11.0(5.6)	1.3(2.6)	5.8(4.2)	9.9(5.4)	14.4(6.4)	11.4(5.6)	0.3(0.3)	3.4(2.7)	–	0.1(1.3)	5.8(8.0)
$G_{SM}(SM)$	15.0(7.2)	10.8(6.3)	1.1(3.3)	5.6(4.9)	9.7(6.1)	14.3(7.1)	11.3(6.3)	0.5(1.1)	3.5(1.9)	0.2(0.8)	–	5.1(6.6)
$G_{SM}(T_{3L})$	17.3(11.0)	13.2(10.1)	3.6(7.1)	8.1(8.7)	12.0(10.0)	16.6(11.0)	13.6(10.1)	2.1(5.1)	0.9(2.2)	2.4(4.9)	2.6(4.1)	–

A_L	SM	$G_{LR}(LR)$	$G_{LR}(R)$	$G_{LR}(Y)$	$G_{SM}(SM)$	$G_{SM}(T_{3L})$
SM	–	50.0(22.8)	63.9(37.3)	45.9(22.0)	35.0(19.2)	61.8(47.4)
$G_{LR}(LR)$	34.1(12.2)	–	15.3(9.3)	4.5(0.6)	93.5(29.9)	123.0(49.5)
$G_{LR}(R)$	42.8(18.5)	9.8(7.2)	–	19.8(9.9)	108.8(39.9)	123.0(60.3)
$G_{LR}(Y)$	31.5(11.8)	2.9(0.4)	12.7(7.6)	–	89.0(29.3)	118.5(48.9)
$G_{SM}(SM)$	23.6(10.1)	65.3(25.3)	75.1(32.4)	62.4(24.8)	–	29.5(18.9)
$G_{SM}(T_{3L})$	40.8(22.8)	84.8(39.7)	84.8(46.9)	81.8(39.3)	19.4(14.4)	–

A_{RFB}	SM	$G_{LR}(LR)$	$G_{LR}(R)$	$G_{LR}(Y)$	$G_{SM}(SM)$	$G_{SM}(T_{3L})$
SM	–	13.6(4.0)	19.0(7.2)	13.1(4.2)	7.8(2.7)	18.5(9.1)
$G_{LR}(LR)$	8.9(3.2)	–	6.4(3.2)	0.6(0.2)	6.9(1.4)	5.8(5.2)
$G_{LR}(R)$	12.6(5.6)	4.0(2.4)	–	7.1(3.0)	13.4(4.6)	0.6(2.0)
$G_{LR}(Y)$	8.6(3.4)	0.6(0.1)	4.8(2.3)	–	6.3(1.6)	6.4(5.0)
$G_{SM}(SM)$	5.0(2.1)	4.6(1.2)	8.9(3.6)	4.1(1.3)	–	12.7(6.6)
$G_{SM}(T_{3L})$	11.8(7.0)	3.3(3.8)	0.7(1.4)	4.0(3.7)	8.0(5.1)	–

Table 4.6: Significance of A_{LL} (*top*), A_L (*middle*) and A_{RFB} (*bottom*) as in Tables 4.3, 4.4 and 4.5 respectively, for the LHC at 14 TeV. The upper triangle is for $M_{Z'} = 1.7$ TeV and the lower, for $M_{Z'}$=2.0 TeV. Entries refer to the significance of the observable integrated in the window $\Delta M_{t\bar{t}} < 100(500)$ GeV.

$A_L \searrow A_{LL}$	SM	$E_6(\chi)$	$E_6(\eta)$	$E_6(\psi)$	$E_6(N)$	$E_6(S)$	$G_{LR}(BL)$	$G_{LR}(LR)$	$G_{LR}(R)$	$G_{LR}(Y)$	$G_{SM}(SM)$	$G_{SM}(T_{3L})$
SM	–	62.6	5.1	10.6	38.7	>300	77.5	3.8	2.7	3.9	4.0	3.0
$E_6(\chi)$		–	10.2	32.7	>300	90.7	>300	7.1	4.6	7.5	7.7	5.2
$E_6(\eta)$			–	48.4	13.1	5.6	9.5	>300	45.3	>300	>300	70.7
$E_6(\psi)$				–	51.7	12.3	28.2	24.2	11.1	26.8	28.2	13.7
$E_6(N)$					–	51.6	>300	8.8	5.4	9.3	9.5	6.2
$E_6(S)$						–	117.8	4.2	3.0	4.3	4.4	3.3
$G_{LR}(BL)$							–	6.6	4.3	6.9	7.1	4.9
$G_{LR}(LR)$	0.8							–	95.9	>300	>300	200.0
$G_{LR}(R)$	0.5							9.3	–	78.9	72.0	>300
$G_{LR}(Y)$	0.9							105.8	5.6	–	>300	151.7
$G_{SM}(SM)$	1.6							0.2	0.2	0.2	–	133.9
$G_{SM}(T_{3L})$	0.5							0.1	0.1	0.1	2.4	–

Table 4.7: Required integrated luminosity (in fb^{-1}) at the LHC at 14 TeV to "distinguish" Z' models from the SM background and among themselves, for (upper triangle) A_{LL} and (lower triangle) A_L, for $M_{Z'}$=2.0 TeV. Models are disentangled if $s = 3$. No value is given for A_L for the E_6-type models because such an asymmetry is too small to be observed.

Spatial	SM	$G_{LR}(LR)$	$G_{LR}(R)$	$G_{LR}(Y)$	$G_{SM}(SM)$	$G_{SM}(T_{3L})$
SM	–	11.4(14.0)	5.6(6.6)	12.2(14.8)	35.7(42.6)	6.4(7.5)
$G_{LR}(LR)$	13.2(30.9)	–	55.0(59.1)	>300(>300)	42.6(55.1)	83.5(94.0)
$G_{LR}(R)$	7.1(14.3)	61.2(118.8)	–	38.7(51.7)	11.3(13.4)	>300(>300)
$G_{LR}(Y)$	13.7(33.0)	>300(>300)	55.3(98.4)	–	52.3(63.0)	56.1(79.6)
$G_{SM}(SM)$	40.0(97.6)	40.9(122.5)	11.8(28.9)	44.4(144.5)	–	14.0(16.6)
$G_{SM}(T_{3L})$	7.8(16.7)	94.0(204.9)	>300(>300)	82.8(161.5)	14.0(37.5)	–

Table 4.8: Required integrated luminosity (in fb^{-1}) at the LHC at 14 TeV to "distinguish" Z' models from the SM background and among themselves, for (upper triangle) $A_{RFB}(A_{OFB})$ and (lower triangle) $A_C(A_F)$, for $M_{Z'}$=2.0 TeV. Models are disentangled if $s = 3$.

Chapter 5

$t\bar{t}$ as a complementary channel

Having considered the most common class of Z' benchmarks in the alternative $t\bar{t}$ channel, determining that its asymmetries may have a role to play in offering additional discriminative power, this chapter continues in a similar vein, considering the benefits of asymmetry variables across different channels. Here, the value of $t\bar{t}$ as a complement to di-lepton and other final states in distinguishing Z's is directly investigated by considering a continuous parametrisation of a minimal, B-L Z' extension of the SM.

On the same footing as top quarks, τ-leptons are also short lived so that their spin information is imprinted in their decay product kinematics [90]. Similarly to top quarks, τ polarisation can be measured by means of its one-prong decays and analyses exist at the LHC already [92]. Naturally, these observables are also affected by the difficulties involving the boosted nature of the final state in the high mass regime discussed in Section 2.5. The case of b-quark final states brings further complications. The displaced vertex tagging allows for the charge measurement of the b-quark in the jet, which is needed in the definition of charge asymmetry in b-quark final states, which therefore seem feasible quantities to deal with. Here the main issue comes from the b-tagging performances at high p_T which are discussed in Section 5.2.2. Nonetheless, one might hope the tagging efficiency to improve due to upgrades in the micro-vertex detectors at both ATLAS and CMS for the $\sqrt{s} = 14$ TeV run (see, e.g., [93]). Regarding spin asymmetries, they can also be defined for b-quarks. If the b-quark hadronises before decaying, it has also been shown its spin information can be preserved by b-hadrons (e.g., Λ_b), albeit with some dilution factors [94]. The subsequent semi-leptonic decays of the latter may enable spin measurements, as pioneered at LEP [95]. It is not clear however, by the same argument as for tops and τs, if the same measurement is possible at the LHC, due to the higher boost of the emerging lepton and the narrower b-jet cone. Despite being nowadays technically challenging and still uncertain for the very near future, as better vertex detectors will be available, it is still interesting to study spin asymmetries for b-quarks in view of if and when such measurements may be available. They are therefore presented in the spirit of suggested observables.

It is the purpose of this work to compare the yield of l^+l^- ($l = e/\mu, \tau$), $b\bar{b}$ and $t\bar{t}$ final states produced at the LHC in presence of a Z' boson and to assess the machine ability to profile the latter in both standard kinematic variables as well as charge/spin asymmetries, by continuously scanning the parameter space of this one-dimensional class of Z' models, defined in terms of the Z' coupling and kinetic mixing parameters, over which benchmark points will be defined along with lines amenable to experimental investigation. As an aside, since the model requires the presence of right-handed neutrinos for anomaly cancellation, as stated in Section 4.1.2, the effect of their inclusion on the aforementioned observables and their ability to distinguish benchmarks is also considered. In doing so, some (but not all) of the standard Z' benchmarks from, e.g., [56] and [96], are borrowed as well as new ones defined. The work contained in this chapter can be found in [2] and is planned as follows. In the next section, the model is described and the calculation is outlined, defining the observables to be studied. Section 5.3 reports and comments on results. Section 5.4 finally presents the conclusions and outlook.

5.1 Framework

An overview of the model studied is presented, with more details available in [97], fixing conventions and relevant features, as well as the details of the code used and the variables that have been analysed.

5.1.1 The minimal Z' model

The general class of models is the one defined by the so-called non-exotic minimal Z' models [2, 45, 54, 97, 98]. Following the conventions of [96], only the relevant parts are summarised, i.e., the gauge and neutrino sectors, and the reader is referred to the latter publication for a complete description of the model.

The term "non-exotic minimal Z'" refers to a description of a $U(1)_{B-L}$ extended gauge sector including the B-L quantum number, introduced in Section 4.1.2. The most general covariant derivative for the theory, including potential kinetic mixing effects, is the SM gauge covariant derivative, as in Chapter 1, extended with the B-L piece:

$$D_\mu \equiv \partial_\mu + ig_S\vec{G}_\mu + ig\vec{W}_\mu + ig'\frac{Y}{2}B_\mu + i(\widetilde{g}Y + g'_1T_{B-L})B'_\mu\,. \tag{5.1}$$

Here, $\vec{G}$ and $\vec{W}$ correspond to the gluons and $SU(2)_L$ gauge bosons contracted with their associated generator while the B and B' fields are the hypercharge and B-L gauge bosons respectively. g'_1 is the new gauge coupling paired with the B-L generator defined in Section 4.1.2 while $\widetilde{g}$ parametrises the degree of kinetic mixing between the B' and B fields which, as explained in Section 3.1.1, induces a component of hypercharge in

its couplings. In this bottom-up description of such models, constraints from gauge unification at some specific yet arbitrary energy scale, on the extra gauge couplings are not considered. Therefore, $\widetilde{g}$ and g'_1 are taken as free parameters. The Z' can thus be pictured as interacting with an effective coupling Y^E and an effective charge g_E:

$$g_E Y^E \equiv \widetilde{g} Y + g'_1 T_{B-L}. \tag{5.2}$$

As any other parameter in the Lagrangian, $\widetilde{g}$ and g'_1 are running parameters [98, 99], therefore their values ought to be defined at some scale. It will be shown in Section 5.1.2 that some of the benchmark Z' models discussed in the previous chapter (see also, e.g., [45, 100]) can be recovered by a suitable definition of both $\widetilde{g}$ and g'_1.

Three right-handed neutrinos are required by the anomaly conditions, and can be used to naturally implement a type-I seesaw mechanism via Yukawa interactions with the SM Higgs field and the new singlet Higgs field required to break the $U(1)_{B-L}$ symmetry and give a mass to the Z'. A general feature of the seesaw mechanism is that the mass eigenstates, called "light" (ν_l) and "heavy" (ν_h) neutrinos, are Majorana particles, $\psi = \psi^c$, meaning they are their own charge conjugates. Because of this, they only have axial couplings to the neutral gauge bosons. This can be derived from the properties of the charge conjugation operator forbidding the vector current for Majorana particles. In order to investigate the impact of their presence, two opposite scenarios are considered: a "decoupled" case, with heavy neutrinos much heavier than (half of the) Z' mass, thereby disallowing $Z' \to \nu_h \nu_h$ decays, and a "very light" case, where the heavy neutrinos are much lighter than the Z' itself (e.g., $m_{\nu_h} = 50$ GeV, compatible with LEP limits [101]). All possible intermediate cases will therefore lie somewhere in between.

5.1.2 Structure of the chiral couplings

To study the asymmetries it is important to understand the chiral structure of the couplings of the Z' gauge boson to fermions, determined by the covariant derivative of Equation 5.1. Due to the mixing between the Z and Z' gauge bosons, the couplings of the Z' to fermions are a function of g'_1 and $\widetilde{g}$. In all generality, such couplings can be separated into vector and axial components, $f_V(g'_1, \widetilde{g})$ and $f_A(g'_1, \widetilde{g})$, respectively, with an interaction term expressed as in Equation 3.5 but with the gauge couplings absorbed into the definitions of the couplings.

Because of universal couplings, the explicit chiral structure of the Z' couplings to up-type quarks, down-type quarks and to charged leptons is independent of the fermion generation, as are its partial decay widths in the approximation of a massless final state. As for the two neutrino mass eigenstates, the see-saw mechanism dictates that their mixing angle from the flavour basis is approximately proportional to the square root of the ratio of their masses [97]. Since the lower mass scenario assumes their mass to be

f	u	d	l	ν_L	ν_R
f_V	$\frac{4g_1'+5\widetilde{g}}{12}$	$\frac{4g_1'-\widetilde{g}}{12}$	$-\frac{4g_1'+3\widetilde{g}}{4}$	0	0
f_A	$-\frac{\widetilde{g}}{4}$	$\frac{\widetilde{g}}{4}$	$\frac{\widetilde{g}}{4}$	$\frac{2g_1'+\widetilde{g}}{2}$	g_1'

Table 5.1: Table summarising the vector and axial vector couplings of the SM fermions plus the neutrino flavour eigenstates in the approximation of no mass mixing between the Z and Z'. u, d, l, ν_L, ν_R denote up-type quarks, down-type quarks, charged leptons and the left and right-handed neutrino flavour eigenstates respectively.

50 GeV, already yielding a mixing angle of order 10^{-6}, they can be well approximated by the flavour eigenstates. The fermion couplings are summarised in Table 5.1, as taken from [2], in the limit of no mass mixing with the Z, since the LEP limits mentioned in Section 3.1.4 constrain this to effectively negligible levels [102]. Expressions for the partial widths to fermions can also be found in [2].

5.1.3 Benchmark models

From the expressions for the fermion couplings, a set of benchmark models can be selected for certain values of $\widetilde{g}$ and g'. Among these are commonly used benchmarks introduced in Chapter 4: the "pure" B-L model is defined by the condition $\widetilde{g} = 0$ (implying no kinetic mixing at tree-level between the B-L Z', sometimes denoted as Z'_{B-L}, and the hypercharge field); the $U(1)_R$ model, for which left-handed fermion charges vanish (recovered here by the condition $\widetilde{g} = -2g_1'$) and the $SO(10)$ inspired $U(1)_\chi$ model, which is given by $\widetilde{g} = -\frac{4}{5}\, g_1'$ (the only orthogonal $U(1)$ extension of the SM hypercharge). The χ model will have axial couplings to up-type quarks; the R model will have equal couplings (in absolute value) to all fermions ($|u_V| \sim |u_A| \sim |d_V| \sim |d_A| \sim |l_V| \sim |l_A|$) while the pure B-L model (for which $\widetilde{g} = 0$) will have $u_A = d_A = l_A \equiv 0$. In this framework, the axial couplings to visible fermions are proportional to $\widetilde{g}$, and hence vanish identically only in the pure B-L model.

Regarding the vector couplings, two additional benchmark scenarios can be identified by requiring some of them to vanish. Analogously to the $U(1)_\chi$ model, the $\not{B}$ ("B-not") and the $\not{L}$ ("L-not") models are defined for the purposes of this study. These three models are characterised by the vanishing vectorial coupling to the up-type quarks, down-type quarks and charged leptons respectively, and are obtained by the following relations:

$$U(1)_\chi \text{ model:} \quad \widetilde{g} = -\frac{4}{5}\, g_1' \quad \rightarrow \quad u_V \sim 0\,, \tag{5.3}$$

$$\not{B} \text{ model:} \quad \widetilde{g} = 4\, g_1' \quad \rightarrow \quad d_V \sim 0\,, \tag{5.4}$$

$$\not{L} \text{ model:} \quad \widetilde{g} = -\frac{4}{3}\, g_1' \quad \rightarrow \quad l_V \sim 0\,. \tag{5.5}$$

As dictated by the coupling dependence of asymmetry observables illustrated in Section 3.2, these models will have trivial asymmetries, up to small EW interference effects, in the corresponding final state (the one with negligible vector coupling) and non-vanishing ones in the other final states. Only the pure B-L model will have trivial asymmetries in all final states. Finally, the R model will have almost the same values for the asymmetries in all final states, which should be maximised from the fully right-handed interaction.

On the scenario line characterised by the relationship between the gauge couplings, specific values for the latter are chosen to recover the normalisations of the well known benchmark models, some of which correspond to those described in [56]. Finally, to recover the $SO(10)$-inspired $U(1)_\chi$ point, its gauge couplings have been rescaled by the usual factor to unify with the GUT normalised hypercharge ($\sqrt{3/8}$ in this case). In the case of the B-L, $\not{B}$ and $\not{L}$ models, normalisations were chosen in a similar region to the other benchmarks with respect to the leptonic limits.

5.2 Calculation and variables

The code used for the study is largely the same as in Chapter 4. Initial state quarks were assumed to be massless while for the top state, $m_t = 172.9$ was taken as the pole mass. The b-quark was taken to have mass $m_b = 4.95$ GeV. The electron and muons were taken as massless while the τ mass used was $m_\tau = 1.77$ GeV. The PDFs used were CTEQ6L1 [18], with factorisation/renormalisation scale set to $Q = \mu = M_{Z'}$. VEGAS [85] was used for the multi-dimensional numerical integrations. A separate program was also used for part of the analysis, based on CalcHEP [103], wherein the model has been independently implemented via the LanHEP module [104] and the FeynRules [105, 106] package. The model files can be found on the HEPMDB database [107] and on the FeynRules website [108].

For all final states, f, a cut in the invariant mass window around the Z' peak was made

$$\left|m_{f\bar{f}} - M_{Z'}\right| < 100 \text{ GeV}\,, \tag{5.6}$$

which enhances the Z' peak with respect to the SM background. Regarding the b-quark final state, this is still not sufficient to isolate the resonance. Consequently, a further selection was implemented implemented:

$$p_T(b) > 300 \text{ GeV}\,. \tag{5.7}$$

5.2.1 Extracting Z' couplings

The ultimate scope of profiling a Z' boson is that of measuring its couplings to fermions. It is clear that one needs as many independent measurements as possible to profile these couplings should a resonance be observed. As a brief aside, some comments on using asymmetries and multiple final state are made in this context. From Section 3.1.3, in the minimal case, 5 independent Z' coupling parameters exist (q_L, u_R, d_R, l_L, e_R, where q_L and l_L identify the quark and lepton doublets, respectively), so that at least 5 independent measurements are required. In [50], it is shown that a set of 4 coefficients (c_q, e_q; $q = u, d$) that are functions of the Z' couplings can be extracted from 4 observables related to charge asymmetry and total cross section in the light lepton channel, obtained by dividing the kinematical domain of the differential cross section. These coefficients are related to those defined in Section 3.2 for a quark initial state and light lepton final state, $f = l$. c_q is proportional to the product of parity symmetric coefficients of Equation 3.10, $C^q C^e$, while e_q is proportional to the antisymmetric counterpart related to charge asymmetry as in Equation 3.16, $A^q A^e$, both for the pure Z' contribution.

It is observed that a degeneracy exists between the dependence on leptonic and quark couplings in this analysis, stemming from the minimal assumption of 5 independent parameters and only 4 independent observables. The leptonic couplings can be rescaled at will, provided the quark couplings are scaled oppositely. Therefore, additional observables are required even for the most minimal assumption on the Z' couplings. Including the total Z' width does not seem to fix the problem, since it enlarges the set of independent parameters to include all fermionic decay modes. Considering different final states is clearly a viable option. Decaying final states also provide spin observables that, being based on polarised amplitudes, cannot be obtained from the fully differential cross section and may provide independent information. Staying with the leptonic final state, the τ polarisation has a different dependence on the quark and leptonic couplings than c_q, e_q. Equation 3.25, for $i = j$, can be written in the spirit of [50] as a new coefficient,

$$f_{q=u,d} \propto (q_R^2 + q_L^2)(e_R^2 - e_L^2) \equiv C^q A^e, \tag{5.8}$$

making manifest the aforementioned sensitivity to the handedness of the Z' couplings. These coefficients can, in principle, be extracted from τ polarisation measurements in a similar way as the c_q and e_q coefficients are from the differential cross section, i.e., by splitting the kinematical domain of A_L^τ in 2 independent regions to then be fitted. However, it is evident that the same quark-lepton degeneracy exists. In fact, it turns out not to be linearly independent from the c and e coefficients when $u_L = d_L$:

$$f_{q=u,d} \propto c_q \frac{e_u - e_d}{c_u - c_d}. \tag{5.9}$$

Although the τ polarisation does not allow for the extraction of the Z' couplings within the 5 parameter minimal assumption, it could still prove to be a useful quantity to

measure. First of all, the channel itself would be essential as a test of universality. Secondly, the polarisation measurement provides an extra set of constraints on the other coefficients that may improve the quality of a fit to the couplings. The ratios

$$\frac{f_u}{c_u} = \frac{f_d}{c_d} \equiv \frac{e_R^2 - e_L^2}{e_R^2 + e_L^2} \tag{5.10}$$

should be equal and are independent of the quark couplings and could serve to reduce some systematics, such as those from PDFs. To break the degeneracy, allowing for a direct fit of the couplings, one could consider observables in non-leptonic final states, i.e. top polarisation or charge asymmetry. Any one of the asymmetry observables in an alternative final state would be sufficient to this end. Furthermore, moving away from the minimal assumption permitting $u_L \neq d_L$ (but still requiring universality), as could occur with Z's arising from more general gauge group extensions, restores the linear independence of one of the τ polarisation coefficients. In this case one still requires the use of an alternative final state to complete the set of independent observables needed to fit directly to the 6 (or more) couplings. Finally, as one moves away from minimal models, it is clear that such observables could be extremely useful to access the couplings of the most general Z'.

5.2.2 Efficiencies and uncertainties

To be able to quantitatively address the distinguishability among the various models and the SM background, a statistical error is associated to each asymmetry observable as defined in Equation 2.4. Again, in this work only estimate statistical uncertainties are considered although systematics may also be important [87, 89]. Their inclusion, however, would require detailed detector simulations which are beyond the scope of this work. Following the discussion in Section 2.5, for the $t\bar{t}$ system, the reconstruction efficiency is taken to be $\varepsilon_t = 10\%$ as in [1], considering all possible decay channels, based on efficiencies quoted by recent experimental papers [91] as well as estimates from MC studies in previous works [109]. This is used to define the charge asymmetry, while for the spin polarisation, taking into account the boosted topology as well as the additional information required from the decay products, a more conservative 5% is assumed.

For the $b\bar{b}$ system, $\varepsilon_b = 10\%$ is taken, based on the 2 b-jet tagging efficiency given in [110], appropriate for the reconstruction of the invariant mass. For the asymmetry measurements, at least one of these jets' charges must also be determined. One way this can be done is the requirement of a prompt, hard lepton originating from the semi-leptonic decay of a b-hadron. The efficiency must therefore be scaled to include a reduction from the leptonic decay branching ratio (BR) of an admixture of b-hadrons (23% [7]), resulting in a very low event rate. Alternatively, the single b-tagging efficiency is quoted to be 50% when summing 1-tag and 2-tags efficiencies at high p_T. The study implies that, while

the 2-tags would yield low rates, the 1-tag alone seems insufficient, given the high rate of mistags from light flavour jets. However, the additional requirements on a muon from the b-jet, necessary for potential charge and polarisation asymmetry measurements, can improve both the tagging and the tagging-over-mistag efficiencies up to intermediate jet p_T [16] while no information is available for very energetic jets. The efficiency of requiring a single b-tagged jet scaled by the semi-leptonic BR to muons (half of the previously quoted fraction) is estimated at 5%. This is assigned to the charge asymmetry observable in the $b\bar{b}$ channel. Regarding the b-hadron helicity, there is no result currently available at the LHC and the main information available is from LEP [94, 95] – a very different collider environment both in energy and hadronic activity – $\varepsilon_b = 2\%$ is taken as an estimate to quantitatively discuss spin observables in this channel. This reflects the likely difficulty with which this observable might be measured at the LHC, due to all of the previously discussed issues. The estimate is made hoping that, for the time scales at which this work could be relevant, the situation will have improved as suggested by the proposed new generation of micro-vertex detector available for the $\sqrt{s} = 14$ TeV run, see, e.g., [93]. However, the reader is reminded that these observables are kept mostly for illustrative purposes and may not be available at the LHC, although the proposed upgrades for micro-vertex detectors may well help to extract them.

For the l^+l^- system, a distinction is made between light leptons (e, μ), for which $\varepsilon_{e,\mu} = 90\%$ [111], and the τs, for which $\varepsilon_\tau = 5\%$. Light leptons will be employed for charge asymmetries only, whilst τs are used to define the spin asymmetry A_L in the leptonic final state. This latter number is based on a recent ATLAS measurement uses 1-prong decays of the form $\tau \to \rho^\pm\nu(\rho^\pm \to \pi^\pm\pi^0)$ (25% of tau's BRs [7]) to measure τ polarisation from W decays [92]. In this particular decay channel, angular momentum conservation, coupled with the left-handed charged current interaction, dictates that a left-handed τ will preferentially decay to a transversely polarised ρ while a right-handed one will prefer a longitudinal ρ. The relative energy shared between the rho decay products is then sensitive to the rho polarisation and can therefore be used to measure A_L^τ. The analysis cites a reconstruction efficiency of 60% and a 20% loss of sensitivity due to detector effects which would combine for an overall $\sim$ 10% efficiency. However, this study is concerned with high mass $\tau^+\tau^-$ pairs for which Z' analyses exist at the LHC [112, 113]. The CMS analysis provides signal selection efficiencies for the possible combinations of hadronic and leptonic τ decays for a Z'_{SSM} resonance. The proportion of $\tau^+\tau^-$ decays containing at least one hadronic tau decay of the type specified above, folding in the associated reconstruction efficiency for the highest mass point of 1 TeV yields 3.1%. This is considerably lower than the analysis on τ polarisation. However it does appear that the efficiencies increase with Z' mass presumably due to the reduction in backgrounds at higher invariant mass. The estimate of 5% is therefore kept as a conservative compromise, assuming that selection efficiencies should improve at higher masses and perhaps also with better statistics. By the same logic as for the $t\bar{t}$ channel, the efficiency to reconstruct the invariant mass of the desired decay mode should be

reduced to account for the additional process of extracting the polarisation information from the decay products. The overall efficiency used to reconstruct and measure the polarisation from a high mass τ pair is therefore taken as 2%.

All figures that will be shown in the following are for the LHC at $\sqrt{s} = 14$ TeV assuming 100 fb^{-1} of integrated luminosity, for a Z' mass of 2.5 TeV and decoupled heavy neutrinos. The mass choice was motivated by the exclusions computed at the time the work was undertaken. In some cases, observables are evaluated also for "light" heavy neutrinos of 50 GeV mass to estimate their impact. Values of an observable in the $(g'_1, \widetilde{g})$ coupling plane can be compared to SM predictions corresponding to the point $(0, 0)$. For the signal, the uncertainty for that value is evaluated to confirm visibility over the background in that channel. Also shown are surface plots of the significance of the observable with respect to the SM prediction, defined as in Equation 4.16, where $A(1)$ and $A(2)$ denote the prediction for an observable of two different hypotheses and $\delta A(i)$ refers to their statistical uncertainty. In this case, the statistical uncertainty of the SM prediction is taken to be zero because its very low cross section at such high invariant masses (especially true for the leptonic final state) would artificially dilute the significance of asymmetries in that region. As such, the SM prediction is taken as a reference value only.

5.3 Results

5.3.1 Exclusion limits

Before considering the asymmetry observables, some recent exclusions from direct searches performed at CMS with ~ 5 fb^{-1} [114], are shown. A more in-depth description of the features pertaining to each possible final state, i.e., BRs and total Z' width can be found in [97]. Notice that ATLAS has also published an equivalent analysis for ~ 5 fb^{-1} [115], but their limits are less tight than the CMS ones. Since this work was completed, the results used for the limits have been superseded by 8 TeV data.

Figure 5.1 presents some recent 95% (Confidence Level) CL exclusions at the LHC in the $(g'_1, \widetilde{g})$ plane (first in [97, 116]), based on the CMS data at $\sqrt{s} = 7$ TeV for the combination of 4.7(9) fb^{-1} in the electron(muon) channels. The benchmark trajectories representing the relationships between $\widetilde{g}$ and g'_1 as well as the specific points chosen to match the normalisations in [56], are shown for reference. It can be seen that, for masses of order 1 TeV, a large part of the parameter space is excluded, becoming more relaxed as one reaches 2.5 TeV.

Table 5.2 collects the maximum allowed g'_1 coupling per given Z' boson mass for the various benchmark models of interest (see Section 5.1.3). Naturally, the $\not{L}$ and $U(1)_\chi$ models, having the weakest couplings to leptons, are the least constrained.

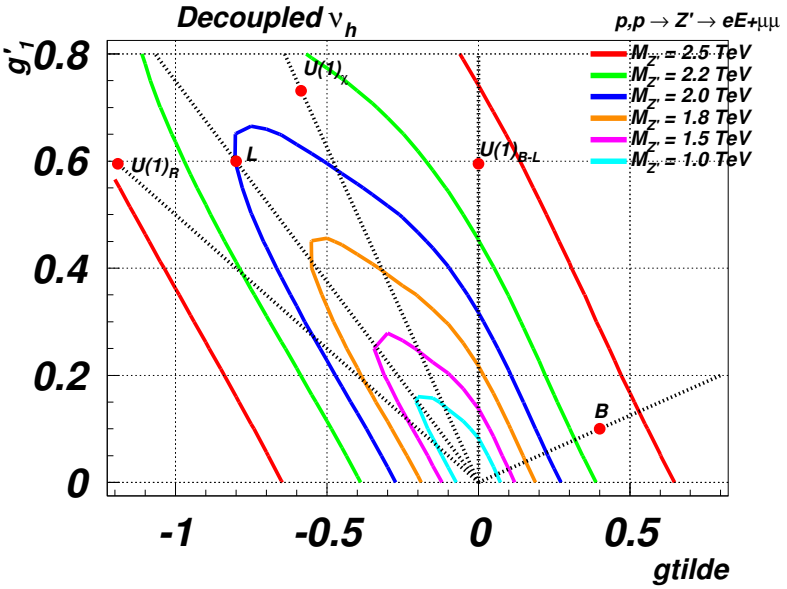

Figure 5.1: Z' exclusions from recent CMS data, at $\sqrt{s} = 7$ TeV for the combination of 4.7 fb^{-1} in the electron channel and of 4.9 fb^{-1} in the muon channel. The dotted black lines refers to the main benchmark models of this analysis (see Section 5.1.3).

$M_{Z'}$ (TeV)	$U(1)_R$	$U(1)_\chi$	$U(1)_{B-L}$	$\not{L}$	$\not{B}$
2.5	0.63	> 0.8	0.75	> 0.8	0.13
2.2	0.39	0.81	0.45	0.83	0.08
2.0	0.27	0.58	0.31	0.60	0.06
1.8	0.19	0.40	0.22	0.41	0.04
1.5	0.12	0.24	0.13	0.25	0.03
1.0	0.075	0.14	0.08	0.15	0.02

Table 5.2: Maximum g'_1 allowed at 95% CL for the benchmark lines of Section 5.1.3.

5.3.2 Event rates

It is instructive at this point to consider the total event rates in each channel. These are shown in Figure 5.2, including the SM background and interference with the EW sector, also folding in the effective reconstruction efficiencies decided upon in Section 5.2.2. To evaluate the total cross sections, the cuts described in Equations 5.6 and 5.7 have been applied to enhance the signal. These figures highlight the different areas of parameter space favoured by each final state and relate directly to the magnitude of the statistical uncertainties in its asymmetries (to be studied below).

The dotted lines also highlight the impact of the light neutrino scenario when the width is increased, leading to a reduction in events. This reduction can be order 40%, 30%, and 20% when considering $pp \to l^+l^-$, $pp \to b\bar{b}$, and $pp \to t\bar{t}$, respectively. The fact that ν_R couples with g'_1, as shown in Table 5.1, is reflected by the deviations from the decoupled

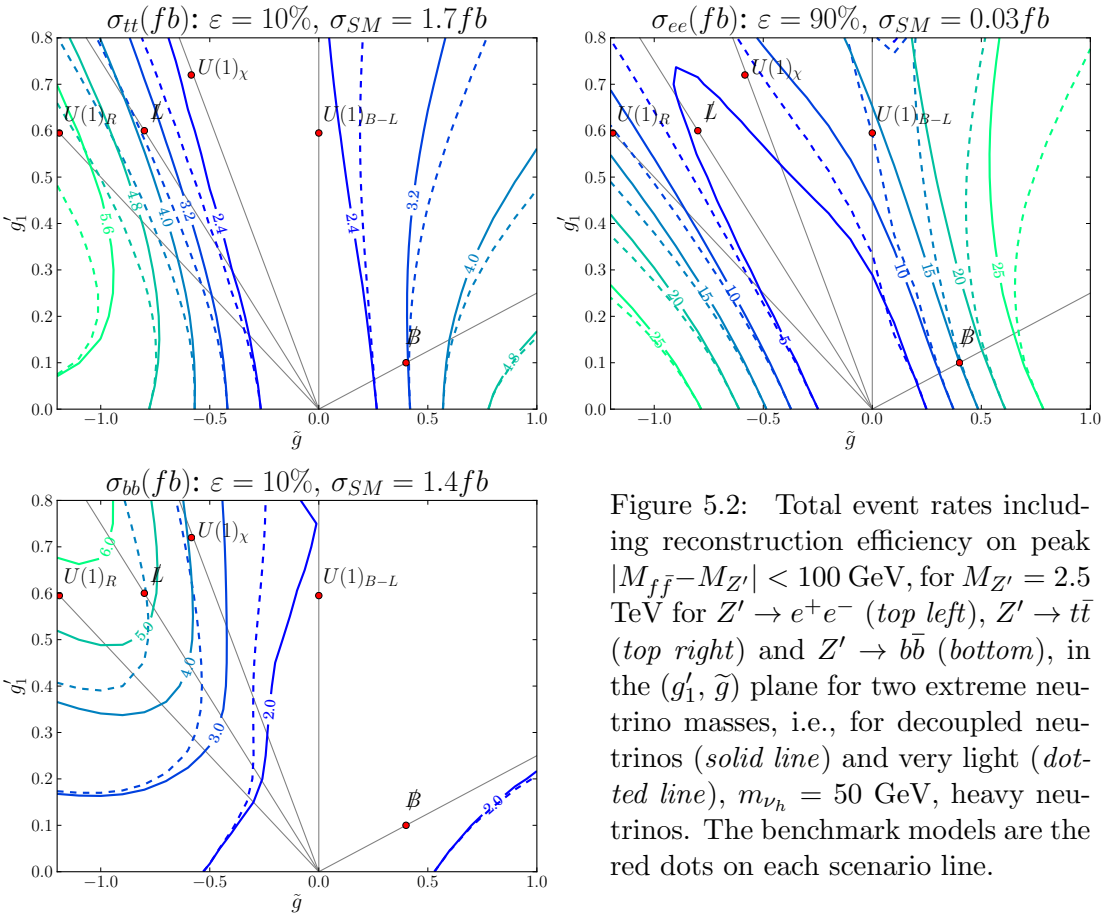

Figure 5.2: Total event rates including reconstruction efficiency on peak $|M_{f\bar{f}} - M_{Z'}| < 100$ GeV, for $M_{Z'} = 2.5$ TeV for $Z' \to e^+e^-$ (*top left*), $Z' \to t\bar{t}$ (*top right*) and $Z' \to b\bar{b}$ (*bottom*), in the $(g_1', \tilde{g})$ plane for two extreme neutrino masses, i.e., for decoupled neutrinos (*solid line*) and very light (*dotted line*), $m_{\nu_h} = 50$ GeV, heavy neutrinos. The benchmark models are the red dots on each scenario line.

scenario increasing with this coupling. If the presence of light heavy neutrinos lowers the rate for a particular final state, directly increasing its relative error and therefore the error of the asymmetries, this will directly influence the central value of the asymmetries. Given that the SM background is not altered by the presence of heavy neutrinos, the net effect of a decrease of signal is to increase the relative SM contribution in the samples. Overall, the values of the asymmetries will therefore be more SM-like, i.e., the central values will shift towards the value obtained in the SM. Obviously, this can happen only when the signal-to-background ratio is altered; in the case of leptons, where the SM contribution is negligible, the shift of the central values of the asymmetries is negligible.

As previously observed, the total rate when leptons are considered is above the fb level for most of the parameter space. The SM contribution is 0.03 fb, some orders of magnitude below the signal whether or not light heavy neutrinos are considered. For the heavy quarks, instead, the SM background is of the same order of the signal, as the former is largely due to QCD while the latter is (despite being resonant) an EW process. Comparing Figures 5.1 and 5.2, it is clear that the shape of the current exclusion limits is driven by the BR of the Z' boson into charged leptons: the limits are weaker where the rates are smaller, i.e., in the region between the $U(1)_\chi$ and the $\not{L}$ scenarios, reiterating the trend in Table 5.2. It is also clear that searches performed in the top-quark final states do not improve this behaviour, since $\sigma(pp \to Z' \to t\bar{t})$ is minimised near the $U(1)_\chi$ line.

However, the b-quark final state cross sections are maximised here, so it was determined whether exclusions derived in this final state could improve the overall results. It turns out that the sensitivity in this channel, for a comparable integrated luminosity, i.e., 5 fb^{-1} as in the analysis in [117], cannot compete with the much cleaner di-lepton final state already discussed, that still yields the tighter constraints in the whole parameter space. It would, however, be interesting to consider this in the light of a more recent $b\bar{b}$ resonance search from the 8 TeV run [110].

5.3.3 Asymmetries

For a complete profile of the model, the charge and spin asymmetry observables are studied at the Z' peak. Performing a scan over the gauge couplings, the integrated values of asymmetries are presented in the $(g'_1, \widetilde{g})$ plane for all three final states ($Z' \to l^+l^-, t\bar{t}, b\bar{b}$). The SM prediction for each observable can then be found at the point (0,0). The observables were computed using the code described in Section 5.2 implementing the cuts in Equations 5.6–5.7 and folding in the relevant reconstruction efficiencies discussed in Section 5.2.2 in order to determine the statistical uncertainties plotted underneath (always for 100 fb^{-1} of integrated luminosity). There is a distinction between the light leptons $l = e, \mu$, to be used in evaluating A_{RFB}, and τs, essential to measuring A_L in the leptonic sector. Results for A_{RFB} and A_L are shown as representatives for charge and spin variables, respectively. The spin polarisation, A_{LL}, is not shown because of its capabilities in the top final state only, since in the massless limit, $\beta \to 1$, the asymmetry becomes maximal. Furthermore, A_{LL} predictions for the top final state are not discussed given that the aim of this work is to compare predictions in different final states to assess their complementarity in distinguishing models.

Charge asymmetry: A_{RFB}

Figure 5.3 shows the rapidity dependent forward-backward asymmetry along with its statistical uncertainty in the chosen three final states. In this case, the electron and muon final states can be used and possibly combined to reduce the statistical uncertainty further. One can clearly see the asymmetry vanishing in each final state along the scenario line corresponding to a zero value of one of the chiral couplings (vector or axial), as described in Section 5.1.3.

The magnitude of the statistical uncertainties matches the total cross section plots in Figure 5.2 in accordance with Equation 2.4 and, outside of the cases near the trajectories where a particular final state has vanishing asymmetries, the uncertainties can be as low as 20% in the case of the top final state. In the leptonic final state, the uncertainties are comparatively smaller, apart from the large spike at the SM point due to the lack of cross section. Finally, the $b\bar{b}$ final state still appears to perform similarly to $t\bar{t}$ with

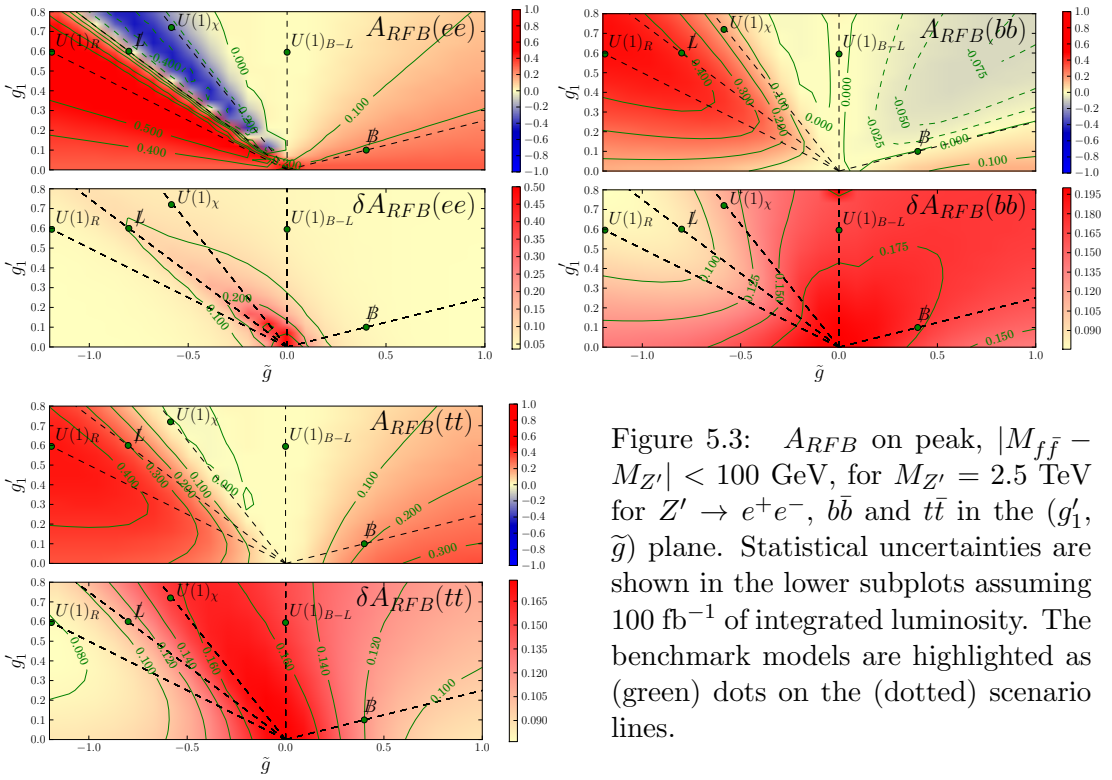

Figure 5.3: A_{RFB} on peak, $|M_{f\bar{f}} - M_{Z'}| < 100$ GeV, for $M_{Z'} = 2.5$ TeV for $Z' \to e^+e^-$, $b\bar{b}$ and $t\bar{t}$ in the $(g_1', \widetilde{g})$ plane. Statistical uncertainties are shown in the lower subplots assuming 100 fb^{-1} of integrated luminosity. The benchmark models are highlighted as (green) dots on the (dotted) scenario lines.

slighty larger uncertainties overall but comparable relative uncertainties in the optimum regions. The sensitivity to the relative sign of the couplings in the final state is blurred due to the dependence on the product of the initial and final state couplings, as discussed in Section 3.2. In fact, the dominance of the up quark in the proton means that the observable is positive definite, since, for universal couplings the observable on peak is proportional to $(A^u)^2$.

The overall assessment of the visibility of the Z' boson suffers from larger uncertainties (compared to A_L, as will be seen later). The significance measure for each channel with respect to the SM prediction is shown in Figure 5.4, where also the coloured plane indicates the final state which offers the highest significance for each pair of coupling values. An integrated luminosity of 100 fb^{-1} is enough to gain a sensitivity equal or greater than 3 almost everywhere. The dominance of the leptonic final state is remarkable, this final state being sufficient to cover most of the parameter space. This is due to the large positive value of this asymmetry for the SM, while in this model the leptonic final state yields a smaller, sometimes negative value for A_{RFB} in most of the parameter space. It is peculiar that, for large negative values of $\widetilde{g}$, where also A^l_{RFB} is large, the already small errors are not sufficiently small to allow one to distinguish the Z' boson from the SM. Nonetheless, a good discrimination power is provided in this corner by the combination of top and bottom quark final states, albeit with smaller significances due to larger uncertainties from poorer reconstruction efficiencies. This reinforces the complementarity of the various channels to cover the parameter space.

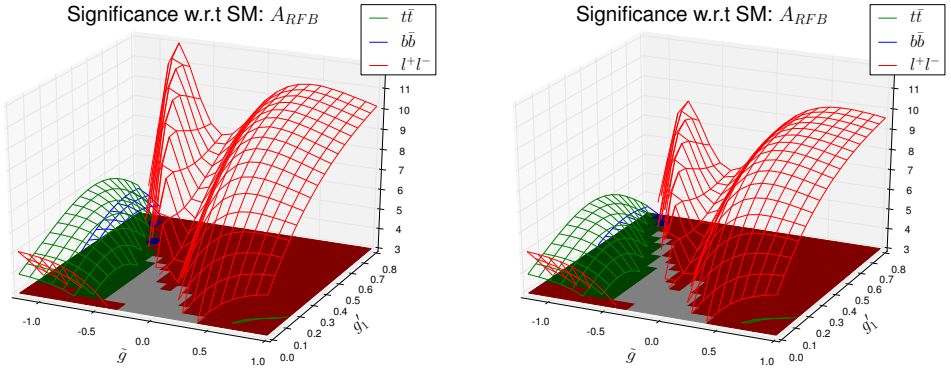

Figure 5.4: Significance of A_{RFB} with respect to the SM prediction on peak, $|M_{f\bar{f}} - M_{Z'}| < 100$ GeV, for $M_{Z'} = 2.5$ TeV for $Z' \to e^+e^-$ (red), $b\bar{b}$ (blue) and $t\bar{t}$ (green) in the $(g'_1, \widetilde{g})$ plane at the LHC at 14 TeV both for decoupled heavy neutrinos (left) and for heavy neutrinos of 50 GeV (right). The coloured projection denotes the final state which offers the most significance for each pair of coupling values. We assume here a luminosity of 100 fb^{-1}.

The effect of introducing the heavy neutrinos is to reduce significances across the board, which results in a slight enlargement of the grey area in which a 3σ significance cannot be obtained in any final state. The reason for this is twofold, although driven by a single cause: the reduction of the signal rates in the considered final state. First, as discussed at the end of Section 5.3.2, the central value of the asymmetry is shifted towards SM values due to a reduced signal-over-SM ratio of events. This does not affect the lepton final state, whose significance is reduced due to the smaller total rates giving larger errors, which naively reduce the significance.

Polarisation asymmetry: A_L

Figure 5.5 shows the spin polarisation asymmetry along with its statistical uncertainty in the usual three final states. Recall that in the case of the leptonic final state labelled ee, the measure would be obtained from the τ final state with the discussed reconstruction efficiency of 5%. Once again and even more clearly than for A_{RFB}, one can see the asymmetry vanishing in each final state where expected. The change in sign of the asymmetry at different points in parameter space corresponds to a change in relative sign of the vector and axial couplings of the Z' boson (or alternatively, the handedness of the coupling) to the final state as discussed in Section 4.1.4. This is most pronounced in the di-lepton case because of the comparatively low SM background, which dilutes the asymmetry in the other final states.

The behaviours of the statistical uncertainties do not greatly differ from those in the A_{RFB} plots as they are largely determined by the cross section values, although they are about a factor of two smaller, making this variable the one with the greatest discrimination power. The exception to this lies in the lepton sector where, since the EW

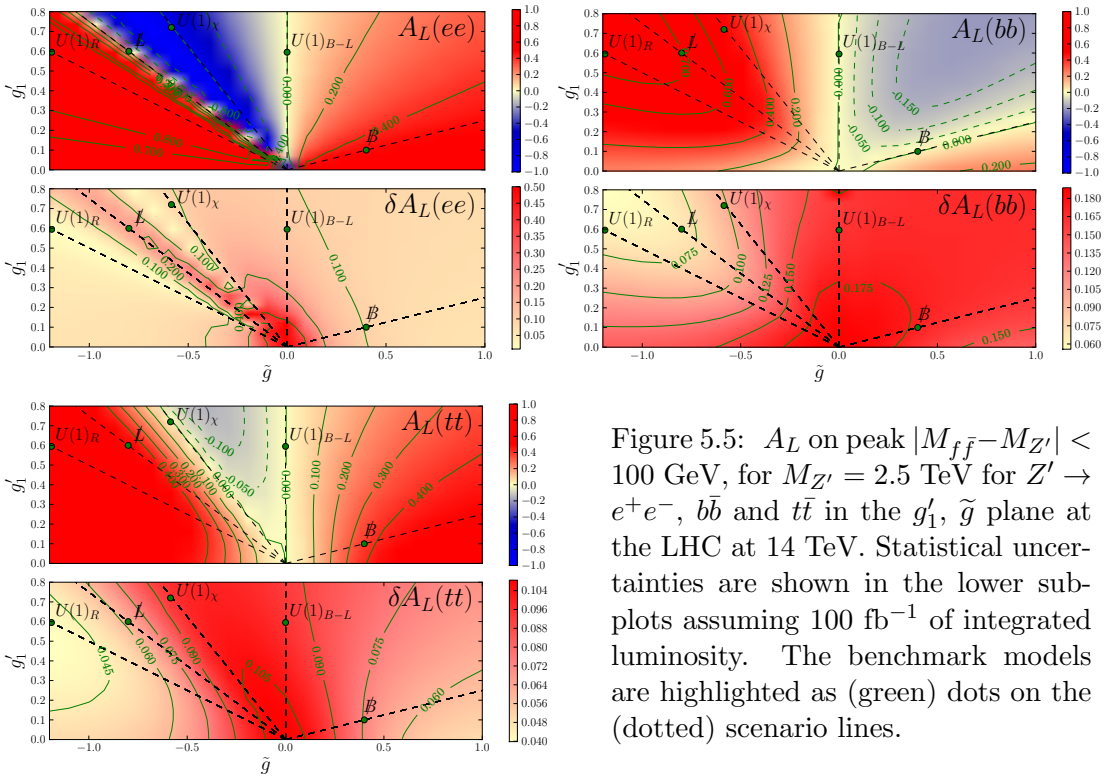

Figure 5.5: A_L on peak $|M_{f\bar{f}} - M_{Z'}| < 100$ GeV, for $M_{Z'} = 2.5$ TeV for $Z' \to e^+e^-$, $b\bar{b}$ and $t\bar{t}$ in the g_1', $\widetilde{g}$ plane at the LHC at 14 TeV. Statistical uncertainties are shown in the lower subplots assuming 100 fb^{-1} of integrated luminosity. The benchmark models are highlighted as (green) dots on the (dotted) scenario lines.

background is so low, when the couplings become fully chiral like on the $U(1)_R$ line, for example, the asymmetry also becomes close to maximal. Considering the dependence of the statistical uncertainty on the value of an asymmetry given in Equation 2.4, the more maximal the asymmetry is, the closer to zero the statistical uncertainty becomes. This leads to extremely high significances as they are defined in this work, as seen in Figure 5.6, where the values in the lepton sector have had to be capped in order to better represent the information.

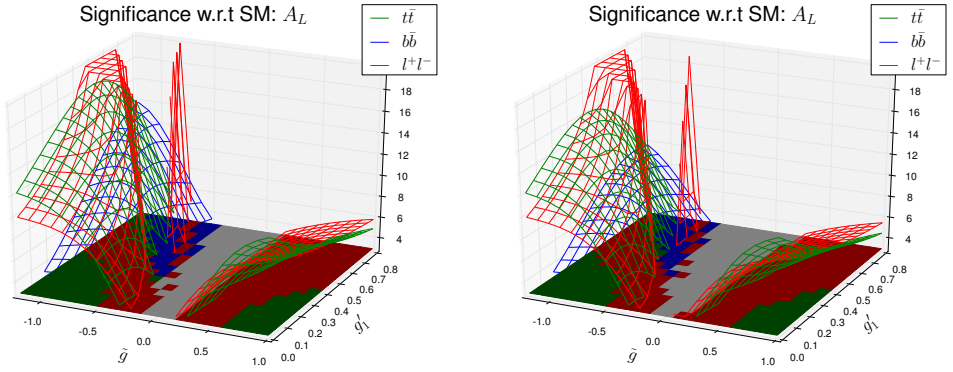

Figure 5.6: Significance of A_L with respect to the SM prediction on peak $|M_{f\bar{f}} - M_{Z'}| < 100$ GeV, for $M_{Z'} = 2.5$ TeV for $Z' \to e^+e^-$ (red), $b\bar{b}$ (blue) and $t\bar{t}$ (green) in the $(g_1', \widetilde{g})$ plane at the LHC at 14 TeV both for decoupled heavy neutrinos (left) and for heavy neutrinos of 50 GeV (right). The coloured projection denotes the final state which offers the most significance for each pair of coupling values. We assume here a luminosity of 100 fb^{-1}.

Overall this gives an indication that all channels could be useful in probing the full parameter space of such a Z' model in complementing one another by having different areas where the sensitivity is best. Significances in excess of 3 appear over almost all of the $(g'_1, \widetilde{g})$ plane. Although leptons almost always provide the best significance, due to the large negative SM value as compared to the large positive signal values over the majority of the parameter space, in the ares between $\not{L}$ and $U(1)_\chi$ where the two are similar for the lepton final state, $b\bar{b}$ and $t\bar{t}$ come into play and provide coverage. The top mode also provides better visibility in the two lower corners of low g'_1 and large absolute value of $\tilde{g}$, a peculiar area of parameter space where the Z' interaction is dominated by the kinetic mixing term. Figure 5.5 confirms that in these areas, the top polarisation has a large deviation from the SM prediction and also corresponds to areas in which the contribution to the cross section is maximised and, therefore, the uncertainties reduced. Again, having coupled heavy neutrinos results in an overall reduction of the signal significance with respect to the SM and in a slight enlargement of the grey area in which a significance of 3 cannot be obtained in any final state. However, comparing Figures 5.4 and 5.6, it is clear that these grey areas overlap only in the region where both gauge couplings g'_1 and $\widetilde{g}$ are small, showing a great complementarity of observables and final states.

5.3.4 Distinguishing benchmarks

So far, how well the asymmetry produced by a Z' boson in this model can be distinguished from the SM background has been investigated. One would also like to disentangle different combinations of gauge couplings, in turn leading to their absolute measurement. Although the full analysis and especially this last part are beyond the scope of this work, the first point can be addressed here.

Figure 5.7 shows that all benchmark models can well be discriminated with 100 fb^{-1} of data if one assumes the availability of all final states in A_L. In particular models that are degenerate in one final state (such as B-L and χ in the case of top quarks) are well separated either using leptons or, eventually, b-quarks. The last frame, displaying the t- versus b-quark case, clearly shows the impact of including heavy neutrinos: represented by dashed crosses, the asymmetries with light ν_h are closer to the SM values and have larger errors.

Table 5.3 collects the significance of each benchmark point with respect to any other when A_L is measured in each of the final states, would the measure in b-quark final state be available, both for decoupled neutrinos (upper triangle) and for $m_{\nu_h} = 50$ GeV (lower triangle). Most of the models are quite distinguishable from one another just by looking at τs, that generally deliver higher discrimination power due to the smaller errors. The only exception is the separation between $\not{L}$ and B-L, both with vanishing asymmetries in the lepton final state. Here, the supplementary information from the top final state

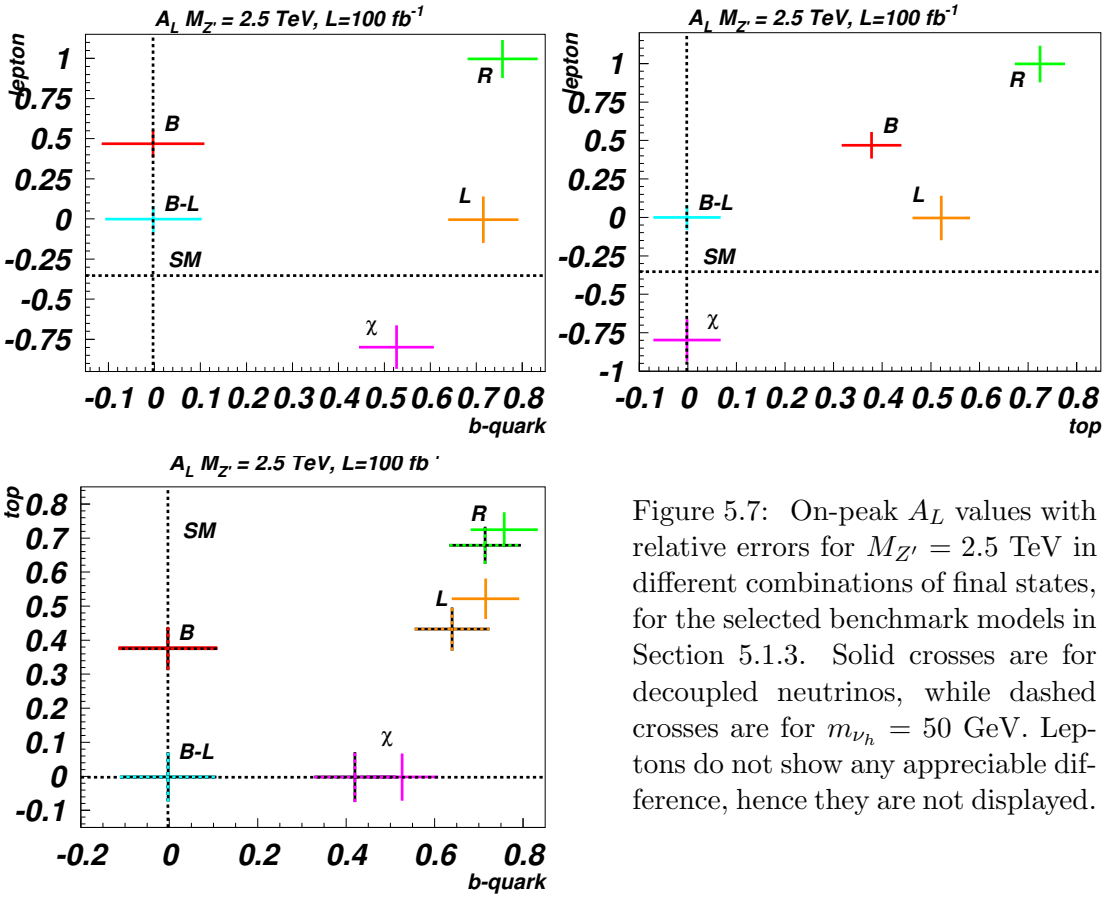

Figure 5.7: On-peak A_L values with relative errors for $M_{Z'} = 2.5$ TeV in different combinations of final states, for the selected benchmark models in Section 5.1.3. Solid crosses are for decoupled neutrinos, while dashed crosses are for $m_{\nu_h} = 50$ GeV. Leptons do not show any appreciable difference, hence they are not displayed.

A_L	$\not{B}$			R			$\not{L}$			B-L			χ		
50 \ dec	τ	t	b	τ	t	b	τ	t	b	τ	t	b	τ	t	b
$\not{B}$		–		2.5	4.3	3.5	2.0	1.7	3.4	2.8	4.1	0	5.6	4.1	2.0
R	2.5	3.7	3.3		–		3.8	2.6	0.3	4.9	8.4	3.7	7.1	8.4	1.0
$\not{L}$	2.0	0.7	2.9	3.8	2.9	0.4		–		0	5.7	3.5	2.8	5.7	0.8
B-L	2.8	4.0	0	4.9	7.6	3.4	0	4.5	2.9		–		3.5	0	2.0
χ	5.6	3.9	1.8	7.1	7.5	1.5	2.8	4.5	1.1	3.5	0	1.9		–	

Table 5.3: Significance for A_L for the LHC at 14 TeV for 100 fb^{-1} and $M_{Z'} = 2.5$ TeV for the common benchmark points in the τ, t, b final states. Upper triangle for decoupled heavy neutrinos and lower triangle for m_{ν_h}=50 GeV.

already proves to be sufficient to discriminate among all the models. If the inclusion of tops already helps to disentangle the models, it is clear that, were it available, the measure in b-quarks would be of great help to fully distinguish them: the discrimination power is always above 4 in at least one final state, with the b-quarks being especially relevant to discriminate between $\not{L}$ and $\not{B}$.

Regarding the inclusion of heavy neutrinos, their impact is that of reducing the absolute value of the asymmetry and to increase its statistical error. τs are not affected by their presence and therefore show the same significance. Additionally, the absolute values of the asymmetries for B-L and $\not{B}$ are not affected by heavy neutrinos, given that the former has vanishing asymmetries everywhere and that the latter has negligible BRs

into them. Therefore, their disentanglement from any other model can only get worse, due to the reduced central values of the latter. The same is true also for χ when tops are considered, given that its asymmetries in this final state are vanishing. When instead models with finite values of the polarisation asymmetry in a specific final state are compared (i.e., R and $\not{L}$ using tops and R, $\not{L}$ and χ using b's), the discrimination power therein gets enhanced when considering coupled heavy neutrinos. The central values change differently and the various models considered here are better separated, despite the slightly larger statistical errors.

5.4 Conclusions

In summary, the feasibility of profiling a Z' boson, possibly discovered at the 14 TeV LHC, thanks to the exploitation of the decays of the new gauge boson into $\tau^+\tau^-$, $t\bar{t}$ and $b\bar{b}$ states has been analysed, with respect to the time-honoured studies of DY channels only (i.e., decays into e^+e^- and $\mu^+\mu^-$ final states). In fact, the former signatures afford one with the possibility of not only defining standard charge asymmetries, the only ones accessible in the latter, but also spin ones. Their measure is certainly feasible for τ and top-quark final states, while, at this moment in time, the b-quark final state may prove difficult, if at all possible, to analyse due to experimental limitations in reconstruction, as well as to the highly boosted kinematics. Further, based on a dedicated parton level simulation, including some selection criteria and realistic detector efficiencies, it has been argued that in this approach neither DY nor any of the above new channels can be used alone to fully probe all the parameter space. Rather, one way to make this possible is to combine two or more of these channels, with the inclusion of spin observables, as the aforementioned final states show different sensitivity to the observables previously studied. The spin polarisation was determined to offer a better discrimination power compared to the charge asymmetry but this effect may be offset by the more involved reconstruction process of the former observable contributing to more uncertainty in an experimental analysis. The presence of light extra states (the heavy neutrinos) can alter the observables under study, and their impact might be resolved.

Ultimately, the goal of profiling an observed resonance would be to measure all the parameters of its fermionic interactions. In the minimal case, as discussed in section 2, there are 5 independent couplings. Following Ref. [50], at least one more linearly independent observable is required than those available in the light lepton sector, where some degeneracy still occurs. Considering multiple final states and their spin asymmetries could provide the necessary measurements to extract the fermionic couplings in this minimal case, that become essential when testing the universality of couplings or when considering models with more general coupling structures. Finally, our continuous scanning of the parameter space highlighted regions where leptonic final states are not

the most sensitive ones, hence where alternative final states would prove to be more effective.

Chapter 6

Multiple Z's from a composite Higgs model

Moving away from standard benchmark Z' scenarios, which tend to be optimally searched for in the di-lepton channel, this chapter presents a study, taken from [118], of the production of top-antitop pairs at the LHC as a testbed for discovering heavy Z' bosons belonging to a composite Higgs model. In these scenarios, such new vector states can be sizeably coupled to the third generation quarks of the SM. Again, their possible appearance in cross section as well as (charge and spin) asymmetry distributions is considered. The calculations are performed in the minimal four-dimensional formulation of such a scenario, namely the 4-Dimensional Composite Higgs Model (4DCHM) [119], which predicts a considerable exotic sector including five new Z's. The scope of DY in accessing the gauge sector of the 4DCHM is only confined to large machine energies and luminosities [118], which further motivates $t\bar{t}$ searches, as one of the main decay modes.

A brief overview of composite Higgs scenarios from strong dynamics will be presented, with a summary of the main features of the 4DCHM in Section 6.1, including some discussion of experimental constraints on such models. A description of the calculations and variables is given in Section 6.3.1. Section 6.4 comments on the parameter scan performed for a number of benchmarks previously considered in [118] and discusses their $t\bar{t}$ phenomenology. Particular attention will be paid to the case of nearly degenerate resonances, highlighting the conditions under which these are separable in the asymmetry observables, especially when they are not in the cross section. The impact of the resonances' intrinsic width on the event rates and various distributions is also discussed, as well as the importance of their exotic heavy quark decay channels. It will be shown that the 14 TeV stage of the LHC will enable one to detect two such states, assuming standard detector performance and machine luminosity. A mapping of the discovery potential of the LHC of these new gauge bosons is given. Section 6.5 summarises the conclusions and outlook.

6.1 Compositeness from strong dynamics

The main motivations for models of compositeness lie in the unique features of QCD and dynamical symmetry breaking. The properties of QCD allow for the dynamical generation of a scale, Λ_{QCD}, at which the strong coupling becomes infinite. Interestingly, this scale seems to naturally appear independently of the cutoff scale, e.g. M_P, and initial (perturbative) value from which the coupling is run down [120]. Furthermore, another scale, f_π, is also introduced in the mechanism of chiral symmetry breaking discussed in Section 1.2, associated with the pions – the NGBs of this broken symmetry. Both of these scales are linked to the strong dynamics of the QCD sector. Speaking loosely, the former mainly originates from the Yang-Mills self-interactions, while the other from the matter interactions.

6.1.1 Technicolour

It is therefore not unreasonable to hope that the unexplained EW scale ($\sim v$) may be generated by the dynamics of a strongly interacting gauge theory with its own, fundamental scale, Λ', analogous to Λ_{QCD}. This new interaction, often called "Technicolour" (TC) [121], can then be used by the appropriate choices of gauge group and exotic "technifermion" matter to generate the EW scale by running from some high energy assumed to be related to a GUT or string theory. EWSB can then occur if one assumes that the EW group is a gauged subgroup of the chiral group of the TC sector. More precisely, the strong TC interactions dynamically break their own chiral group, leading to a set of NGBs which are eaten by the gauge fields of the EW group to give them a mass of order $f \sim v$, the pion constant of the TC theory. Thus the longitudinal components of the EW gauge bosons correspond, in the high energy limit, to composite NGBs, as opposed to the case of the Higgs mechanism where they are fundamental scalar degrees of freedom. This is, in fact analogous to the pions from chiral symmetry breaking in QCD which, in the absence of the Higgs mechanism, would still break EW symmetry and lead to $\mathcal{O}(30\text{ MeV})$ masses for the EW gauge bosons [122].

Additionally, like the K, η, ρ and other colour singlet bound states in QCD, a host of new techi-meson and techni-baryon states are expected to exist. The phenomenology of TC models is diverse and offers many possibilities although it is generally true that they tend not to predict a light scalar state like the one observed at the LHC, assuming it does have the properties of a SM Higgs. In fact, TC is often called a Higgsless theory since a CP-even scalar meson is not needed for EWSB. Many approximate features are deduced from rescaling QCD properties and above the validity of the effective composite sector Lagrangian, only non perturbative calculations are viable. The models are also generally confronted with relatively strong constraints from EWPTs and require an extended gauge sector to generate fermion masses. Thus, although minimal TC realisations are

disfavoured, the idea that new strong dynamics might be behind EWSB remains an attractive one by virtue of the absence of fundamental scalar fields whose masses are not protected by any symmetry. The topcolour [76] model, used as a benchmark in the $t\bar{t}$ resonance exclusion plots from the LHC shown in Section 3.1.6, is an example of such a high scale strong interaction in which the Higgs arises as a strongly bound $t\bar{t}$ state.

6.1.2 The Higgs boson as a pNGB

The important difference between TC models and the effective realisation considered in this work is the existence of the Higgs boson as a pNGB of a dynamically broken global symmetry of a new strong sector. This property makes the field naturally light in the same way that the pions are naturally lighter than the rest of the QCD hadronic spectrum. Little Higgs models [123] are an example of constructions of the Higgs boson as a pNGB using a non linear sigma model description of the Goldstone modes arising from the spontaneous breaking of a global symmetry. A general pNGB can be described in this way by parametrising the broken degrees of freedom by a field:

$$U = \vec{f}\exp\left(i\frac{\vec{\pi}}{\vec{f}}\right), \tag{6.1}$$

where the constant vector $\vec{f}$ describes the symmetry breaking alignment that breaks a subset of the generators, t^a, of the global symmetry group. The fields $\vec{\pi}$ are each associated to a broken generator as $\vec{\pi} = \pi^a t^a$, and transform with a linear shift under the gauge transformation parameters in these directions.

$$\begin{aligned} U &\to U e^{i\vec{\alpha}}, \\ \vec{\pi} &\to \vec{\pi} + \vec{\alpha}. \end{aligned} \tag{6.2}$$

This is analogous to a Higgs mechanism where the Higgs mass has been taken to infinity, thereby decoupling the physical Higgs mode. The kinetic term for the U field, expanded in terms of the π^as lead to massless Goldstones with typical derivative interactions, ensured by the requirement that the action be invariant under the shift symmetry:

$$|\partial_\mu U|^2 \simeq |\partial_\mu \vec{\pi}|^2 + \frac{1}{f^2}|\partial_\mu \vec{\pi}|^2|\vec{\pi}|^2 + \cdots . \tag{6.3}$$

Such interactions are non-renormalisable by definition. The cut-off, Λ_f, of the theory is determined to be the point at which the irrelevant operators become relevant, i.e. when the theory becomes non perturbative. A one-loop computation of the wavefunction renormalisation enforces $\Lambda_f \lesssim 4\pi f$ [124]. The purpose of these descriptions are therefore to soften the hierarchy problem up to this scale, above which new physics must still appear, often associated with a new strong sector.

Specific choices of global symmetries can then be partially gauged to obtain gauge interactions with the pNGBs which do not incur mass corrections with divergences quadratically sensitive to a cutoff [124]. Typically, these involve the presence of more than one scalar multiplet breaking a global symmetry group which is partly gauged. An example of this would be a global $SU(3) \times SU(3)$ broken to $SU(2) \times SU(2)$ by a pair of U fields in the fundamental representation. If one of the $SU(3)$ factors is promoted to a gauge group, the gauge interactions break the product to the vectorial subgroup $SU(3)_V$ with half of the NGBs eaten by the gauge fields of the broken directions. The remaining NGBs from the broken axial $SU(3)$ can have radiatively generated mass terms that are therefore naturally suppressed and also protected from quadratic divergences by the underlying symmetry.

The interactions of the pNGBs are then characterised by the underlying global and gauge symmetries. One can generate the desired quartic potential radiatively by further enlarging the gauge structure as well as protect top-induced mass corrections by the introduction of heavy top partners [124]. These kinds of models can be constructed to embed the SM EW gauge group and always predict an extended gauge sector. One common realisation is via dimensional deconstruction [125] where a product of partially gauged global symmetries, e.g. $(SU(3)_L \times SU(3)_R)^n$, are connected by a set of "sigma" fields transforming as bi-doublets of the $SU(3)_L \times SU(3)_R$ factors forming what is known as a "moose" model. Although beyond the scope of this thesis, many realisations of the former exist and have interesting connections with models of extra dimensions. Each "site" can be viewed as a point on a discretised extra direction, whose geometry is dictated by the f constants of the sigma fields between individual sites.

A common choice of global symmetry breaking in these models is $SO(5)/SO(4)$. This particular structure is the minimal choice required to obtain the four degrees of freedom needed for the complex Higgs doublet with the additional merit that it transforms in the fundamental of the residual $SO(4)$. The benefit of this feature is that, looking back at Equation 1.15, $SO(4)$ is an accidental symmetry of the Higgs potential. If one decomposes $\phi^\dagger\phi$ in terms of the individual components of the complex Higgs doublet:

$$\begin{aligned} \phi &= \begin{pmatrix} \varphi_0 + i\varphi_1 \\ \varphi_2 + i\varphi_3 \end{pmatrix}, \\ \phi^\dagger\phi &= \sum_{i=0}^{3} \varphi_i^2, \end{aligned} \tag{6.4}$$

the quantity is manifestly invariant under the aforementioned $SO(4)$ transformation. This is connected to chiral symmetry in that $SO(4)$ is locally isomorphic to $SU(2) \times SU(2)$. One can therefore re-express this symmetry of the Higgs potential as an $SU(2)_L \times SU(2)_R$ invariant Lagrangian in which the Higgs field transforms as a bidoublet, $H \to LHR^\dagger$. EWSB preserves the diagonal (vectorial) subgroup of this global symmetry,

$SU(2)_V$. This is manifest when writing the Higgs field in the aforementioned form:

$$\begin{aligned} H =& (\tilde{\phi}, \phi), \\ \langle H \rangle =& \frac{v}{\sqrt{2}} \begin{pmatrix} 1 & 0 \\ 0 & 1 \end{pmatrix}, \end{aligned} \tag{6.5}$$

where v is the usual Higgs VEV ϕ, while $\tilde{\phi}$ are defined as in Equation 1.14 and Section 1.4 respectively. The remnant invariance is under the vectorial transformation $H \to VHV^\dagger$. In the absence of hypercharge, this would dictate that the W and Z have the same mass. Turning on hypercharge then modifies the relation to include $\cos\theta_W$, elucidating the particular relationship between the two eigenstates as feature of an underlying, weakly broken global symmetry. A connection can be made to the statement in Section 3.1 that this mass ratio is preserved as long as new scalars breaking extra $U(1)$s are EW doublets (or singlets). Having this residual global symmetry in the pNGB Higgs sector will therefore help to realise EWSB consistent with the observed EW boson mass spectrum.

6.2 The minimal 4D composite Higgs model

The model considered in this work is a general effective description of these types of models, developed in [119, 126], where a minimal amount of exotic fields are considered to realise a composite Higgs boson as a pNGB of a global symmetry group G spontaneously broken down to H. It is designed to be a 2-site deconstruction of a 5D theory proposed in [127] with, as defined above, a symmetry breaking scale, f. The global symmetry breaking structure of the physical scalar sector is based on the $SO(5)/SO(4)$ coset. Additional fields include fermionic partners to third generation quarks and gauge fields which describe vector bound states of the strongly interacting sector. The decomposition and global/gauge structure is shown schematically in Figure 6.1 taken from [119].

The idea of partial compositeness [126, 128] is combined with this description to outline a mechanism by which hierarchical fermion masses can be obtained by generating masses for the third generation quarks. In few words, the Ultra-Violet (UV) physics is assumed to induce linear couplings between SM fermions and fermionic composite operators with matching quantum numbers that lead to mass mixing between these two. The full scaling dimension of the operator then determines the relevance of the coupling with a given fermion and thus the degree of mixing between the two and ultimately its mass. The fermionic partners are only included for third generation quarks in order to generate top and bottom masses. These are chosen to live in 5 dimensional, vector representations of $SO(5)$ and a pair of these is added for each of the top and bottom in order to radiatively generate the desired EWSB potential for the composite Higgs. The new gauge fields are used to describe low lying vector excitations of the composite states. A detailed description of the model as well as other phenomenological analyses

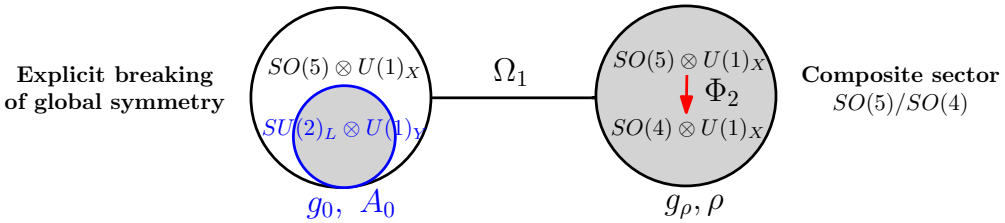

Figure 6.1: Pictorial 'Moose diagram' representation of the symmetries of the 4D composite Higgs model. White circles denote global symmetries while shaded circles correspond to gauge symmetries.

can be found in [118, 119, 129, 130]; the main features will be summarised in this section, beginning with a summary of the exotic particle spectrum in Table 6.1.

Neutral Gauge Bosons	$Z_{1,\ldots5}$
Charged Gauge Bosons	$W^{\pm}_{1,.3}$
Charge $+2/3$ quarks	$T_{1,\ldots8}$
Charge $-1/3$ quarks	$B_{1,\ldots8}$
Charge $+5/3$ quarks	$\tilde{T}_{1,2}$
Charge $-4/3$ quarks	$\tilde{B}_{1,2}$

Table 6.1: Extra particle content of the 4DCHM with respect to the SM. An increasing number in the label of a particle corresponds to a larger mass of the particle itself.

The important sector for the purposes of this study is that of the neutral gauge bosons and how they arise in conjunction with the Higgs field as a consequence of the particular global group structure of the two sites. The structure of the model is shown pictorially in Figure 6.1. For the reasons described in the previous section, the Higgs degrees of freedom are described as Goldstone bosons arising from the breaking of $SO(5)$ to $SO(4)$, with an extra, unbroken global $U(1)$ symmetry whose presence will be explained later. The general global group $SO(5) \times U(1)_X$ is denoted by G. The four scalar degrees of freedom are embedded in the sigma field associated to this breaking, Φ. These can be written in a way that makes manifest the transformation properties of the Higgs field, ϕ, under the unbroken $SO(4)$. Following Equation 6.1, the specific symmetry breaking alignment and Goldstone modes are:

$$\vec{f} = (0\,0\,0\,0\,f)^T; \qquad \vec{\pi} = \begin{pmatrix} 0_4 & \phi \\ \phi^T & 0 \end{pmatrix}. \tag{6.6}$$

It is clear that ϕ is a four component object that will transform as a vector under the remnant $SO(4)$.

In order to obtain vector resonances, another chiral product group, $G_L \times G_R$, is invoked and the diagonal subgroup of G_R and G, gauged. With reference to Figure 6.1, the fields and gauge couplings associated to gauging $SO(5)$ are g (henceforth g^*) and ρ while the subscript, X refers to the $U(1)_X$ group. Another non-linear sigma field, Ω parametrises

the breaking of the chiral group to its vectorial subgroup $G_L \times G_R \to G_V$, yielding the necessary amount of Goldstone modes to be absorbed by the gauge fields, giving them a mass of order fg^*. The gauging procedure can be expressed by considering the covariant derivatives acting on the two sigma fields responsible for breaking the two global symmetries thereby 'linking' the two sites

$$\begin{aligned} D_\mu \Omega &= \partial_\mu - i\Omega\rho^\mu + iA_\mu\Omega, \\ D_\mu \Phi &= \partial_\mu + i\rho^\mu\Phi. \end{aligned} \tag{6.7}$$

Where an unphysical 'gauge field' is assigned to G_L as should be treated as a classical source for the chiral current. Counting the 10 broken generators of $SO(5)$ along with the $U(1)$, one therefore expects 11 new, massive gauge bosons which are comprised of 5 neutral and 3 charged states. This is analogous to the way in which the appearance of the ρ mesons can be described by fundamental gauge multiplets of $SU(2)$ in QCD since they are higher spin excitations of the pions, which are triplets of the remnant $SU(2)$ post chiral symmetry breaking. The intention of including these additional $SO(5) \times U(1)_X$ resonances is to account for the lowest lying new composite states that may be accessible at the LHC.

The remaining 4 Goldstone bosons, transforming adequately as a vector of the remnant $SO(4)$ are identified with the SM Higgs field. The SM gauge group is then obtained by partially gauging the $SU(2)_L \times U(1)_Y$ subgroup of the remnant $SO(4) \times U(1)_X$ with the correct hypercharge obtained as a combination of T^3_R and X and EWSB subsequently occurring as in the SM. The model recovers the massless photon but predicts mixings between the 5 extra neutral gauge states and the Z and hence modifications to Z observables with respect to the SM. In particular, the new resonances have non universal couplings to third generation fermions due to their partial compositeness. Detailed leading order expressions for the masses and couplings of these resonances are summarised in [3]. Of these, the chiral top couplings of the Z's at leading order i.e. purely due to the elementary-composite mixing before EWSB, $G^{L,R}_{Z_i}$, are collected here for reference.

$$\begin{aligned} g^L_{Z_0}(t) = \frac{e}{s_\omega c_\omega}(\frac{1}{2} - \frac{2}{3}s^2_\omega), \quad g^R_{Z_0}(t) &= \frac{e}{s_\omega c_\omega}(-\frac{2}{3}s^2_\omega), \\ g^L_{Z_1}(t) \sim 0, \quad g^R_{Z_1}(t) &\sim 0, \\ g^L_{Z_2}(t) = \frac{e}{6c_\omega}\frac{s_\psi}{c_\psi}\frac{1}{(1+F_L)}(1 - \frac{c^2_\psi}{s^2_\psi}F_L), \quad g^R_{Z_2}(t) &= \frac{2e}{3c_\omega}\frac{s_\psi}{c_\psi}\frac{1}{(1+F_R)}(1 - \frac{c^2_\psi}{s^2_\psi}F_R), \\ g^L_{Z_3}(t) = -\frac{e}{2s_\omega}\frac{s_\theta}{c_\theta}\frac{1}{(1+F_L)}(1 - \frac{c^2_\theta}{s^2_\theta}F_L), \quad g^R_{Z_3}(t) &\sim 0, \\ g^L_{Z_4}(t) = g^R_{Z_4}(t) = 0, \quad g^L_{Z_5}(t) &\sim g^R_{Z_5}(t) \sim 0, \end{aligned} \tag{6.8}$$

where the mixing angle, ψ, is defined by $\tan\psi = s_\psi/c_\psi = \sqrt{2}g'/g^*$ and s_ω and c_ω compactly refer to the sine and cosine of the Weinberg angle. The parameters $F_{L,R}$ are functions of the effective mass parameters of the composite fermionic sector and its

mixing with the SM third generation fermions which can be found in [3] and are not important for the purposes of this work. An important feature of this model is that three of the five resonances are approximately inert with respect to the top quark. The Z_4 is completely inert to all orders While the Z_1 and Z_5 receive some interactions with tops at order $\xi = v/f$. However, the Z_1 is completely inert with respect to the light quarks and so is not expected to be produced significantly at a hadron collider. The Z_5 simply has ξ suppressed couplings compared to $Z_2, 3$ and therefore, only two new states are realistically expected to be observable in this channel at the LHC.

The 20 new fermionic states are vector-like with respect to the SM and couple directly to the new resonances. The phenomenology of the new gauge bosons is largely influenced by whether or not the mass scale of the fermions is low enough compared to the gauge boson masses such that the decay channel of the latter into the former opens. This divides the analysis of the parameter space into two regimes, as described in [118], both of which will be considered in the context of $t\bar{t}$ phenomenology. The case in which the vector quark decay channels are closed, resulting in narrower resonances, is studied through benchmarks (b), (d) and (f) defined in Tabs. 20 and 21 of [118]. The opposite case of wide Z's is characterised by the coloured benchmarks (green, magenta, yellow) as given in Tabs. 19 and 22 of [118]. These were initially defined to be studied in the di-lepton channel and have been adapted by this study. A set of tables detailing the masses, widths and couplings to the SM quark sector of the Z and the two Z's of interest (labelled Z_2 and Z_3) is included in Appendix B.

The model has a total of 13 free parameters, of which f and g^* are considered to be the most important, describing the extra gauge sector and the global symmetry breaking scale. The benchmarks are therefore characterised by specific values of the two while a scan was performed in [3] over the remaining parameters. This was needed to identify points consistent with the various physical constraints imposed by the electromagnetic coupling, the Z mass, the Fermi constant, the top and bottom masses and the Higgs VEV: e, M_Z, G_F, m_t, m_b, v. The Higgs mass was required to lie within the range dictated by the ATLAS and CMS [9] results of 2012: 124 GeV $\leq m_H \leq$ 126 GeV. A tolerance level was also set on the predicted top and bottom masses of 170 GeV $\leq m_t \leq$ 175 GeV and 3 GeV $\leq m_b \leq$ 6 GeV respectively. The $W^- t\bar{b}$, $Zt\bar{t}$ and $Zb\bar{b}$ couplings were also required to be consistent with data [131]. In scanning the 4DCHM parameter space, it was also ensured that the additional gauge boson masses considered were not in conflict with current LHC direct searches for heavy gauge bosons, specifically with the data reported in [114, 132]. The reference masses for the analysis were kept of order 2 TeV or larger mostly due to EWPT considerations discussed in [118] and references therein. The final important constraints taken into account were those of direct searches for the exotic vector-like quarks which, being coloured objects, can be pair produced via QCD processes and observed through their subsequent decay into third generation SM quarks and associated bosons (W, Z, h). These searches [133] in the different assumed decay

channels for the heavy quarks typically exclude masses of order 600 GeV and were also taken into account.

6.3 Calculation

In this section, the details of the calculations performed, i.e., the tools used and the kinematical variables analysed, are summarised.

6.3.1 Tools

An implementation of the model exists in the the LanHEP/CalcHEP environment [103, 104, 134] and was used for the spectrum generation and is described in more detail in [118]. The code exploited for the study of the asymmetries is, as in the last two chapters, defined through the HELAS subroutines [83], and built up by means of MadGraph [84]. It was used to compute the $t\bar{t}$ invariant mass distributions and asymmetries of the various benchmarks. Initial state quarks were assumed to be massless whereas for the final state top (anti-)quarks the particular m_t values predicted by the benchmark was used. The CTEQ6L1 [18] PDFs were used, with factorisation/renormalisation scale set to $Q = \mu \sim M_{Z_{2,3}}$ with VEGAS [85] exploited for multi-dimensional phase space integrations.

6.3.2 Asymmetries

The asymmetries considered in this work are largely the same as in previous chapters with the exception of the charge asymmetry. That is, the spin polarisation and correlation asymmetries are implemented as defined in Equations 2.12 and 2.13 while a new observable A^*_{FB} is utilised to measure the charge asymmetry. This stems from the reasoning in Section 4.2, suggesting that the previously used observables, which either performed kinematical cuts or compared the number of tops and antitops within a limited rapidity window, do not benefit from significances which outweigh the associated reduction in statistics. As such, a variable which uses the full sample is taken, defining the reference z-direction – from which the angular distribution of the $t\bar{t}$ system is measured – on an event-by-event basis, as the direction of the $t\bar{t}$ boost, $y_{t\bar{t}}$ [32]:

$$A^*_{FB} = \frac{N(\cos\theta^* > 0) - N(\cos\theta^* < 0)}{N(\cos\theta^* > 0) + N(\cos\theta^* < 0)}. \tag{6.9}$$

The angle θ^* is taken as the polar angle in the $t\bar{t}$ rest frame from this reference z axis. This allows exploits the correlation of the true quark direction and $y_{t\bar{t}}$ without losing any events, at the price of lower central values for the observable. The lower

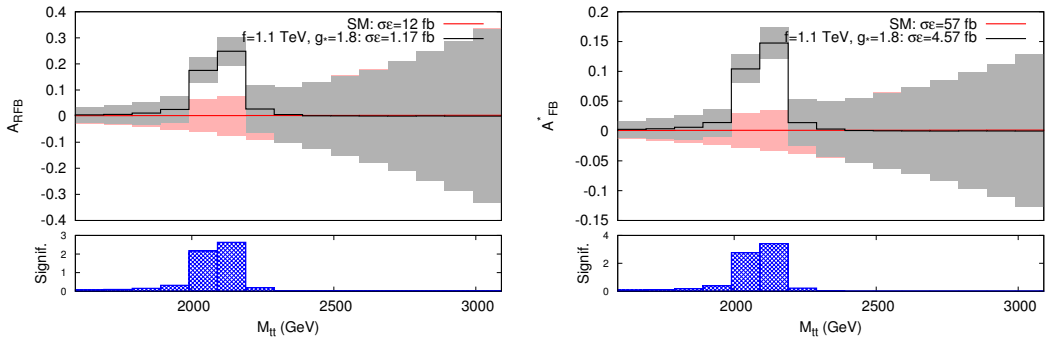

Figure 6.2: Comparison of the A_{RFB} (*left*) and A^*_{FB} (*right*) incarnations of the charge asymmetry for a benchmark point with $f = 1.1$ TeV and $g^* = 1.8$ at the 14 TeV LHC with 300 fb^{-1}. Grey(Pink) shading represents the statistical error on the 4DCHM(SM) rates, in black(red) solid lines. The legend labels also indicate the value of the fiducial cross section for each observable, folding in an assumed 10% reconstruction efficiency, which is then used to compute the binned theoretical significance measure shown in each subplot.

central values arise from a larger contamination from gg initiated $t\bar{t}$ events, which will be distributed around a zero net $t\bar{t}$ rapidity, smeared by PDFs. The events with low $y_{t\bar{t}}$ are therefore more likely to contain these events. The importance of the two competing effects, statistics against central value, was considered by comparing this observable to the A_{RFB} incarnation, determined to be the best performer in Chapters 4 and 5. The statistical significance gained in A^*_{FB} was found to outweigh the gg dilution avoided in making the rapidity cuts in A_{RFB}. An example of this behaviour is shown in Figure 6.2. The key comparison can be made at the level of the theoretical significance, which is higher in the case of A^*_{FB}, even though it has twice as low a central value. This can be understood by comparing the fiducial cross sections of the two observables, where the rapidity cut reduces that of A_{RFB} by a factor ~ 5. The non-linear dependence of the uncertainty on an asymmetry means that a factor 2 in value is outweighed by a factor 5 in the cross section in terms of the theoretical significance. Therefore A^*_{FB} will be used as the charge asymmetry observable of choice for the remainder of this thesis.

6.4 Results

This section is divided into two parts. Firstly, results of the scan over the 4DCHM parameter space, described in Section 6.2 and in more detail in [3], are presented. These were interpreted in the context of potential resonant signals in $t\bar{t}$ where at least one $Z' \to t\bar{t}$ signal may be established, assuming $\sqrt{s} = 7, 8$ and 14 TeV at the LHC. Secondly, the aforementioned benchmarks are profiled in $t\bar{t}$ cross section and asymmetry observables. As in the previous chapters, the limitations of this work as a parton level study require the estimation of reconstruction efficiencies associated with each of the

observables. Following the discussion in Section 2.5 and the estimates in Chapter 5, the cross section and charge asymmetry observables are assigned a 10% efficiency, while the spin observables are assigned 5%, to take into account the additional information required to correlate the kinematical properties of the boosted top decay products to the observables. The distributions presented assume a mass resolution of 100 GeV, consistent with experimental results in boosted resonance searches [37, 38, 74].

6.4.1 Parameter scan

In order to determine the parameter space of the 4DCHM where at least one $Z' \to t\bar{t}$ signal can be established, the scan over the fermionic parameters of the model was performed, as described in [118], for various choices of the model scale f and gauge coupling constant g_*. As stressed in [118, 3], these two parameters completely determine the neutral (and charged) gauge boson mass spectrum. The $t\bar{t}$ cross section for each allowed scan point was computed with the use of both MadGraph and CalcHEP for the LHC at 7, 8 and 14 TeV in presence of the following selection cut:

$$\frac{M_{Z_2}+M_{Z_3}}{2} - 3\frac{\Gamma_{Z_2}+\Gamma_{Z_3}}{2} < M_{t\bar{t}} < \frac{M_{Z_2}+M_{Z_3}}{2} + 3\frac{\Gamma_{Z_2}+\Gamma_{Z_3}}{2} \tag{6.10}$$

for the lightest Z' bosons where $M_{t\bar{t}}$ is the invariant mass of the $t\bar{t}$ final state[1].

The signal S is defined as the difference between the total cross section $T(= S + B)$ in the full 4DCHM (including the SM) and the SM background only, B, so that interference effects in the $q\bar{q}$ channel between the Z's and γ, Z are taken in account in the former, and the dimensional significance σ has been defined as $S/\sqrt{B}$ (with unit $\sqrt{\text{fb}}$). The actual significance measure can be recovered by multiplying by $\sqrt{\varepsilon\mathcal{L}}$, where $\varepsilon = 10\%$ is the estimated selection efficiency for the $t\bar{t}$ final state, as discussed in the previous section and $\mathcal{L} = 5, 20$ and 300 fb^{-1} (for $\sqrt{s} = 7, 8$ and 14 TeV, respectively) for the integrated collider luminosity.

Figure 6.3 presents the results of the scans for three choices of model scale, f, and coupling constant, g_*, in terms of scatter plots in the m_{T_1}/Γ_{Z_2} plane (results for Γ_{Z_3} are very similar), with the corresponding dimensional significance σ, for the 8 and 14 TeV stages. m_{T_1} denotes the lightest top partner mass and therefore at which point the decay channel of the Z' into these heavy objects is open. In some cases the latter is negative, owing to the fact that, for very large widths, the selection cuts in Equation 6.10 sample large interference effects which are not positive definite. Results of the scan for the 7 TeV stage of the LHC are not presented since the resulting dimensional significances are rather similar to the ones for the 8 TeV stage with statistical significances smaller by a factor of 2 or so.

[1] Due to large Z' widths in certain region of the parameters space lower(upper) bounds on the selection cut have been imposed to be the maximum(minimum) between the ones of Equation 6.10 and $2m_t(\sqrt{s})$.

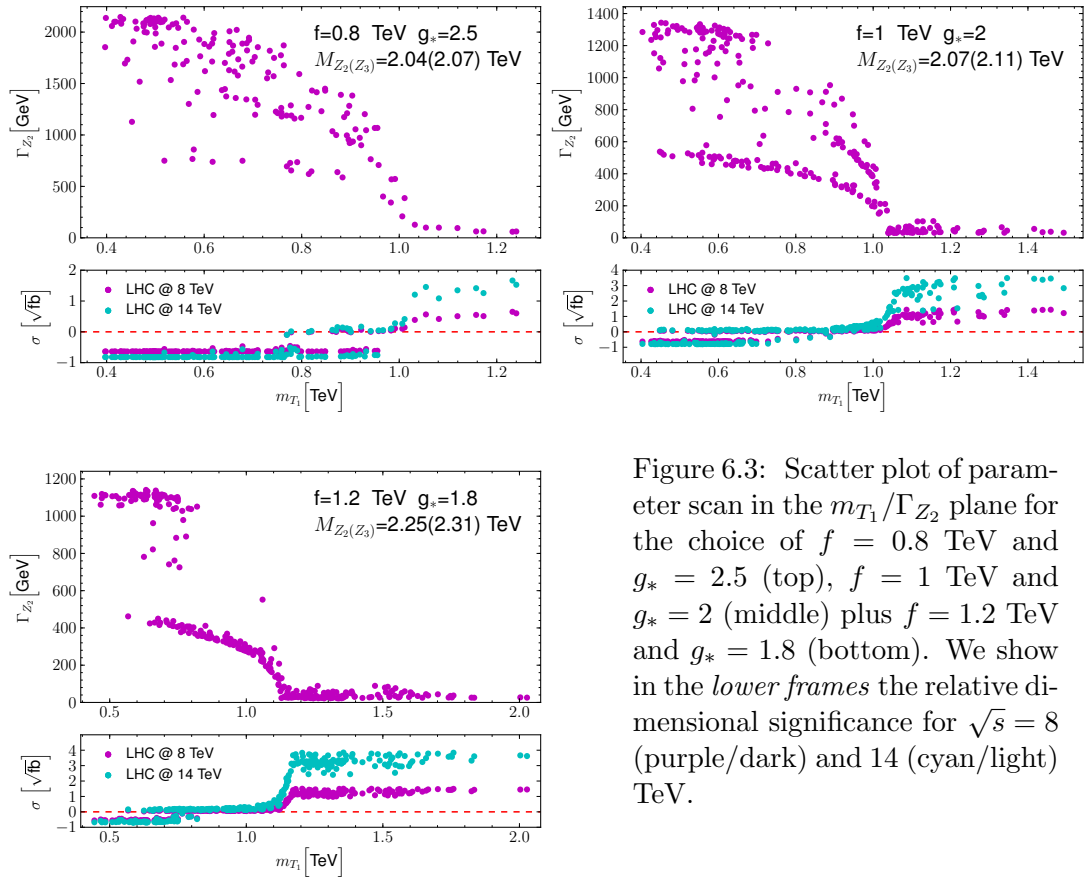

Figure 6.3: Scatter plot of parameter scan in the m_{T_1}/Γ_{Z_2} plane for the choice of $f = 0.8$ TeV and $g_* = 2.5$ (top), $f = 1$ TeV and $g_* = 2$ (middle) plus $f = 1.2$ TeV and $g_* = 1.8$ (bottom). We show in the *lower frames* the relative dimensional significance for $\sqrt{s} = 8$ (purple/dark) and 14 (cyan/light) TeV.

One can see the clear relationship between the mass scale of the heavy third generation partners and the visibility of the resonances in that, once their Z' decay channel becomes kinematically accessible, the widths grow substantially and prevent any significant deviations from the SM background. More importantly, the significances are negative in this region, an artefact of the inclusion of non positive-definite interference effects in the signal definition. They simply report that the parameter point with extremely wide Z's predicts a deficit with respect to the SM for said interference effects, which grow with the resonance width. These are left negative to differentiate the narrow and extremely wide regimes. The off peak effects of such widths of order the gauge boson masses themselves have consequences down to very low invariant masses, perhaps even near the $t\bar{t}$ threshold. These may not only already be constrainable with current LHC data but would certainly require analyses with background estimates beyond leading order to have a more precise prediction of the overall shape and normalisation of the invariant mass spectrum. Without this, it is difficult to make meaningful statements about these deficits in the production cross section over a large $M_{t\bar{t}}$ range and, as such, no physical meaning is associated to their negative significances. It is evident that the intended resonant analyses become difficult beyond the limit in which the Z's are narrow and cannot decay into the heavy fermions. This is further emphasised by Figure 6.4, collecting all scanned points, where the correlation of the dimensional significance with m_{B_1} – the lightest bottom partner mass – is also shown. The reliance of the significance

of the Z' signal on a narrow resonance hypothesis is evident.

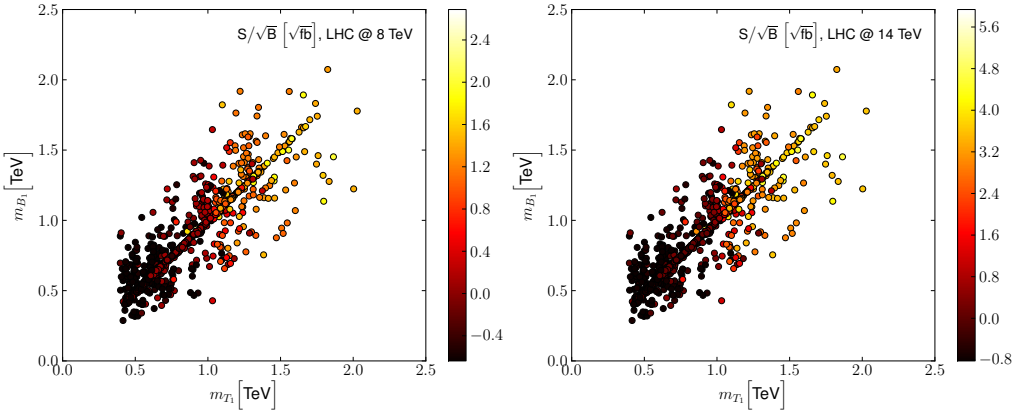

Figure 6.4: Scatter plot of scanned points showing the dimensional significance in the m_{T_1}/m_{B_1} plane in the colour bar. The points represent the low mass cut, singling out Z_2 and Z_3, for the LHC at 8 TeV (*left*) and 14 TeV (*right*).

6.4.2 Benchmark studies

In this subsection, the scope of the $t\bar{t}$ final state in profiling Z' bosons of the 4DCHM for the case of the LHC at 14 TeV in energy and 300 fb^{-1} in luminosity is considered as the results in the previous subsection clearly highlighted a limited scope in this respect at lower values of $\sqrt{s}$ and $\mathcal{L}$. Moreover, the parameter scan has shifted the focus primarily on cases where the resonances remain narrow, although the effects of allowing them to become very wide will be shown later via the coloured benchmarks. The illustrative measure of "theoretical significance" of an asymmetry prediction, defined in Equation 4.16, is used as in the previous studies. The observables considered here are the invariant mass distributions of the top-antitop pair, $M_{t\bar{t}}$, which will be sampled in terms of the cross section as well as the asymmetries metioned in Section 6.3.1. As discussed therein, A^*_{FB} was chosen as the charge asymmetry observable as it provided better significances than the cut based observables.

Figures 6.5, 6.6 and 6.7 show the differential values of the cross section (σ) and three asymmetries (A_L, A_{LL} and A^*_{FB}) as a function of $M_{t\bar{t}}$, with each figure referring to the following three benchmarks of [118], respectively: (b) $f = 0.8$ TeV and $g^* = 2.5$; (c) $f = 1$ TeV and $g^* = 2$; (f) $f = 1.2$ TeV and $g^* = 1.8$. Recall that the mass scale of the two lightest (and nearly degenerate in mass) gauge boson resonances, Z_2 and Z_3, is given by $M_{\text{lightest}} = fg_*$ and notice that the heaviest one, Z_5, has a mass between 600 GeV and 1 TeV above such a value, depending on the benchmark. Furthermore, the mass difference between M_{Z_2} and M_{Z_3} is at most 60 GeV or so.

These points in parameter space correspond to the case of small Z' widths, i.e., where the threshold for the gauge boson decays in pairs of heavy fermions has not been reached.

Therefore, one may hope to resolve the individual Z_2, Z_3 and Z_5 peaks in the cross section already. Unfortunately, this is not the case. For a start, one should note that the invariant mass resolution of $t\bar{t}$ pairs is realistically of order 100 GeV or so (somewhat better for semileptonic decay channels and somewhat worse for fully hadronic/leptonic ones) so that it is not generally possible to separate the Z_2 and Z_3 peaks (they do however cluster together in what looks like a single wider resonance). The (isolated) Z_5 peaks never emerges over the background. These two points are made explicit for all benchmarks by the two top frames in Figures 6.5, 6.6 and 6.7. The left frames show the differential cross sections binned over (artificially) narrow $M_{t\bar{t}}$ bins, of 5 GeV, whereas the right ones use a much larger (and more realistic) 100 GeV resolution. Despite this, in most cases, a significance $S/\sqrt{B}$ larger than 5 can be achieved after an event sample of $\mathcal{L} = 300$ fb^{-1} has been collected for signal (S) and background (B), i.e., for benchmarks (c) and (f). For benchmark (b), instead, the significance is only above 3.

Under these circumstances, where a detection either cannot be established with enough significance or cannot resolve the nearby resonances, the ability to exploit the three asymmetries is crucial. In fact, all of these complement the scope of the cross section, as in all cases they offer a similar level of theoretical significance for the signal, so their contributions can be combined to increase significance (where needed), albeit for the case of Z_2 and Z_3 only, not Z_5. Furthermore, among the asymmetries, A_L is unique in offering the chance to separate (in presence of resolution and efficiency estimates) Z_2 and Z_3, as the two objects contribute to the asymmetry in opposite directions, unlike the case of A_{LL} and A^*_{FB}, which predict an excess in the same direction, so that the result is here indistinguishable from the case of a lone wider resonance. This is exemplified in last three rows of Figures 6.5, 6.6 and 6.7. Referring to Section 3.2, the distinguishability is owed to the sensitivity of A_L and A^*_{FB} to the relative handedness of the Z' couplings. For the latter observable, however, this sensitivity extends to both the initial and final state which does not give it the same distinguishing power as A_L. This is particularly relevant if one notices that it appears a generic feature of this model from the tables in Appendix B that the Z_2 and Z_3 have predominantly right- and left-handed top couplings, respectively.

As illustrated in [118], if one allows for the heavy fermion masses to be lighter than half the mass of the Z' states, their widths grow substantially. The aforementioned coloured benchmarks are representative of this phenomenological situation. They are modifications of the $f = 1.2$ TeV and $g_* = 1.8$ point. The corresponding cross section and asymmetry distributions are found in Figures 6.8, 6.9 and 6.10. With a growing width, the ability to resolve the presence of the Z_2 and Z_3 resonances degrades substantially and, with it, the discriminative power of A_L between the two nearby peaks. This is not surprising, as in this case the effects induced by the two gauge bosons, Z_2 and Z_3, which are opposite in sign, start overlapping in invariant mass hence cancelling each other. In contrast, for the cross section and A_{LL} as well as A^*_{FB} this is not the case, so that these

observables are more robust in comparison. Altogether the Z_2 and Z_3 signals should remain accessible so long as their widths are less than $\mathcal{O}(10\%)$ of their masses, see the first two coloured benchmarks (green and magenta). For the other one (yellow), the case in which the masses and widths are comparable, which is also when the $M_{t\bar{t}}$ resolution is actually less than $\Gamma_{Z'}$, any discovery power vanishes.

6.5 Conclusions

In this chapter, it has been emphasised that the $t\bar{t}$ final state can be an efficient LHC probe of the neutral gauge sector of the 4DCHM that represents a complete framework for the physics of a composite Higgs boson as a pNGB and incorporates the mechanism of partial compositeness. The latter implies that, alongside the SM gauge bosons, only the third generation quarks (unlike the first two and all leptons) of the SM are mixed with their composite counterparts, so that the $pp(q\bar{q}) \to Z' \to t\bar{t}$ process emerges as an obvious discovery channel.

It is shown that such a model can enable the detection of two of the three accessible (i.e., sufficiently coupled to the initial quarks) Z' bosons of the 4DCHM already by data taken at 7 and 8 TeV, albeit in limited regions of parameter space, i.e., those with the smallest possible Z' masses, yet compatible with all current experimental data. Once the CERN machine will reach the 14 TeV stage, detection will be guaranteed essentially up to the kinematical limit of the machine itself, so long that the Z' boson of the 4DCHM are sufficiently narrow, i.e., with widths being at most 10% of the masses.

Other than discovering such possible new states, the LHC (at maximal energy and luminosity) could afford, under the same width conditions, the possibility of profiling the Z' couplings, thanks to the fact that one can use $t\bar{t}$ samples to define charge and spin asymmetries, which are particularly sensitive to the chiral couplings of the new gauge bosons. Furthermore, these observables, unlike the cross section, once mapped in invariant mass, also enable one to separate the two resonances, Z_2 and Z_3, that the 4DCHM predicts to be very close in mass, in fact closer than the standard mass resolution afforded by top-antitop pairs. This feature of asymmetries presents an additional benefit compared to the last two studies, which only considered single Z' models. One could exploit the cancellation effect observed in A_L but not in A_{FB}^* to deduce the presence of nearly degenerate resonances without relying on the appearance of their distributions in $M_{t\bar{t}}$ by correlating the two observed asymmetries and comparing to predictions from single resonances as will be shown in the next chapter.

These conclusions have been reached including both tree-level EW and QCD backgrounds (the latter dominated by $pp(gg) \to t\bar{t}$), including interference effects (where applicable, i.e., in the $pp(q\bar{q}) \to t\bar{t}$ subprocess), through a parton level simulation, in

presence of realistic detector resolution and statistical error estimates. In this connection, before closing, it should be acknowledged that systematic uncertainties, requiring a more involved study beyond parton level, have been neglected [87, 89]. However, this is not expected to undermine the main results.

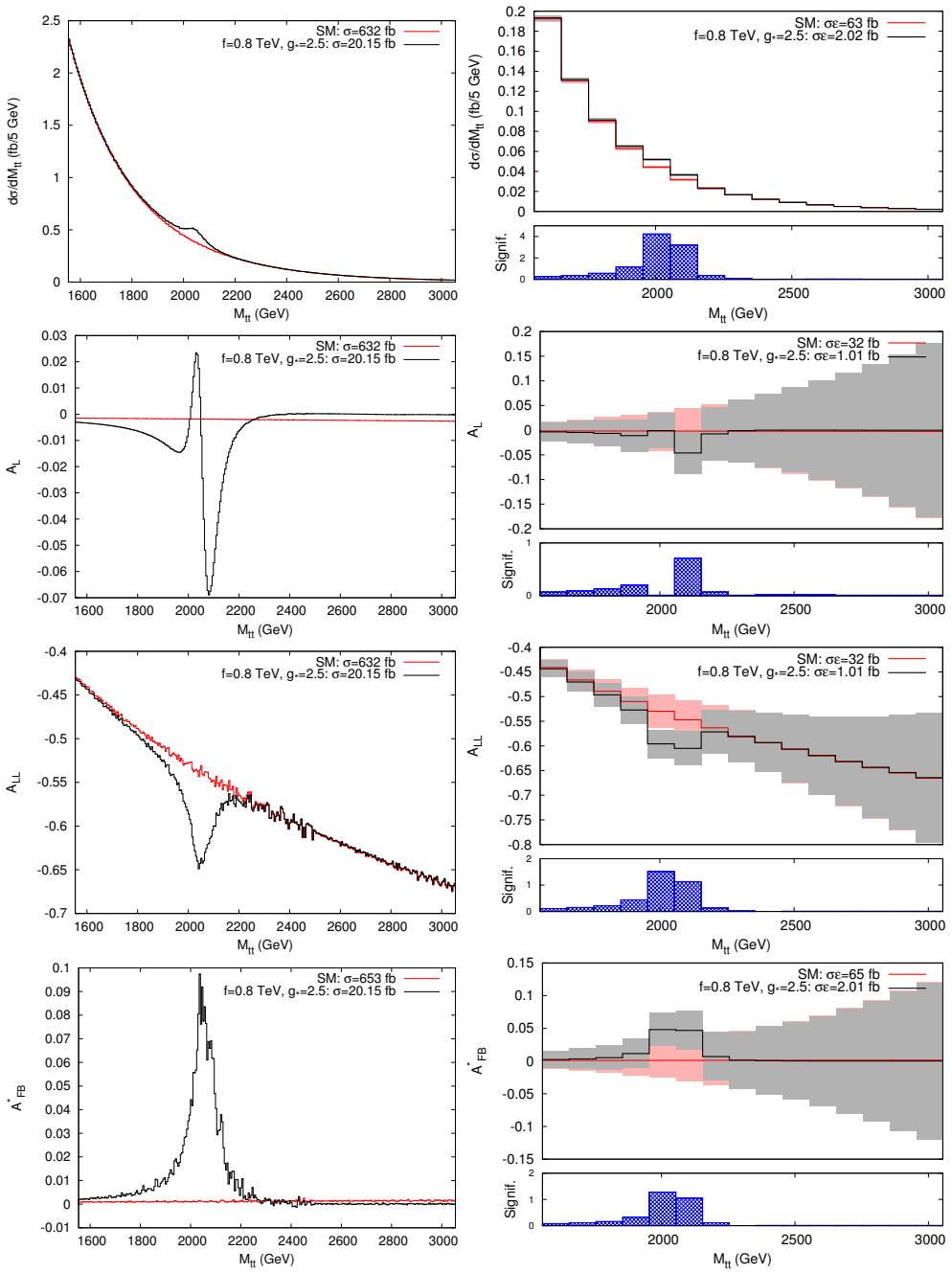

Figure 6.5: Cross section and asymmetries as a function of the $t\bar{t}$ invariant mass for the f =0.8 TeV, g_* =2.5 benchmark at the 14 TeV LHC with 300 fb^{-1}. The left column shows the fully differential observable. Right plots (*upper frames*) include estimates of statistical uncertainty assuming a realistic 100 GeV mass resolution and also display (*lower frames*) the theoretical significance assuming a 10(5)% reconstruction efficiency for the cross section and A^*_{FB} (A_{LL} and A_L). Grey(Pink) shading represents the (statistical) error on the 4DCHM(SM) rates, in black(red) solid lines. Masses and widths of the gauge bosons are $M[\Gamma]_{Z_2,Z_3} = 2048[61]$ GeV, $2068[98]$ GeV.

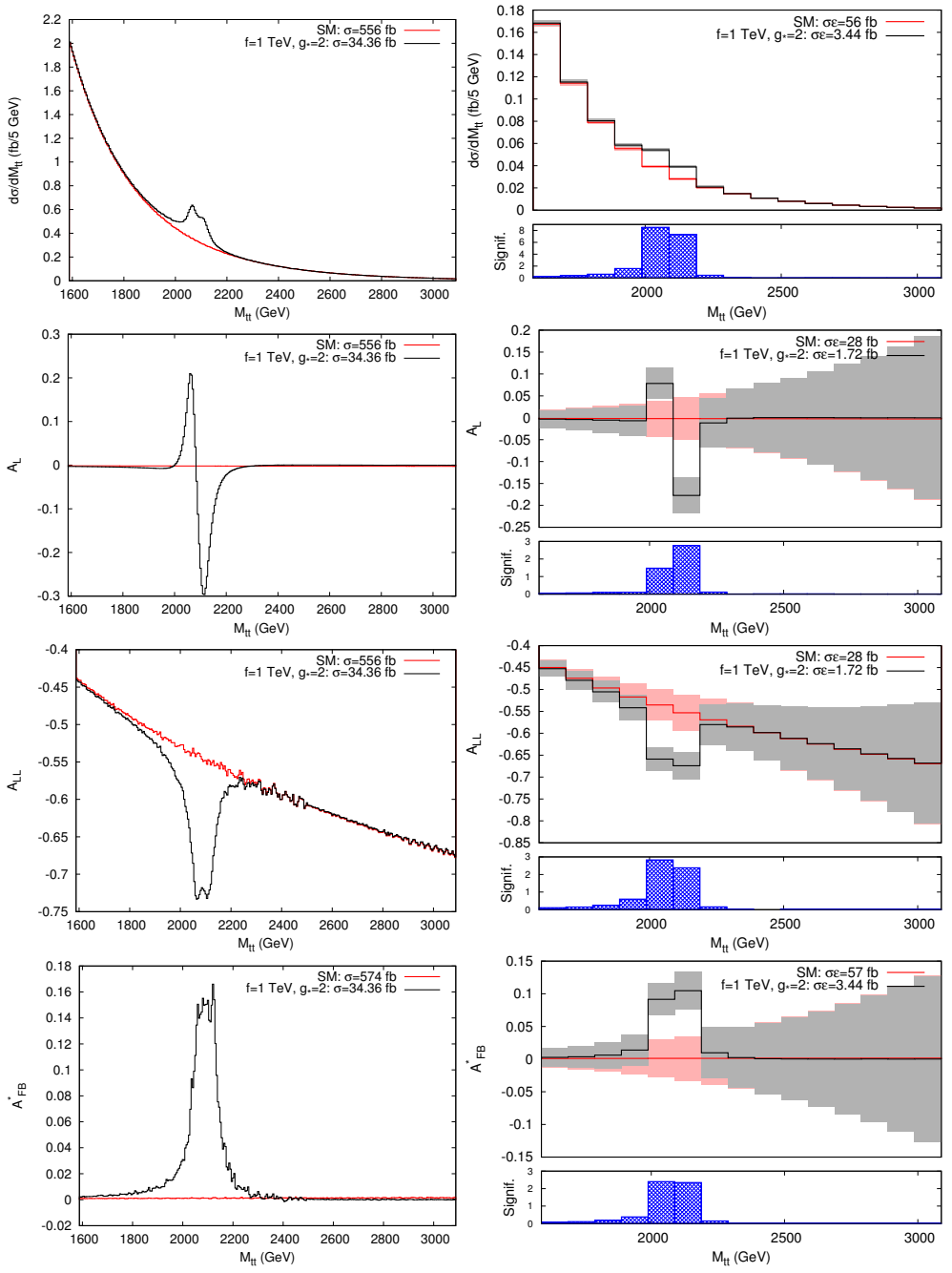

Figure 6.6: Cross section and asymmetries as a function of the $t\bar{t}$ invariant mass for the $f = 1$ TeV, $g_* = 2$ benchmark at the 14 TeV LHC with 300 fb^{-1}. The left column shows the fully differential observable. Right plots (*upper frames*) include estimates of statistical uncertainty assuming a realistic 100 GeV mass resolution and also display (*lower frames*) the theoretical significance assuming a 10(5)% reconstruction efficiency for the cross section and A^*_{FB} (A_{LL} and A_L). Grey(Pink) shading represents the (statistical) error on the 4DCHM(SM) rates, in black(red) solid lines. Masses and widths of the gauge bosons are $M[\Gamma]_{Z_2,Z_3} = 2066[39]$ GeV, $2111[52]$ GeV.

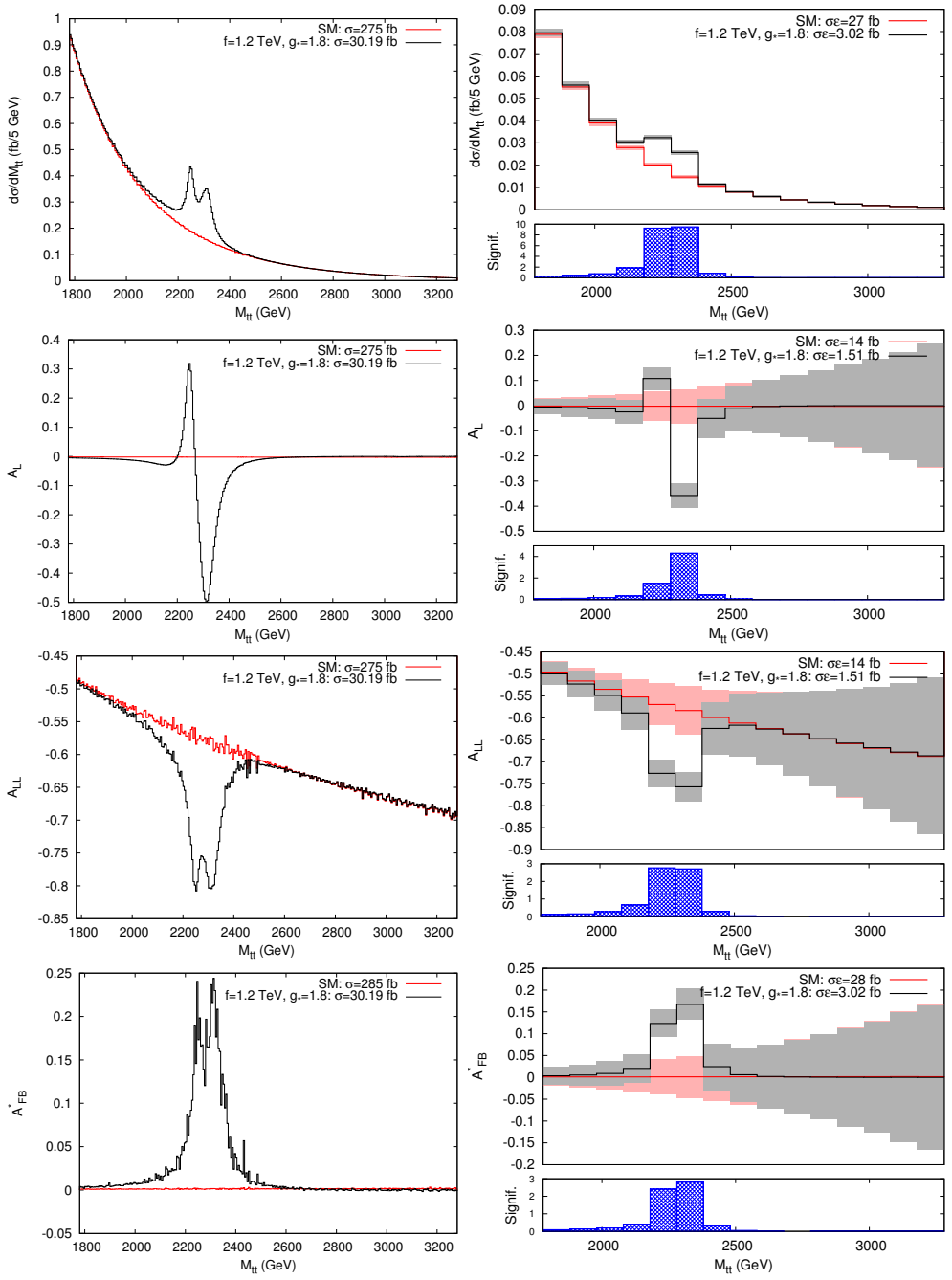

Figure 6.7: Cross section and asymmetries as a function of the $t\bar{t}$ invariant mass for the f =1.2 TeV, g_* =1.8 benchmark at the 14 TeV LHC with 300 fb^{-1}. The left column shows the fully differential observable. Right plots (*upper frames*) include estimates of statistical uncertainty assuming a realistic 100 GeV mass resolution and also display (*lower frames*) the theoretical significance assuming a 10(5)% reconstruction efficiency for the cross section and A^*_{FB} (A_{LL} and A_L). Grey(Pink) shading represents the (statistical) error on the 4DCHM(SM) rates, in black(red) solid lines. Masses and widths of the gauge bosons are $M[\Gamma]_{Z_2,Z_3} = 2249[32]$ GeV, $2312[55]$ GeV.

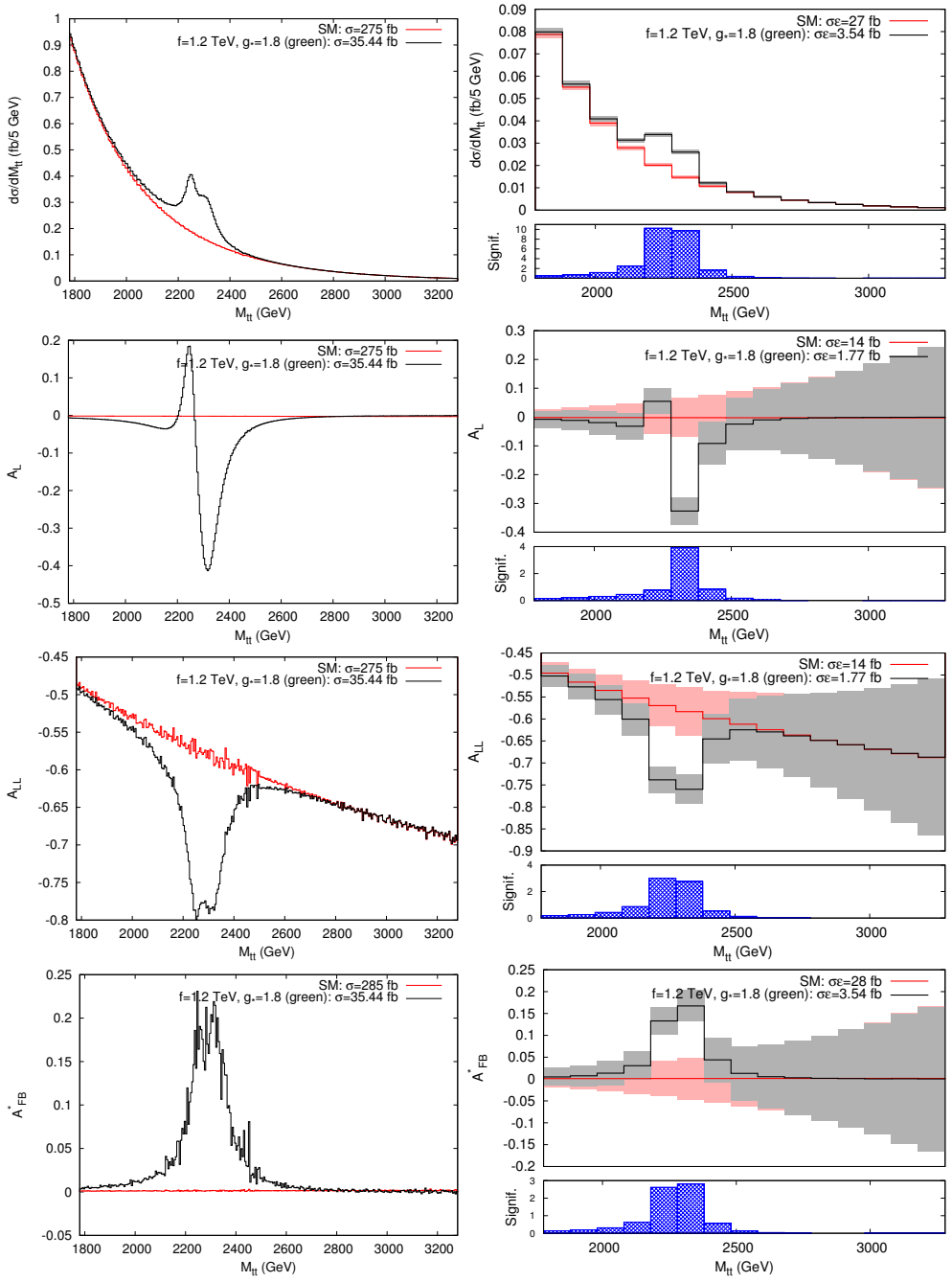

Figure 6.8: Cross section and asymmetries as a function of the $t\bar{t}$ invariant mass for the f =1.2 TeV, g_* =1.8 (green) benchmark at the 14 TeV LHC with 300 fb^{-1}. The left column shows the fully differential observable. Right plots (*upper frames*) include estimates of statistical uncertainty assuming a realistic 100 GeV mass resolution and also display (*lower frames*) the theoretical significance assuming a 10(5)% reconstruction efficiency for the cross section and A^*_{FB} (A_{LL} and A_L). Grey(Pink) shading represents the (statistical) error on the 4DCHM(SM) rates, in black(red) solid lines. Masses and widths of the gauge bosons are $M[\Gamma]_{Z_2,Z_3} = 2249[48]$ GeV, $2312[86]$ GeV.

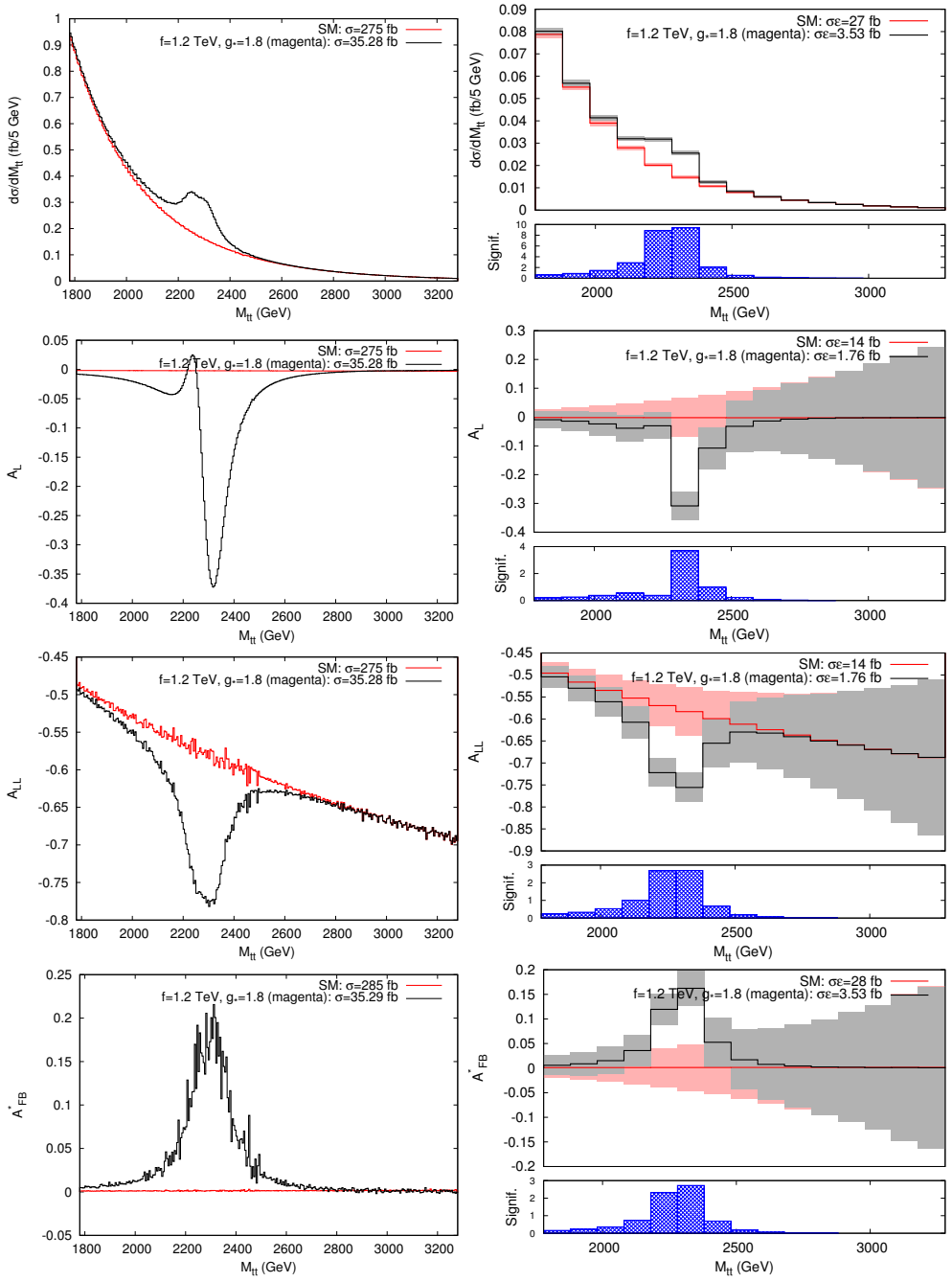

Figure 6.9: Cross section and asymmetries as a function of the $t\bar{t}$ invariant mass for the f =1.2 TeV, g_* =1.8 (magenta) benchmark at the 14 TeV LHC with 300 fb^{-1}. The left column shows the fully differential observable. Right plots (*upper frames*) include estimates of statistical uncertainty assuming a realistic 100 GeV mass resolution and also display (*lower frames*) the theoretical significance assuming a 10(5)% reconstruction efficiency for the cross section and A^*_{FB} (A_{LL} and A_L). Grey(Pink) shading represents the (statistical) error on the 4DCHM(SM) rates, in black(red) solid lines. Masses and widths of the gauge bosons are $M[\Gamma]_{Z_2,Z_3} = 2249[75]$ GeV, $2312[104]$ GeV.

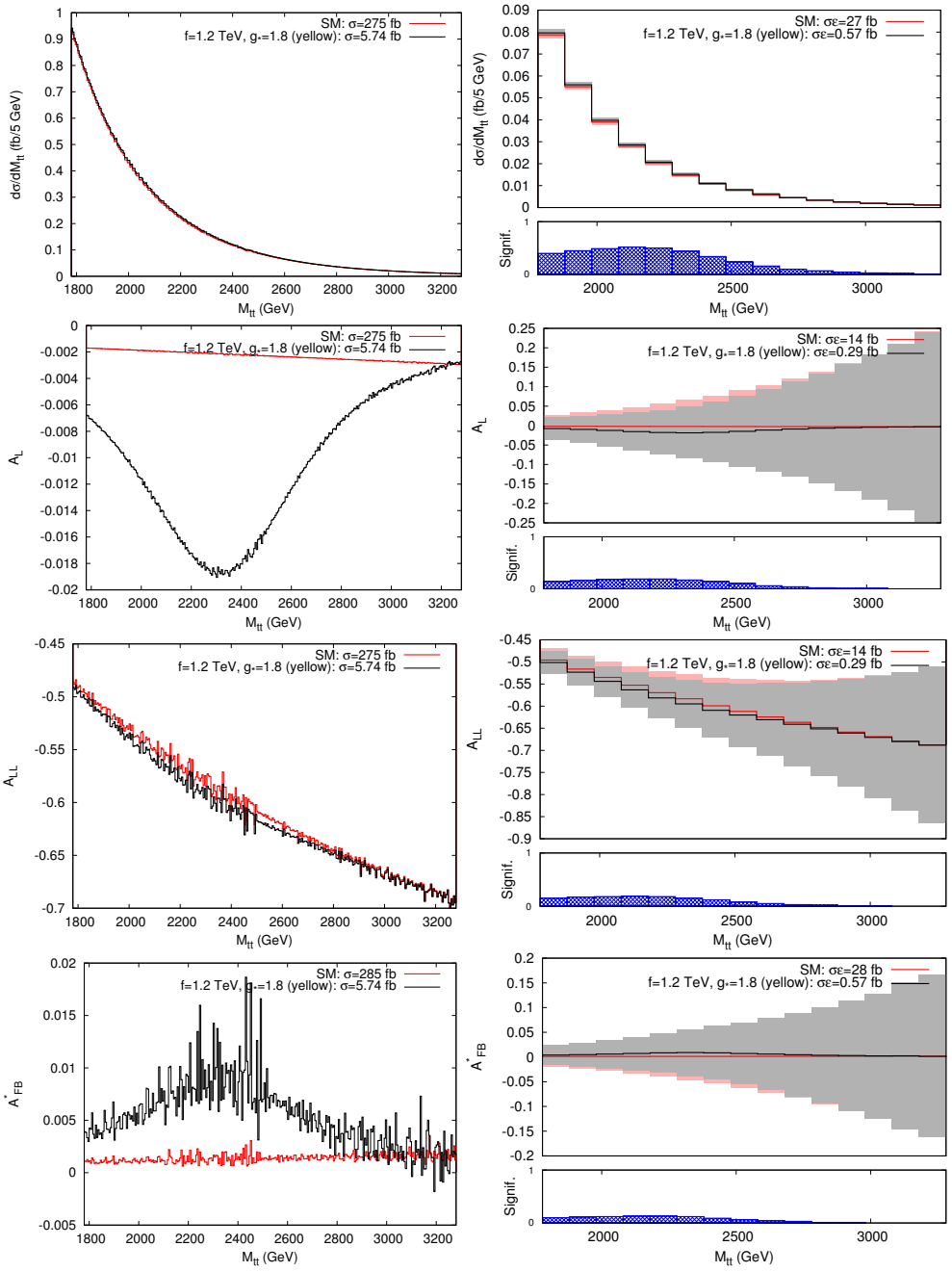

Figure 6.10: Cross section and asymmetries as a function of the $t\bar{t}$ invariant mass for the f =1.2 TeV, g_* =1.8 (yellow) benchmark at the 14 TeV LHC with 300 fb^{-1}. The left column shows the fully differential observable. Right plots (*upper frames*) include estimates of statistical uncertainty assuming a realistic 100 GeV mass resolution and also display (lower frames) the theoretical significance assuming a 10(5)% reconstruction efficiency for the cross section and A^*_{FB} (A_{LL} and A_L). Grey(Pink) shading represents the (statistical) error on the 4DCHM(SM) rates, in black(red) solid lines. Masses and widths of the gauge bosons are $M[\Gamma]_{Z_2,Z_3} = 2249[1099]$ GeV, $2312[822]$ GeV.

Chapter 7

Uncovering multiple Z's in a model of extra dimensions

The last chapter considers a model that was more amenable to $t\bar{t}$ searches in that it has an enhanced coupling to third generation quarks which particularly motivates this channel over the traditional di-lepton one. All of the other previously considered resonances had large leptonic signals with which $t\bar{t}$ could rarely compete due to the poor reconstruction efficiencies but rather complement in providing spin asymmetry observables. A new, interesting aspect of these observables was revealed in the last chapter regarding multiple resonances. It was shown that the polarisation asymmetry, A_L, elucidated the presence of two nearby resonances which could not be resolved in the other observables (see Figure 6.6, for example) when the chiral couplings of the two objects were different enough. Specifically the two resonances, having predominantly left- and right-handed couplings, respectively, preferred opposite sign A_L values which, given the fact that the QCD prediction is zero, made for a striking signal. As the width of the resonances increased, the two contributions began to overlap and actually cancel. This chapter is based on the observations that such behaviour cannot be reproduced by models of single resonances thereby providing a possible way to unambiguously identify multiply resonant new physics using asymmetries. In the minimal scenario of Z' couplings outlined in Section 3.1.3, the coupling dependences of the charge and spin polarisation asymmetries of Equations 3.25 and 3.26 imply that a single resonance should not be able to generate A_{FB} without also having a signal in A_L . The model studied in the previous chapter appears to demonstrate how this may be possible with more than one Z'.

In this final chapter, the correlation between the two asymmetries in $t\bar{t}$ will be exploited to identify the presence of quasi-degenerate states in a resonant signal at the LHC. As an example, a model where the SM EW sector is allowed to propagate in large extra dimensions of TeV^{-1} size while the colour sector is localised will be considered. It will be shown that, assuming current experimental constraints from the 7 and 8 TeV

runs and taking into account the estimated top (anti-top) reconstruction efficiencies, the 14 TeV upgraded LHC with the planned integrated luminosity $L = 100$ fb^{-1} could access these quasi-degenerate multiple resonances and explore for the first time the rich phenomenology in the asymmetry observables. The main outcome would be to have measurable quantities, complementary to the usual total and differential cross sections, capable of distinguishing a quasi-degenerate, multiply resonant spectrum from a "standard" single resonance that could present a similar signal in a "bump hunt". This would be useful if the degeneracy is more severe than the mass resolution of the search channel, in this case the di-jet or $t\bar{t}$ channels.

The existence of large extra dimensions compactified in the TeV range [63], for which the fundamental string or quantum gravity scale is in turn rather low [62, 135, 136, 137, 138], is a scenario that is often easily testable at the LHC. The consequences of this in the context of additional gauge bosons were introduced in Section 3.1, where allowing a gauge sector to propagate in the bulk led to an infinite tower of KK resonances with masses occurring in multiples of the compactification scale, R^{-1}. If the gauge symmetry is also spontaneously broken, the KK gauge bosons will receive an additional mass contribution analogously to EWSB in the SM. Further, if one dismisses the traditional assumption that all SM gauge bosons propagate in the same compact space [139, 140, 141] and instead allows for the more general case whereby the SM gauge structure arises from branes extended in different compact directions, one realises a scenario that provides an ideal testbed for the purposes of this study. A general setup in which (quasi-)degenerate resonances are likely to occur is in such models of extra dimensions with relatively large compactification scales. Most generally, since the tree-level KK masses of the gauge bosons are integer multiples[1] of R^{-1}, one may expect that the KK EW gauge sector of such a theory would be near-degenerate since $R^{-1} >> g(g')v$ where $g(g')$ and v denote the $SU(2)_L(U(1)_Y)$ gauge couplings and the SM Higgs VEV, respectively. Later on, the fact that particles propagating in the bulk in such models generically incur loop-induced mass splittings that can be important, particularly at high compactification scales, will be discussed. Allowing the gauge sector to propagate in the bulk typically results in strong limits on this scale coming from lower mass bounds on KK excitations from resonance searches or EWPTs depending on the specific localisation of different parts of the particle spectrum. The consequences of more complex localisations will be expanded upon in the next section.

Within this construct, a realisation which complies with current stringent bounds from di-jet and $t\bar{t}$ events emerging after the 7 and 8 TeV runs is identified which remains accessible at the 14 TeV stage. This is the one where only the EW gauge bosons can appear as KK excitations, but not the gluons. In addition, one can localise fermions

[1] This is true for the case of one extra dimension of compactification radius R, but depends on the specific compactification volume in the case of more than one extra dimension, although the compactification scales still remain the only parameters that define the approximate scale of the KK masses. The case of one flat extra dimension is assumed here for simplicity.

between the bulk and our brane in such a way that the production of leptonic final states is depleted with respect to that of both light and heavy quarks, given that the latter are notoriously less accessible than the former in the LHC environment. Since the sensitivity of LHC data is maximal to either processes induced by QCD effects (as opposed to those due to EW interactions) or to very clean final states involving only leptons (as opposed to both light and heavy quarks), one is not confronted with the very stringent bounds that would emerge if gluons (necessarily yielding di-jet and $t\bar{t}$ final states) propagated in the large extra dimensions or EW gauge bosons propagating therein could decay in leptons. Therefore, the investigation of the effects of the extra dimensional propagation of the EW gauge bosons yielding both light and heavy quarks in the final state remains viable also in the light of the most recent data.

It is the purpose of this chapter to investigate the case of the neutral EW gauge bosons, i.e., the $U(1)_Y$ and $SU(2)_L$ states of the SM, γ and Z, and their KK excitations (or admixtures thereof), henceforth denoted as $\tilde{\gamma}'$ and $\tilde{Z}'$, respectively, produced from quark-antiquark scattering at the LHC and yielding $t\bar{t}$ pairs in the final state. After accounting for existing lower bounds on the compactification scale from direct searches in di-jet and $t\bar{t}$ data samples generated at 7 and 8 TeV, it will be shown that one will be able to observe at least the first excitation of the EW states at the 14 TeV stage in $t\bar{t}$ final states. Further, while the extraction of information on the additional excitations would be desirable to disentangle the extra dimensional model from alternative new physics scenarios, the ability of defining both charge and spin asymmetries in $t\bar{t}$ final states (unlike the case of di-jets) can potentially disentangle the two states (despite these appearing degenerate and unresolvable in the invariant mass distribution), consequently distinguishing this BSM scenario from those involving individual resonances.

The plan of the chapter is as follows. The next section expands on the KK expansion in the context of a more general SM-like theory, with particular attention paid to the embedding of chiral fermions. Section 7.2 describes the model that is used as an example in more detail, discussing the effects of radiative mass corrections arising from the compactification procedure on the couplings of new resonances and finally establishing a scenario that lies outside of current LHC limits. In Section 7.3, the observables studied are summarised, largely by reference to previous chapters and the findings presented. Finally, Section 7.4 presents the conclusions.

7.1 Populating the bulk

The mechanism of KK decomposition described in Section 3.1 is readily generalised to the case of non-Abelian groups and a more complex gauge structure such as that of the SM. The model which considers the full SM to exist in the bulk is known as Universal Extra Dimensions (UED) [142] and has some interesting features related to obtaining

chiral matter in higher dimensions. This section gives a brief overview of how one could promote a general theory to higher dimensions.

One of the subtleties that exists is that, in the non-Abelian case, the gauge invariance of the theory is no longer manifest at each KK level. Performing a gauge transformation as in Section 1.7 on a 5D Abelian gauge field and expanding the gauge transformation parameter in a Fourier series, one can see that each KK level respects an analogous transformation rule:

$$\begin{aligned} A'_M(x,y) &= A_M(x,y) - \frac{1}{g}\partial_M \alpha(x,y), \\ &= \sum_n \left[A_M^{(n)}(x) e^{i\frac{ny}{R}} + h.c.\right] - \sum_n \left[\frac{1}{g}\partial_M \alpha^{(n)}(x) e^{i\frac{ny}{R}} + h.c.\right], \\ &= \sum_n A_M^{(n)\prime}(x) e^{i\frac{ny}{R}}. \end{aligned} \tag{7.1}$$

However, given the more complex transformation property in a non-Abelian theory as in Equation 1.11, the additional term in the transformation will mix different KK levels in a non trivial way. The notions of gauge invariance in a non-Abelian theory are complex and well beyond the scope of this phenomenological analysis of an extra dimensional model and will therefore not be discussed further.

Assuming that the SM gauge structure can be extended into the bulk in a similar way to Section 3.1, the gauge bosons should each receive a tower of KK partners with increasing mass related to the compactification scale. While the case of a scalar particle is even simpler than a vector boson, some subtleties exist in formulating theories with chiral matter embedded into higher dimensions. Again, using five dimensions as an example, a basis of gamma matrices is required that satisfies a 5D version of the Clifford algebra in Equation 1.3. This can be simply provided by:

$$\begin{aligned} \Gamma^M &= (\gamma^\mu, -i\gamma^5), \\ \left\{\Gamma^M, \Gamma^N\right\} &= -2g^{MN}. \end{aligned} \tag{7.2}$$

A 5D Dirac equation can then be written down as a direct generalisation of Equation 1.1:

$$\mathcal{L}_5 = \bar{\Psi}(i\partial_M \Gamma^M - m)\Psi. \tag{7.3}$$

Here, Ψ must be a Dirac fermion since the 4-spinor is the lowest dimension irreducible representation of the 5D Lorentz group. The ∂_5 operator yields a KK mass component upon KK decomposition, as in the vector boson case, leading to a zero mode of mass m and a tower of KK modes with masses $m_n^2 = m^2 + n^2/R^2$. The problem lies in the fact that the zero mode, which should eventually represent a SM field, is a Dirac spinor while the fundamental matter representations used in the SM are 2 component Weyl spinors because of its chiral nature. Heuristically, another way of looking at this is that in an even number of spatial dimensions, a parity transformation is equivalent to a rotation.

This means that a 5D Lorentz transformation on a Dirac spinor can transform elements of its left- and right-handed Weyl components into one another such that parity is not a good discrete symmetry of the action.

7.1.1 Orbifold compactification

The solution to this problem is to modify the compactified space by introduction so-called "orbifold" boundary conditions. In addition to the periodicity conditions imposed by the circular geometry, a further identification is made between opposite points on the circle, $y = -y$, reducing the space into a line segment of length πR. This can be represented technically as changing the geometry to the quotient space: $S_1 \to S_1/\mathbb{Z}_2$. $\mathbb{Z}_2$ represents the parity transformation $y \to -y$ under which the action should still be symmetric although translational symmetry around the circle has now been globally broken.

A consequence of this procedure is the introduction of "fixed points" on the orbifold which map to themselves under the $\mathbb{Z}_2$ flip. These would be the end points of the line segment. The behaviour of these fields at these boundaries must therefore be defined which subsequently characterises their transformation properties under the y-parity. Depending on the choice of Dirichlet or Neumann boundary conditions, the fields get assigned positive or negative parity $\phi(x, -y) = \pm\phi(x, y)$, respectively for scalar or vector fields. With spinors, the simplest realisation of the $\mathbb{Z}_2$ action which admits an invariant 5D kinetic term is $\psi(x, -y) = \pm\gamma^5\psi(x, y)$. In the Weyl basis, this dictates that the left- and right-handed components of this field, as defined by the projection operators P_L and P_R introduced in Section 1.5, transform oppositely or each have one of the types of boundary conditions. Another condition imposed by gauge kinetic terms is that the A_μ and A_5 components defined in Section 3.1 must have opposite parity.

The choice of parity eigenvalue is then reflected in the Fourier components of the decomposed field. It is more transparent to decompose the field in the trigonometric basis functions as they are eigenfunctions of the parity transformation. A generic field will therefore look like:

$$\Phi(x, y) = \phi^0(x) + \sum_n \phi^{(n)} \cos\left(\frac{ny}{R}\right) + \tilde{\phi}^{(n)} \sin\left(\frac{ny}{R}\right). \tag{7.4}$$

It is clear from the boundary conditions that fields with positive parity will have zero modes while those with negative parities will not and that a different component of the KK modes will be selected depending on the parity assignment. Denoting fields with

parity eigenvalue $P = \pm$ as $\Phi_\pm$,

$$\begin{aligned}\Phi_+(x,y) &= \phi^0(x) + \sum_n \phi_+^{(n)} \cos\left(\frac{ny}{R}\right), \\ \Phi_-(x,y) &= \sum_n \tilde{\phi}_-^{(n)} \sin\left(\frac{ny}{R}\right),\end{aligned} \tag{7.5}$$

one sees that the orbifold boundary conditions have "projected out" half of the degrees of freedom. In particular, one of either the gauge field or its scalar fifth component will not have a zero mode. The previously complex scalar field of Section 3.1 has now become real. In order to obtain chiral matter, two fields $\Psi_\pm$ are introduced with opposite transformations under the $\mathbb{Z}_2$. Again, half of their states will be projected out, but the chirality of the zero mode will depend on the choice of eigenvalue, $\pm\gamma^5$:

$$\begin{aligned}\Psi_+(x,y) &= P_R\Psi_+^0(x) + \sum_n P_R\psi_+^{(n)} \cos\left(\frac{ny}{R}\right) + P_L\chi_+^{(n)} \sin\left(\frac{ny}{R}\right), \\ \Psi_-(x,y) &= P_L\Psi_-^0(x) + \sum_n P_L\psi_-^{(n)} \cos\left(\frac{ny}{R}\right) + P_R\chi_-^{(n)} \sin\left(\frac{ny}{R}\right).\end{aligned} \tag{7.6}$$

A 5D theory with chiral zero mode fermions can therefore be obtained, with the price of introducing a vector-like pair of fermions at each KK level.

7.1.2 KK parity

The idea of KK number conservation was touched upon in Section 3.1, being the remnant $U(1)$ symmetry upon compactification associated to momentum conservation in the fifth direction. This dictates that any interaction between particles in the decomposed theory must respect $\sum_i n_i = 0$, where n_i is the KK number of each field. For example, it would constrain KK particles to always be pair produced from a SM zero mode. It was mentioned, however, that the orbifold boundary conditions globally break translational symmetry around the extra direction. This is tantamount to a violation of momentum and thus KK number conservation. This can be seen imagining a particle were travelling through a boundary of the segment, upon which it would appear to discontinuously change its momentum and be facing in the opposite direction.

The symmetry that does remain is a new parity about the midpoint of the line segment. It is related to the fact that, in this geometry, momentum conservation can only be violated in a specific way and can be expressed as a conservation of KK parity, defined as $(-1)^n$, such that KK number can only be violated in units of two. Although the KK number violating interactions are not present at tree-level, that fact that this is no longer a good symmetry of the theory implies that they can be generated radiatively. A classic example of this would be the coupling of a second level KK particle to a pair of SM zero modes that is induced at one-loop level. Another interesting implication of

this symmetry is that the lightest KK particle is now stable and represents a possible dark matter candidate.

7.1.3 Localising fields

Given that a model can be extended into a certain number of extra spatial dimensions, one may also want to restrict certain sectors to not "feel" the extra dimensions. The most well known example of this is in the Arkani-Hamed–Dvali–Dimopoulos (ADD) model of extra dimensions [62, 63] where linearised gravity is generalised to five dimensions, akin to the original KK theory, and coupled to the SM localised on a 3-brane in the bulk. Most generally the action of a theory can be written in terms of bulk and localised sectors:

$$S_5 = \int d^4x dy \, \mathcal{L}_{\text{bulk}} + \delta(y) \left(\mathcal{L}_{\text{brane}} + \mathcal{L}_{\text{int}} \right), \tag{7.7}$$

where the "int" term specifies interactions between the bulk and localised fields. In the case of ADD, the Einstein-Hilbert action is used and reduces to a KK theory with massive gravitons (and additional vectors and scalars for more than 5 dimensions) couplings to the energy momentum tensor of the SM on the brane. The coupling constant of gravity, however, is reduced by a volume factor, as discussed in Section 3.1, related to the number and geometry of the compact space, thereby providing a potential bridge between the TeV and Planck scales via the extra dimensional volume [143].

Although gravity is not the focus of this work, the same principle can be generalised to localise different sectors present in a model. The main consequences of this localisation is that the presence of a brane explicitly violates the translational invariance in the extra direction. This means that interactions with the localised sector will no longer conserve KK number and therefore the existence of KK parity is also no longer an issue outside of interactions contained within the bulk sector. That is to say, in the action of Equation 7.7, KK parity conservation will only apply within interactions described by $\mathcal{L}_{\text{bulk}}$ while the explicit brane-bulk interactions contained in $\mathcal{L}_{\text{int}}$ will be universal across KK levels. Having a localised sector therefore generally removes the dark matter candidate present in the UED case. One final consequence of having interactions with a localised sector is that the volume normalisation factor occurring from the integral over the compact space, discussed in Section 3.1, implies that the KK modes couple more strongly to the localised sector than the zero modes do. For gauge interactions with localised fermions, the factor is $\sqrt{2}$ since only one gauge field is present in the vertex.

7.2 The Model

A large amount of theoretical and phenomenological literature exists on models which place the whole SM particle content [142] or sometimes only its gauge sector [140, 141] in the bulk. The main difference between the two being the delocalisation of fermions which requires an orbifold compactification, described in Section 7.1.1, in order to obtain chiral states. These can be seen as extensions of the ADD scenario. The framework for a model where a selection of the SM gauge structure is allowed to propagate in the bulk is motivated in [144] and represents a mixture of the two pictures. Given the choice of localising any combination of the gauge groups and matter representations, a number of combinations are possible. The study lends itself to the (t, l, l) realisation of [144] (henceforth AADD), where t, l denote "transverse" and "longitudinal" and refer to the orientation of the $(SU(3)_C,\ SU(2)_L,\ U(1)_Y)$ gauge groups with respect to the extra dimension. This implies that the colour sector is localised while the EW one propagates in the bulk, gaining KK excitations.

In order to realise a model with scales accessible at the LHC, the leptonic sector is also allowed to propagate in the bulk. The orbifold compactification necessary to accommodate fermions in the bulk preserves KK-parity, suppressing the interactions of the EW KK resonances with the SM leptonic sector. This is because, as explained in Section 7.1.2, the KK number violating interactions that would allow a vertex between a KK $\tilde{Z}'$ and a pair of SM leptons is generated radiatively. Moreover, the interaction is only present from the second KK level and even levels thereon thanks to KK parity. This simultaneously removes the traditional di-lepton channel from searches for such resonances and (multi-TeV) limits via the constraints from EWPTs [145, 146] that typically arise from a fully localised fermion sector. In addition, having kept the quark sector localised along with the gluons leads to an enhancement of the couplings of the KK resonances to quarks relative to its SM zero-modes as explained in Section 7.1.3. Ultimately, the model is one in which EW gauge bosons have KK excitations, $\tilde{\gamma}'$ and $\tilde{Z}'$, couplings universally to the quark sector with an enhancement of $\sqrt{2}$ to their SM gauge quantum numbers and with loop-suppressed couplings to the lepton sector which are neglected here. As far as their interactions with quarks are concerned, these particles are heavy copies of their SM counterparts. It is assumed that EWSB takes place in the bulk[2] but that these contributions are small compared to the compactification radius as discussed in the introduction. The assumption of quasi-degeneracy will be elaborated on in the next section. The tree-level widths of the resonances are therefore used assuming only contributions from quarks with a small ($\sim 3\%$) k-factor to account for NLO QCD contributions.

[2]The general case of bulk and localised scalars breaking a gauge symmetry in the bulk is discussed in [145], showing that a localised scalar induces mixing between the gauge bosons KK levels while the bulk scalar lead to KK-diagonal EW mass terms.

This specific realisation of an extra dimensional model will be used, compatible with current LHC limits, as an example of the scenario in which asymmetries can be used to deduce the presence of quasi-degenerate resonances beyond the mass resolution of the search channel. In this case, although the di-jet channel represents a more sensitive mode with respect to the signal as shown in Section 7.2.3, the asymmetries of $t\bar{t}$ turn out to be essential in identifying the presence of more than one particle. In any case, one would not expect the mass resolutions of both channels to differ greatly at such high p_T and, further, the large uncertainties associated to jet energy scale are likely to further compromise the ability to resolve nearby peaks in both invariant mass spectra.

7.2.1 Radiative mass corrections and mixing

A typical feature of "universal" type models of extra dimensions, where some of the SM matter content is allowed to exist in the bulk, is that KK excitations receive radiative mass corrections beyond those that occur in a 4D realisation. Considering one extra dimension for simplicity, these corrections originate from the violation of 5D space-time symmetries caused by the compactification of the extra direction [147]. 5D loop contributions which do not break these symmetries will simply contribute to the field strength renormalisation of the 5D fields. Specifically, a circle compactification violates Lorentz invariance at long distances and can accommodate loop contributions with non-zero winding number around the extra dimensional space and yield universal, finite corrections to the two point function proportional to $\frac{1}{R^2}$ and independent of KK number. Furthermore, the orbifold projection induces yet more contributions arising from the orbifold fixed points which violate translational invariance. Therefore, loop diagrams where a particle encounters such a boundary and flips its 5D momentum will also induce logarithmic corrections proportional to the KK mass $\frac{n}{R}$. The two types of corrections are termed "bulk" and "orbifold" respectively and contribute only to the 5th component of the field strength renormalisation factor which, upon KK decomposition of the action, corresponds to a mass correction to the 4D KK modes.

Consequently, the assumption that the gauge boson excitations at each KK level will essentially be degenerate with a mass of $\frac{n}{R}$ is not necessarily a good one, depending on the particular realisation of the model. The indirect importance of such mass splittings lies in the subsequent modification of the mixing between the neutral gauge bosons $\tilde{\gamma}'$ and $\tilde{Z}'$ which will, in turn, affect the exact coupling structure of the mass eigenstates. While at leading order, one can assume that the mixing between the hypercharge and T_3 gauge bosons, B' and W_3', will proceed identically to the SM with EWSB ($\theta = \theta_W$, where θ is the mass mixing angle between the resonances in AADD and θ_W is the Weinberg angle), mass splittings will drive the mixing back towards the pure gauge states. This would invalidate the assumption that such resonances will couple like "copies" of the SM γ and Z stated in [144]. The mass matrices of the neutral sector are schematically

shown for a generic KK level:

$$M_{\text{tree}} \sim v^2 \begin{pmatrix} g^2 & gg' \\ gg' & g'^2 \end{pmatrix} + \begin{pmatrix} M_{KK}^2 & 0 \\ 0 & M_{KK}^2 \end{pmatrix}, \tag{7.8}$$

$$\Rightarrow \theta = \theta_W,$$

$$M_{\text{rad}} \sim M_{\text{tree}} + \begin{pmatrix} \delta M_{W_3'}^2 & 0 \\ 0 & \delta M_{B'}^2 \end{pmatrix}, \tag{7.9}$$

$$\Rightarrow \theta \to 0, \quad \text{as} \quad |\Delta M^2| \gg g^2(g'^2)v^2.$$

Here, the mass matrices are shown at tree-level (tree) and including the radiative corrections (rad) from compactification and localised quarks. M_{KK} represents the KK mass contributions $\sim n/R$ and $|\Delta M^2|$ is the mass splitting incurred from the two radiative contributions, $|\delta M_{W_3'}^2 - \delta M_{B'}^2|$. One can see that the mixing will deviate from the EW angle once the splitting becomes comparable to the EW mass contributions, which can certainly be the case for large compactification scales. That said, in this case, the gauge bosons of interest do not interact strongly, which ensures that the splitting effects will not be too large.

For the UED realisation addressed in [147], the aforementioned corrections to the neutral gauge sector masses result in a mass splitting of about 6% of the compactification scale, R. The case of AADD closely resembles UED with regards to the EW sector, the only difference being that the localisation of quarks makes them couple universally to all KK modes. Thus the mass corrections to each KK level will resemble those of UED with the 5D quark contribution removed and replaced by a normal 4D SM vacuum polarisation with enhanced couplings. As shown in [147], fermions do not contribute to the gauge boson masses via orbifold corrections which are dominant over the bulk corrections for all KK levels, particularly with increasing R^{-1} meaning that localising quarks should not have a big effect on the mass splitting. One would also expect an additional negative logarithmic contribution from these localised fermions to each gauge boson proportional to $g'^2 \sum_q Y_q$ and $g^2 \sum_q T(f)$ respectively, where Y denote hypercharge and $T(f)$ denotes the trace of the generators $\text{Tr}[t_A t_B]$ in the fundamental representation of $SU(2)$. It was calculated that the corrections are small compared to those arising from the bulk particle content and decrease the mass splitting by about 1% (see Appendix C). It is fair to say that this keeps the model within the quasi-degenerate regime since the mass resolutions of the $t\bar{t}$ or di-jet channels are not expected to be much better than 5%. The splitting is, however, large enough to significantly affect the mixing structure of the KK EW gauge boson couplings.

Ultimately, in the context of using asymmetries to probe observed resonances in the $t\bar{t}$ spectrum, it is evident that having too large mass splittings will first and foremost reduce the problem to a study of multiple single resonances as opposed to a quasi-degenerate spectrum. Therefore, the regime to be considered is where the mass splitting

could be large enough to induce non SM-like mixings (and therefore couplings) while maintaining a quasi-degeneracy in the first KK level so that the $t\bar{t}$ mass resolution does not permit one to fully resolve the two resonances in the cross section. This is chiefly because this study intends to highlight the possibility of using differential asymmetry observables to distinguish such a case from a single resonance in a way that is not possible using a differential cross section analysis. In models with a large enough mass splitting, regular resonance search methods will be sufficient to recognise the presence of two new bosons while, if not, an analysis of asymmetries will do so. A number of results for the illustrative limit of fully degenerate resonances as a "worst case scenario" are presented while also including some observables for the spectrum with radiative corrections.

7.2.2 Off-diagonal widths

An important point to make is that, while mass splittings will affect the mixing of the KK resonances, in the exactly degenerate limit, the mixing angle, θ, should not be a physical parameter around the resonance peak. This is clear since the mixing of two degenerate states simply amounts to a redistribution of couplings which can only yield differences in widths coming from (small) top mass effects. With this principle in mind, it was found to be extremely important to include off-diagonal widths in order to prevent artificial effects arising as a function of the mixing angle. When multiple resonances have common decay channels and a mass splitting comparable to their intrinsic decay widths, it may occur that imaginary parts of one-loop diagrams mixes the two states via their width [148]. In this case, the propagators must be treated as a matrix with the off-diagonal components from these loops potentially altering their resonant structure. The size of these effects is maximised in the degenerate limit and it will be shown later that including these effectively removes the mixing angle as a physical parameter up to (small) interference effects with the SM and higher KK gauge bosons. In order to highlight these points, the phenomenology of the neutral KK resonances is investigated in both extreme cases: SM-like couplings γ' and Z' ($\theta = \theta_W$) and maximally "unmixed" gauge states W_3' and B' (θ =0), which turn out to show large differences in the asymmetry observables when not including the off-diagonal effects. Since the unmixed limit corresponds in a sense to the restoration of the EW gauge symmetry, one would expect the off-diagonal effects to vanish in this limit. As such, the phenomenology of the unmixed case corresponds to the "true" observable while artefacts from not including off-diagonal effects will arise once the mixing angle is switched on.

7.2.3 LHC limits on R^{-1}

The nature of the model ensures that the new resonances couple in an enhanced manner to quarks while simultaneously having suppressed couplings to leptons. This dictates

that the strongest constraints on the model will not come from EWPTs nor traditional di-lepton resonance searches but rather from di-jet and possibly $t\bar{t}$ searches. With this in mind it is instructive to estimate the current limits on the compactification scale, R^{-1}, using the most recent LHC (CMS) analyses available in the two channels, in order to use a reasonable value for this parameter in our study. The latest di-jet resonance search for $\sqrt{s}$ =8 TeV and 19.6 fb^{-1} [149] is used while for $t\bar{t}$ the most constraining analysis was found to be the boosted resonance search in the lepton+jets channel at $\sqrt{s}$ =7 TeV with full luminosity [38].

Such searches determine limits on the enhancement of the "unfolded" $t\bar{t}$ production cross section in the case of the lepton+jet search and $\sigma \times BR(Z' \to j\bar{j}) \times \mathcal{A}$ (Acceptance) for the di-jet search. Both use a "bump hunt" binned analysis, fitting the background plus a single-resonance signal shape with the cross section as a free parameter. Consequently, the analysis is rather sensitive to the signal shape. The fact that any interference effects are *a priori* neglected in model independent limits means that the limits that are obtained for this model will be in the approximate case of degenerate resonances not interfering with the SM gauge bosons, in order to best match the assumed signal shape. The production rate is computed for the model as a function of R^{-1} which is equated with $M_{\tilde{\gamma}'} \approx M_{\tilde{Z}'}$ and compared with the CMS data to obtain a qualitative, yet instructive, limit on the compactification scale. In addition to neglecting the interference effects, which are indeed small compared to the QCD background, only the first KK level of resonances was considered when computing the signal cross sections. This is also to best match the assumed signal shape used in the experimental analyses. The effects of the higher KK resonances are strongly reduced at high scales ($\geq$2 TeV) due to low parton luminosities while at the lowest scales ($\sim$1 TeV) the first resonance is enough to exclude the model. Note that, within these simplifications, the production rates between the SM-like mixed and unmixed cases do not differ significantly even without including the aforementioned off-diagonal width effects. For the di-jet analysis, an important additional contribution will arise from KK W-boson contributions as well as t-channel exchanges of all possible new gauge bosons. The former will contribute to the signal cross section while it is argued that the latter will be present as a continuum correction and would thus be absorbed into the normalisation of the background fit. As such, only s-channel exchanges of KK gauge bosons are deemed to contribute to the visible signal cross section. Furthermore, an additional kinematical cut of pseudorapidity separation between the jets $\Delta\eta_{jj}$ <1.3 is imposed along with the requirement that both jets be central ($|\eta|$ <2.5).

In Figure 7.1, the $t\bar{t}$ and di-jet production rate in AADD to the limits quoted from CMS resonance searches in the two channels are compared. The di-jet rates are unsurprisingly large since the resonance couples with a factor $\sqrt{2}$ larger than the SM case leading to a limit of order 3.1 TeV on R^{-1}. The fact that this analysis was performed on 8 TeV data compared to 7 for $t\bar{t}$ along with the higher multiplicity of light quark final

states and better reconstruction efficiency suggests that the latter analysis will not be able to compete in setting such limits. The $t\bar{t}$ limits are based on particular assumed widths (1% and 10% of the mass) of the resonances. The previously introduced "Topcolor" [76] benchmark model that is constrained in this analysis has been left on the figures for comparison. Given that, in this scenario, the tree-level width contributions come only from quarks and give a contribution of about 5% of the mass, the predictions are compared to both cases, understanding that the true limit should lie somewhere in between. It appears that the exclusion is rather sensitive to this assumption since, in the narrow case, AADD rates are higher than the Topcolor ones while in the wide case they are lower, which may be a direct consequence of the ∼5% widths. This channel yields a limit on R^{-1} of about 1.5-1.7 TeV, which is much lower than the di-jet case at 8 TeV, as expected. Driven by these rough limits, subsequent results are simulated for a compactification scale of 3 TeV in order to present the phenomenology of the AADD model.

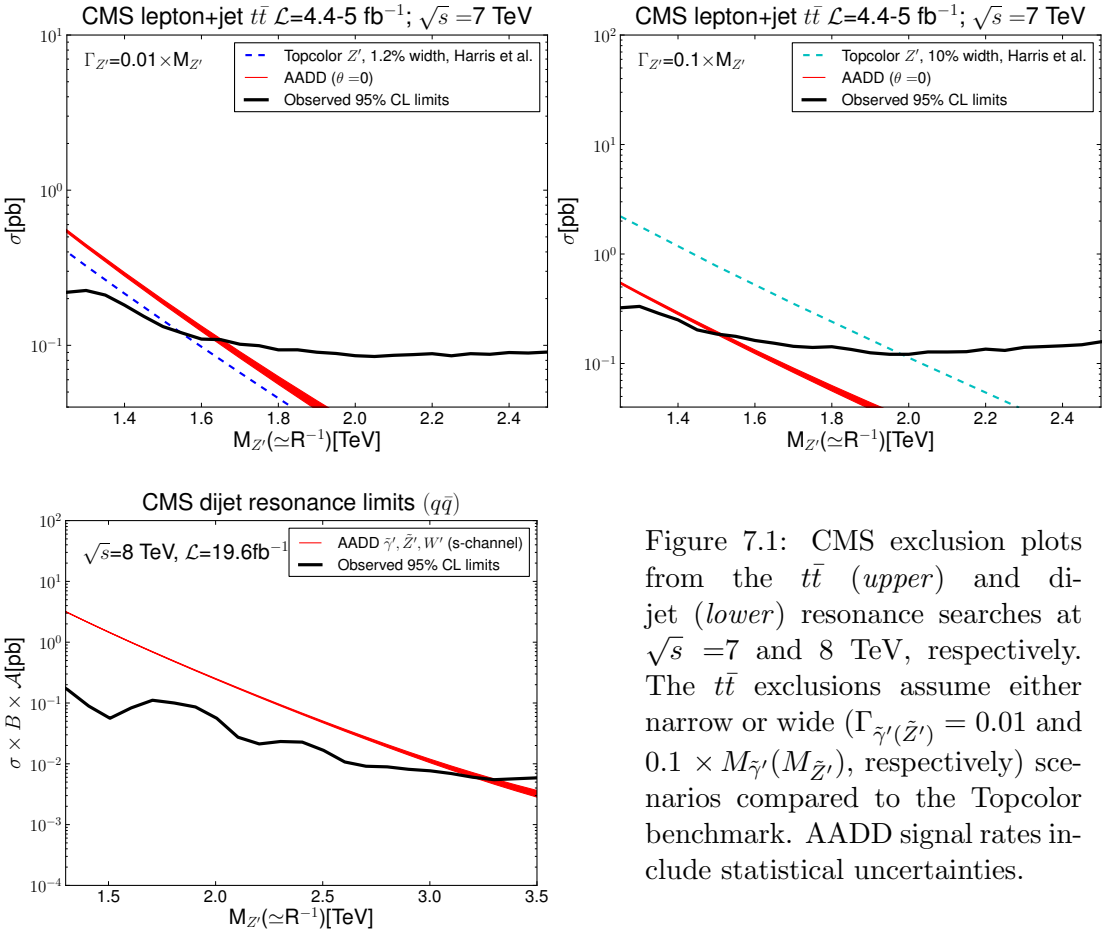

Figure 7.1: CMS exclusion plots from the $t\bar{t}$ (*upper*) and di-jet (*lower*) resonance searches at $\sqrt{s}$ =7 and 8 TeV, respectively. The $t\bar{t}$ exclusions assume either narrow or wide ($\Gamma_{\tilde{\gamma}'(\tilde{Z}')} = 0.01$ and $0.1 \times M_{\tilde{\gamma}'}(M_{\tilde{Z}'})$, respectively) scenarios compared to the Topcolor benchmark. AADD signal rates include statistical uncertainties.

7.3 Results

The numerical results are now presented for the phenomenology of the AADD model as a benchmark for a quasi-degenerate two-resonance scenario preferentially coupled to

$t\bar{t}$. As suggested by Sections 7.2.1 and 7.2.3, a compactification scale of $R^{-1} = 3$ TeV is chosen as the reference point. The code exploited, as in previous chapters, is based on helicity amplitudes, defined through the HELAS subroutines [83], and built up by means of MadGraph [84]. Initial state quarks have been taken as massless whereas for the final state top (anti)quarks, $m_t = 175$ GeV has been taken. The CTEQ6L1 [18] PDFs were used with factorisation/renormalisation scale set to the compactification scale, $Q = \mu = R^{-1}$. In each case, the BSM signal including (small) inteference with the EW zero modes (γ,Z) is laid against the tree-level SM background dominated by QCD and supplemented by EW production for completeness, all at LO. The focus is on differential cross section and asymmetry observables binned around the resonance peak region in invariant mass, $|M_{t\bar{t}} - R^{-1}| < 500$ GeV. The results should not, qualitatively, be affected by the choice of R^{-1}. First, the results for the exactly degenerate limit will be shown, highlighting the importance of including off-diagonal effects, before moving on to the radiatively split spectrum. A comparison of the degenerate AADD model with generic single Z's in the asymmetry observables will be made to underline the fact that they can be very useful in identifying the presence of quasi degenerate, multiple resonances when these cannot be resolved in the invariant mass spectrum. Following the various discussions in Section 2.5 and subsequent chapters, the reconstruction efficiency of the $t\bar{t}$ signal is assumed to be 10%. Further, the two asymmetry observables considered are A^*_{FB} for the charge asymmetry as defined in Section 6.9 and the spin polarisation A_L used throughout this thesis. As in Chapter 6, the reconstruction efficiency estimates are taken to be 10% and 5% for the two asymmetries respectively.

7.3.1 Invariant mass and asymmetry spectra

Invariant mass profiles in the standard cross section as well as charge and spin asymmetries for both SM-like "mixed" ($\theta = \theta_W$) and the pure "unmixed" ($\theta = 0$) case for the LHC at 14 TeV are shown. The relative contributions of the two resonances to the aforementioned observables are decomposed to highlight the fact that, while the invariant mass spectrum views these as a single bump, the asymmetries may allow one to deduce the presence of multiple states. As discussed in Section 7.2.1, the mixing parameter, θ, should not be physical in the degenerate limit. This appears to be the case for the invariant mass spectra in Figure 7.2, where the observable quantity in black reveals the presence of a single resonance, with both contributions and their interference adding coherently to form a Breit–Wigner-like peak. The predictions for both mixed and unmixed cases are rather similar, differing by less than 10%. The signal (S) is, unsurprisingly, very visible above the Background (B), as indicated by the large significances, $S/\sqrt{S+B}$, in the right-hand subplots even after folding the estimated 10% reconstruction efficiency.

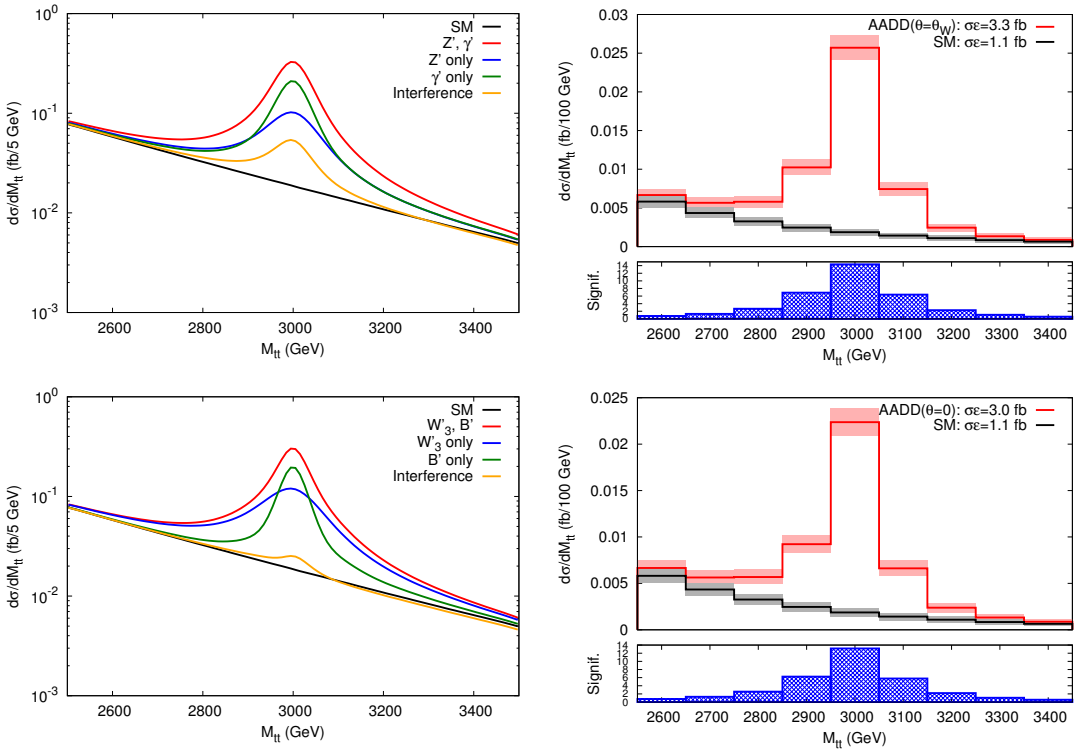

Figure 7.2: The $t\bar{t}$ invariant mass (M_{tt}) distribution of the cross section for the AADD model with $R^{-1} = 3$ TeV. The upper two plots show the case where the couplings are Z-like and γ-like while the lower two plots show the case where they are B-like and W_3-like. The left column highlights the contributions from the two resonances and their interference. The right column shows the observables, incorporating a 10% reconstruction efficiency on the $t\bar{t}$ system, statistical uncertainties and mass resolution estimates for the LHC at 14 TeV, with 100 fb^{-1} of integrated luminosity. The lower subplots on the right hand side measure the bin-by-bin significance of the signal in standard deviations.

In contrast, the asymmetries highlight a very different phenomenology. A clear difference can be noted between the prediction for the unmixed and mixed cases in Figures 7.3 and 7.4 respectively. This is the unphysical artefact coming from the omission of off-diagonal width contributions discussed in Section 7.2.1. Figure 7.5 shows that the inclusion of these effects makes the prediction for the mixed case consistent with that of the unmixed case, where the off-diagonal terms are zero by construction, restoring the mixing angle to an unphysical parameter. The predictions for the unmixed case and the mixed case with off-diagonal widths agree up to small interference effects away from the peak where the off-diagonal terms become small and the latter begins to agree with the mixed case without their inclusion. These deviations are more pronounced in the asymmetries and are likely due to the approximation of only considering off-diagonal effects in the degenerate first level KK resonances. The unmixed scenario is therefore taken to represent the "true" observables in this study.

In the upper-left plot of Figure 7.3, a characteristic dip in A_L appears as a consequence

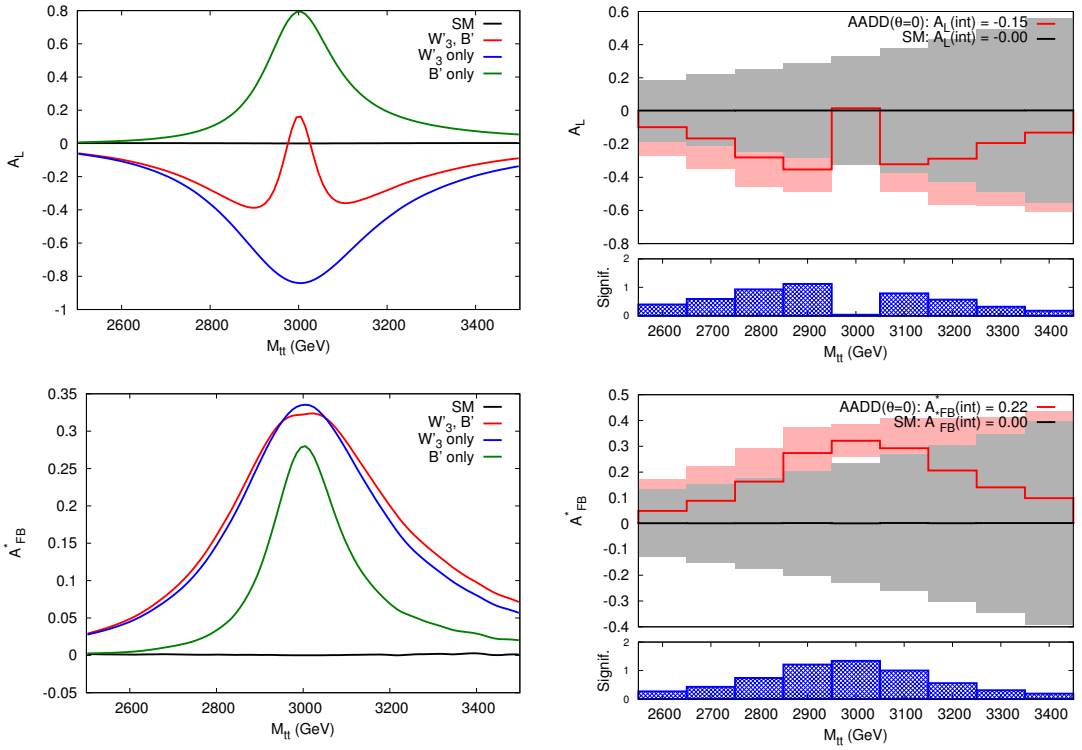

Figure 7.3: The $t\bar{t}$ invariant mass (M_{tt}) distribution of the A_L and A^*_{FB} asymmetries for the AADD model with $R^{-1} = 3$ TeV where the couplings are B-like and W_3-like ($\theta = 0$). The left column shows each of their contributions individually compared to the total (in red). The right column shows the observables as they could be seen at the LHC at 14 TeV, with 100 fb^{-1} of integrated luminosity, incorporating a 10(5)% reconstruction efficiency on the $t\bar{t}$ system for $A^*_{FB}(A_L)$ and statistical uncertainties. The lower subplots on the right hand side measure the bin-by-bin significance of the signal as defined in Equation 4.16.

of the two superimposed objects having different widths and couplings. The effects from the wider resonance come in around the edges of the deviation, pushing the value of the observable towards the preferred one for its set of couplings while, near the centre of the distribution, the contribution from the narrower resonance pulls it towards the latter's preferred value. This effect is not as evident in the case of A^*_{FB}, shown in the lower left plot of Figure 7.3, owing to the dominant contribution to the process coming from the up quark initial state. In the limit where only this state contributes, $A^*_{FB}(t\bar{t})$ is always positive in such a model with universal fermionic interactions, as can be inferred from Equation 3.26. In order to give a complete description of asymmetry effects, in the two left-hand side plots of Figure 7.3, the observables A_L and A^*_{FB} are decomposed into contributions from each individual resonance plotted alongside their combination compared to the SM, emphasising the competition between them. The coupling dependence of such observables allows for this special phenomenology and these observables like to be large since the W'_3 couplings are purely left-handed, maximising the parity asymmetric coefficient in Equation 3.16. The right-hand side plots of Figure 7.3 display the two observables, A_L and A^*_{FB}, with statistical uncertainties at the 14 TeV

LHC after 100 fb^{-1} of integrated luminosity folding in a 10(5)% reconstruction efficiency. The significances in this case are defined as in Equation 4.16 and are lower than those of the invariant mass distribution. Nonetheless, the signal range is rather wide and an integrated value of the observable could provide adequate statistical significance to be observable above the background prediction as will be shown later in Section 7.3.2.

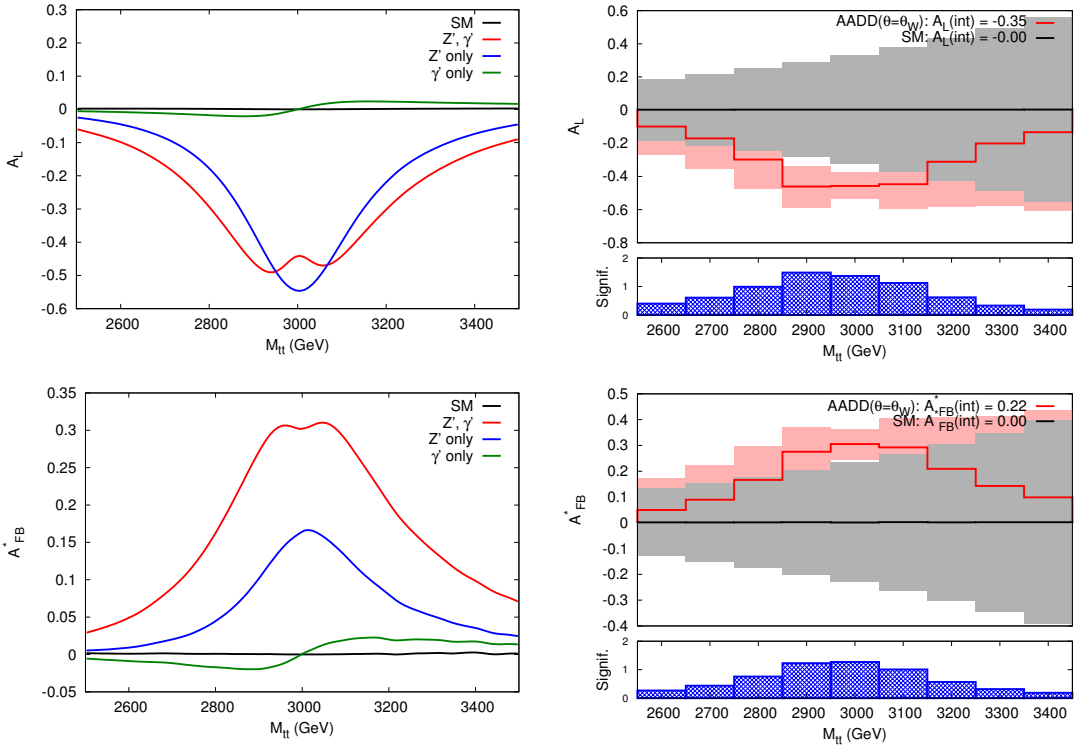

Figure 7.4: Identical plots to Figure 7.3 except where the couplings are Z-like and γ-like ($\theta = \theta_W$) instead. This corresponds to the unphysical case where off-diagonal matrix elements have not been considered, resulting in differing phenomenology occuring with the variation of an unphysical parameter, θ.

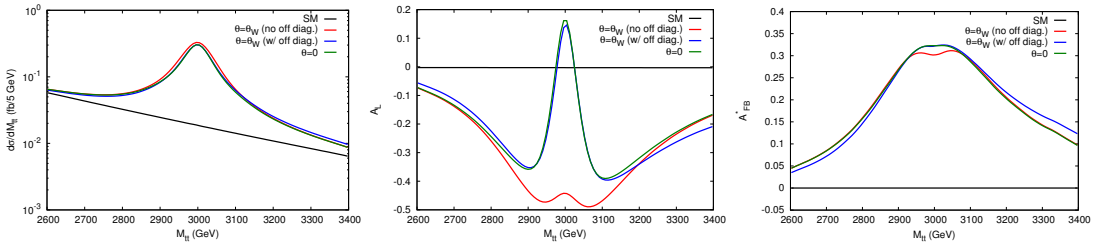

Figure 7.5: Differential distributions in $M_{t\bar{t}}$ for σ, A_L and A^*_{FB} comparing the SM-like mixed AADD with and without off-diagonal width contributions to the unmixed case.

Although the "dip" feature of the AADD scenario is visible in the binned A_L figures, it is about the only thing that suggests a differing phenomenology from that of a single resonance. Furthermore, the large amount of luminosity required to achieve a more statistically significant differential analysis of asymmetry observables that could confirm

the presence of multiple resonances indicates that one may need to rely more on integrated quantities. The next section will show that the phenomenology of this model, displaying generic features of quasi-degenerate states, will allow it to be statistically separated from single resonance scenarios using only integrated asymmetries.

Before moving to the integrated analysis, the cross section and asymmetry observables are also shown for the split spectrum case ($M_{B'}$=2.98 TeV, $M_{W_3'}$=3.13 TeV), where the radiative mass corrections have been taken into account as described in Section 7.2.1 and Appendix C. This drives the mass mixing to zero and brings the model to the edge of the quasi-degenerate regime. Namely, the splitting – of order 150 GeV – becomes comparable to the estimated mass resolution and corresponds to about 5% of R^{-1}. However, it seems from Figure 7.6 that both the invariant mass distribution and the forward-backward asymmetry still do not resolve two distinct peaks. The spin polarisation asymmetry, A_L, however, clearly distinguishes between the opposing contributions of the two peaks in an even more striking way than in the degenerate case because the two contributions no longer have to compete at the same invariant mass. This is reminiscent of the types of signals seen in the 4DCHM scenarios of Chapter 6. Another consequence of this is that the integrated value of the observable becomes closer to zero. As will be shown in the next section, a single resonance does not generate a forward-backward asymmetry without simultaneously generating a polarisation asymmetry. Thus, the cancellation in the integrated prediction of A_L combined with a nonzero A_{FB}^* will serve as the distinguishing feature.

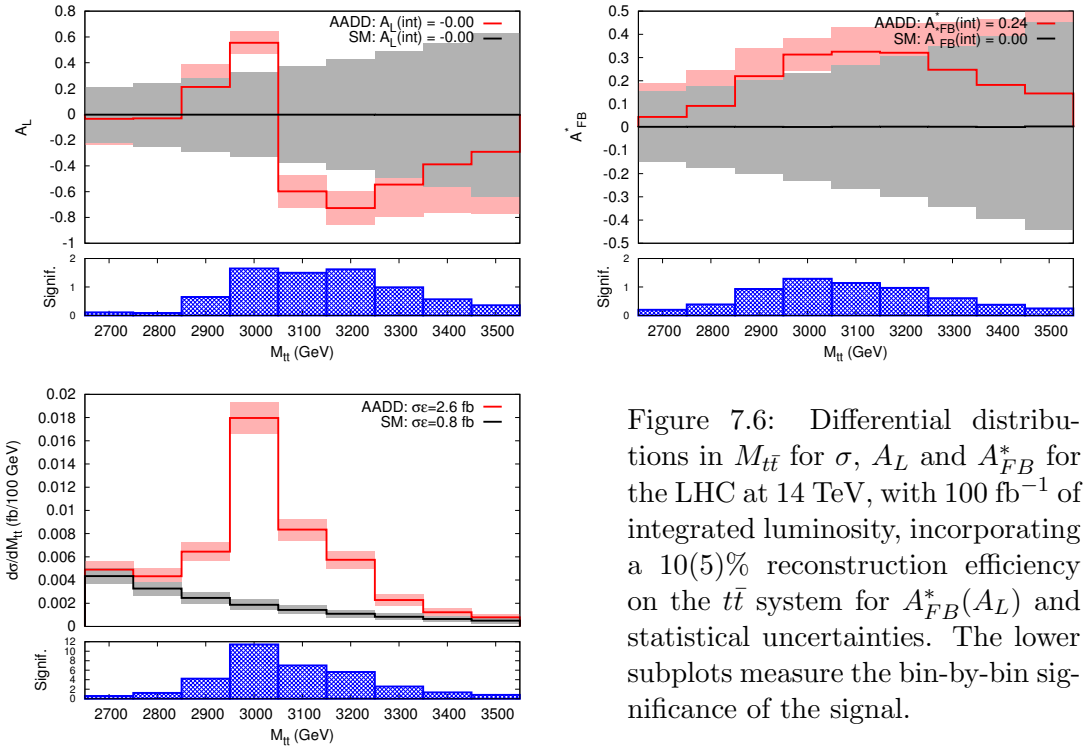

Figure 7.6: Differential distributions in $M_{t\bar{t}}$ for σ, A_L and A_{FB}^* for the LHC at 14 TeV, with 100 fb^{-1} of integrated luminosity, incorporating a 10(5)% reconstruction efficiency on the $t\bar{t}$ system for $A_{FB}^*(A_L)$ and statistical uncertainties. The lower subplots measure the bin-by-bin significance of the signal.

7.3.2 Degeneracy versus a single resonance

Having confirmed that the presence of multiple degenerate resonances alters the phenomenology of asymmetry observables, this feature can be used to distinguish AADD from models with a single resonance. In order to provide a testbed for this, a set of "toy" models of a single resonance were created, designed to be indistinguishable from the degenerate AADD model in a resonance search. This was done by tuning the widths and the couplings and establishing appropriate parameters such that the invariant mass distribution of the points matched those of the AADD. In the massless limit, given a fixed width chosen to resemble the effect of two AADD resonances, the cross section can be modelled as some coefficient incorporating phase space and PDF convolutions multiplying the chiral coupling coefficients of Equation 3.10. This was used to fit these phase space and PDF convolutions for the u and d initial states respectively by considering $\sigma(pp \to t\bar{t})$ and $\sigma(pp \to b\bar{b})$ for a set of randomly selected u and d chiral couplings respectively. For $t\bar{t}$, the d couplings were set to zero and for $b\bar{b}$, the u couplings. The fitted coefficients could then be used to generate a scan over the set of allowed chiral couplings, while keeping the cross section fixed.

The observables generated are shown in Figure 7.7, which represents a random selection of 3 points fulfilling these conditions. The minimal assumption of universal couplings across fermion generations was made in order to simplify the parameter scan, leaving only the up and down-type chiral couplings $u_{L,R}$ and $d_{L,R}$ as inputs. The other frequent assumption associated with Z's of fixing the charges of each SM representation was ignored, as requiring $u_L = d_L$ was over-constraining for a toy model, not necessarily meant to represent a physically motivated scenario coming from any particular gauge group extension. The distributions confirm that there are many possible combinations for values of charge and spin asymmetries for seemingly identical resonance cross sections. This is, of course, not surprising following the discussion of the coupling dependencies in Section 3.2 which also implie that the two asymmetry observables are correlated due to their identical dependence on the final state couplings. Note that the observables in AADD appear to remain distinguishable from any of the lettered benchmarks.

With this in mind, a scan was performed over all possible up and down-type couplings allowed while keeping the single resonance cross section (65 fb integrated 500 GeV either side of the resonance) and line-shape (i.e., width) fixed in order to compare and cross-correlate the two asymmetry observables. In addition, a less constrained parameter scan was also made over any combination of couplings and a random choice of width to see whether the separation power of the asymmetries still holds. Here, the chiral couplings were sampled over an interval $\{0, 1\}$ while the widths were chosen to be a random value $\leq 10\%$ of the mass (3 TeV). Both sets of points are shown in Figure 7.8, where the AADD case is plotted as an ellipse representing the 1σ statistical uncertainties in the asymmetries. The tree-level SM prediction is included for reference, matching the

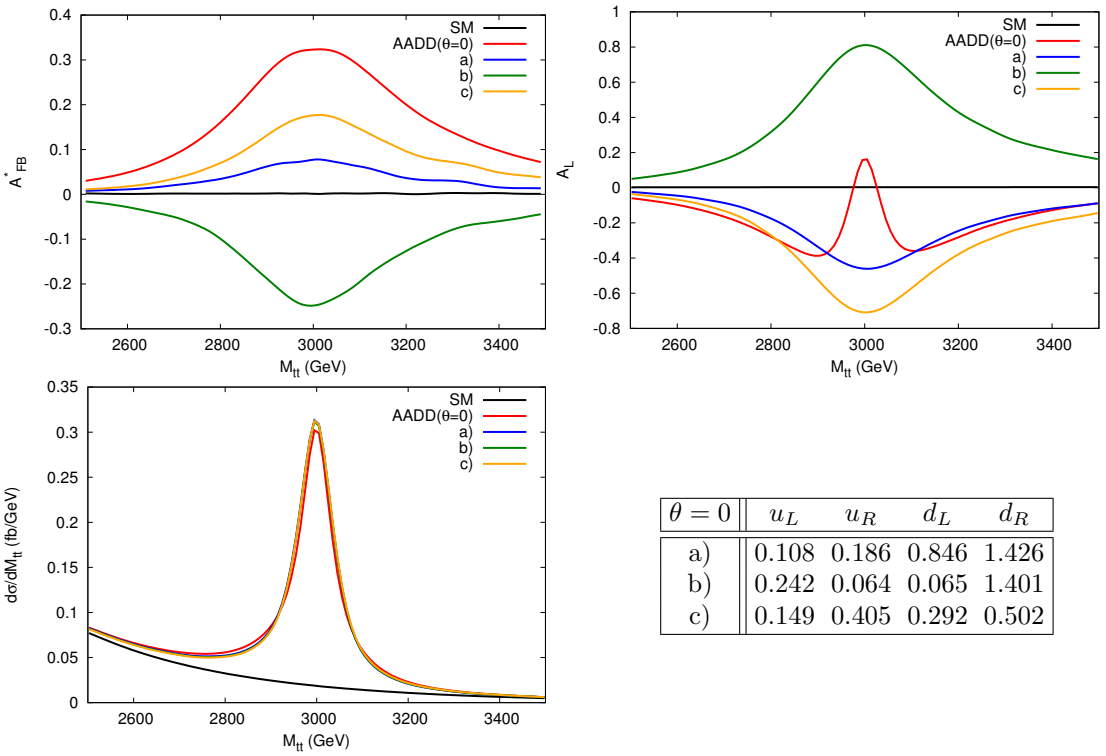

$\theta = 0$	u_L	u_R	d_L	d_R
a)	0.108	0.186	0.846	1.426
b)	0.242	0.064	0.065	1.401
c)	0.149	0.405	0.292	0.502

Figure 7.7: Differential distributions in $M_{t\bar{t}}$ for σ, A_L and A^*_{FB} comparing the AADD with three selected scan points modelling a single resonance with random couplings generated with its widths fixed to match the cross section of each case of AADD. The randomly chosen couplings are summarised in the lower right table.

case when the up-type couplings of a single resonance are purely vector-like ($u_L = u_R$). The observables plotted are integrated values of the asymmetry over an invariant mass of 500 GeV either side of the resonance mass, for the LHC at 14 TeV and 100 fb^{-1} of integrated luminosity, using statistical uncertainty and reconstruction efficiency estimates consistent with the rest of this study.

Firstly, it is confirmed that the AADD scenario is distinguishable from the SM background in either observable. The profiles of the single resonance scan points show a clear quadratic relationship between the two observables. This can be understood if one assumes that the u-quark initial state dominates the production: A_L will be proportional to the parity asymmetric coupling combination while A^*_{FB} will go as the square of this quantity as discussed in Section 3.2. In the case where the invariant mass distribution was constrained to match the AADD rate, the maximum values of A_L and A^*_{FB} are bounded by the maximum absolute value of the couplings. In the unconstrained scan, with the area covered by the points widens slightly due to the larger possible S/B, A_L becoming unbounded while A_{FB} is limited to be positive and somewhat less than A_L. This, again, follows from the coupling dependence of both observables. The parameter scans show that the AADD resonances, in the degenerate limit, can be fully disentangled from any possible single resonance that may produce a similar invariant mass profile in a

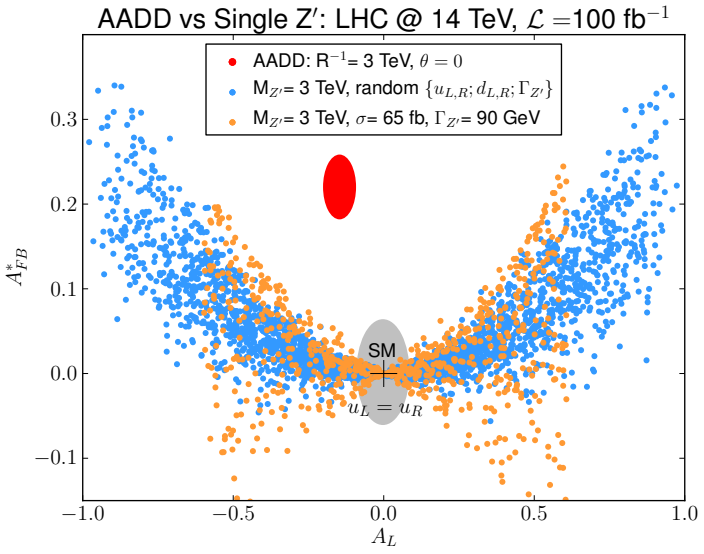

Figure 7.8: Scatter plots showing predicted values of A_L and A_{FB}^* for AADD with $R^{-1} = 3$ TeV at the LHC, compared to the two sets of scanned points. The first represents a scan over random couplings of a single 3 TeV resonance with a fixed width constrained to match the AADD invariant mass distribution (Figure 7.7). The second shows a scan where the couplings are randomly chosen over the ranges $\{0, 1\}$ and the resonance width is randomly chosen to be $\leq 10\%$ of the mass. The tree-level SM value is shown for reference and ellipses represent the 1σ statistical uncertainties assuming a 10(5)% reconstruction efficiency on the $t\bar{t}$ system for $A_{FB}^*(A_L)$.

bump hunt, within this treatment of reconstruction efficiencies and uncertainties. This suggests that in the scenario that multiple resonances are observed at the LHC but are masked by a quasi-degeneracy, one may be able to use the asymmetry observables to tell that the signal is coming from more than one resonance. Indeed, any signal appearing as a single peak with asymmetry values outside of the area spanned by the points in Figure 7.8 will be a "smoking gun" for degenerate multiple-resonance physics.

7.4 Conclusions

A realistic example of a model (denoted as AADD) of two quasi-degenerate resonances preferentially decaying to $t\bar{t}$ final states was established where the presence of the two new particles cannot be distinguished from a generic single resonance scenario in bump hunt searches. The importance of radiative mass corrections in this model was highlighted, in that they induce splittings that bring the model towards the edge of the quasi-degenerate scenario. However, these were calculated to be about 5% of the compactification scale, R^{-1}, ensure that the splittings remain below the $t\bar{t}$ and di-jet mass

resolutions. In the discussion of radiative mass splittings, quasi degeneracy and subsequent mass mixing, the importance of a correct treatment of off-diagonal width contributions in this regime was also stressed. By first considering the degenerate limit as a "worst case scenario" for these purposes, it was found that the omission of off-diagonal-widths led to potentially misleading artefacts which made the mass mixing angle, θ, appear as a physical parameter even though it should not have. The latest LHC results from di-jet and $t\bar{t}$ resonance searches were used to obtain rough limits on the compactification scale from resonance searches at the LHC in order to examine a viable model.

Having expanded on the properties of asymmetry observables in previous chapters, it was demonstrated that both charge and spin asymmetries are required to distinguish this scenario from not only any singly resonant signal which mimics the invariant mass distribution of the model but also any possible observed narrow resonance in $t\bar{t}$ searches. This is owed to the unique features of said asymmetries, that cannot be reproduced in the presence of only one resonant state decaying to $t\bar{t}$ pairs. In fact, this analysis can serve to probe similar models of multiple quasi-degenerate resonances and a prediction for A_L, A_{FB}^* from such a model lying outside the possible values for a single resonance is likely and would signal the presence of multiply resonant physics.

All the results have been obtained at parton level, yet in presence of realistic statistical uncertainties and reconstruction efficiencies, so they should undergo a certain degree of scrutiny in presence of $t\bar{t}$ decays, parton shower and hadronisation. However, the main conclusions of our work are not expected to change substantially. In addition, the likely boosted nature of the top final state may suggest the need for alternative techniques for measuring top polarisation which do not rely on reconstructing the invariant mass of the top pair. It remains to be seen how the upgraded LHC will be able to deal with spin measurements in boosted tops, but what is clear is that, should they manage to measure the quantity with sufficient accuracy, it would shed much light on the coupling structure and potentially degenerate nature of an observed Z'.

Chapter 8

Conclusions and outlook

A number of studies of the phenomenology of Z's through the $t\bar{t}$ channel has been presented with particular emphasis placed on the power of asymmetry observables. The fact that the top quark, being an unstable object which preserves its charge and spin information through to its decay products, allows for the definition of spin asymmetries makes it a promising candidate for providing additional information on the chiral couplings of a new observed resonance. This is particularly important given the fact that the top quark often plays an important role in models of EWSB beyond the SM Higgs mechanism. This is owed to its large mass and consequent contribution to the unstable radiative corrections to the Higgs mass which plague to SM in its basic form, as mentioned in Chapters 1 and 2. Various ways in which a Z' can occur in BSM theories were discussed in Chapter 3, underlining their ubiquity in new physics models. Demonstrating the unique dependences on the Z' chiral couplings offered by the additional asymmetries, the power of these observables is investigated in a variety of BSM scenarios containing these new neutral vector resonances.

It is clear that the complex, six-body final state yielded by $t\bar{t}$ production, discussed in Chapter 2, will contribute to a relatively low reconstruction efficiency compared to simple, cleaner final states such as the di-lepton one, which are traditionally used to search for Z's. As the scale of new physics is continually pushed up by past and current collider searches, the additional complications of a boosted system come into play. These aspects must be taken into account and, although only a limited amount of experimental analyses are available which consider high energy tops, jet substructure and pruning methods are available and are being used in a few of these to dedicatedly identify these objects. In particular, specific methods to extract spin information from the boosted top decay products also exist. One of the main aspects of these is a move away from the requirement of a full reconstruction of the $t\bar{t}$ invariant mass, relying rather on more accessible properties of the decay products such as their energy fractions or transverse momentum spectra. This is largely to avoid the angular resolution issues that arise from highly collimated decay products. It is also interesting to note that the hadronic decay

modes become more useful since lepton isolation is also one of the primary selection requirements that suffers from boosted decays. It is fair to say that, given the relatively early stages of the LHC experiments, this domain is still under development and data from the upcoming 14 TeV run will shed much light on the scope of these methods as well as their efficiencies and associated systematic uncertainties. However, it remains true that any final state in which spin asymmetries can be defined will necessarily involve decaying objects in order to transmit their spin information. Therefore, such difficulties can be seen as an irreducible aspect of extracting spin observables.

The reality and importance of these features can be traced in this thesis through the gradual move with each chapter towards increasingly conservative stances on the estimated reconstruction efficiencies associated to each $t\bar{t}$ observable. This caution is also reflected in the assumptions concerning the $t\bar{t}$ mass resolution, with the eventual preference of using integrated observables rather than those presented differentially in $M_{t\bar{t}}$. The major source of uncertainty in this regard, identified in Section 2.5, stems from the fact that the studies presented in this thesis are all performed at parton-level, without including the subsequent decay and reconstruction of the tops. While it was clearly necessary to make use of the most recent available information from experimental analyses and other, more complete phenomenological investigations, the ultimate estimates used remained approximate and – to a degree – subjective. In this sense, the only attitude permitted is that of conservatism, with the knowledge that the results presented are of an illustrative nature, and should serve as a motivating basis for more precise analyses.

As such, one of the main aims of subsequent work will be a validation of the observations presented concerning how much the conclusions are affected by the application of a full $t\bar{t}$ decay chain and subsequent detector-level reconstruction. In this regard, there is nonetheless cause for optimism in that, while it may not be possible to obtain results for the various asymmetries in the exact form presented in this work, these observables should nonetheless represent the kind of behaviour one might expect to obtain. Fully integrated measures of spin observables should be obtainable via the boosted methods mentioned in Section 2.5. Moreover, although hope for the full reconstruction of $M_{t\bar{t}}$ in such measurements may have to be discarded, it is not unconceivable that – with sufficient statistics – top polarisation could be presented differentially in a less "demanding" variable such as top p_T, which can still display a characteristic resonant shape. These kind of analyses necessarily require high statistics and are therefore better suited to the high energy and high luminosity, upcoming LHC run during which the understanding of systematics associated with b-tagging and jet energy scale, amongst others, will be better understood.

Within the confines of the parton-level analyses presented here, assuming that the general idea of the results will remain, subject to a full simulation, the potential of asymmetries in the context of resonant physics has been demonstrated. It is hoped that the idea of using $t\bar{t}$ as a useful alternative channel to profile a Z' has been conveyed. Firstly, in

Chapter 4, a direct comparison of the channel was performed by using a set of common $U(1)$ benchmarks considered in di-lepton analyses. Here, the reconstruction efficiency issues were clear to see, even though the studies employed the most optimistic assumptions regarding these. However, the asymmetries, particularly the spin polarisation, were confirmed to exhibit new and interesting dependencies on the chiral Z' couplings, hinting at the fact that these could eventually be used to distinguish models that could not be via cross section measurements. At the same time, the fact that this channel could only be competitive at best with regards to the di-lepton channel motivated its use as a complementary final state, rather than a straight discovery mode. This is particularly true for these types of models that bear no suppression in leptonic couplings or enhancements to third generation interactions.

This led to the study presented in Chapter 5, where $t\bar{t}$ was considered in conjunction with the di-lepton and $b\bar{b}$ modes as part of an overall strategy of distinguishing variants of a minimal Z' extension of the SM. Here, the possibility that another decaying final state might provide spin asymmetries, namely $\tau^+\tau^-$, was considered. In addition to the conclusion that, in many cases, more than one final state may be required to access a maximum of the model's parameter space and also separate certain benchmarks, the – perhaps more interesting – view considering the ultimate extraction of the Z' couplings was discussed. Section 3.1.3 points out that, assuming even the most minimal set of parameters characterising the fermionic couplings of a single Z' leads to 5 independent quantities. Section 5.2.1 suggests that the e^+e^- and $\mu^+\mu^-$ channels may not be sufficient to fully disentangle them. Interestingly, although the unique coupling dependence of the spin polarisation on these couplings was shown in Section 3.2, it was also discovered that its measurement does not represent a unique piece of information assuming only a single final state is used. That is to say, assuming universal Z' interactions, the measurement of τ polarisation in addition to a set of 4 observables provided by the light di-lepton channel is inadequate as a fifth observable. This further motivates the inclusion of $t\bar{t}$ to provide complementary information via its cross section or any asymmetry observable. These can be used to simultaneously break the observed degeneracy in the quark and leptonic couplings shown in Section 5.2.1 and provide the needed information to fit the minimal set of parameters (excluding the width). Finally, moving away from the minimal assumptions towards a more general case of up to 24 free parameters (including right-handed neutrinos) clearly necessitates the use of as many independent observables as possible, of which $t\bar{t}$ and spin asymmetries can provide a good number.

The two studies performed up to this point were investigating models that were not particularly tailored to $t\bar{t}$ searches but rather were familiar to the theoretical and experimental community as popular and simple benchmark choices. It was therefore important to move on to models which lent themselves to $t\bar{t}$ in order to get a better idea of its use as a discovery channel and the benefits that asymmetry observables may offer in such circumstances. To this end, two rather different models were considered in Chapters 6

and 7 respectively. The first one stemmed from a comprehensive effective description of the Higgs as a pNGB, also employing the notion of partial compositeness to yield the large top mass and consequently strong couplings between new physics and third generation quarks. This 4DCHM is a prime example of the type of BSM scenario for which $t\bar{t}$ could be one of the main discovery channels thanks to the presence of 5 neutral resonances, of which it was determined that two were likely accessible via this channel at the LHC. Having identified regions in the parameter space – consistent with experimental constraints – where the resonances would be clearly visible in this channel (essentially when the heavy exotic quark decay modes are kinematically unavailable, leading to relatively narrow Z's), a number of benchmarks were investigated in $t\bar{t}$. The results not only highlighted their clear visibility in $t\bar{t}$ but also hinted at the use of A_L to distinguish the two resonances which are often too close in mass to be well separated in the differential cross section. $t\bar{t}$ thus presents itself as a primary discovery channel for these models in regions of parameter space compatible with EWPTs, where the exotic quark states are too heavy to be excluded by current searches, particularly knowing that the traditional di-lepton mode is only accessible for very large integrated luminosities [118]. Finally, the interesting phenomenological behaviour of the two resonances having different chiral top couplings motivated the next study, which aimed to utilise this as a novel way to identify quasi-degenerate resonances.

Although the model used in Chapter 7 was of a more unusual nature, its Z's did have a rather different, extra dimensional origin to previously considered scenarios while providing an ideal testbed for the method investigated therein. The arranged localisation and delocalisation of the QCD and EW sectors respectively represented one of the many possibilities offered in the string-inspired, brane-world scenarios. This specific arrangement simultaneously led to loop-suppressed leptonic couplings and significantly enhanced quark couplings. In these models, one would naively expect a near degeneracy of the neutral KK EW gauge bosons given the democratic assignment of their KK mass component. However, it was discussed that, as the compactification scale of such a model is increased, motivated largely by the strong bounds from di-jet searches shown to apply to this realisation, the importance of the radiatively-induced mass splitting also increases. Although such effects were calculated to be of order 5%, the consequences with regards to the couplings of the new objects were significant. These considerations motivated taking the objects to couple as the pure T_3 and hypercharge gauge bosons, rather than the typical heavy "copies" of the Z and photon cited in the literature [144]. The importance, in this context, of off diagonal width effects were also considered and led to a more consistent formulation of the observables, in which the mixing angle vanished as a physical parameter in the fully degenerate limit. Using this model as an example of a scenario consistent with current experimental limits in which the mass splitting is too small to be effectively resolved in the di-jet and $t\bar{t}$ search channels, the phenomenology of asymmetries was investigated. It revealed an interesting interplay, not dissimilar to that observed in the previous chapter, between the two resonances. It was further

shown, using fully integrated observables, that the presence of two resonances could be deduced by correlating the charge and spin asymmetry observables to demonstrate that, at least within the assumption of universal quark couplings, the signal predicted by AADD could not be replicated by a single Z', no matter what its couplings were. Thus, given the observation of a Z' in a channel with mediocre mass resolution such as di-jet or $t\bar{t}$, a "smoking gun "for multiply resonant physics was identified using $t\bar{t}$ charge and spin asymmetries.

We are currently in the early stages of an extremely exciting time for particle physics, having just observed a resonance consistent with the SM Higgs and with the high energy run of the LHC around the corner. It is clear that the $t\bar{t}$ channel will contribute a large amount of events to be analysed for evidence of physics beyond the SM. Furthermore, it is not unconceivable that this may occur in the form of a resonant signal either in this or other channels, perhaps in multiple ones. As discussed in this thesis, this type of signature could indicate a plethora of scenarios ranging from gauge group extensions to extra dimensions, new strong dynamics or any combination thereof - with or without supersymmetry. This reinforces the importance of characterising the properties of such an object in order to narrow down the possibilities by determining, for example, if it has enhanced or suppressed couplings to certain sectors and whether or not these couplings have a particular chiral structure. It is hoped that this thesis has underlined the fact that the $t\bar{t}$ final state, with its asymmetries, can provide an essential window into addressing such issues and complement other channels in the goal of characterising the properties of a new resonance.

Appendix A

Z' helicity amplitude calculation

The details of the helicity amplitude calculation for the production and decay of a Z' of mass $M_{Z'}$ and width $\Gamma_{Z'}$ are presented, using the methods of [78] and cross checked by results from [79]. The initial state quarks are assumed to be massless with momenta q_i while the final state fermions have mass m_f and momenta p_i. The interactions of the Z' are parameterised as in Equation 3.7, with $q_{L,R}$ and $f_{L,R}$ denoting the initial and final state couplings to respectively. The unpolarised amplitude can be written in terms of two spinor strings corresponding to the initial and final state currents contracted with the Z' propagator in unitary gauge

$$\begin{aligned} G^{\mu\nu}(\lambda,\kappa,\alpha,\beta) = &-\bar{v}(q_2,\kappa)\cdot[\gamma^\mu(g'_L P_L + g'_R P_R)]\cdot u(q_1,\lambda) \\ &\times \bar{u}(p_2,\beta)\cdot[\gamma^\nu(g_L P_L + g_R P_R)]\cdot v(p_1,\alpha), \end{aligned} \tag{A.1}$$

$$\mathcal{M}(\lambda,\kappa,\alpha,\beta) = \frac{-(\eta_{\mu\nu} - \frac{k_\mu k_\nu}{M^2_{Z'}})G^{\mu\nu}(\lambda,\kappa,\alpha,\beta)}{s - M^2_{Z'} + i\Gamma_{Z'}M_{Z'}}. \tag{A.2}$$

The helicity arguments, λ,κ, of the Dirac spinors, u,v, label the initial state while α,β label the final state. The Dirac spinors can be expressed in the Weyl basis, with the corresponding representation of the Dirac matrices given by

$$s = \begin{pmatrix} s_L \\ s_R \end{pmatrix}; \quad \bar{s} = (s^\dagger_R, s^\dagger_L); \quad \gamma^\mu = \begin{pmatrix} 0 & \sigma^\mu_+ \\ \sigma^\mu_- & 0 \end{pmatrix}; \quad \sigma^\mu_\pm = (1, \pm\sigma^i). \tag{A.3}$$

The zero mass of the initial state causes the momentum dependent $k^\mu = (q_1+q_2)^\mu$ terms to vanish by the Dirac equation leaving only the term contracted with $g^{\mu\nu}$ to compute:

$$\begin{aligned} G^\mu_\mu(\lambda,\kappa,\alpha,\beta) = \eta_{\mu\nu}&[q_R v^\dagger_R(q_2,\kappa)\cdot\sigma^\nu_+\cdot u_R(q_1,\lambda) + q_L v^\dagger_L(q_2,\kappa)\cdot\sigma^\nu_-\cdot u_L(q_1,\lambda)] \\ &\times [f_R u^\dagger_R(p_1,\alpha)\cdot\sigma^\mu_+\cdot v_R(p_2,\beta) + f_L u^\dagger_L(p_1,\alpha)\cdot\sigma^\mu_-\cdot v_L(p_2,\beta)]. \end{aligned} \tag{A.4}$$

Using the Fierz identities given in [78] to remove the Lorentz contractions to give

$$\begin{aligned} G^{\mu}_{\mu}(\lambda,\kappa,\alpha,\beta) =& 2f_R q_R [v_R^{\dagger}(q_2,\kappa)\cdot u_R(q_1,\lambda)\, u_R^{\dagger}(p_1,\alpha)\cdot v_R(p_2,\beta) \\ & - v_R^{\dagger}(q_2,\kappa)\cdot v_R(p_2,\beta)\, u_R^{\dagger}(p_1,\alpha)\cdot u_R(q_1,\lambda)] \\ & + 2f_L q_L [v_L^{\dagger}(q_2,\kappa)\cdot u_L(q_1,\lambda)\, u_L^{\dagger}(p_1,\alpha)\cdot v_L(p_2,\beta) \\ & - v_L^{\dagger}(q_2,\kappa)\cdot v_L(p_2,\beta)\, u_L^{\dagger}(p_1,\alpha)\cdot u_L(q_1,\lambda)] \\ & + 2f_R q_L [v_L^{\dagger}(q_2,\kappa)\cdot v_R(p_2,\beta)\, u_R^{\dagger}(p_1,\alpha)\cdot u_L(q_1,\lambda)] \\ & + 2f_L q_R [v_R^{\dagger}(q_2,\kappa)\cdot v_L(p_2,\beta)\, u_L^{\dagger}(p_1,\alpha)\cdot u_R(q_1,\lambda)] \end{aligned} \tag{A.5}$$

The Weyl spinors can then be expanded in terms of helicity eigenspinors $\chi_{\pm}(\vec{p})$:

$$\begin{aligned} \chi_{+}(\vec{p}) = N_{\chi}\begin{pmatrix} |\vec{p}| + p_z \\ p_x + ip_y \end{pmatrix}; \quad \chi_{-}(\vec{p}) = N_{\chi}\begin{pmatrix} -p_x + ip_y \\ |\vec{p}| + p_z \end{pmatrix}; \\ N_{\chi} = \frac{1}{\sqrt{2|\vec{p}|(|\vec{p}| + p_z)}} \end{aligned} \tag{A.6}$$

which satisfy

$$\frac{\vec{\sigma}\cdot\vec{p}}{|\vec{p}|}\chi_{\lambda}(\vec{p}) = \lambda\chi_{\lambda}(\vec{p}) \tag{A.7}$$

and are related to the chiral Weyl spinors of momentum, $\vec{p}$, and helicity, λ, by

$$\begin{aligned} u(p,\lambda)_R &= \omega_{\lambda}\chi_{\lambda}(\vec{p}) = v(p,-\lambda)_R; \\ u(p,\lambda)_L &= \omega_{-\lambda}\chi_{\lambda}(\vec{p}) = -v(p,-\lambda)_L; \\ \omega_{\pm} &= \sqrt{E \pm |\vec{p}|}. \end{aligned} \tag{A.8}$$

In terms of helicity eigenstates, the amplitude, aside from the propagator denominator, reads

$$\begin{aligned} G^{\mu}_{\mu}(\lambda,\kappa,\alpha,\beta) =& 2f_R q_R \Big[\omega_{-\kappa}\omega_{\lambda}\omega_{\alpha}\omega_{-\beta}\Big(\big(\chi^{\dagger}_{-\kappa}\cdot\chi_{\lambda}\big)\big(\chi^{\dagger}_{\alpha}\cdot\chi_{-\beta}\big) - \big(\chi^{\dagger}_{-\kappa}\cdot\chi_{-\beta}\big)\big(\chi^{\dagger}_{\alpha}\cdot\chi_{\lambda}\big)\Big)\Big] \\ & + 2f_L q_L \Big[\omega_{\kappa}\omega_{-\lambda}\omega_{-\alpha}\omega_{\beta}\Big(\big(\chi^{\dagger}_{-\kappa}\cdot\chi_{\lambda}\big)\big(\chi^{\dagger}_{\alpha}\cdot\chi_{-\beta}\big) - \big(\chi^{\dagger}_{-\kappa}\cdot\chi_{-\beta}\big)\big(\chi^{\dagger}_{\alpha}\cdot\chi_{\lambda}\big)\Big)\Big] \\ & - 2f_R q_L \Big[\omega_{\kappa}\omega_{-\lambda}\omega_{\alpha}\omega_{-\beta}\Big(\big(\chi^{\dagger}_{-\kappa}\cdot\chi_{-\beta}\big)\big(\chi^{\dagger}_{\alpha}\cdot\chi_{\lambda}\big)\Big)\Big] \\ & - 2f_L q_R \Big[\omega_{-\kappa}\omega_{\lambda}\omega_{-\alpha}\omega_{\beta}\Big(\big(\chi^{\dagger}_{-\kappa}\cdot\chi_{-\beta}\big)\big(\chi^{\dagger}_{\alpha}\cdot\chi_{\lambda}\big)\Big)\Big] \end{aligned} \tag{A.9}$$

Substituting momenta in the CM frame for a partonic CM energy, $\hat{s}$

$$\begin{aligned} q_{1,2} &= \tfrac{\sqrt{\hat{s}}}{2}(1,0,0,\pm 1) \\ p_{1,2} &= (E_P, \pm\vec{P}) \\ \vec{P} &= \sqrt{E_P^2 - m_f^2}(\sin\theta\cos\phi, \sin\theta\sin\phi, \cos\theta) \\ E_P &= \frac{\sqrt{\hat{s}}}{2} \end{aligned} \tag{A.10}$$

and computing for explicit helicities gives, up to an azimuthal phase and as in equation 3.18:

$$\begin{aligned} A(+,-,\pm,\pm) &= \mp \tfrac{\hat{s}}{2}\sin\theta\sqrt{1-\beta^2}q_R(f_L + f_R); \\ A(-,+,\pm,\pm) &= \mp \tfrac{\hat{s}}{2}\sin\theta\sqrt{1-\beta^2}q_L(f_L + f_R); \\ A(+,-,\pm,\mp) &= \tfrac{\hat{s}}{2}(1 \pm \cos\theta)q_R(f_L(1\mp\beta) + f_R(1\pm\beta)); \\ A(-,+,\pm,\mp) &= \tfrac{\hat{s}}{2}(1 \mp \cos\theta)q_L(f_L(1\mp\beta) + f_R(1\pm\beta)). \end{aligned} \tag{A.11}$$

Appendix B

4DCHM Benchmark points

The exact numerical values of the masses, widths (limited to the new resonances) and couplings of the Z, Z_2 and Z_3 gauge bosons to the light quarks (u, d, c, s) and also to the top quark in terms of left- and right-handed coefficients defined in [3] for the benchmark points of [118] adopted in this work are given. The Z_5 state is neglected, as it is shown to be inaccessible in the $t\bar{t}$ channel. Such values are reported in Tabs. B.1-B.5.

(b)

	M_{Z_i}(GeV)	Γ_{Z_i}(GeV)
Z_2	2048	61
Z_3	2068	98

(c)

	M_{Z_i}(GeV)	Γ_{Z_i}(GeV)
Z_2	2066	39
Z_3	2111	52

(f)

	M_{Z_i}(GeV)	Γ_{Z_i}(GeV)
Z_2	2249	32
Z_3	2312	55

Table B.1: Table of the masses and widths of the neutral gauge resonances limited to Z_2 and Z_3 for the benchmarks of [118] with $f = 0.8$ TeV, $g_* = 2.5$ (b), $f = 1$ TeV, $g_* = 2$ (c) and $f = 1.2$ TeV, $g_* = 1.8$ (f).

(green)

	M_{Z_i}(GeV)	Γ_{Z_i}(GeV)
Z_2	2249	48
Z_3	2312	86

(magenta)

	M_{Z_i}(GeV)	Γ_{Z_i}(GeV)
Z_2	2249	75
Z_3	2312	104

(yellow)

	M_{Z_i}(GeV)	Γ_{Z_i}(GeV)
Z_2	2249	1099
Z_3	2312	822

Table B.2: Table of the masses and widths of the neutral gauge resonances limited to Z_2 and Z_3 for the coloured benchmark points of [118] in green, magenta and yellow.

(b)

	$g^L_{Z_i}(u,c)$	$g^R_{Z_i}(u,c)$	$g^L_{Z_i}(d,s)$	$g^R_{Z_i}(d,s)$
Z	0.256	−0.115	−0.313	0.057
Z_2	0.0075	0.048	0.017	−0.024
Z_3	−0.086	−0.004	0.084	0.002

(c)

	$g^L_{Z_i}(u,c)$	$g^R_{Z_i}(u,c)$	$g^L_{Z_i}(d,s)$	$g^R_{Z_i}(d,s)$
Z	0.256	−0.115	−0.313	0.057
Z_2	0.012	0.061	0.019	−0.031
Z_3	-0.110	−0.003	0.109	0.002

(f)

	$g^L_{Z_i}(u,c)$	$g^R_{Z_i}(u,c)$	$g^L_{Z_i}(d,s)$	$g^R_{Z_i}(d,s)$
Z	0.256	−0.115	−0.313	0.057
Z_2	0.015	0.069	0.020	−0.034
Z_3	−0.125	−0.002	0.123	0.001

Table B.3: Table of the couplings of the up and down quark to the neutral sector limited to Z, Z_2 and Z_3 for the benchmarks of [118] with $f = 0.8$ TeV, $g_* = 2.5$ (b), $f = 1$ TeV, $g_* = 2$ (c) and $f = 1.2$ TeV, $g_* = 1.8$ (f). The couplings of the coloured benchmark points, labelled green, magenta and yellow are identical to those of (f).

(b)

	$g^L_{Z_i}(t)$	$g^R_{Z_i}(t)$
Z	0.248	−0.123
Z_2	−0.108	−0.603
Z_3	0.481	0.009

(c)

	$g^L_{Z_i}(t)$	$g^R_{Z_i}(t)$
Z	0.251	−0.120
Z_2	−0.091	−0.571
Z_3	0.377	0.006

(f)

	$g^L_{Z_i}(t)$	$g^R_{Z_i}(t)$
Z	0.252	−0.118
Z_2	−0.106	−0.486
Z_3	0.427	0.006

Table B.4: Table of the couplings of the top quark to the neutral sector limited to Z, Z_2 and Z_3 for the lettered benchmarks of [118] with $f = 0.8$ TeV, $g_* = 2.5$ (b), $f = 1$ TeV, $g_* = 2$ (c) and $f = 1.2$ TeV, $g_* = 1.8$ (f).

(green)

	$g^L_{Z_i}(t)$	$g^R_{Z_i}(t)$
Z	0.251	−0.117
Z_2	−0.143	−0.617
Z_3	0.591	0.010

(magenta)

	$g^L_{Z_i}(t)$	$g^R_{Z_i}(t)$
Z	0.251	−0.117
Z_2	−0.162	−0.694
Z_3	0.666	0.0118

(yellow)

	$g^L_{Z_i}(t)$	$g^R_{Z_i}(t)$
Z	0.248	−0.120
Z_2	−0.190	−0.790
Z_3	0.795	0.027

Table B.5: Table of the couplings of the top quark to the neutral sector limited to Z, Z_2 and Z_3 for the coloured benchmark points of [118] in green, magenta and yellow.

Appendix C

Fermionic contribution to the KK vector boson self energy

The calculation of the one-loop contribution to a $U(1)$ gauge boson self-energy contribution from a massive fermion is presented. This was performed to determine the mass splitting effect of localised quarks on the KK EW gauge bosons of the AADD model studied in Chapter 7. The interaction was parameterised with generic chiral fermionic couplings:

$$i\gamma^{\mu}\left(P_L\, g_L + P_R\, g_R\right), \tag{C.1}$$

defining $P_{L,R}(1\mp\gamma^5)$. The amplitude is comprised of the fermionic trace and propagator factors integrated over the free momentum, k:

$$\Pi^{\mu\nu}(p^2) = \int \frac{d^4k}{(2\pi)^4} \frac{\mathrm{Tr}\left[\gamma^{\mu}\left(P_L\, g_L + P_R\, g_R\right)(\not{k} - m_f)\gamma^{\nu}\left(P_L\, g_L + P_R\, g_R\right)(\not{p} - \not{k} + m_f)\right]}{(k^2 - m_f^2)((k-p)^2 - m_f^2)}. \tag{C.2}$$

Introducing Feynman parameters [65], the integral takes the simplified form:

$$\begin{aligned} \Pi^{\mu\nu}(p^2) &= \int_0^1 dx \int \frac{d^4l}{(2\pi)^4} \frac{\Gamma^{\mu\nu}}{\left(l^2 - \Delta\right)^2}, \\ \Delta &= m_f^2 - x(1-x)p^2\,; \quad l = k - xp, \end{aligned} \tag{C.3}$$

where the trace evaluates, keeping only even powers of l, to:

$$\Gamma^{\mu\nu} = 2(g_L^2 + g_R^2)\left[g^{\mu\nu}\left(1 - \tfrac{2}{d}\right)l^2 - x(1-x)(p^2\, g^{\mu\nu} - 2p^{\mu}p^{\nu})\right] - 4g_L\, g_R m_f^2\, g^{\mu\nu}. \tag{C.4}$$

Moving to $d = 4 - \epsilon$ dimensions, a transmutation scale of μ^ϵ is picked up and the evaluation of two integrals is required, whose divergent and finite pieces reduce to:

$$\begin{aligned}\mathcal{I}_1 &= \int \frac{d^d l}{(2\pi)^d} \frac{1}{(l^2-\Delta)^2}, \\ &= \frac{i}{(4\pi)^2}\left(\frac{2}{\epsilon} - \log\Delta - \gamma + \log(4\pi) + \mathcal{O}(\epsilon)\right),\end{aligned} \tag{C.5}$$

$$\begin{aligned}\mathcal{I}_2 &= \frac{1}{d}\int \frac{d^d l}{(2\pi)^d} \frac{l^2}{(l^2-\Delta)^2}, \\ &= \frac{-i\Delta}{2(4\pi)^2}\Gamma\left(\tfrac{\epsilon}{2}-1\right)\left(\frac{4\pi}{\Delta}\right)^{\frac{\epsilon}{2}},\end{aligned} \tag{C.6}$$

$$\begin{aligned}(2-\epsilon)\mathcal{I}_2 &= -\frac{i\Delta}{(4\pi)^2}\left(1-\tfrac{\epsilon}{2}\right)\Gamma\left(\tfrac{\epsilon}{2}-1\right)\left(1+\frac{\epsilon}{2}\log\frac{4\pi}{\Delta}+\mathcal{O}(\epsilon^2)\right), \\ &= \Delta\,\mathcal{I}_1.\end{aligned} \tag{C.7}$$

Taking the massless limit first, expanding $\mu^\epsilon = (1 + \epsilon \log\mu)$, the self energy can be written as:

$$\begin{aligned}\Pi_0^{\mu\nu}(p^2,\mu) = &-\frac{2i}{(4\pi)^2}(g_L^2+g_R^2)\int_0^1 dx\,\left(x(1-x)(p^2\,g^{\mu\nu}-2p^\mu p^\nu) - g^{\mu\nu}\Delta_0\right) \\ &\times\left(\frac{2}{\epsilon}-\log\Delta_0-\gamma+\log(4\pi)+\log\mu^2\right),\end{aligned} \tag{C.8}$$

where $\Delta_0 = -x(1-x)p^2$. Keeping only divergent and finite terms for $\epsilon \to 0$:

$$\Pi_0^{\mu\nu}(p^2,\mu) = \frac{4i}{(4\pi)^2}(g_L^2+g_R^2)\,p^2\int_0^1 dx\,x(1-x)\left(g^{\mu\nu}-\frac{p^\mu p^\nu}{p^2}\right)\left(\log\frac{p^2}{\Lambda^2}+\log(-x(1-x))\right). \tag{C.9}$$

The modified minimal subtraction ($\overline{MS}$) scheme has been anticipated and a cutoff, Λ, introduced such that:

$$\frac{2}{\epsilon} - \gamma + \log(4\pi) + \log\mu^2 \equiv \log\Lambda^2. \tag{C.10}$$

The Feynman parameter integrals to compute are then:

$$\mathcal{I}_1^x = \int_0^1 dx\,x(1-x) = -\frac{1}{6}, \tag{C.11}$$

$$\mathcal{I}_2^x = \int_0^1 dx\,x(1-x)\log(-x(1-x)) = -\frac{1}{6}\left(\frac{5}{3}-i\pi\right), \tag{C.12}$$

giving:

$$i\Pi_0^{\mu\nu}(p^2,\Lambda) = \frac{(g_L^2+g_R^2)}{24\pi^2}p^2\left(g^{\mu\nu}-\frac{p^\mu p^\nu}{p^2}\right)\left(\log\frac{p^2}{\Lambda^2}+\frac{5}{3}-i\pi\right). \tag{C.13}$$

In the massive case using the same scheme, Δ_0 is replaced with $\Delta = p^2\tilde{\Delta}$ and an extra chirality-flipped term occurs:

$$\begin{aligned}\Pi^{\mu\nu}(p^2, m_f, \mu) = -\frac{2i}{(4\pi)^2}\int_0^1 dx \Bigg[(g_L^2+g_R^2)\Big(x(1-x)(p^2\,g^{\mu\nu}-2p^\mu p^\nu)-p^2 g^{\mu\nu}\tilde{\Delta}\Big) \\ + 2g_L g_R m_f^2 g^{\mu\nu}\Bigg]\left(\frac{2}{\epsilon}-\log\tilde{\Delta}-\log p^2-\gamma+\log(4\pi)+\log\mu^2\right), \\ \to \frac{2i}{(4\pi)^2}\int_0^1 dx\left[2x(1-x)(g_L^2+g_R^2)(p^2\,g^{\mu\nu}-p^\mu p^\nu)-(g_L-g_R)^2 m_f^2\,g^{\mu\nu}\right] \\ \times\left(\log\frac{p^2}{\Lambda^2}+\log\tilde{\Delta}\right).\end{aligned} \tag{C.14}$$

The Feynman integrals to compute are then in terms of $\tilde{\Delta} = \rho - x(1-x)$, with $\rho = \frac{m_f^2}{p^2}$:

$$\begin{aligned}\mathcal{I}_3^x &= \int_0^1 dx\,\log\left(\rho - x(1-x)\right), \\ &= \log\rho + 2 - 2u\tan^{-1}\left(\frac{1}{u}\right),\end{aligned} \tag{C.15}$$

$$\begin{aligned}\mathcal{I}_4^x &= \int_0^1 dx\,x(1-x)\log\left(\rho - x(1-x)\right), \\ &= \frac{1}{6}\log\rho - \frac{2}{3}\rho - \frac{5}{18} + \frac{1}{3}(2\rho+1)u\tan^{-1}\left(\frac{1}{u}\right),\end{aligned} \tag{C.16}$$

$$u \equiv \sqrt{4\rho-1}, \tag{C.17}$$

giving:

$$i\Pi^{\mu\nu}(p^2, m_f, \mu) = \frac{p^2}{8\pi^2}\left[\left(g^{\mu\nu}-\frac{p^\mu p^\nu}{p^2}\right)\Pi_T + \frac{p^\mu p^\nu}{p^2}\Pi_L\right], \tag{C.18}$$

$$\begin{aligned}\Pi_T &= (g_L^2+g_R^2)f_T + \rho\, g_L g_R f_L, \\ \Pi_L &= -\frac{1}{2}f_L,\end{aligned} \tag{C.19}$$

$$\begin{aligned}f_T(p^2, m_f, \Lambda) = \frac{1}{3}\Bigg(2\,(5\rho+1)\,u\tan^{-1}\left(\frac{1}{u}\right) - 10\rho \\ + (1-3\rho)\log\left(\frac{m_f^2}{\Lambda^2}\right) - \frac{5}{3}\Bigg),\end{aligned} \tag{C.20}$$

$$f_L(p^2, m_f, \Lambda) = 2\left(\log\frac{m_f^2}{\Lambda^2} - 2u\tan^{-1}\left(\frac{1}{u}\right) + 2\right). \tag{C.21}$$

The Π_T term will ultimately contribute to the correction to the two point function annd the contribution to the KK vector boson mass can be calculated for each quark by inserting the appropriate chiral couplings to the SM quarks times a factor $\sqrt{2}$. Replacing

the bulk quark contributions of [147] with these corrections gave an overall reduction of the mass splitting between W_3' and B' of around 1% of the compactification scale, R^{-1}. The cutoff value chosen was $20R^{-1}$ keeping to the choices made in [147]. This is about a 15% effect and does not change the fact that the splitting incurred is dominant over the EW mass contributions and therefore drives the mixing toward the pure $SU(2)_L$ and hypercharge states. The main reason this is so small is because the orbifold corrections dominate the mass splittings and do not have any contributions from bulk fermions, who only contribute via the finite bulk terms, whose removal has a negligible effect on the splitting.

References

[1] L. Basso, K. Mimasu, and S. Moretti, JHEP **1209**, 024 (2012), 1203.2542.

[2] L. Basso, K. Mimasu, and S. Moretti, JHEP **1211**, 060 (2012), 1208.0019.

[3] D. Barducci, S. De Curtis, K. Mimasu, and S. Moretti, (2012), 1212.5948, To appear in Phys. Rev. D.

[4] E. Accomando, K. Mimasu, and S. Moretti, (2013), 1304.4494, To appear in JHEP.

[5] S. Glashow, Nucl.Phys. **22**, 579 (1961); S. Weinberg, Phys. Rev. Lett. **19**, 1264 (1967); A. Salam, Conf. Proc. **C680519**, 367 (1968).

[6] M. Srednicki, *Quantum Field Theory* (Cambridge University Press, 2007).

[7] Particle Data Group, J. Beringer *et al.*, Phys. Rev. **D86**, 010001 (2012).

[8] B. W. Lee, C. Quigg, and H. Thacker, Phys. Rev. Lett. **38**, 883 (1977); M. S. Chanowitz and M. K. Gaillard, Nucl. Phys. **B261**, 379 (1985); T. Appelquist and M. S. Chanowitz, Phys. Rev. Lett. **59**, 2405 (1987).

[9] ATLAS Collaboration, G. Aad *et al.*, Phys. Lett. **B716**, 1 (2012), 1207.7214; CMS Collaboration, S. Chatrchyan *et al.*, Phys. Lett. **B716**, 30 (2012), 1207.7235.

[10] CMS Collaboration, S. Chatrchyan *et al.*, CERN Report No. CMS-PAS-HIG-13-005, 2013 (unpublished); ATLAS Collaboration, G. Aad *et al.*, CERN Report No. ATLAS-CONF-2013-014, ATLAS-COM-CONF-2013-025, 2013 (unpublished).

[11] ATLAS Collaboration, G. Aad *et al.*, CERN Report No. ATLAS-CONF-2013-040, ATLAS-COM-CONF-2013-048, 2013 (unpublished); ATLAS Collaboration, G. Aad *et al.*, CERN Report No. CERN-PH-EP-2013-102, 2013 (unpublished), 1307.1432.

[12] S. Dawson, (1998), hep-ph/9901280.

[13] D0 Collaboration, S. Abachi *et al.*, Phys. Rev. Lett. **74**, 2632 (1995), hep-ex/9503003; CDF Collaboration, F. Abe *et al.*, Phys. Rev. Lett. **74**, 2626 (1995), hep-ex/9503002.

[14] CMS Collaboration, S. Chatrchyan *et al.*, CERN Report No. CMS-PAS-TOP-12-001, 2012 (unpublished).

[15] Tevatron Electroweak Working Group, CDF Collaboration, D0 Collaboration, Fermilab Report No. FERMILAB-TM-2504-E, CDF-NOTE-10549, D0-NOTE-6222, 2011 (unpublished), 1107.5255.

[16] CMS Collaboration, S. Chatrchyan *et al.*, CERN Report No. CMS-PAS-BTV-11-004, 2012 (unpublished); ATLAS Collaboration, G. Aad *et al.*, CERN Report No. ATLAS-CONF-2012-097, ATLAS-COM-CONF-2012-089, 2012 (unpublished).

[17] E. Eichten, I. Hinchliffe, K. D. Lane, and C. Quigg, Rev. Mod. Phys. **56**, 579 (1984).

[18] See http://hep.pa.msu.edu/cteq/public/cteq6.html.

[19] P. Nason, S. Dawson, and R. K. Ellis, Nucl. Phys. **B303**, 607 (1988); W. Beenakker, H. Kuijf, W. van Neerven, and J. Smith, Phys. Rev. **D40**, 54 (1989); W. Beenakker, W. L. van Neerven, R. Meng, G. A. Schuler, and J. Smith, Nucl. Phys. **B351**, 507 (1991); M. L. Mangano, P. Nason, and G. Ridolfi, Nucl. Phys. **B373**, 295 (1992).

[20] W. Bernreuther, M. Fucker, and Z. Si, Int. J. Mod. Phys. **A21**, 914 (2006), hep-ph/0509210; S. Moretti, M. R. Nolten, and D. A. Ross, Phys. Lett. **B639**, 513 (2006;), hep-ph/0603083; J. H. Kuhn, A. Scharf, and P. Uwer, Eur. Phys. J. **C51**, 37 (2007), hep-ph/0610335; W. Hollik and M. Kollar, Phys. Rev. **D77**, 014008 (2008), 0708.1697; W. Bernreuther, M. Fucker, and Z.-G. Si, Phys. Rev. **D78**, 017503 (2008), 0804.1237.

[21] M. Czakon, P. Fiedler, and A. Mitov, Phys. Rev. Lett. **110**, 252004 (2013), 1303.6254.

[22] ATLAS Collaboration, G. Aad *et al.*, CERN Report No. ATLAS-CONF-2012-149, 2012 (unpublished); CMS Collaboration, S. Chatrchyan *et al.*, CERN Report No. CMS-PAS-TOP-12-006, 2012 (unpublished); CMS Collaboration, S. Chatrchyan *et al.*, CERN Report No. CMS-PAS-TOP-12-007, 2012 (unpublished).

[23] Particle Data Group, J. Beringer *et al.*, Phys. Rev. **D86**, 010001 (2012).

[24] R. Dalitz and G. R. Goldstein, Phys. Rev. **D45**, 1531 (1992); L. Sonnenschein, Phys. Rev. **D72**, 095020 (2005), hep-ph/0510100; B. A. Betchart, R. Demina, and A. Harel, (unpublished) (2013), 1305.1878.

[25] R. Brown, D. Sahdev, and K. Mikaelian, Phys. Rev. Lett. **43**, 1069 (1979); J. H. Kuhn and G. Rodrigo, Phys. Rev. **D59**, 054017 (1999), hep-ph/9807420.

[26] CDF Collaboration, T. Aaltonen *et al.*, Phys. Rev. **D83**, 112003 (2011), 1101.0034; D0 Collaboration, V. M. Abazov *et al.*, Phys. Rev. **D84**, 112005 (2011), 1107.4995.

[27] O. Antunano, J. H. Kuhn, and G. Rodrigo, Phys. Rev. **D77**, 014003 (2008), 0709.1652.

[28] Z.-q. Zhou, B. Xiao, Y.-k. Wang, and S.-h. Zhu, Phys. Rev. **D83**, 094022 (2011), 1102.1044.

[29] R. Vega and J. Wudka, Phys. Rev. **D53**, 5286 (1996), hep-ph/9511318.

[30] M. Jezabek and J. H. Kuhn, Phys. Lett. **B207**, 91 (1988); M. Jezabek and J. H. Kuhn, Phys. Lett. **B329**, 317 (1994), hep-ph/9403366.

[31] G. Mahlon and S. J. Parke, Phys. Rev. **D53**, 4886 (1996), hep-ph/9512264.

[32] D. Krohn, T. Liu, J. Shelton, and L.-T. Wang, Phys. Rev. **D84**, 074034 (2011), 1105.3743.

[33] A. Papaefstathiou and K. Sakurai, JHEP **1206**, 069 (2012), 1112.3956.

[34] W. Bernreuther, A. Brandenburg, Z. Si, and P. Uwer, Int. J. Mod. Phys. **A18**, 1357 (2003), hep-ph/0111346.

[35] M. Baumgart and B. Tweedie, (2012), 1212.4888.

[36] CMS Collaboration, S. Chatrchyan *et al.*, CERN Report No. CMS-PAS-JME-10-013, 2011 (unpublished); ATLAS Collaboration, G. Aad *et al.*, CERN Report No. ATLAS-CONF-2012-065, ATLAS-COM-CONF-2012-095, 2012 (unpublished).

[37] ATLAS Collaboration, G. Aad *et al.*, JHEP **1301**, 116 (2013), 1211.2202; ATLAS Collaboration, G. Aad *et al.*, JHEP **1209**, 041 (2012), 1207.2409; CMS Collaboration, S. Chatrchyan *et al.*, JHEP **1209**, 029 (2012), 1204.2488.

[38] CMS Collaboration, S. Chatrchyan *et al.*, CERN Report No. CMS-PAS-EXO-11-093, 2012 (unpublished).

[39] J. Shelton, Phys. Rev. **D79**, 014032 (2009), 0811.0569; D. Krohn, J. Shelton, and L.-T. Wang, JHEP **1007**, 041 (2010), 0909.3855.

[40] B. Fuks, M. Klasen, F. Ledroit, Q. Li, and J. Morel, Nucl. Phys. **B797**, 322 (2008), 0711.0749.

[41] R. Hamberg, W. van Neerven, and T. Matsuura, Nucl. Phys. **B359**, 343 (1991); C. Anastasiou, L. J. Dixon, K. Melnikov, and F. Petriello, Phys. Rev. **D69**, 094008 (2004), hep-ph/0312266; K. Melnikov and F. Petriello, Phys. Rev. **D74**, 114017 (2006), hep-ph/0609070.

[42] U. Baur, O. Brein, W. Hollik, C. Schappacher, and D. Wackeroth, Phys. Rev. **D65**, 033007 (2002), hep-ph/0108274.

[43] P. Langacker, R. W. Robinett, and J. L. Rosner, Phys. Rev. **D30**, 1470 (1984); M. Dittmar, A. Djouadi, and A.-S. Nicollerat, Phys. Lett. **B583**, 111 (2004), hep-ph/0307020.

[44] A. Leike, Phys. Rept. **317**, 143 (1999), hep-ph/9805494.

[45] M. S. Carena, A. Daleo, B. A. Dobrescu, and T. M. Tait, Phys. Rev. **D70**, 093009 (2004), hep-ph/0408098.

[46] P. Langacker, Rev. Mod. Phys. **81**, 1199 (2008), 0801.1345.

[47] T. G. Rizzo, (2009), hep-ph/0610104.

[48] J. Erler, P. Langacker, S. Munir, and E. Rojas, JHEP **0908**, 017 (2009), 0906.2435; J. Erler, P. Langacker, S. Munir, and E. Rojas, AIP Conf. Proc. **1200**, 790 (2010), 0910.0269.

[49] C. Coriano, A. E. Faraggi, and M. Guzzi, Phys. Rev. **D78**, 015012 (2008), 0802.1792; C. P. Hays, A. V. Kotwal, and O. Stelzer-Chilton, Mod. Phys. Lett. **A24**, 2387 (2009), 0910.1770.

[50] F. Petriello and S. Quackenbush, Phys. Rev. **D77** (2008), 0801.4389; Y. Li, F. Petriello, and S. Quackenbush, Phys. Rev. **D80** (2009), 0906.4132.

[51] J. Erler, P. Langacker, S. Munir, and E. Rojas, JHEP **1111**, 076 (2011), 1103.2659.

[52] P. Athron, S. King, D. Miller, S. Moretti, and R. Nevzorov, Phys. Rev. **D80**, 035009 (2009), 0904.2169; P. Athron *et al.*, Phys. Lett. **B681**, 448 (2009), 0901.1192.

[53] E. Accomando, S. De Curtis, D. Dominici, and L. Fedeli, Phys. Rev. **D79**, 055020 (2009), 0807.5051; E. Accomando, S. De Curtis, D. Dominici, and L. Fedeli, Phys. Rev. **D83**, 015012 (2011), 1010.0171.

[54] E. Salvioni, G. Villadoro, and F. Zwirner, JHEP **0911**, 068 (2009), 0909.1320; E. Salvioni, A. Strumia, G. Villadoro, and F. Zwirner, JHEP **1003**, 010 (2010), 0911.1450.

[55] P. Osland, A. Pankov, A. Tsytrinov, and N. Paver, Phys. Rev. **D79**, 115021 (2009), 0904.4857.

[56] E. Accomando, A. Belyaev, L. Fedeli, S. F. King, and C. Shepherd-Themistocleous, Phys. Rev. **D83**, 075012 (2010), 1010.6058.

[57] H. Georgi and S. Glashow, Phys. Rev. Lett. **32**, 438 (1974).

[58] R. Mohapatra and J. C. Pati, Phys. Rev. **D11**, 2558 (1975).

[59] J. L. Hewett and T. G. Rizzo, Phys. Rept. **183**, 193 (1989).

[60] D. Chung *et al.*, Phys. Rept. **407**, 1 (2005), hep-ph/0312378.

[61] M. J. Strassler and K. M. Zurek, Phys. Lett. **B651**, 374 (2007), hep-ph/0604261.

[62] N. Arkani-Hamed, S. Dimopoulos, and G. Dvali, Phys. Lett. **B429**, 263 (1998); N. Arkani-Hamed, S. Dimopoulos, and G. R. Dvali, Phys. Rev. **D59**, 086004 (1999), hep-ph/9807344.

[63] I. Antoniadis, Phys. Lett. **B246**, 377 (1990).

[64] R. Sundrum, (2005), hep-th/0508134.

[65] M. Peskin and D. Schroeder, *An introduction to quantum field theory* (Westview press, 1995).

[66] L. H. Ryder, *Quantum Field Theory*, 2 ed. (Cambridge University Press, 1996).

[67] G. Cacciapaglia, C. Csaki, G. Marandella, and A. Strumia, Phys. Rev. **D74**, 033011 (2006), hep-ph/0604111.

[68] L. Maiani, (2013), 1303.6154, (unpublished).

[69] CDF Collaboration, T. Aaltonen *et al.*, Phys. Rev. Lett. **102**, 091805 (2009), 0811.0053; CDF Collaboration, T. Aaltonen *et al.*, Phys. Rev. Lett. **102**, 031801 (2009), 0810.2059.

[70] ATLAS Collaboration, G. Aad *et al.*, CERN Report No. ATLAS-CONF-2013-017, 2013 (unpublished); CMS Collaboration, S. Chatrchyan *et al.*, CERN Report No. CMS-PAS-EXO-12-061, 2013 (unpublished).

[71] E. Accomando, D. Becciolini, A. Belyaev, S. Moretti, and C. Shepherd-Themistocleous, (2013), 1304.6700.

[72] S. Godfrey and T. A. Martin, Phys. Rev. Lett. **101**, 151803 (2008), 0807.1080; R. Diener, S. Godfrey, and T. A. W. Martin, Phys. Rev. **D83** (2010), 1006.2845.

[73] CDF Collaboration, T. Aaltonen *et al.*, Phys. Rev. **D84**, 072004 (2011), 1107.5063; CDF Collaboration, T. Aaltonen *et al.*, Phys. Rev. **D84**, 072003 (2011), 1108.4755.

[74] ATLAS Collaboration, G. Aad *et al.*, CERN Report No. ATLAS-CONF-2012-136, 2012 (unpublished); CMS Collaboration, S. Chatrchyan *et al.*, CERN Report No. CMS-PAS-TOP-11-009, 2012 (unpublished); CMS Collaboration, S. Chatrchyan *et al.*, CERN Report No. CMS-PAS-B2G-12-005, 2013 (unpublished); CMS Collaboration, S. Chatrchyan *et al.*, CERN Report No. CMS-PAS-B2G-12-006, 2013 (unpublished).

[75] V. Abazov *et al.*, Phys. Lett. Letters **B668**, 98 (2008).

[76] C. T. Hill, Phys. Lett. **B345**, 483 (1995), hep-ph/9411426.

[77] P. H. Frampton and S. L. Glashow, Phys. Lett. **B190**, 157 (1987).

[78] K. Hagiwara and D. Zeppenfeld, Nucl. Phys. **B274**, 1 (1986).

[79] M. Arai, N. Okada, K. Smolek, and V. Simak, Acta Phys. Polon. **B40**, 93 (2008), 0804.3740.

[80] H. Georgi, *Lie algebras in particle physics* (Westview Press, 1999).

[81] A. E. Faraggi and D. V. Nanopoulos, Mod. Phys. Lett. **A6**, 61 (1991).

[82] C. Coriano, A. E. Faraggi, and M. Guzzi, Eur. Phys. J. **C53**, 421 (2008), 0704.1256.

[83] H. M. K. Hagiwara, J. Kanzaki and I. Watanabe, *HELAS: HELicity Amplitude Subroutines for Feynman diagram evaluations*, 2000.

[84] T. Stelzer and W. F. Long, Comput. Phys. Commun. **81**, 357 (1994), hep-ph/9401258.

[85] G. P. Lepage, Report No. CLNS-80/447, 1980 (unpublished).

[86] B. Xiao, Y.-K. Wang, Z.-Q. Zhou, and S.-h. Zhu, Phys. Rev. **D83**, 057503 (2011), 1101.2507.

[87] J. L. Hewett, J. Shelton, M. Spannowsky, T. M. Tait, and M. Takeuchi, Phys. Rev. **D84**, 054005 (2011), 1103.4618.

[88] J. H. Kuhn and G. Rodrigo, JHEP **1201**, 063 (2012), 1109.6830.

[89] E. Alvarez, Phys. Rev. **D85**, 094026 (2012), 1202.6622.

[90] G. Altarelli *et al.*, editors, *Z physics at LEP-1* Vol. 1, CERN, 1989.

[91] CMS Collaboration, G. Bayatian *et al.*, CERN Report No. CERN-LHCC-2006-001, CMS-TDR-008-1, 2006 (unpublished); ATLAS Collaboration, G. Aad *et al.*, CERN Report No. CERN-LHCC-99-14, ATLAS-TDR-14, 1999 (unpublished); ATLAS Collaboration, G. Aad *et al.*, CERN Report No. CERN-LHCC-99-15, ATLAS-TDR-15, 1999 (unpublished).

[92] ATLAS Collaboration, G. Aad *et al.*, Eur. Phys. J. **C72**, 2062 (2012), 1204.6720.

[93] J. Olzem, JINST **6**, C12039 (2011).

[94] B. Mele and G. Altarelli, Phys. Lett. **B299**, 345 (1993); G. Bonvicini and L. Randall, Phys. Rev. Lett. **73**, 392 (1994), hep-ph/9401299; A. F. Falk and M. E. Peskin, Phys. Rev. **D49**, 3320 (1994), hep-ph/9308241; M. Tung, J. Bernabeu, and J. Penarrocha, Phys. Lett. **B418**, 181 (1998), hep-ph/9706444.

[95] ALEPH Collaboration, D. Buskulic *et al.*, Phys. Lett. **B365**, 437 (1996); OPAL Collaboration, G. Abbiendi *et al.*, Phys. Lett. **B444**, 539 (1998), hep-ex/9808006; DELPHI Collaboration, P. Abreu *et al.*, Phys. Lett. **B474**, 205 (2000).

[96] L. Basso, S. Moretti, and G. M. Pruna, JHEP **1108**, 122 (2011), 1106.4762.

[97] L. Basso, *Phenomenology of the minimal B-L extension of the Standard Model at the LHC*, PhD thesis, University of Southampton, 2011, 1106.4462.

[98] F. del Aguila, M. Masip, and M. Perez-Victoria, Nucl. Phys. **B456**, 531 (1995), hep-ph/9507455; P. H. Chankowski, S. Pokorski, and J. Wagner, Eur. Phys. J. **C47**, 187 (2006), hep-ph/0601097; A. Ferroglia, A. Lorca, and J. van der Bij, Annalen Phys. **16**, 563 (2007), hep-ph/0611174.

[99] F. del Aguila, G. Coughlan, and M. Quiros, Nucl. Phys. **B307**, 633 (1988).

[100] T. Appelquist, B. A. Dobrescu, and A. R. Hopper, Phys. Rev. **D68**, 035012 (2003), hep-ph/0212073.

[101] The ALEPH, DELPHI, L3, OPAL, SLD Collaborations, the LEP Electroweak Working Group, the SLD Electroweak and Heavy Flavour Groups, Phys. Rept. **427**, 257 (2006), hep-ex/0509008.

[102] DELPHI Collaboration, P. Abreu *et al.*, Z.Phys. **C65**, 603 (1995).

[103] A. Pukhov, *CalcHEP 2.3: MSSM, structure functions, event generation, batchs, and generation of matrix elements for other packages*, 2004, hep-ph/0412191.

[104] A. Semenov, *LanHEP: A Package for automatic generation of Feynman rules in gauge models*, 1996, hep-ph/9608488; A. Semenov, *LanHEP - a package for automatic generation of Feynman rules from the Lagrangian. Updated version 3.1*, 2010, 1005.1909.

[105] N. D. Christensen and C. Duhr, Comput. Phys. Commun. **180**, 1614 (2009), 0806.4194.

[106] N. D. Christensen *et al.*, Eur. Phys. J. **C71**, 1541 (2011), 0906.2474.

[107] G. Brooijmans *et al.*, *Les Houches 2011: Physics at TeV Colliders New Physics Working Group Report*, 2012, 1203.1488.

[108] See https://feynrules.irmp.ucl.ac.be/wiki/b-l-sm.

[109] M. Frank, A. Hayreter, and I. Turan, Phys. Rev. **D84**, 114007 (2011), 1108.0998.

[110] S. Chatrchyan *et al.*, CERN Report No. CMS-PAS-EXO-12-023, 2013 (unpublished).

[111] See https://twiki.cern.ch/twiki/bin/view/cmspublic/swguidecategory.

[112] CMS Collaboration, S. Chatrchyan *et al.*, Phys. Lett. **B716**, 82 (2012), 1206.1725.

[113] ATLAS Collaboration, G. Aad *et al.*, CERN Report No. ATLAS-CONF-2013-066, 2013 (unpublished).

[114] CMS Collaboration, S. Chatrchyan *et al.*, Phys. Lett. **B714**, 158 (2012), 1206.1849.

[115] ATLAS Collaboration, G. Aad *et al.*, JHEP **1211**, 138 (2012), 1209.2535.

[116] L. Basso, O. Fischer, and J. van der Bij, Phys. Rev. **D87**, 035015 (2013), 1207.3250.

[117] CMS Collaboration, S. Chatrchyan *et al.*, CERN Report No. CMS-PAS-EXO-11-008, 2012 (unpublished).

[118] D. Barducci, A. Belyaev, S. De Curtis, S. Moretti, and G. M. Pruna, JHEP **1304**, 152 (2013), 1210.2927.

[119] S. De Curtis, M. Redi, and A. Tesi, JHEP **1204**, 042 (2012), 1110.1613.

[120] C. T. Hill and E. H. Simmons, Phys. Rept. **381**, 235 (2003), hep-ph/0203079.

[121] S. Weinberg, Phys. Rev. **D13**, 974 (1976); L. Susskind, Phys. Rev. **D20**, 2619 (1979).

[122] S. F. King, Rept.Prog.Phys. **58**, 263 (1995), hep-ph/9406401.

[123] N. Arkani-Hamed, A. G. Cohen, and H. Georgi, Phys. Lett. **B513**, 232 (2001), hep-ph/0105239.

[124] M. Schmaltz and D. Tucker-Smith, Ann. Rev. Nucl. Part. Sci. **55**, 229 (2005), hep-ph/0502182.

[125] N. Arkani-Hamed, A. G. Cohen, and H. Georgi, Phys. Rev. Lett. **86**, 4757 (2001), hep-th/0104005.

[126] G. Giudice, C. Grojean, A. Pomarol, and R. Rattazzi, JHEP **0706**, 045 (2007), hep-ph/0703164.

[127] K. Agashe, R. Contino, and A. Pomarol, Nucl. Phys. **B719**, 165 (2005), hep-ph/0412089.

[128] R. Contino, (2010), 1005.4269.

[129] D. Barducci, L. Fedeli, S. Moretti, S. Curtis, and G. Pruna, JHEP **1304**, 038 (2013), 1212.4875.

[130] D. Barducci *et al.*, (2013), 1302.2371.

[131] ALEPH Collaboration, DELPHI Collaboration, L3 Collaboration, OPAL Collaboration, SLD Collaboration, LEP Electroweak Working Group, SLD Electroweak Group, SLD Heavy Flavour Group, S. Schael *et al.*, Phys. Rept. **427**, 257 (2006), hep-ex/0509008.

[132] ATLAS Collaboration, G. Aad *et al.*, Phys. Lett. **B701**, 50 (2011), 1103.1391; CMS Collaboration, S. Chatrchyan *et al.*, JHEP **1208**, 023 (2012), 1204.4764; ATLAS Collaboration, D. f. t. A. C. Hayden, EPJ Web Conf. **28**, 12003 (2012), 1201.4721.

[133] CMS Collaboration, S. Chatrchyan *et al.*, Phys. Lett. **B716**, 103 (2012), 1203.5410; CMS Collaboration, S. Chatrchyan *et al.*, Phys. Rev. Lett. **107**, 271802 (2011), 1109.4985; CMS Collaboration, S. Chatrchyan *et al.*, JHEP **1205**, 123 (2012), 1204.1088; CMS Collaboration, S. Chatrchyan *et al.*, CERN Report No. CMS-PAS-EXO-11-066, 2012 (unpublished).

[134] A. Belyaev, N. D. Christensen, and A. Pukhov, Comput. Phys. Commun. **184**, 1729 (2013), 1207.6082.

[135] I. Antoniadis and C. Bachas, Phys. Lett. **B450**, 83 (1999), hep-th/9812093.

[136] J. D. Lykken, Phys. Rev. **D54**, 3693 (1996), hep-th/9603133; I. Antoniadis and B. Pioline, Nucl. Phys. **B550**, 41 (1999), hep-th/9902055; K. Benakli and Y. Oz, Phys. Lett. **B472**, 83 (2000), hep-th/9910090.

[137] C. Burgess, L. E. Ibanez, and F. Quevedo, Phys. Lett. **B447**, 257 (1999), hep-ph/9810535; K. Benakli, Phys. Rev. **D60**, 104002 (1999), hep-ph/9809582.

[138] G. Shiu and S. H. Tye, Phys. Rev. **D58**, 106007 (1998), hep-th/9805157; Z. Kakushadze and S. H. Tye, Nucl. Phys. **B548**, 180 (1999), hep-th/9809147; G. Aldazabal, L. E. Ibanez, and F. Quevedo, JHEP **0001**, 031 (2000), hep-th/9909172; L. E. Ibanez, C. Munoz, and S. Rigolin, Nucl. Phys. **B553**, 43 (1999), hep-ph/9812397.

[139] I. Antoniadis and K. Benakli, Phys. Lett. **B326**, 69 (1994), hep-th/9310151.

[140] I. Antoniadis, K. Benakli, and M. Quiros, Phys. Lett. **B331**, 313 (1994), hep-ph/9403290; K. Benakli, Phys. Lett. **B386**, 106 (1996), hep-th/9509115; I. Antoniadis and M. Quiros, Phys. Lett. **B392**, 61 (1997), hep-th/9609209; I. Antoniadis, S. Dimopoulos, and G. Dvali, Nucl. Phys. **B516**, 70 (1998), hep-ph/9710204; A. Pomarol and M. Quiros, Phys. Lett. **B438**, 255 (1998), hep-ph/9806263.

[141] P. Nath and M. Yamaguchi, Phys. Rev. **D60**, 116004 (1999), hep-ph/9902323; P. Nath and M. Yamaguchi, Phys. Rev. **D60**, 116006 (1999), hep-ph/9903298; W. J. Marciano, Phys. Rev. **D60**, 093006 (1999), hep-ph/9903451; R. Casalbuoni, S. De Curtis, D. Dominici, and R. Gatto, Phys. Lett. **B462**, 48 (1999), hep-ph/9907355; C. D. Carone, Phys. Rev. **D61**, 015008 (2000), hep-ph/9907362.

[142] T. Appelquist, H.-C. Cheng, and B. A. Dobrescu, Phys. Rev. **D64**, 035002 (2001), hep-ph/0012100.

[143] T. Han, J. D. Lykken, and R.-J. Zhang, Phys. Rev. **D59**, 105006 (1999), hep-ph/9811350; G. F. Giudice, R. Rattazzi, and J. D. Wells, Nucl. Phys. **B544**, 3 (1999), hep-ph/9811291.

[144] E. Accomando, I. Antoniadis, and K. Benakli, Nucl. Phys. **B579**, 3 (2000), hep-ph/9912287.

[145] M. Masip and A. Pomarol, Phys. Rev. **D60**, 096005 (1999), hep-ph/9902467.

[146] A. Strumia, Phys. Lett. **B466**, 107 (1999), hep-ph/9906266.

[147] H.-C. Cheng, K. T. Matchev, and M. Schmaltz, Phys. Rev. **D66**, 036005 (2002), hep-ph/0204342.

[148] G. Cacciapaglia, A. Deandrea, and S. D. Curtis, Phys. Lett. **B682**, 43 (2009), 0906.3417.

[149] CMS Collaboration, S. Chatrchyan *et al.*, CERN Report No. CMS-PAS-EXO-12-016, 2012 (unpublished).